MONASH University

Stability Analysis of Horizontal Convection Under the Centrifugal Buoyancy Approximation

by

Peyman Mayeli

A thesis submitted for the degree of

Doctor of Philosophy

at Monash University in 2021

Department of Mechanical and Aerospace Engineering

To my late grandfather, **Ali Davoudi**, whom I lost during my Ph. D.

To my dear wife, **Solmaz**, for her incredible patience and support during all of this journey.

Copyright notice

Abstract

This thesis classifies different possible scenarios for numerical simulation of natural convection problems in two main categories as compressible and incompressible. Then, an incompressible approach from the incompressible category called the 'Gay-Lussac approximation' is selected for further study. This approach is distinguished against classical implementation of the Oberbeck—Boussinesq approximation by extending the density variations beyond only the gravity term of the momentum equation. Indeed, under the Gay-Lussac approach, density variations are taken into account in any term of the governing equations where density appears; i.e. the advection and convection terms of the momentum and energy equations, respectively, associated with the continuity equation via a linear density state equation. Such a treatment leads to emergence of the Gay-Lussac parameter as a product of the volumetric thermal expansion coefficient and reference temperature difference as a modifier of the aforementioned terms. The Gay-Lussac parameter also emerges in the linear density state equation that confines its alteration to $0 \leq Ga \leq 2$ for a physical density value.

The Gay-Lussac approach is simplified in two steps. In the first step, it is shown that ignoring density ratio from the continuity equation brings no difference to the produced results compared to the original form of this approach. Then, the centrifugal approximation is introduced by extending the density variations only to the advection term of the momentum equation beyond the gravity term, appropriate to capture the centrifugal effects for rotating buoyancy-driven systems. Both simplified Gay-Lussac approach and centrifugal approximations were applied to the annulus and square cavity benchmark problems and it is shown that, the centrifugal buoyancy approximations works slightly better than the convectional Oberbeck—Boussinesq approximation.

One of the natural convection phenomena that features intrinsic rotation (in the form of an overturning circulation) at any Rayleigh number is horizontal convection, in which a fluid is heated unevenly across a horizontal boundary. In this thesis, the centrifugal approximation is adopted to study the non-Boussinesq effects and stability analysis (both locally and globally) of horizontal convection over an enclosed rectangular enclosure with an aspect ratio of height to length of 0.16 at a fixed unity Prandtl number. In this respect, the linearised Navier—Stokes equations under the centrifugal approximation are derived and solved to determine the stability thresholds considering non-Boussinesq effects. Linear stability analysis indicates that in the range of $4.23 \times 10^8 \leq Ra \leq 6.50 \times 10^8$, there is a maximum Gay-Lussac parameter that beyond which the buoyancy-driven flow becomes unstable to infinitesimal perturbations. It is also found that all

transitions to three-dimensional instabilities occurs through an oscillatory mode. A weakly nonlinear Stewart–Landau analysis is also conducted that indicates all three-dimensional instability consistently occurs through a supercritical bifurcation.

An Orr–Sommerfeld type stability analysis is conducted on extracted velocity profiles to determine the local (convective) stability properties of the flow. This analysis demonstrates the precendence of the transverse rolls against the longitudinal rolls instability. An entropy generation analysis is also conducted for the horizontal convection to determine the heat transfer mechanism evolution both locally and globally. The entropy generation analysis indicates that the Gay-Lussac parameter applies no effect on the heat transfer mechanism in the conduction-dominated regime but it weakens convection at high Rayleigh number. Finally, Nusselt number is scaled against the Rayleigh number at different Gay-Lussac parameters indicating that, in the convection-dominated regime, a higher Gay-Lussac parameter is associated with a lower average Nusselt number.

Publications during enrollment

Mayeli, P., & Sheard, G. J. 2021 Buoyancy-driven flows beyond the Boussinesq approximation: A brief review. *International Communications in Heat and Mass Transfer* **125**, 105316.

Mayeli, P., Tsai, T., & Sheard, G. J. 2022 Linear stability analysis of horizontal convection under a Gay-Lussac type approximation. *International Journal of Heat and Mass Transfer* **182**, 121929.

Mayeli, P., & Sheard, G. J. 2022 An entropy generation analysis of horizontal convection under the centrifugal buoyancy approximation. *International Communications in Heat and Mass Transfer* **133**, 105923.

Mayeli, P., & Sheard, G. J. 2021 An efficient and simplified Gay-Lussac approach in secondary variables form for the non-Boussinesq simulation of free convection problems. *International Journal for Numerical Methods in Fluids* **93** (11), 3264-3279.

Mayeli, P., & Sheard, G. J. 2021 A simplified and efficient Gay-Lussac approach for non-Boussinesq treatment of natural convection problems. *Numerical Heat Transfer, Part B: Fundamentals* **80** (5-6), 683-702.

Mayeli, P., & Sheard, G. J. 2021 A centrifugal buoyancy formulation for Boussinesq-type natural convection flows applied to the annulus cavity problem.. *International Journal for Numerical Methods in Fluids* **93** (3), 683-702.

Mayeli, P., & Sheard, G. J. 2021 Natural convection and entropy generation in square and skew cavities due to large temperature differences: A Gay-Lussac-type vorticity stream-function approach. *International Journal for Numerical Methods in Fluids* **93** (7), 2396-2420.

Mayeli, P., & Sheard, G. J. Weakly nonlinear bifurcation behaviour and local stability of horizontal convection under the centrifugal buoyancy approximation. *International Journal of Heat and Mass Transfer* Under review.

Mayeli, P., & Sheard, G. J. 2018 A comparison between Boussinesq and non-Boussinesq approx-

imations for numerical simulation of natural convection in an annulus cavity, In proceeding of the 21th Australian Fluid Mechanics Conference, Adelaide, Australia.

Mayeli, P., & Sheard, G. J. 2020 Studying natural convection problem in a square cavity by a new vorticity stream-function approach, In proceeding of the 22th Australian Fluid Mechanics Conference, Brisbane, Australia.

Thesis including published works declaration

I hereby declare that this thesis contains no material which has been accepted for the award of any other degree or diploma at any university or equivalent institution and that, to the best of my knowledge and belief, this thesis contains no material previously published or written by another person, except where due reference is made in the text of the thesis.

This thesis includes six original papers published in peer reviewed journals and two submitted publications. The core theme of the thesis is publication based. The ideas, development and writing up of all the papers in the thesis were the principal responsibility of myself, Peyman Mayeli, working within the department of the Mechanical and Aerospace Engineering under the supervision of Professor Gregory J. Sheard.

In the case of six chapters, my contribution to the work involved the following:

Thesis Chapter	Publication Title	Status	Nature and % of student contribution	Co-author name(s) Nature and % of Co-author's contribution	Co-author(s), Monash student Y/N
1	Buoyancy-driven flows beyond the Boussinesq approximation: A brief review	Published	90%, Constructing general framework and writing draft	Gregory J. Sheard, 10%	No
2	An efficient and simplified Gay-Lussac approach in secondary variables form for the Non-Boussinesq simulation of free convection problems	Published	90%, Constructing general framework and writing draft	Gregory J. Sheard, 10%	No
2	A simplified and efficient Gay-Lussac approach for non-Boussinesq treatment of natural convection problems	Published	90%, Constructing general framework and writing draft	Gregory J. Sheard, 10%	No
3	A centrifugal buoyancy formulation for Boussinesq-type natural convection flows applied to the annulus cavity problem	Published	90%, Constructing general framework and writing draft	Gregory J. Sheard, 10%	No
3	Natural convection and entropy generation in square and skew cavities due to large temperature differences: A Gay-Lussac-type vorticity stream-function approach	Published	90%, Constructing general framework and writing draft	Gregory J. Sheard, 10%	No
4	Linear stability analysis of horizontal convection under a Gay-Lussac type approximation	Published	85%, Constructing general framework and writing draft	Gregory J. Sheard, 10%,Tzekih Tsai, 5%	No, No
5	An entropy generation analysis of horizontal convection under the centrifugal buoyancy approximation	Published	90%, Constructing general framework and writing draft	Gregory J. Sheard, 10%	No

Student name: Peyman Mayeli

Student signature: 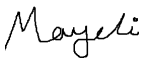

Date: 2/12/2021

I hereby certify that the mentioned declaration correctly reflects the nature and extent of the student's and co-authors' contributions to this work. In instances where I am not the responsible author I have consulted with the responsible author to agree on the respective contributions of the authors.

Main Supervisor name: Gregory J. Sheard

Main Supervisor signature: 

Date: 2/12/2021

Acknowledgements

I would like to thank my main supervisors, Prof. Gregory Sheard for all the assistance and guidance he provided over the duration of my candidature. He provided direction and precious support without which this work would not have been possible. I would like to more extend my sincere thanks to Prof. Gregory Sheard for his patience during different steps of this project. That was impossible for me to reach this record of publications during my enrollment without his support.

I would like to to thank my dear friends in SheardLab, whose ideas contributed greatly to the material presented in this thesis.

I am grateful to the Department of Mechanical and Aerospace Engineering, Monash University, for providing the post-graduate office and resources necessary for the completion of this study. Furthermore, I wish to acknowledge the staff of Monash high performance computing facilities (MonArch), and the National Computational Infrastructure (NCI) for providing the computational facilities which were essential to this work.

To my late grandfather Ali Davoudi, without his support, I would not be here today. I am forever indebted to him. Finally, I would like to thank my wife, Solmaz, for her love, patience and support during all critical time of my candidature.

Nomenclature

Any parameter that is not listed here is denoted explicitly in the text.

Symbol	Description
A	Height to length aspect ration
A	Amplitude of a signal
$\boldsymbol{A}$	Generalised eigenvalue matrix (left-hand side)
$\boldsymbol{B}$	Generalised eigenvalue matrix (right-hand side)
Be	Bejan number
Br	Brinkman number
Fr	Froude number
$\mathbf{e}_g$	unit vector in gravity direction
g	gravitational acceleration
Ga	Gay-Lussac parameter ($\beta\Delta\theta$)
H	Height
k	thermal conductivity
k	wavenumber
L	Length
$\boldsymbol{n}$	normal vector of the surface
N_f	Number of Fourier modes
Nu	Nusselt number
p	pressure
$p*$	modified pressure
P	Dimensionless pressure
Pr	Prandtl number
q	heat
Ra	Rayleigh number
S	Entropy
S_Θ	Entropy generation due to heat transfer
S_ψ	Entropy generation due to fluid friction
$t*$	time
t	dimensionless time
T	Temperature
$\boldsymbol{u}$	velocity vector
$\boldsymbol{U}$	Dimensionless velocity vector
$\boldsymbol{x}$	Cartesian coordinate vector
$\boldsymbol{X}$	Cartesian dimensionless coordinate vector

Continued on the next page.

Greek Symbols

α	thermal diffusivity
α	traveling wave numbers in X direction
β	isobaric expansion coefficient
β	traveling wave numbers in Z direction
ϵ	an infinitesimal perturbation
ε	relative temperature difference
θ	physical temperature
Θ	dimensionless temperature
μ	eigenvalue
μ	dynamic viscosity
ν	kinematic viscosity
ρ	density
σ	perturbation growth rate
τ	time interval
ϕ	gravitational potential
$\tilde{\phi}$	gneric symbol representing a perturbation flow variable
χ	irreversibility distribution ratio
ψ	stream-function
ω	vorticity
ω	angular frequency

Subscript

avg	average
b	base flow
c	cold
cr	critical
h	hot
k	wavenumber
loc	local
ref	reference
tot	total
0	reference value

Superscript

$\hat{}$	refers to an eigenmode
$'$	small perturbation quantity
$\bar{}$	mean value

Contents

List of Figures

List of Tables

Chapter 1

1 Introduction and literature review

Natural convection describes the flow and associated heat transport generated by temperature or species molar concentration differences in the presence of gravity in which, denser fluid seeks to descend whereas less dense fluid seeks to rise. This phenomenon plays an important role in human life from micro/nano scale transport aerosol in the air to large scales of the order of hundreds of kilometers causing different weather conditions and oceanic flow patterns [1].

Understanding of different natural convection related phenomena is possible through both experimental and numerical simulations [2]. Numerical simulation of natural convection problems is mainly performed under the Boussinesq approximation which is not the only available option in this respect. In the next subsection, fundamental assumptions of the Boussinesq approximation is introduced. Thereafter, different possible scenarios for numerical simulation of natural convection problems are reviewed.

1.1 What is meant by non-Boussinesq approximation?

The well-known Boussinesq (also known as Oberbeck—Boussinesq) approximation is the most common approach for the numerical simulation of natural convection problems. This classic approach is established based on the following fundamental assumptions [3]:

- Small temperature difference
- Negligible viscous heat dissipation
- Constant thermophysical properties
- Small hydrostatic pressure variations
- Linear density state equation

Accurate performance of the Oberbeck—Boussinesq (OB) approximation depends on the satisfaction of thees conditions, but in practice, there are many applications that violate one or more of these. Imposed restrictions to apply the OB approximation encourages researchers to use other approaches beyond the valid range of this approximation performance. A review of different possible scenarios for numerical simulation

of natural convection problems is performed and the outcome is published as a research paper entitled “Buoyancy-driven flows beyond the Boussinesq approximation: A brief review”.

1.2 Published paper

The published paper reviewing different possible scenarios for numerical simulation of natural convection problems is provided in the following.

International Communications in Heat and Mass Transfer 125 (2021) 105316

Contents lists available at ScienceDirect

International Communications in Heat and Mass Transfer

journal homepage: www.elsevier.com/locate/ichmt

Buoyancy-driven flows beyond the Boussinesq approximation: A brief review

Peyman Mayeli *, Gregory J. Sheard

Department of Mechanical and Aerospace Engineering, Monash University, VIC 3800, Australia

ARTICLE INFO

Keywords:
Non-Boussinesq approximation
Non-Oberbeck—Boussinesq approximation
Buoyancy-driven flows
Free convection
Compressible natural convection

ABSTRACT

The well-known Boussinesq (also known as Oberbeck—Boussinesq) approximation is still the most common approach for the numerical simulation of natural convection problems. However, the accurate performance of this approximation is mainly restricted by small temperature differences. This encourages researchers and engineers to use other approaches beyond the range of validity of the Boussinesq approximation, especially when buoyancy-driven flows are generated by large temperature differences. This paper assembles and classifies the various approaches for numerical simulation of laminar natural convection, including Boussinesq and non-Boussinesq approximations for Newtonian fluids. These classifications reside under two overarching classes capturing compressible and incompressible approaches, respectively. This review elaborates on the different approaches and formulations adopted within each category.

1. Introduction

Natural convection (NC) describes the flow and associated heat transport generated by temperature or species molar concentration differences. The addition of an external momentum source (a fan, for example) creates the sister class of convection known as mixed convection. This paper focuses solely on pure natural convection problems in the absence of external momentum forcing and the different possible scenarios for their numerical simulation.

The name most synonymous with modelling natural convection is Joseph Valentin Boussinesq, who in 1897 proposed the striking simplification of the natural convection problem that now bears his name: the Boussinesq model [1] neglects density differences except in the gravity term of the momentum equation. Crucially, this permitted NC flows to be treated within an incompressible framework, greatly increasing their mathematical tractability. Almost fifty years after Claude Navier (in 1850) and George Stokes (in 1845) contributed to the development of the Navier—Stokes (NS) equations governing fluid motion, Boussinesq [1] established his famous approximation for NC problems. Later, Josef [2] recognised that Anton Oberbeck in 1879 [3] had earlier applied the same concept in his description of heat conduction in liquids accounting for currents driven by thermal gradients. The model is now commonly referred to as the Oberbeck—Boussinesq (OB) approximation in recognition of their respective contributions. The OB approximation is established based on the following assumptions:

- Small temperature differences
- Negligible viscous heat dissipation
- Constant thermophysical properties
- Linear density state equation
- Small hydrostatic pressure variations

Under the OB approximation, density variations are confined just to the gravity term of the momentum equation, and their effects are ignored in other terms. Simple implementation, rapid convergence rate, and outstanding accuracy over small temperature differences are benefits of the OB approximation. Under the OB approximation, density and temperature are connected via a linear density state equation using the definition of volumetric thermal expansion. The expansion coefficient value is typically taken at some reference temperature of the working fluid. Another less appreciated fundamental assumption of the OB approximation, is small hydrostatic pressure variations over the height of the physical domain compared to the thermodynamic pressure variations inside the system. This ratio is characterized by the dimensionless barometric number ($Ba = gH/RT$) [4].

One of the pioneering studies to determine the accurate range of the OB approximation performance was performed by Gray & Giorgini [5]. Considering all fluid properties as linear functions of two state variables (temperature and pressure) at a reference temperature of $T_0 = 15\ ^\circ C$ and

* Corresponding author.
E-mail addresses: peyman.mayeli@monash.edu (P. Mayeli), Greg.Sheard@monash.edu (G.J. Sheard).

https://doi.org/10.1016/j.icheatmasstransfer.2021.105316

Nomenclature

Ba	barometric number	Pr	Prandtl number
c_p	specific heat at constant pressure	R	ideal gas constant
e_g	the unit vector in the gravity direction	Ra	Rayleigh number
Ec	Eckert number	T	temperature
Fr	Froude number	u	velocity vector
Ga	Gay-Lussac parameter ($\beta\Delta\theta$)	U	dimensionless velocity vector
H	height	α	thermal diffusivity
k	thermal conductivity	β	isobaric expansion coefficient
L	reference length	ε	relative temperature difference
p	pressure	θ	physical temperature
P	dimensionless pressure	Θ	dimensionless temperature
Pth	thermodynamic pressure	μ	dynamic viscosity
		ν	kinematic viscosity
		ρ	density

a reference pressure of $p_0 = 1$ atm, they extracted the valid temperature difference range of the OB approximation application in air and water as respectively less than 28.6 ° C and 1.25 ° C at a limited length scale of $L_{ref} \leq 8.3 \times 10^4$ cm and $L_{ref} \leq 2.4 \times 10^5$ cm. To neglect the pressure work term in the energy equation, they obtained the ranges of $\Delta T/L_{ref} \leq 1020$ cm/ ° C and $\Delta T/L_{ref} \leq 9.9 \times 10^4$ cm/ ° C for air and water, respectively. Additionally, to safely ignore the viscous dissipation relative to the thermal diffusion term of the energy equation, they obtained length scales $L_{ref} \leq 4.1 \times 10^5$ cm and $L_{ref} \leq 3.5 \times 10^6$ cm for air and water, respectively.

There are many scientific and industrial applications in which temperature differences and length scales are beyond the regime of validity of the OB approximation. Foundry processes, thermal insulation systems in nuclear reactors, solar collectors, and astrophysical MHD simulations are some examples in which temperature differences are of the order of several hundred kelvin, or in which the length scale exceeds hundred kilometres. In these situations, the OB approximation yields inaccurate results. Available numerical algorithms that attempt to improve upon the OB approximation are less abundant in the literature. This paper seeks to classify numerical algorithms within two main categories: compressible and incompressible. These two categories and their sub-categories are presented in the context of a flowchart in Fig. 1. In section 2, compressible-flow approaches are introduced, and in section 3, incompressible approaches are reviewed. A brief conclusion is drawn in section 4. An exhaustive collation of the literature review pertaining to each of the identified sub-categories is beyond the scope of this review.

2. Compressible-flow based approximations

The first category of remedies to the limitations of the OB approximation is built upon the concept of compressibility, which leads to the introduction of the Mach number. As shown in Fig. 1, compressible treatment of the NS equations is possible in two fashions: Fully compressible and weakly compressible approaches. We start with the introduction of the fully compressible approach and numerical problems associated with that. Then, the weakly compressible approach is introduced and discussed.

2.1. Fully compressible approximation

Theoretically, the perfect simulation of NC is possible via the fully compressible form of the NS equations, since minimal approximations are introduced in this approach. The governing equations for a compressible Newtonian fluid, respectively derived from the principles of conservation of mass, momentum and energy, and closed by a density state equation are,

$$\begin{cases} \dfrac{\partial \rho^*}{\partial t^*} + \nabla \cdot (\rho^* \boldsymbol{u}) = 0, \\ \dfrac{\partial (\rho^* \boldsymbol{u})}{\partial t^*} + \nabla \cdot (\rho^* \boldsymbol{u} \otimes \boldsymbol{u}) = -\nabla\ p + \rho^* g \boldsymbol{e}_g + \mu \nabla \cdot \boldsymbol{\tau}^*, \\ \dfrac{\partial (\rho^* {c_p}^* T)}{\partial t^*} + \nabla \cdot \left(\rho^* {c_p}^* \boldsymbol{u} T\right) = k \nabla^2 T + \dfrac{\mathrm{D}p}{\mathrm{D}t^*} + \mu \varphi \\ p = f(\rho^*, T) \end{cases}, \tag{1}$$

It should be noted the energy equation does not have a unique form. Different forms of the energy equation including specific heat at constant volume (c_v) or shear stress ($\boldsymbol{\tau}$) may be found in ref. [6]. Using dimensionless parameters based on diffusion velocity scale ($u_0 = \alpha/L$),

$$t = \frac{t^* \alpha}{L^2}, \boldsymbol{X} = \frac{\boldsymbol{x}}{L}, \boldsymbol{U} = \frac{\boldsymbol{u} L}{\alpha}, P = \frac{p L^2}{\rho_0 \alpha^2}, \Theta = \frac{T}{T_0}, \rho = \frac{\rho^*}{\rho_0}, c_p = \frac{{c_p}^*}{c_{p0}}, \varepsilon = \frac{\Delta T}{2T_0}, \tag{2}$$

the dimensionless form of the fully compressible NS equations may be

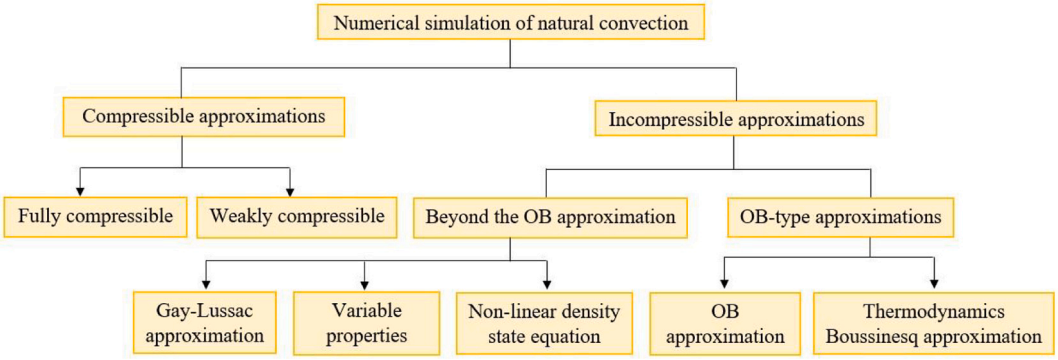

Fig. 1. Classification of different approximations for numerical simulation of the natural convection problems.

expressed as follows,

$$\begin{cases} \dfrac{\partial \rho}{\partial t} + \nabla \cdot (\rho \boldsymbol{U}) = 0, \\ \dfrac{\partial (\rho \boldsymbol{U})}{\partial t} + \nabla \cdot (\rho \boldsymbol{U} \otimes \boldsymbol{U}) = -\nabla P + \dfrac{RaPr}{2\varepsilon} \rho \boldsymbol{e}_g + Pr \nabla \cdot \boldsymbol{\tau}, \\ \dfrac{\partial (\rho \Theta)}{\partial t} + \nabla \cdot (\rho \boldsymbol{U} \Theta) = \nabla^2 \Theta + 2\varepsilon Ec \dfrac{\mathrm{D}P}{\mathrm{D}t} + 2\varepsilon Ec Pr \Phi \\ P = f(\rho, \Theta) \end{cases} \tag{3}$$

The choice for the reference velocity in NC is not unique. Another common choice for the reference velocity is the gravity velocity scale ($u_0 = \sqrt{g\beta\Delta TL}$), leading to different pre-factors. The presented dimensionless equation of state is also valid for an ideal diatomic gas ($R/R_0 = 1$, $c_p = 1$). Using Stokes' hypothesis for the bulk viscosity ($\lambda = -2/3\mu$), the dimensionless form of the stress tensor ($\boldsymbol{\tau}$) and dissipation term (Φ) for a 2D flow field in Cartesian coordinates are,

$$\boldsymbol{\tau} = \nabla \boldsymbol{U} + (\nabla \boldsymbol{U})^T - (2/3)(\nabla \cdot \boldsymbol{U}) \boldsymbol{I}, \tag{4}$$

$$\Phi = 2\left[\left(\frac{\partial U}{\partial X}\right)^2 + \left(\frac{\partial V}{\partial Y}\right)^2\right] + \left(\frac{\partial U}{\partial Y} + \frac{\partial V}{\partial X}\right)^2 - \frac{2}{3}\left[\left(\frac{\partial U}{\partial X} + \frac{\partial V}{\partial Y}\right)^2\right] \tag{5}$$

Compressible flow is characterized by the Mach number. In compressible buoyancy-driven flows, the square of the Mach number for an ideal gas may be recast as,

$$Ma^2 = \frac{{u_0}^2}{\gamma (\partial p/\partial \rho)_T} = \frac{(\alpha/L)^2}{\gamma R T_0} = \frac{(\alpha/L)^2}{(\gamma - 1) c p_0 T_0} = \frac{2\varepsilon}{(\gamma - 1)} \frac{(\alpha/L)^2}{c p_0 \Delta T} = \frac{2\varepsilon}{(\gamma - 1)} Ec. \tag{6}$$

Regarding the maximum value of the relative temperature difference of unity ($\varepsilon_{max} = 1$), the maximum Mach number in NC is bounded by the square root of the Eckert number ($Ma_{max} = \sqrt{2Ec(\gamma - 1)^{-1}}$). Another advantage of Eq. (6) is replacement of the $2\varepsilon Ec$ in the energy equation by $(\gamma - 1)Ma^2$. Thus, the energy equation may be rewritten as,

$$\frac{\partial (\rho \Theta)}{\partial t} + \nabla \cdot (\rho \boldsymbol{U} \Theta) = \nabla^2 \Theta + (\gamma - 1) Ma^2 \left(\frac{\mathrm{D}P}{\mathrm{D}t} + Pr \Phi\right) \tag{7}$$

When expressed in this form, it can be seen that the energy equation under the incompressible assumption is recovered as the Mach number approaches zero ($Ma \to 0, \rho \to 1$).

Fully compressible NS solvers are developed in two fashions: pressure-based and density-based. In brief, density-based algorithms are developed so that density is updated through the continuity equation, and pressure is obtained from the equation of state. The Roe scheme [7] is a popular method in this category. On the other hand, in pressure-based algorithms, the continuity equation becomes a constraint (Poisson equation) for pressure, and density is updated via the equation of state. While pressure-based algorithms can be applied across the entire spectrum of the Mach number, density-based solvers face serious convergence problems within the near-zero Mach number regime [8], as pressure wave speed approaches infinity as $Ma \to 0$. This is important because Mach number is typically very small for most NC problems. For instance, numerical simulation of NC in the square cavity benchmark problem (with two horizontal adiabatic sides and two vertical hot and cold isothermal walls) at a high relative temperature difference of $\varepsilon = 0.6$ and $Ra = 10^5$ indicates the maximum Mach number is equal to 3.68×10^{-4} [9]. Thus, applying density-based solvers on NC problems requires numerical treatments such as preconditioning and using a dual time-step strategy [10,11]. Although pressure-based algorithms would appear to be more suitable for NC problems, but for enclosed domains (having no inflow-outflow), conserving initial mass should be considered for a physical answer [12].

Many researchers have performed numerical simulations of NC problems under the fully compressible approach. NC in square cavity benchmark problem up to $Ra = 10^6$ and $\varepsilon = 0.6$ is numerically simulated in refs. [12–16]. Reported data corresponding to $\varepsilon = 0.01$ in refs. [12, 15, 16] confirm that the fully compressible approach gives identical results to the incompressible OB approximation. El-Gendi & Aly [17] analysed unsteady compressible NC in square and sinusoidal cavity up to a huge temperature difference of 2000 K. Darbandi and Hosseinizadeh [18] studied NC in a deep vertical-cavity, concluding that the maximum Nusselt number initially increases and then decreases as the length to height ratio increases with a little different pattern for different Rayleigh numbers. NC in a horizontal concentric annulus cavity at $Ra = 4.7 \times 10^4$ and $\varepsilon = 0.33$ under the fully compressible assumption is performed by Weiss and Smith [11]. A similar study within the OB regime ($\Delta T = 26.3\ ^\circ C$) was performed by Volkov *et al.* [19]. The aspect ratio of the outer to inner cylinder diameters in both studies was fixed at 2.6 to enable comparison with the experimental data reported by Kuhen & Goldstein [20]. Yamamoto *et al.* [21] simulated compressible NC of air around a circular cylinder in free space as an external flow and validated their results against the experimental data of Kuhen & Goldstein [20]. Then, they extended their calculations for NC of horizontal pipes containing hot liquid with three different solid to air conductivity ratio. Fu *et al.* [22] simulated a compressible NC problem in a vertical open channel for industrial applications. In this respect, they presented two equations, which separately correlates the average Nusselt number to the Rayleigh number and the length of the channel for a broad range of temperature differences. A similar study of compressible NC in an inclined open channel for a limited range of the Rayleigh number has been performed by Talukdar *et al.* [23]. Following Fu *et al.* [22], they presented a relation for the average Nusselt number as a function of Rayleigh number and inclination angle suitable for engineering applications.

2.2. Weakly compressible approximation

The second subcategory under the umbrella of compressible flow assumption, i.e. weakly compressible approach, is developed to resolve numerical problems associated with small Mach number NC problems. This approach is also sometimes called as the low Mach number scheme (LMS). Another advantage of the LMS approximation is that it permits larger time steps for explicit methods. Under the LMS approximation developed by Paulucci [24], acoustic sound waves are filtered from the fully compressible approach for the low Mach number regime, and the total pressure is split into a global/uniform thermodynamic pressure (p_{th}) and a local hydrodynamic pressure (p_h) as $p_{tot} = p_{th} + p_h$. This simplification is performed based on asymptotic analysis that states $p_{th}/p_0 \cong O(1)$ and $p_h/p_0 \cong O(Ma^2)$ [24]. Under the LMS approximation, local hydrodynamic pressure (obtained from a Poisson equation) acts in the momentum equation to establish a balance amongst advection, buoyancy, and diffusion terms, while thermodynamic pressure is used to update density during the solution procedure. Under the LMS approximation, the governing equations for an ideal gas are expressed as,

$$\begin{cases} \dfrac{\partial \rho^*}{\partial t^*} + \nabla \cdot (\rho^* \boldsymbol{u}) = 0, \\ \dfrac{\partial (\rho^* \boldsymbol{u})}{\partial t^*} + \nabla \cdot (\rho^* \boldsymbol{u} \otimes \boldsymbol{u}) = -\nabla p_h + \rho^* \boldsymbol{e}_g + \nabla \cdot \boldsymbol{\tau}^*, \\ \rho^* {c_p}^* \left(\dfrac{\partial T}{\partial t^*} + \boldsymbol{u} \cdot \nabla T\right) = \kappa \nabla^2 T + \dfrac{\mathrm{d}p_{th}}{\mathrm{d}t}, \\ p_{\mathrm{th}} = \rho^* R T. \end{cases} \tag{8}$$

Using the group of dimensionless parameters introduced earlier in Eq. (6) accompanied by a dimensionless thermodynamic pressure ($P_{th} = p_{th}/p_0$), the dimensionless form of the governing equations for an ideal gas are expressed as follows [25].

$$\begin{cases} \dfrac{\partial \rho}{\partial t} + \nabla \cdot (\rho \boldsymbol{U}) = 0, \\ \dfrac{\partial (\rho \boldsymbol{U})}{\partial t} + \nabla \cdot (\rho \boldsymbol{U} \otimes \boldsymbol{U}) = -\nabla P + \dfrac{RaPr}{2\varepsilon} \rho \boldsymbol{e}_g + Pr \nabla \cdot \boldsymbol{\tau}, \\ \rho \left(\dfrac{\partial \Theta}{\partial t} + \boldsymbol{U} \cdot \nabla \Theta \right) = \nabla^2 \Theta + \Gamma \dfrac{\mathrm{d}P_{th}}{\mathrm{d}t}, \\ P_{th} = \rho \Theta. \end{cases} \tag{9}$$

In Eq. (9), Γ is a measure of the resilience of the fluid ($\Gamma = (\gamma - 1)/\gamma$), where γ is the heat capacity ratio ($\gamma = c_p/c_v$). The buoyancy term in both of Eqs. (3) and (9) is expressed by a gL^3/α^2 pre-factor that is replaced by a Froude number, characterising the ratio of inertia to gravity,

$$\frac{gL^3}{\alpha^2}\rho = \frac{gL}{(\alpha/L)^2}\rho = \frac{gL}{{u_0}^2}\rho = \frac{1}{Fr}\rho. \tag{10}$$

To express the Froude number as a Product of Ra, Pr, and ε, we may use the Rayleigh number definition. Within the compressible/weakly-compressible approaches, the Rayleigh number is expressed slightly differently compared to its incompressible definition

$$Ra_{comp.} = Pr\frac{g{\rho_0}^2(T_h - T_c)L^3}{T_o{\mu_0}^2} = \frac{g\beta\Delta T L^3}{\nu\alpha} = Ra_{incomp.} \tag{11}$$

Comparing incompressible and compressible Rayleigh number definitions give the following relation for the Froude number,

$$\underbrace{2\varepsilon = (T_h - T_c)/T_o}_{\text{Compressible}} = \underbrace{\beta\Delta T = RaPrFr}_{\text{Incompressible}} \rightarrow Fr = 2\varepsilon \Big/ RaPr. \tag{12}$$

Eq. (9) has one more unknown (P_{th}) concerning the number of equations. For open systems, thermodynamic pressure may be simply approximated by the atmospheric pressure. However, for the enclosed domains, an extra equation is required to close the system of equations. Combining the energy equation with the equation of state and continuity from Eq. (9) yields,

$$\nabla \cdot \boldsymbol{U} = \frac{1}{p_{th}} \left[\nabla^2 \Theta - \frac{1}{\gamma} \frac{\mathrm{d}P_{th}}{\mathrm{d}t} \right] \tag{13}$$

Using the Gauss divergence theorem, it can be shown that integration of $\nabla \cdot \boldsymbol{U}$ over a closed domain is zero, thus

$$\frac{\mathrm{d}P_{th}}{\mathrm{d}t} = \frac{\gamma}{V} \int_S \frac{\partial \Theta}{\partial x_j} n_j \mathrm{d}S. \tag{14}$$

In Eq. (14), S and V refer to the surface and volume of the physical domain, respectively. The integrand of Eq. (14) is the residual of the energy equation that asymptotically goes to zero for a steady-state solution ($\mathrm{d}P_{th}/\mathrm{d}t \rightarrow 0$). Computing thermodynamic pressure variations from Eq. (14) does not guarantee strict mass conservation [9]. Knowing initial mass inside the system (m_0), Le Quéré et al. [26] suggested applying the concept of mass conservation for an enclosed domain to update thermodynamic pressure:

$$m_0 = \frac{P_0 V}{RT_0} = \frac{P_{th} V}{RT} \rightarrow P_{th} = \underbrace{\left(\frac{P_0 V}{T_0}\right)}_{cte} \Big/ \int_V \mathrm{d}V \Big/ T. \tag{15}$$

A comprehensive study of the NC under the LMS approximation in the square cavity benchmark problem is performed by Paolucci and Chenoweth [25,27]. They found that by increasing temperature differences, critical Ra for stationary and oscillatory instabilities are decreased. Their stability analysis results under LMS approximation for a differential relative temperature difference indicates that flow becomes unsteady at $Ra = 1.93 \times 10^8$ [27]. A similar study of the NC problem under the LMS approximation in the square cavity is also performed by Wang et al. [28]. They extracted power-law scaling of the average Nusselt number for the different range of Ra at different ε and determined critical Rayleigh number at $\varepsilon = 0.2$, 0.4, and 0.6. A benchmark solution for the square cavity problem is provided by Le Quéré *et al.* [29]. Le Quéré *et al.* [26] applied LMS approximation for different relative temperature differences in a deep cavity with an aspect ratio of 8 to study the transition to unsteadiness. A similar study of a deep vertical-cavity emphasizing stability analysis is also performed by Suslov and Paolucci [30,31]. Paillere *et al.* [9] compared results of the LMS approach against the fully compressible approach for both small ($\varepsilon = 0.01$) and large ($\varepsilon = 0.6$) temperature differences up to $Ra = 10^5$. They showed the LMS model could simulate NC with high fidelity and negligible differences compared to the hyperbolic fully compressible NS equations. Elmo & Cioni [32] used LMS approximation for a pebble bed of a nuclear reactor. Kumar & Natarajan [33] investigated the role of discrete conservation in numerical simulations of thermos-buoyant flows in enclosures and devised two different pressure-based numerical algorithms under LMS approximation that violate either the equation of state or a conservation law at the discrete level, leading to two different classes of algorithms. Tyliszczak [34] applied the projection method with a second-order temporal accuracy of Adams-Bashforth/Adams-Moulton methods to the LMS approach.

Finally, in the compressible framework, the idea of splitting the total pressure into a spatially uniform and a local pressure is also presented under the homobaricity approach [35]. This approach was originally developed for gaseous flow with zero viscosity; similar to the LMS approach, equation of state and energy equations are treated by the spatially uniform thermodynamic pressure while the hydrodynamic local pressure acts solely in the momentum equation. Cherkasov *et al.* [36] applied this approach for a 1D boundary layer problem along the vertical plate.

3. Incompressible approximations

Approaches within the incompressible-flow framework will now be explored. As shown in Fig. 1, the incompressible category is divided into the OB type approximations and algorithms beyond the OB approximations. The OB-type approximations will be covered first, and then we introduce different non-OB subcategories will be discussed.

3.1. OB type approximations

The OB-type approximations may be divided into two groups; the first being the original OB approximation and the second being the thermodynamic Boussinesq approximation.

3.1.1. OB approximation

When the OB approach conditions [5] are met, density variations are assumed to be negligible except via the gravity term. Neglecting viscous heat dissipation and pressure work terms, governing equations in the dimensional form under the OB approximation are expressed as follows,

$$\begin{cases} \rho/\rho_0 (\nabla \cdot \boldsymbol{u}) = 0 \\ \rho/\rho_0 (\partial \boldsymbol{u}/\partial t^* + \boldsymbol{u} \cdot \nabla \boldsymbol{u}) = -(1/\rho_0)\nabla p + \nu \nabla^2 \boldsymbol{u} + (\rho/\rho_0) g \boldsymbol{e}_g \\ \rho/\rho_0 (\partial T/\partial t^* + \boldsymbol{u} \cdot \nabla T) = \alpha \nabla^2 T. \end{cases} \tag{16}$$

To relate temperature variations to density, a linear density state equation ($\rho/\rho_0 = 1 - \beta\theta$) is derived from the volumetric thermal expansion coefficient definition. Under the OB approximation, all ρ/ρ_0 pre-factors are considered equal to unity except in gravity term, which is replaced by the linear density state equation. The result is,

$$\begin{cases} \nabla \cdot \boldsymbol{u} = 0 \\ \partial \boldsymbol{u}/\partial t^* + \boldsymbol{u} \cdot \nabla \boldsymbol{u} = -(1/\rho_0)\nabla p + \nu \nabla^2 \boldsymbol{u} + (1 - \beta\theta) g \boldsymbol{e}_g \\ \partial T/\partial t^* + \boldsymbol{u} \cdot \nabla T = \alpha \nabla^2 T. \end{cases} \tag{17}$$

In the next step, a modified pressure is introduced as $p^* = p + \rho_0 \phi$, where ϕ is the gravitational potential whose gradient opposes the gravitational acceleration vector, i.e. $\nabla \phi = -g\boldsymbol{e}_g$. The modified pressure absorbs $g\boldsymbol{e}_g$ term in the momentum equation and just the $\beta\theta g\boldsymbol{e}_g$ remains

as the buoyancy term. Using the same dimensionless parameters in Eq. (2) except with a different dimensionless temperature defined as $\Theta = (T - T_0)/\Delta T$, the dimensionless form of the governing equations become,

$$\begin{cases} \nabla \cdot \boldsymbol{U} = 0, \\ \partial \boldsymbol{U}/\partial t + \boldsymbol{U} \cdot \nabla \boldsymbol{U} = -\nabla P + Pr \nabla^2 \boldsymbol{U} - RaPr\Theta \boldsymbol{e}_g, \\ \partial \Theta/\partial t + \boldsymbol{U} \cdot \nabla \Theta = \nabla^2 \Theta. \end{cases} \tag{18}$$

There are a vast number of works that have adopted the OB approximation. As the focus of this review is on the approaches beyond the original OB approximation, interested readers are directed to relevant review papers with a focus on specific geometry including the annulus [37,38], triangular [39,40], parallelogram [41], non-square [42], and rectangular-shaped [43] cavities or particular topics within NC such as localized heating [44] or internal heat sources [45].

3.1.2. Thermodynamic Boussinesq approximation

Under the OB approximation, dissipated heat due to viscous friction and work of pressure stress are removed from the energy equation as their effects are assumed to be negligible. Decisions as to whether heat dissipation or pressure work terms may be neglected are typically made based on comparing order-of-magnitude arguments, but this causes a thermodynamical paradox. The momentum equations compel the dissipation of kinetic energy due to fluid friction (diffusion terms). However, under the OB approximation, heat produced by this process is not captured by the energy equation. Separately, the absence of the pressure work in the energy equation lacks a logical relation between the internal energy and work performed upon the fluid. Using Gibbs and entropy balance equations, it can be shown that when these contributions are omitted from the energy equation, the described thermodynamic system recognizes heat conduction (and not viscous friction) as the only source of irreversibility. This prompted to development of an elaborated version of the OB approximation under different names including 'deep convection' [46], 'thermodynamic' [47], and 'extended' [5] Boussinesq approximations. The thermodynamic paradox is discussed in detail in refs. [48, 49], where it is concluded that removing pressure work and viscus dissipated heat remains a paradox for enclosed domains. Pons and Le Quéré [50] presented a dimensionless form of the governing equations under the thermodynamic Boussinesq model in which the effect of both dissipated heat due to viscous friction and work of pressure stress were considered in the energy equation. When both terms mentioned above are considered in the energy equation, the governing equations for an ideal gas are,

$$\begin{cases} \nabla \cdot \boldsymbol{U} = 0, \\ \partial \boldsymbol{U}/\partial t + \boldsymbol{U} \cdot \nabla \boldsymbol{U} = -\nabla P + Pr \nabla^2 \boldsymbol{U} - RaPr\Theta \boldsymbol{e}_g, \\ \partial \Theta/\partial t + \boldsymbol{U} \cdot \nabla \Theta = \nabla^2 \Theta + EcPr\Phi - Ar\Gamma Ba \boldsymbol{U} \cdot \boldsymbol{e}_g, \end{cases} \tag{19}$$

where Φ is the dissipation term (Eq. (5)) of a divergence-free flow field and the barometric number is defined by the ratio of potential energy variations to thermodynamic pressure variations ($Ba = gH/R\Delta T$). Ar is the aspect ratio of the geometry ($Ar = L/H$). Since the net product of $EcPr$ is minimal for gaseous flow in the Boussinesq regime, Pons and Le Quéré [51] ignored dissipated heat due to viscous friction. They found that when the magnitude of the barometric number becomes more extensive than $0.01/\Gamma$, its effect in the energy equation is no longer negligible in the square cavity benchmark problem. A variant of the thermodynamic Boussinesq approximation whereby the pressure work is neglected and only the viscous dissipation term is retained, is broadly used for numerical simulation of NC in porous media. An excellent review of free/mixed convection in saturated porous media considering viscous dissipation is performed by Nield [52].

3.2. Non-OB approximations

Approaches residing in the second category of the incompressible approximations attempt to increase the OB approximation accuracy so that the formulation is applicable for a larger spectrum of temperature differences. With reference to Fig. 1, three subcategories are identified in this class: the Gay-Lussac approximation, non-linear density state equation, and approaches based on variable thermophysical properties.

3.2.1. Gay-Lussac approximation

Under the Gay-Lussac approximation, density variations are not confined only to gravity term in contrast to the OB approximation. In this approach, the ρ/ρ_0 pre-factors are expressed in terms of Gay-Lussac parameter ($Ga = \beta\Delta\theta$) as follows,

$$\rho/\rho_0 = 1 - \beta\theta = 1 - \beta\Delta\theta\Theta = 1 - Ga\Theta. \tag{20}$$

Considering all density variations of Eq. (16) and replacing them with Eq. (20) yields the following dimensionless form of the governing equations, which is known as the Gay-Lussac approximation,

$$\begin{cases} (1 - Ga\Theta)(\nabla \cdot \boldsymbol{U}) = 0 \\ \partial \boldsymbol{U}/\partial t + (1 - Ga\Theta)\boldsymbol{U} \cdot \nabla \boldsymbol{U} = -\nabla P + Pr \nabla^2 \boldsymbol{U} - RaPr\Theta \boldsymbol{e}_g \\ \partial \Theta/\partial t + (1 - Ga\Theta)\boldsymbol{U} \cdot \nabla \Theta = \nabla^2 \Theta. \end{cases} \tag{21}$$

Eq. (21) is made dimensionless with the same dimensionless parameters applied for the OB approximation. Having a physical density requires $\rho/\rho_0 > 0$ and consequently $1 - Ga\Theta > 0$ that gives $Ga < 1/\Theta$. When the dimensionless temperature is defined as $\Theta = (T - T_0)/\Delta T$, then the minimum and maximum dimensionless temperatures alter between ± 0.5 that gives $Ga < 2$ constraint for the Gay-Lussac parameter to have a physical density value. This approximation has thus far found only limited application in the literature. Pesso & Piva [53] applied the Gay-Lussac approximation for the square cavity benchmark problem for a broad range of Rayleigh ($10 \leq Ra \leq 10^8$) and Prandtl number ($0.0071 \leq Pr \leq 7.1$). Their calculations indicate a reverse relation between Ga and the average Nusselt number. They also presented an analytical relation predicting the average Nusselt number as a function of Ra, Pr, and Ga. Lopez *et al.* [54] presented a Gay-Lussac type approach for the treatment of rapidly rotating flows, in which instead of considering density variations in any term of the governing equations including density, buoyancy effects were extended just to the centrifugal part of the advection term to capture centrifugal effects in rapidly rotating flows. Mayeli & Sheard [55,56] continued this approach for NC in the annulus cavity with large temperature differences up to $\varepsilon = 0.2$. They compared obtained results against the LMS and OB approximations, concluding that extending density variations to the advection term slightly improves the Gay-Lussac type approximation flow-related data.

3.2.2. Non-linear density state equation

The full density state equation is $\rho/\rho_0 = 1 + \sum_{i=1}^{n}(-\beta\theta)^i$, that is derived from the volumetric thermal expansion coefficient definition. The OB approximation is established based on a linear density state equation ($n = 1$), which works very well for the small temperature differences. However, as the temperature differences become large, higher terms of the density state relation may no longer be negligible. Another justification for applying a non-linear density state relation comes from the unconventional behaviour of some fluids such as water at temperatures close to or equal to the temperature of maximum density (T_{max}). In this situation, the linear density state relation may not be valid, even for small temperature differences. For instance, the density-temperature relationship of cold water in the vicinity of 4 °C does not obey a linear function. The non-linear density state equation of water ($\rho/\rho_{max} = 1 - \beta\theta^q$ where $\beta = 9.29 \times 10^{-6}(^\circ\mathrm{C})^{-q}$ and $q = 1.894$) proposed by Gebhart and Mollendorf [57] is a popular equation in this category. Defining a dimensionless temperature named *inversion parameter* as $\Theta_m = (T_{max} - T_c)/(T_h - T_c)$ which relates the temperature of the maximum density to the hot and cold reference temperatures accompanied by a modified Rayleigh number defined as $Ra = g\beta\Delta T^q L^3/\nu\alpha$, the dimensionless momentum equation is expressed as follows in this category,

$$\partial \boldsymbol{U}/\partial t + \boldsymbol{U} \cdot \nabla \boldsymbol{U} = -\nabla P + Pr \nabla^2 \boldsymbol{U} - RaPr(\Theta - \Theta_m)^q \boldsymbol{e}_g. \tag{22}$$

For $0 < \Theta_m < 1$, T_{max} lies between the hot and cold reference temperatures. Thus, studies in this category focus on this regime and the corresponding flow patterns due to different inversion parameters. One of the pioneer studies in this category was performed by Nansteel *et al.* [58] in the small range of the Rayleigh number in a rectangular cavity with three different height to length aspect ratios. They found that the inversion parameter near 0.5 ($\Theta_m = 0.5$) results in a counter-rotating pair of vortices arranged horizontally in the enclosure. Similar behavior of dual rotating vortices in this problem is also reported by Braga & Viskanta [59]. Osorio *et al.* [60] studied this problem in an inclined square cavity. Another pioneering study in this category for the annulus cavity using a 4th-order density state equation is performed by Vasseur *et al.* [61]. They noticed a secondary vortex pair at the top of the inner cylinder for a limited range of inversion parameters. Raghavarao & Sanyasiraju [62] repeated this problem with a second-order density equation of state. They noticed a uni-cellular flow pattern at $\Theta_m = 0$ and 1, and a bi- cellular flow pattern at $\Theta_m = 0.5$. Ho & Lin [63] studied the NC of water close to its maximum density in eccentric annulus using Gebhart and Mollendorf equation of state [57]. Studying the NC of water around the horizontal cylinder in free space using a 4th-order density state equation is performed by Wang *et al.* [64]. In this category, the quadratic density state equation is also used for numerical simulation of the oscillatory NC in the square cavity [65].

3.2.3. *Variable thermophysical properties*

In the OB regime limit, the thermophysical properties of the working fluid are considered constant, which is a valid assumption for small temperature differences. However, when the temperature differences become large enough, the constant properties assumption is no longer valid, especially for working fluids sensitive to the temperature differences. Since most of the compressible/weakly compressible simulations are devoted to large temperature differences, the idea of applying variable thermophysical properties is applied by default to the formulation in those works [15–17,22–32]. This approach is also pursued in an incompressible category beyond the OB approximation. One of the pioneer studies in this category is performed by Zhong *et al.* [66]. Their numerical results of NC via variable thermophysical properties approach in the square cavity for air as working fluid confirms that up to $\varepsilon = 0.05$, the results of OB is valid. Also, at $\varepsilon \cong 0.1$, OB still correctly predicts overall heat transfer, but it over predicts the maximum vertical velocity by approximately 20%. Zhong *et al.* [66] also presented a relation for relative temperature difference as a function of the Rayleigh number determining the OB approximation's valid performance. Leal *et al.* [67] continued this approach and concluded that the properties variation effects are considerable even within the OB regime. Hernández & Zamora [68] applied this approach for vertical channels. Mahony *et al.* [69] studied the annulus cavity problem under variable thermophysical properties assumption. They found that the OB assumption over-predicts the tangential velocity and the temperature gradient near the hot inner cylinder while under-predicting both close to the cold outer cylinder. In this category, a similar study of the annulus cavity considering eccentric effects is also performed by Shahraki [70].

4. Conclusion

This review provides a general framework of different numerical approaches beyond the Oberbeck—Boussinesq approximation for buoyancy-driven flows. Two main approaches, compressible and incompressible, are distinguished, with different strategies elucidated within each class. A brief review of pioneering studies in each category is also performed. This short communication paper does not cover the broader literature on non-Oberbeck—Boussinesq natural convection, but the presented framework, in theory, may categorize any publication in this field of study. The literature survey indicates that, however the current compressible approaches work with high accuracy for natural convection problems associated with large temperature differences, but it seems the main challenge of the future non-Oberbeck—Boussinesq approximations would be improving the accuracy of the computations while retaining the simplicity of an incompressible approach.

Declaration of Competing Interest

None.

Acknowledgements

This research was supported by the Australian Research Council through Discovery Project DP180102647. P. M. is supported by a Monash Graduate Scholarship and a Monash International Postgraduate Research Scholarship.

References

[1] J. Boussinesq, Theorie Analytique de la Chaleur, Gauthier-Villars, Paris, 1897.
[2] D.D. Josef, Stability of Fluid Motions II, Springer, Berlin, 1976.
[3] A. Oberbeck, Ueber die Wärmeleitung der Flüssigkeiten bei Berücksichtigung der Strömungen infolge von Temperaturdifferenzen, Annual Rev Chem 7 (1879) 271.
[4] S. Lenz, M. Krafczyk, M. Geier, S. Chen, Z. Guo, Validation of a two-dimensional gas-kinetic scheme for compressible natural convection on structured and unstructured meshes, Int. J. Thermal Sci. 136 (2019) 299–315.
[5] D.D. Gray, A. Giorgini, The validity of the Boussinesq approximation for liquids and gases, Int. J. Heat Mass Transf. 19 (5) (1976) 545–551.
[6] J.D. Anderson, Computational fluid dynamics: the basics with applications, McGraw-Hill, 1995.
[7] P.L. Roe, Approximate Riemann solvers, parameter vectors, and different schemes, J. Comput. Phys. 43 (2) (1981) 357–372.
[8] K.C. Karki, S.V. Patankar, Pressure based calculation procedure for viscouse flows at all speeds in arbitrary configurations, AIAA J. 27 (9) (1989) 1167–1174.
[9] H. Paillere, C. Viozat, A. Kumbaro, I. Toumi, Comparison of low Mach number models for natural convection problems, Heat Mass Transf. 36 (2000) 567–573.
[10] E. Turkel, Review of preconditioning methods for fluid dynamics, Appl. Numer. Math. 12 (1–3) (1993) 257–284.
[11] J.M. Weiss, W.A. Smith, Preconditioning applied to variable and constant density flows, AIAA J. 33 (11) (1995) 2050–2057.
[12] S. Mazumder, On the use of the fully compressible Navier-Stokes equations for the steady-state solution of natural convection problems in closed cavities, ASME: *J. Heat Transf.* 129 (2007) 387–390.
[13] Y.H. Choi, C.L. Merkle, The Application of Preconditioning in Viscous Flows, J. Comput. Phys. 105 (2) (1993) 207–223.
[14] S.T. Yu, B.N. Jiang, J. Wu, N.S. Liu, A Div-Curl-Grad Formulation for compressible buoyant flows solved by the least-squares finite-element method, Comput. Methods Appl. Mech. Eng. 137 (1) (1996) 59–88.
[15] J. Vierendeels, B. Merci, E. Dick, Numerical study of natural convective heat transfer with large temperature differences, Int. J. Numer. Methods heat fluid flow 11 (4) (2001) 329–341.
[16] M. Drabandi, S.F. Hosseinizadeh, Numerical simulation of thermobuoyant flow with large temperature Variation, JTHT 20 (2) (2006).
[17] M.M. El-Gendi, A.M. Aly, Numerical simulation of natural convection using unsteady compressible Navier-stokes equations, Int. J. Numer. Methods heat fluid flow 27 (11) (2017) 2508–2527.
[18] M. Drabandi, S.F. Hosseinizadeh, Numerical Study of natural convection in vertical enclosures using a novel non-Boussinesq algorithm, Numer. Heat Transf. Part A 52 (9) (2007) 849–873.
[19] K.N. Volkov, V.N. Emel'yanov, A.G. Karpenko, Preconditioning of Navier–Stokes equations in the computation of free convective flows, Comput. Math. Math. Phys. 55 (2015) 2080–2093.
[20] T.H. Kuhen, R.J. Goldstein, An experimental and theoretical study of natural convection in the annulus between horizontal concentric cylinders, J. Fluid Mech. 74 (4) (1976) 695–719.
[21] S. Yamamoto, D. Niiyama, B.R. Shin, A numerical method for natural convection and heat conduction around and in a horizontal circular pipe, Int. J. Heat Mass Transf. 47 (26) (2004) 5781–5792.
[22] W.S. Fu, C.G. Li, C.P. Huang, J.C. Huang, An investigation of a high temperature difference natural convection in a finite length channel without Boussinesq assumption, Int. J. Heat Mass Transf. 52 (11–12) (2009) 2571–2580.
[23] D. Talukdar, C.G. Li, M. Tsubokura, Numerical investigation of laminar compressible natural convection flow in asymmetrically and isothermally heated open-ended inclined channel, Int. J. Heat Mass Transf. 130 (2019) 83–97.
[24] S. Paolucci, On the filtering of sound from the Navier-Stokes equations, Technical report 9, Sandia National Laboratories, 1982. SAND 82–8257.
[25] D.R. Chenoweth, S. Paolucci, Natural convection in an enclosed vertical air layer with large horizontal temperature differences, J. Fluid Mech. 169 (1986) 173–210.
[26] P. Le Quéré, R. Masson, P. Perrot, A Chebyshev collocation algorithm for 2D non-Boussinesq convection, J. Comput. Phys. 103 (2) (1992) 320–335.
[27] S. Paolucci, D.R. Chenoweth, Transition to chaos in a differentially heated vertical cavity, J. Fluid Mech. 201 (1989) 379–410.

[28] Q. Wang, S.N. Xia, R. Yan, D.J. Sun, Z.H. Wan, Non-Oberbeck-Boussinesq effects due to large temperature differences in a differentially heated square cavity filled with air, Int. J. Heat Mass Transf. 128 (2019) 479–491.
[29] P. Le Quéré, C. Weisman, H. Paillère, J. Vierendeels, E. Dick, R. Becker, M. Braack, J. Locke, Modelling of natural convection flows with large temperature differences: a benchmark problem for low Mach number solvers. Part 1. Reference solutions, Esaim Math Model Numer Anal **39** (3) (2005) 609–616.
[30] S.A. Suslov, S. Paolucci, Non-linear analysis of convection flow in a tall vertical enclosure under non-Boussinesq conditions, J. Fluid Mech. 344 (1997) 1–41.
[31] S.A. Suslov, S. Paolucci, Stability of natural convection flow in a tall vertical enclosure under non-Boussinesq condition, Int. J. Heat Mass Transf. 38 (12) (1995) 2143–2157.
[32] M. Elmo, O. Cioni, Low Mach number model for compressible flows and application to HTR, Nucl. Eng. Des. 222 (2–3) (2003) 117–124.
[33] M. Kumar, G. Natarajan, On the role of discrete mass conservation for non-Boussinesq flow simulations in enclosures, Int. J. Heat Mass Transf. 104 (2017) 1283–1299.
[34] A. Tyliszczak, Projection method for high-order compact schemes for low Mach number flows in enclosures, Int. J. Numer. Methods heat fluid flow 24 (5) (2014) 1141–1174.
[35] S.G. Cherkasov, Some special features of description of thermal and dynamic processes in gases in the approximation of homobaricity, High Temp. 48 (2010) 422–426.
[36] S.G. Cherkasov, A.V. Anan'ev, L.A. Moiseeva, Limitations of the Boussinesq model on the example of laminary natural convection of gas between vertical isothermal walls, High Temp. 56 (2018) 878–883.
[37] D. Angeli, G.S. Barozzi, M.W. Collins, O.M. Kamiyo, A critical review of buoyancy-induced flow transitions in horizontal annuli, Int. J. Therm. Sc. 49 (2010) 2231–2241.
[38] H.K. Dawood, H.A. Mohammedb, Nor Azwadi Che Sidik, K.M. Munisamy, M. A. Wahid, Forced, natural and mixed-convection heat transfer and fluid flow in annulus: A review, Int. Commun. Heat & Mass **62** (2015) 45–57.
[39] S.C. Saha, M.M.K. Khan, A review of natural convection and heat transfer in attic-shaped space, Energy Build 43 (2011) 2564–2571.
[40] O.M. Kamiyo, D. Angeli, G.S. Barozzi, M.W. Collins, V.O.S. Olunloyo, S.O. Talabi, A Comprehensive review of natural convection in triangular enclosures, ASME: Appl. Mech. Rev 63 (6) (2010), 060801–1:13.
[41] A. Baïri, E. Zarco-Pernia, J.M. García de María, A review on natural convection in enclosures for engineering applications, The particular case of the parallelogrammic diode cavity, Appl. Therm. Eng. 63 (2014) 304–322.
[42] D. Das, M. Roy, T. Basak, Studies on natural convection within enclosures of various (non-square) shapes – A review, Int. J. Heat Mass Transf. 106 (2017) 356–406.
[43] I.V. Miroshnichenko, M.A. Sheremet, Turbulent natural convection heat transfer in rectangular enclosures using experimental and numerical approaches: A review, Renew. Sust. Energ. Rev. 82 (2018) 40–59.
[44] H.F. Öztop, P. Estellé, W.M. Yan, K. Al-Salem, J. Orfi, O. Mahian, A brief review of natural convection in enclosures under localized heating with and without nanofluids, Int. Commun. Heat & Mass 60 (2015) 37–44.
[45] S. Pandey, Y.G. Park, M.Y. Ha, An exhaustive review of studies on natural convection in enclosures with and without internal bodies of various shapes, Int. J. Heat Mass Transf. 138 (2019) 762–795.
[46] E.A. Spiegel, G. Veronis, On the Boussinesq approximation for a compressible fluid, Astrophys. J. 131 (1960) 442.
[47] J.A. Dutton, G.H. Fichtl, Approximate equations of motion for gases and liquid, J. Atmos. Sci. 26 (2) (1969) 241–254.
[48] A. Barletta, Comments on a paradox of viscous dissipation and its relation to the Oberbeck–Boussinesq approach, Int. J. Heat Mass Transf. 51 (2008) 6312–6316.
[49] A. Barletta, Local energy balance, specific heats and the Oberbeck-Boussinesq approximation, Int. J. Heat Mass Transf. 52 (2009) 5266–5270.
[50] M. Pons, P. Le Quéré, An example of entropy balance in natural convection, Part 2: the thermodynamic Boussinesq equations, Comptes Rendus Mécanique 333 (2) (2005) 133–138.
[51] M. Pons, P. Le Quéré, Modeling natural convection with the work of pressure-forces: a thermodynamic necessity, Int. J. Numer. Meth. Heat & Fluid Flow. 17 (3) (2007) 322–332.
[52] D.A. Nield, The modeling of viscous dissipation in a saturated porous medium, ASME J. Heat Transf. 129 (2007) 1459–1463.
[53] T. Pesso, S. Piva, Laminar natural convection in a square cavity: low Prandtl numbers and large density differences, Int. J. Heat Mass Transf. 52 (2009) 1036–1043.
[54] J.M. Lopez, F. Marques, M. Avila, The Boussinesq approximation in rapidly rotating flows, J. Fluid Mech. 737 (2013) 56–77.
[55] P. Mayeli, G. Sheard, A new formulation for Boussinesq-type natural convection flows applied to the annulus cavity problem, Int. J. Numer. Methods Fluids 93 (3) (2021) 683–702.
[56] P. Mayeli, G. Sheard, Natural convection and entropy generation in square and skew cavities due to large temperature differences: A Gay-Lussac-type vorticity stream-function approach, Int. J. Numer. Methods Fluids (2021), https://doi.org/10.1002/fld.4980.
[57] B. Gebhart, J.C. Mollendorf, A new density relation for pure and saline water, Deep-Sea Res. 24 (1977) 831–848.
[58] M.W. Nansteel, K. Medjani, D.S. Lin, Natural convection of water near its density maximum in a rectangular enclosure: low Rayleigh number calculations, Phys. Fluids 30 (1987) 312–317.
[59] S.L. Braga, R. Viskanta, Transient natural convection of water near its density extremum in a rectangular cavity, Int. J. Heat Mass Transf. 35 (4) (1992) 861–875.
[60] A. Osorio, R. Avila, J. Cervantes, On the natural convection of water near its density inversion in an inclined square cavity, Int. J. Heat Mass Transf. 47 (19–20) (2004) 4491–4495.
[61] P. Vasseur, L. Robillard, B. Chandra Shekar, Natural convection heat transfer of water within a horizontal cylindrical annulus with density inversion effects, ASME: *J. Heat Transf.* 105 (1) (1983) 117–123.
[62] C.V. Raghavarao, Y.V.S.S. Sanyasiraju, Natural convection heat transfer of cold water between concentric cylinders, For high Rayleigh numbers – a numerical study, Int. J. Eng. Sci. **32** (1994) 1437–1450.
[63] C.J. Ho, Y.H. Lin, Natural convection heat transfer of cold water within an eccentric horizontal cylindrical annulus, ASME: J. Heat Transf. 110 (1988) 894–900.
[64] P. Wang, R. Kahawita, D.L. Nguyen, Transient natural convection with density inversion from a horizontal cylinder, Phys. Fluids A 4 (1992) 71–85.
[65] C.H. Lee, J.M. Hyun, H.S. Kwak, Oscillatory enclosed buoyant convection of a fluid with the density maximum, Int. J. Heat Mass Transf. 43 (19) (2000) 3747–3751.
[66] Z.Y. Zhong, K.T. Yang, J.R. Lioyd, Variable property effects in laminar natural convection in a square enclosure, ASME: J. Heat Transf. 107 (1985) 133–138.
[67] M.A. Leal, H.A. Machado, R.M. Cotta, Integral transform solutions of transient natural convection in enclosures with variable fluid properties, Int. J. Heat Mass Transf. 43 (2000) 3977–3990.
[68] J. Hernández, B. Zamora, Effects of variable properties and non-uniform heating on natural convection flows in vertical channels, Int. J. Heat Mass Transf. 48 (3–4) (2005) 793–807.
[69] D.N. Mahony, R. Kumar, E.H. Bishop, Numerical investigation of variable property effects on laminar natural convection of gases between two horizontal isothermal concentric cylinders, ASME: J. Heat Transf. 108 (4) (1986) 783–789.
[70] F. Shahraki, Modeling of buoyancy-driven flow and heat transfer for air in a horizontal annulus: effects of vertical eccentricity and temperature-dependent properties, Numer. Heat Transf. Part A 42 (6) (2002) 603–621.

1.3 Different possible scenarios for numerical simulation of natural convection

Classification of different approximations is performed in the context of a flowchart as shown in Fig. 1.1 [3]. As seen, the flow-chart resides under two overarching classes capturing compressible and incompressible approaches.

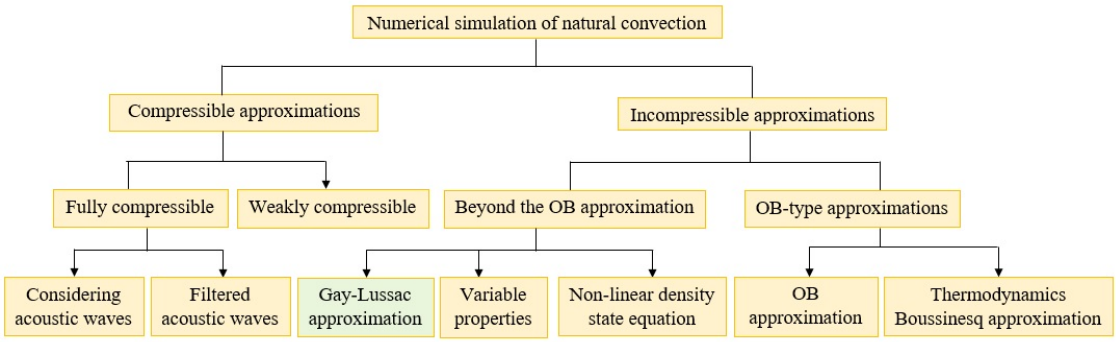

Figure 1.1: Classification of different approximations for numerical simulation of natural convection problems.

This thesis deals with a subclass of the Gay-Lussac approximation (highlighted in green in Fig. 1.1), sometimes referred to as a centrifugal approximation, which lies within the domain of incompressible approaches beyond the OB approximation. In brief, the Gay-Lussac approximation is distinguished against the conventional OB approximation by extending the density variations beyond only the gravity term of the momentum equation. This approximation will be discussed in details in the next two chapters.

1.4 Aims and structure of the thesis

The overarching aim of this thesis is to investigate the Gay-Lussac and related approximations for buoyancy in contrast to the conventional OB approximation, via consideration of several canonical benchmark problems. Focus is directed to the effects of these alternative approximations to the stability of a class of natural convection known as horizontal convection. The rest of the thesis is organised as follows: In the next chapter, the Gay-Lussac approximation and a simplified version of this approach are introduced,

and pertinent dimensionless parameters will be defined. In chapter 3, a Gay-Lussac type approach called the centrifugal approximation is introduced. In chapter 4, linearised Navier—Stokes equations under the centrifugal approximation are derived. A linear stability analysis of horizontal convection is conducted and stability thresholds are sought. In chapter 5, perturbation equations for an Orr-Sommerfeld type stability analysis are derived and a local stability analysis is performed. Heat transfer mechanism evolution is investigated and Nusselt number is scaled against the Rayleigh number. Finally, chapter 6 summarises findings of the research and gives some suggestions for future studies.

Chapter 2

2 The Gay-Lussac approximation

This chapter introduces the governing equations under the Gay-Lussac approximation. In this respect, governing equations under the Gay-Lussac approximation are derived and pertinent dimensionless numbers including Rayleigh, Prandtl and Froude numbers associated with the Gay-Lussac parameter are introduced. Then, the simplified Gay-Lussac approximation is presented in both primary and secondary variables form. The difference of the produced results under the two approximations are compared in two benchmark problems demonstrating that the simplified Gay-Lussac approximation gives identical results to the Gay-Lussac approximation with a lower computational cost.

2.1 Governing equations under the Gay-Lussac approximation

Under the OB approximation, density variations are ignored except within the gravity term of the momentum equation. However, under the Gay-Lussac (GL) approximation [4] as an incompressible approach, the density variations are extended beyond the gravity term. Dimensional form of the Navier—Stokes equations with thermal transport under the GL approximation in the absence of any additional force and negligible viscus heat dissipation after being divided by a reference density (ρ_0) may be expressed as,

$$(\rho/\rho_0)\nabla \cdot \boldsymbol{u} = 0, \tag{2.1}$$

$$\frac{\partial \boldsymbol{u}}{\partial t^*} + (\rho/\rho_0)(\boldsymbol{u} \cdot \nabla)\boldsymbol{u} = -(1/\rho_0)\nabla p + \nu\nabla^2\boldsymbol{u} + (\rho/\rho_0)g\mathbf{e}_g, \tag{2.2}$$

$$\frac{\partial T}{\partial t^*} + (\rho/\rho_0)(\boldsymbol{u} \cdot \nabla)T = \alpha\nabla^2 T, \tag{2.3}$$

and following the OB approximation by substitution a linear density state relation ($\rho/\rho_0 = 1 - \beta\Delta\theta$) into the governing equation yields

$$(1 - \beta\Delta\theta)\nabla \cdot \boldsymbol{u} = 0, \tag{2.4}$$

$$\frac{\partial \boldsymbol{u}}{\partial t^*} + (1 - \beta\Delta\theta)(\boldsymbol{u} \cdot \nabla)\boldsymbol{u} = -(1/\rho_0)\nabla p + \nu\nabla^2\boldsymbol{u} + (1 - \beta\Delta\theta)g\mathbf{e}_g, \tag{2.5}$$

$$\frac{\partial T}{\partial t^*} + (1 - \beta\Delta\theta)(\boldsymbol{u} \cdot \nabla)T = \alpha\nabla^2 T. \tag{2.6}$$

In Eqs. (2.1) to (2.6), $\boldsymbol{u}, p, \nu, \alpha$ and T represent dimensional velocity, pressure, kinematic viscosity, thermal diffusivity and temperature, respectively. In addition, the density ratio is ignored in the transient terms. With respect to the continuity equation under the GL approximation, it may be interesting for the reader to see/check how the (ρ/ρ_0) prefactor appears. Starting from the compressible form of the continuity equation

$$\frac{\partial \rho}{\partial t} + \nabla \cdot (\rho \boldsymbol{u}) = 0 \rightarrow \frac{\partial \rho}{\partial t} + \rho \nabla \cdot u + u \nabla \cdot \rho = 0, \tag{2.7}$$

and applying the impressibility constraint ($\rho = cte$) gives

$$\rho \nabla \cdot u = 0. \tag{2.8}$$

Dividing of Eq. (2.8) by a reference density (similar to what is done for the momentum and energy equations) yields the density ratio prefactor for the continuity equation. In the next step, a modified pressure $p^* = p + \rho_0 \phi$ is defined that absorbs the hydro-static effects into the hydro-dynamic pressure. Here, ϕ is the gravitational potential whose gradient opposes the gravitational acceleration vector, that is, $\nabla \phi = -g \mathbf{e}_g$, where $\mathbf{e}_g$ represents the unit vector in the direction of gravity. Using the following non-dimensionlisation of variables,

$$t = \frac{t^* \alpha}{L^2}, \boldsymbol{X} = \frac{\boldsymbol{x}}{L}, \boldsymbol{U} = \frac{\boldsymbol{u} L}{\alpha}, P = \frac{p^* L^2}{\rho \alpha^2}, \Theta = \frac{\theta}{\Delta \theta} = \frac{T - T_0}{T_h - T_c}, Ga = \beta \Delta \theta, \tag{2.9}$$

one can derive the dimensionless form of the governing equation under the Gay-Lussac approximation,

$$(1 - Ga\Theta) \nabla \cdot \boldsymbol{U} = 0, \tag{2.10}$$

$$\frac{\partial \boldsymbol{U}}{\partial t} + (1 - Ga\Theta)(\boldsymbol{U} \cdot \nabla) \boldsymbol{U} = -\nabla P + Pr \nabla^2 \boldsymbol{U} - RaPr\Theta \mathbf{e}_g, \tag{2.11}$$

$$\frac{\partial \Theta}{\partial t} + (1 - Ga\Theta)(\boldsymbol{U} \cdot \nabla)\Theta = \nabla^2 \Theta. \tag{2.12}$$

Eqs. (2.10) to (2.12) introduce the Prandtl number

$$Pr = \frac{\nu}{\alpha}, \tag{2.13}$$

characterising the ratio of the molecular to thermal dissipation and the Rayleigh number

$$Ra = \frac{g\beta\Delta\theta L^3}{\nu\alpha}, \tag{2.14}$$

characterising the ratio of buoyancy to viscous and thermal dissipation. As seen, the governing equations under the OB approximation are recovered as the GL parameter (Ga) approaches zero. Under this approximation, $(1 - Ga\Theta)$ acts as a modifier on different terms, and its effect becomes stronger by increasing Ga (and consequently $\Delta\theta$), but in practice Ga cannot exceed a specified value to avoid an unphysical (negative) density,

$$\rho/\rho_0 = 1 - \beta\theta = 1 - \beta\Delta\theta\Theta = 1 - Ga\Theta. \tag{2.15}$$

Eq. (2.15) indicates that, Ga cannot exceed $Ga_{max} = 2$ based on the defined dimensionless temperature, as it leads to a negative value for the density, i.e. $0 \leq Ga \leq 2$.

2.2 Governing equations under the simplified Gay-Lussac approximation

In this thesis, a simplified Gay-Lussac (SGL) approximation [5, 6] is proposed by omitting density variations from the continuity equation,

$$\nabla \cdot \boldsymbol{U} = 0, \tag{2.16}$$

$$\frac{\partial \boldsymbol{U}}{\partial t} + (1 - Ga\Theta)(\boldsymbol{U} \cdot \nabla)\boldsymbol{U} = -\nabla P + Pr\nabla^2 \boldsymbol{U} - RaPr\Theta\mathbf{e}_g, \tag{2.17}$$

$$\frac{\partial \Theta}{\partial t} + (1 - Ga\Theta)(\boldsymbol{U} \cdot \nabla)\Theta = \nabla^2\Theta. \tag{2.18}$$

As seen, the governing equations under the SGL approximation are consistent with the governing equations under the OB approximation, except for the pre-factors of the advection and convection terms of the momentum and energy equations, respectively. The roles of these pre-factors are to modify the advection/convection terms locally throughout the flow, physical effects that are ignored under the OB approximation. Indeed, regions of the thermo-flow field having a higher magnitude of the non-OB advection/convection contributions described by $|\Theta(\boldsymbol{U} \cdot \nabla)\boldsymbol{U}|$ and $|\Theta(\boldsymbol{U} \cdot \nabla)\Theta|$, respectively, will experience more deviations from the OB buoyancy approximation. The strength of these contributions is proportional to Ga, with $Ga \to 0$ ($\Delta\theta \to 0$), recovering the

classical OB approximation.

The GL-parameter may also be expressed as a product of Rayleigh, Prandtl, and Froude numbers ($Ga = RaPrFr$)), where the Froude number characterises the ratio of inertia to gravity ($Fr = \alpha^2/gL^3$) based on thermal dissipation velocity scale $u_0 = \alpha/L$. Thus, an alternate form of the governing equations under the SGL approximation may be expressed as

$$\nabla \cdot \boldsymbol{U} = 0, \tag{2.19}$$

$$\frac{\partial \boldsymbol{U}}{\partial t} + (1 - RaPrFr\Theta)(\boldsymbol{U} \cdot \nabla)\boldsymbol{U} = -\nabla P + Pr\nabla^2 \boldsymbol{U} - RaPr\Theta \mathbf{e}_g, \tag{2.20}$$

$$\frac{\partial \Theta}{\partial t} + (1 - RaPrFr\Theta)(\boldsymbol{U} \cdot \nabla)\Theta = \nabla^2\Theta. \tag{2.21}$$

The GL parameter is also equal to twice of the relative temperature difference that appears in the governing equation under the compressible/weakly-compressible approaches (See [3], section 2.2)

$$2\varepsilon = (T_h - T_c)/T_0 = \beta\Delta\theta = Ga. \tag{2.22}$$

Therefore, a more concise form of the governing equations under the SGL approximation may be expressed using ε instead of Ga,

$$\nabla \cdot \boldsymbol{U} = 0, \tag{2.23}$$

$$\frac{\partial \boldsymbol{U}}{\partial t} + (1 - 2\varepsilon\Theta)(\boldsymbol{U} \cdot \nabla)\boldsymbol{U} = -\nabla P + Pr\nabla^2 \boldsymbol{U} - RaPr\Theta \mathbf{e}_g, \tag{2.24}$$

$$\frac{\partial \Theta}{\partial t} + (1 - 2\varepsilon\Theta)(\boldsymbol{U} \cdot \nabla)\Theta = \nabla^2\Theta. \tag{2.25}$$

A secondary variables form of the governing equations can be obtained for two-dimensional flow fields by defining the vorticity ($\omega = \partial V/\partial X - \partial U/\partial Y$) and stream-function ($U = \partial\psi/\partial Y; V = -\partial\psi/\partial X$). The secondary variables form of the governing equations under the SGL approximation therefore becomes,

$$\nabla^2\psi = -\omega, \tag{2.26}$$

$$\frac{\partial \omega}{\partial t} + (1 - 2\varepsilon\Theta)\left(\frac{\partial\psi}{\partial Y}\frac{\partial\omega}{\partial X} - \frac{\partial\psi}{\partial X}\frac{\partial\omega}{\partial Y}\right) = Pr\nabla^2\omega + RaPr\frac{\partial\Theta}{\partial X}, \tag{2.27}$$

$$\frac{\partial \Theta}{\partial t} + (1 - 2\varepsilon\Theta)\left(\frac{\partial\psi}{\partial Y}\frac{\partial\Theta}{\partial X} - \frac{\partial\psi}{\partial X}\frac{\partial\Theta}{\partial Y}\right) = \nabla^2\Theta. \tag{2.28}$$

In the remainder of this chapter, the proposed simplified approach is studied via two different benchmark problems.

2.3 Published papers

The primary form of the governing equations is applied to study free convection in the square cavity benchmark problem with different inclination angles. This work is published as a research paper entitled "A simplified and efficient Gay-Lussac approach for non-Boussinesq treatment of natural convection problems". The secondary variables form of the governing equations under the SGL approximation is used to study free convection in the annulus cavity benchmark problem and it is published as a research paper entitled "An efficient and simplified Gay-Lussac approach in secondary variables form for the non-Boussinesq simulation of free convection problems". In both works, governing equations are solved using a control volume finite element method (CVFEM) solver which is described in the published works.

NUMERICAL HEAT TRANSFER, PART B: FUNDAMENTALS
2021, VOL. 80, NOS. 5–6, 115–135
https://doi.org/10.1080/10407790.2021.1946310

A simplified and efficient Gay-Lussac approach for non-Boussinesq treatment of natural convection problems

Peyman Mayeli and Gregory J. Sheard

Department of Mechanical and Aerospace Engineering, Monash University, Clayton, Victoria, Australia

ABSTRACT

Under the Boussinesq approximation for buoyancy driven flows, density variations are restricted to the gravity term. In contrast, the Gay-Lussac (GL) approach is developed based on considering density variations in any term of the Navier—Stokes equations in which density appears. In both incompressible approaches, a linear density state equation is adopted to relate density variations to temperature differences. In this article, a simplified Gay-Lussac (SGL) approach with a reduced computational cost is proposed in which density variations are omitted from the continuity equation. It is shown that the SGL approach gives identical results to the traditional GL approach in both transient and steady states. Then, performance of the SGL approach at high relative temperature differences up to $\varepsilon = 0.3$ is evaluated against the low Mach number scheme and the Boussinesq approximations. In this respect, natural convection in square cavity benchmark problem at three different inclination angles ($\gamma = 0$ and $\pm\pi/6$) is simulated up to $Ra = 10^7$ at $Pr = 1$ and results are analyzed in terms of the local and average Nusselt number, and the skin friction coefficient. Comparing computational cost of simulations at $Ra = 10^7$ indicates the introduced SGL approach has 17% and 11% less computational cost using upwind and central schemes, respectively, compared to the traditional GL approach, while the convergence rate is not affected by the proposed simplification. Comparing the Nusselt number shows a negligible difference between the SGL and the Boussinesq approximations at high relative temperature differences, both deviating from the low Mach number scheme. Finally, by comparing the friction coefficient results obtained by the SGL approach against the weakly compressible approach it is concluded that the GL family approaches require serious revisions to outperform the Boussinesq approximation as an incompressible approach for buoyancy driven flows with high relative temperature differences.

ARTICLE HISTORY
Received 14 April 2021
Accepted 17 June 2021

1. Introduction

The well-known Boussinesq approximation [1] is still the most common approach for the numerical simulation of natural convection (NC) problems. The general idea of treating natural convection (NC) as incompressible by ignoring density variations except in the buoyancy term first was proposed by Oberbeck [2], which is why the approximation's is sometimes referred to as the Oberbeck—Boussinesq (OB) approximation. Under the OB approximation, a linear state equation is adopted to relate density variations to temperature differences. The OB approximation due to its great accuracy of performance for problems associated by differential temperature differences

CONTACT Peyman Mayeli peyman.mayeli@gmail.com Department of Mechanical and Aerospace Engineering, Monash University, Room 354, Level 3, Woodside Building for Technology and Design, 20 Exhibition Walk, Clayton, VIC 3800 Australia.

Nomenclature

Be_{ave}	average Bejan number
c_f	skin friction coefficient
D	diffusion operator
e_g	unit vector in gravity direction
g	gravitational acceleration
Ga	Gay-Lussac number ($\beta\Delta\theta$)
L_{ref}	reference length
N	Nonlinear operator
Nu_{ave}	average Nusselt number
Nu_{loc}	local Nusselt number
p	pressure
p^*	modified pressure
P	dimensionless pressure
P_{th}	thermodynamic pressure
Pr	Prandtl number
R	ideal gas constant
Ra	Rayleigh number
S	surface
T	temperature
x	coordinate vector
X	dimensionless coordinate vector
u	velocity vector
U	dimensionless velocity vector
α	thermal diffusivity
β	isobaric expansion coefficient
γ	cavity inclination angle
ε	relative temperature difference
η	heat capacity ratio
θ	physical temperature
Θ	dimensionless temperature
μ	dynamic viscosity
ν	kinematic viscosity
ρ	density
ρ_0	reference density
τ_w	wall shear stress
ϕ	gravitational potential

Subscript

ave	average
c	cool
h	hot
loc	local
ref	reference
tot	total

has been used as the basis of many benchmark natural convection problems in different geometries such as rectangular [3–8], triangular [9–12] and annulus [13–15] enclosures.

One of the fundamental assumptions of the OB approximation is small temperature differences, which justifies restricting density variations to the buoyancy term. Indeed, applying the OB approximation on cases that are featuring large density variations produces inaccurate results [16]. Foundry processes, astrophysical magnetohydrodynamics [17], thermal insulation systems in nuclear reactors [18] and solar collectors [19–20] are samples that such a situation may take place. Numerical techniques that seek to circumvent the limitations of the OB approximation are less abundant in the literature. In general, non-OB approximations for NC problems occupy two general categories, compressible and incompressible.

The first category of the non-OB algorithms is developed by retaining compressibility within the Navier—Stokes equations, which leads to the introduction of the Mach number. This strategy is seldom used for numerical simulation of NC problems due to instability at small order of compressibility ratio for density-based compressible flow solvers; examples include Vierendeels *et al.* [21], Fu *et al.* [22], Busto *et al.* [23], and Bermúdez *et al.* [24]. Small orders of Mach umber in natural convection problems motivated the use of the low Mach number scheme (LMS). Under the this approximation developed by Paulucci [25], acoustic waves are removed from the governing equation and total pressure is split into two main parts a global (uniform) thermodynamic pressure which is obtained from the equation of state and used for updating the density variations through the solution procedure, and a local hydrodynamic pressure which acts in the momentum equations to establish a balance among advection, buoyancy, and diffusion terms. Vierendeels *et al.* [26] and Becker & Braack [27] applied this technique for numerical simulation of the square cavity benchmark problem with large temperature differences beyond the validity of the OB regime.

The second category of the non-OB approximations are developed under the fundamental assumption of incompressibility. One of the remedies to avoid the OB approximation in this

category is the Gay-Lussac (GL) approach, which is developed based on considering density variations beyond the gravity term. Under the GL approximation, buoyancy effects are taken into account wherever density appears in the governing equations. Such a strategy invokes the GL parameter as a product of the volumetric thermal expansion coefficient and the reference temperature difference ($Ga = \beta\Delta\theta$). Under the GL approach, a pre-factor of $(1 - Ga\Theta)$ acts as a modifier on the aforementioned terms in dimensionless form of the governing equations. The strength of this pre-factor and its modification effects become more visible by increasing the GL parameter at high temperature differences. It can also be shown that governing equations under the GL approach recover the OB approximation as $Ga \to 0$. For instance, the square cavity benchmark problem with large density variations was analyzed under the GL approach by Pesso & Piva [28]. A GL-type approximation is also possible by extension of buoyancy effects to one of the advection or convection terms of the momentum and energy equations, respectively. In this category, a GL-type approach is proposed by Lopez *et al.* [29] in which density variations were extended only to the centrifugal part of the advection term to capture centrifugal effects arising from background rotation in those rapidly rotating flows. This approach continued by Mayeli & Sheard [30–31]. They showed that the GL parameter may be expressed in terms of the Rayleigh, Prandtl and Froude numbers ($Ga = RaPrFr$). Since the GL parameter appears in the dimensionless form of the linear density relation, a maximum value $Ga_{max} = 2$ should be considered to avoid an unphysical (negative) density. Such a constraint also confines the maximum physical value of the Froude number at each Rayleigh and Prandtl number to $2/RaPr$ ($Fr_{\max} = 2/RaPr$). Mayeli & Sheard [30–31] also established a relation for the GL-type family approach that matches the Froude number corresponding to a given relative temperature difference (ε) at each Ra and Pr as $Fr = 2\varepsilon/RaPr$.

Another incompressible-based strategy to go beyond the OB approximation is considering nonlinear terms via retention of higher terms (e.g. square and cubic terms) of the density state relation, that enables the non-OB category to a wider spectrum of temperature difference. A nonlinear density state relation may also justify strange behavior of some fluids at temperatures close or equal maximum density. For instance, the density-temperature relationship of cold water in the vicinity of 4 °C does not obey a linear function. In this situation, the linear density state relation may not be valid anymore even for small temperature differences within valid temperature difference range of the OB regime. For these types of problems, a dimensionless temperature known as the inversion parameter is defined which relates the temperature of the maximum density to the hot and cold reference temperatures. Since for inversion parameter values smaller than unity the temperature corresponding to the maximum density lies between the hot and cold reference temperatures, studies in this category are focused on this range and the corresponding flow patterns due to different inversion parameters. For instance, this strategy was used by Li *et al.* [32] for natural convection of water near its maximum density in an eccentric annulus cavity.

Under the OB approximation, dissipated heat due to viscous friction and work of pressure stress are removed from the energy equation as their effects are supposed to be negligible. Justification for omission of dissipation and pressure work terms are made based on order of magnitude arguments, but thermodynamically speaking, removing these items brings a paradox to entropy generation budget. It should be noted that the momentum equations captures dissipation of momentum due to fluid friction (diffusion terms) but the equivalent dissipated heat is not captured in the energy equation under the OB approximation. In addition, absence of the pressure work in the energy equation causes a mismatch between the internal energy and work done upon the fluid. Using Gibbs and local entropy balance equations, it can be shown that when these terms are neglected in the energy equation, the thermodynamic system described under the OB approximation recognizes only heat conduction as a source of irreversibility and neglects irreversibilities due to viscous friction. This inspired development of a more comprehensive form of the

energy equation under the OB approximation referred to various names such as 'deep convection' [33], 'thermodynamic' [34], and 'extended' [35] Boussinesq approximations. Pons & Le Quéré [36] applied the thermodynamic Boussinesq approximations for natural convection problems and concluded that when the dimensionless adiabatic temperature gradient is larger than 0.01, the pressure work effects are no longer negligible.

In the limit of small temperature differences of the OB operating regime, thermophysical properties of the working fluid are considered as constant. This is a correct assumption as small temperature differences do not impose significant effects on the thermophysical properties of the fluid, but as soon as temperature differences become large enough, the assumption of constant properties may not be valid anymore, especially for working fluids sensitive to temperature differences. The idea of the variable properties (often as a function of temperature) is considered as a separate class of approaches beyond the OB approximation, though in this subcategory, still other fundamentals of the OB approximation are applied. According to Leal *et al.* [37], the property variation effects are considerable even well within the OB regime. Many works have been done in this type of incompressible treatment of the governing equations beyond the OB approximation that are focused on checking/comparing the thermo-flow field when thermophysical properties are considered as constant (OB approximation) or treated variable as a function of temperature or even pressure. This strategy was used by Souza *et al.* [38] where all properties of the working fluid including viscosity, thermal conductivity and also heat capacity were considered as functions of temperature for numerical simulation of NC in an inclined square cavity (including zero leaning angle).

In this article, a simplified Gay-Lussac (SGL) approach is presented for buoyancy driven flows in which density variations are extended to the advection/convection terms of the momentum and energy equations, respectively. In other words, under the SGL approach, density variations are omitted only from the continuity equation. An square cavity benchmark problem is selected to show that the results of the GL and SGL approaches are consistent in both transient and steady state levels, but the SGL has a simpler form with cheaper computational cost. Subsequently, performance of the SGL as an efficient representative of the GL family is tested against the OB and weakly compressible approximations at high relative temperature differences in square cavity benchmark problem with different leaning angles.

The rest of the article is organized as follows: Section 2 presents the aforementioned GL and SGL formulation and also governing equations under the LMS approximation. Section 3 introduces the geometry and boundary conditions of the problem and concerns about numerical considerations including used code accuracy and mesh size dependency. In Section 4, similar performance of the GL and SGL approximations with a reduced computational cost for the SGL approach is proved. In Section 5, the mismatch among SGL, OB and LMS approximations is scrutinized, and finally conclusions are drawn in Section 6.

2. Gay-Lussac and simplified Gay-Lussac approximations

Under the OB approximation, density variations are ignored except within the gravity term. An incompressible non-OB treatment of the governing equation is the GL approach that is established based on considering the density variations beyond the gravity term. Starting with the dimensional form of the incompressible Navier—Stokes equations with thermal transport in the absence of any additional force and negligible viscus heat dissipation,

$$\begin{cases} (\rho/\rho_0)\nabla \cdot u = 0, \\ \partial \boldsymbol{u}/\partial t^* + (\rho/\rho_0)(\boldsymbol{u}\cdot\nabla)u = -(1/\rho_0)\nabla p + \nu\nabla^2\boldsymbol{u} + (\rho/\rho_0)\boldsymbol{e_g}, \\ \partial T/\partial t^* + (\rho/\rho_0)(\boldsymbol{u}\cdot\nabla)T = \alpha\nabla^2 T. \end{cases} \tag{1}$$

Following the OB approach, substitution a linear density state relation ($\rho/\rho_0 = 1 - \beta\theta$) into the governing equation yields

$$\begin{cases} (1-\beta\theta)\nabla\cdot u = 0, \\ \partial \boldsymbol{u}/\partial t^* + (1-\beta\theta)(\boldsymbol{u}\cdot\nabla)u = -(1/\rho_0)\nabla p + \nu\nabla^2\boldsymbol{u} + (\rho/\rho_0)\boldsymbol{e_g}, \\ \partial T/\partial t^* + (1-\beta\theta)(\boldsymbol{u}\cdot\nabla)T = \alpha\nabla^2 T. \end{cases} \tag{2}$$

In Eq. (2), p^* is a modified pressure introduced as $p^* = p + \rho_0\phi$, where ϕ is the gravitational potential. Using dimensionless parameters

$$t = \frac{t^*\alpha}{L^2}, \boldsymbol{X} = \frac{\boldsymbol{x}}{L}, \ \boldsymbol{U} = \frac{\boldsymbol{u}L}{\alpha}, P = \frac{p^*L^2}{\rho\alpha^2}, \ \Theta = \frac{\theta}{\Delta\theta} = \frac{T-T_0}{T_h - T_c}, Ga = \beta\Delta\theta, \tag{3}$$

one can derive the dimensionless form of the governing equation under the GL approximation,

$$\begin{cases} (1-Ga\Theta)\nabla\cdot U = 0, \\ \partial \boldsymbol{U}/\partial t + (1-Ga\Theta)(\boldsymbol{U}\cdot\nabla)U = -\nabla P + Pr\nabla^2\boldsymbol{U} - RaPr\Theta\boldsymbol{e_g}, \\ \partial\Theta/\partial t + (1-Ga\Theta)(\boldsymbol{U}\cdot\nabla)\Theta = \nabla^2\Theta, \\ \Theta(\boldsymbol{X},0) = \boldsymbol{U}(\boldsymbol{X},0) = 0. \end{cases} \tag{4}$$

Eq. (4) introduces the Prandtl number $Pr = \nu/\alpha$ characterizing the ratio of the molecular to thermal dissipation and the Rayleigh number $Ra = g\beta\Delta\theta {L_{\text{ref}}}^3/\nu\alpha$ characterizing the ratio of buoyancy to viscous and thermal dissipation. As seen, governing equations under the OB approximation are recovered as $Ga \to 0$ ($\Delta\theta \to 0$). Under the GL approximation, $(1 - Ga\Theta)$ acts as a modifier on different terms, and its effect becomes more pronounced by increasing Ga (and consequently $\Delta\theta$), but in practice Ga cannot exceed a specified value to avoid an unphysical (negative) density

$$\rho/\rho_0 = 1 - \beta\theta = 1 - \beta\Delta\theta\Theta = 1 - Ga\Theta > 0. \tag{5}$$

Eq. (5) indicates that the maximum Ga cannot exceed 2 ($Ga_{max} = 2$) based on the defined dimensionless temperature. In this study, a simplified Gay-Lussac (SGL) approximation is proposed by omitting density variations only from the continuity equation

$$\begin{cases} \nabla\cdot U = 0, \\ \partial \boldsymbol{U}/\partial t + (1-Ga\Theta)(\boldsymbol{U}\cdot\nabla)U = -\nabla P + Pr\nabla^2\boldsymbol{U} - RaPr\Theta\boldsymbol{e_g}, \\ \partial\Theta/\partial t + (1-Ga\Theta)(\boldsymbol{U}\cdot\nabla)\Theta = \nabla^2\Theta, \\ \Theta(\boldsymbol{X},0) = \boldsymbol{U}(\boldsymbol{X},0) = 0. \end{cases} \tag{6}$$

As seen, the governing equations under the SGL approximation are consistent with the governing equations under the OB approximation, except for the pre-factors of the advection/convection terms in the momentum and energy equations, respectively. The roles of these pre-factors are to modify the strength of the advection/convection terms locally throughout the flow, physics that is ignored in the OB approximation. Indeed, regions of the thermo-flow field having a higher magnitude of the non-OB advection/convection described by $|\Theta(\boldsymbol{U}\cdot\nabla)\boldsymbol{U}|$ and $|\Theta(\boldsymbol{U}\cdot\nabla)\Theta|$, respectively, will experience more deviations from the OB buoyancy approximation. The strength of the pre-factors modification is proportional to Ga, magnitude with $Ga \to 0$ ($\Delta\theta \to 0$) recovering the classical OB approximation. The GL-parameter is a product of Rayleigh, Prandtl, and Froude numbers ($Ga = RaPrFr$) where the Froude number characterizes the ratio of inertia to gravity. Thus, another form of the governing equations under the SGL approximation may be expressed as

$$\begin{cases} \nabla \cdot \boldsymbol{U} = 0, \\ \partial \boldsymbol{U}/\partial t + (1 - RaPrFr\Theta)(\boldsymbol{U} \cdot \nabla)\boldsymbol{U} = -\nabla P + Pr\nabla^2 \boldsymbol{U} - RaPr\Theta \boldsymbol{e_g}, \\ \partial \Theta/\partial t + (1 - RaPrFr\Theta)(\boldsymbol{U} \cdot \nabla)\Theta = \nabla^2 \Theta. \end{cases} \tag{7}$$

As mentioned earlier, in this study results are compared against the LMS approximation. Governing equations under the LMS approximation are expressed as [25–27]

$$\begin{cases} \partial \rho/\partial t^* + \nabla \cdot (\rho \boldsymbol{u}) = 0, \\ \partial(\rho \boldsymbol{u})/\partial t^* + \nabla \cdot (\rho \boldsymbol{u} \otimes \boldsymbol{u}) = -\nabla p^* + \ \nabla \cdot \boldsymbol{\tau} + \rho g \boldsymbol{e}_g, \\ \rho c_p(\partial T/\partial t^* + \boldsymbol{u} \cdot \nabla T) = k\nabla^2 T + \mathrm{d}p_{\mathrm{th}}/\mathrm{d}t^*, \\ P_{th} = \rho R T, \\ T(\boldsymbol{X}, 0) = T_0, p_{th}(0) = p_0, \boldsymbol{u}(\boldsymbol{x}, 0) = 0. \end{cases} \tag{8}$$

In Eq. (8), $p_{\mathrm{th}}(t)$ is the (spatially uniform) thermodynamic pressure, and c_p is the specific heat at constant pressure, which may be expressed in terms of heat capacity ratio ($\eta = c_p/c_v$) and the gas constant (R) as $c_p = \eta R/(\eta - 1)$. Also, $\boldsymbol{\tau}$ is the stress tensor that under Stokes's hypothesis for bulk viscosity ($\lambda = -2/3\mu$) is defined as

$$\boldsymbol{\tau} = \nabla \boldsymbol{u} + (\nabla \boldsymbol{u})^T - 2/3(\nabla \cdot \boldsymbol{u})\boldsymbol{I}. \tag{9}$$

In natural convection simulation via compressible/weakly-compressible approach, Prandtl number is introduced as defined earlier, but the Rayleigh number is expressed slightly differently compared to the incompressible flow, as

$$Ra = 2\varepsilon Pr \frac{g{\rho_0}^2 L^3}{{\mu_0}^2}. \tag{10}$$

In Eq. (10), ε is the relative temperature difference defined as $\varepsilon = (T_h - T_c)/2T_0$, so that $T_h = T_0(1 + \varepsilon)$ and $T_c = T_0(1 - \varepsilon)$. Comparing ε and Ga definitions gives an interesting relation for the Froude number at each Rayleigh and Prandtl number, as

$$\underbrace{2\varepsilon = (T_{\mathrm{h}} - T_{\mathrm{c}})/T_o}_{\text{Compressible}} = \underbrace{\beta \Delta\theta = Ga = RaPrFr}_{\text{Incompressible}} \rightarrow Fr = 2\varepsilon/RaPr. \tag{11}$$

Another advantage of Eq. (11) is expressing Ga by the relative temperature difference definition ($Ga = 2\varepsilon$). Thus, another form of the governing equations under the SGL approximation may be obtained using ε instead of Ga and/or three dominant dimensionless parameters i.e. Ra, Pr and Fr as

$$\begin{cases} \nabla \cdot \boldsymbol{U} = 0, \\ \partial \boldsymbol{U}/\partial t + (1 - 2\varepsilon\Theta)(\boldsymbol{U} \cdot \nabla)\boldsymbol{U} = -\nabla P + Pr\nabla^2 \boldsymbol{U} - RaPr\Theta \boldsymbol{e_g}, \\ \partial \Theta/\partial t + (1 - 2\varepsilon\Theta)(\boldsymbol{U} \cdot \nabla)\Theta = \nabla^2 \Theta \end{cases} \tag{12}$$

Finally, it should be noted that the physical range of the relative temperature difference ($0 \leq \varepsilon \leq 1$), gives a consistent constraint for physical range of Ga ($0 \leq Ga \leq 2$).

3. Description of the problem and numerical method

A schematic of the considered problem, i.e. square cavity at an inclination angle of γ which is considered equal to 0 and $\pm\pi/6$ in this study, is depicted in Figure 1. The applied thermal boundary conditions include two constant temperature and two adiabatic walls with a zero velocity boundary condition along all surfaces. For this problem, the reference length is equal to one

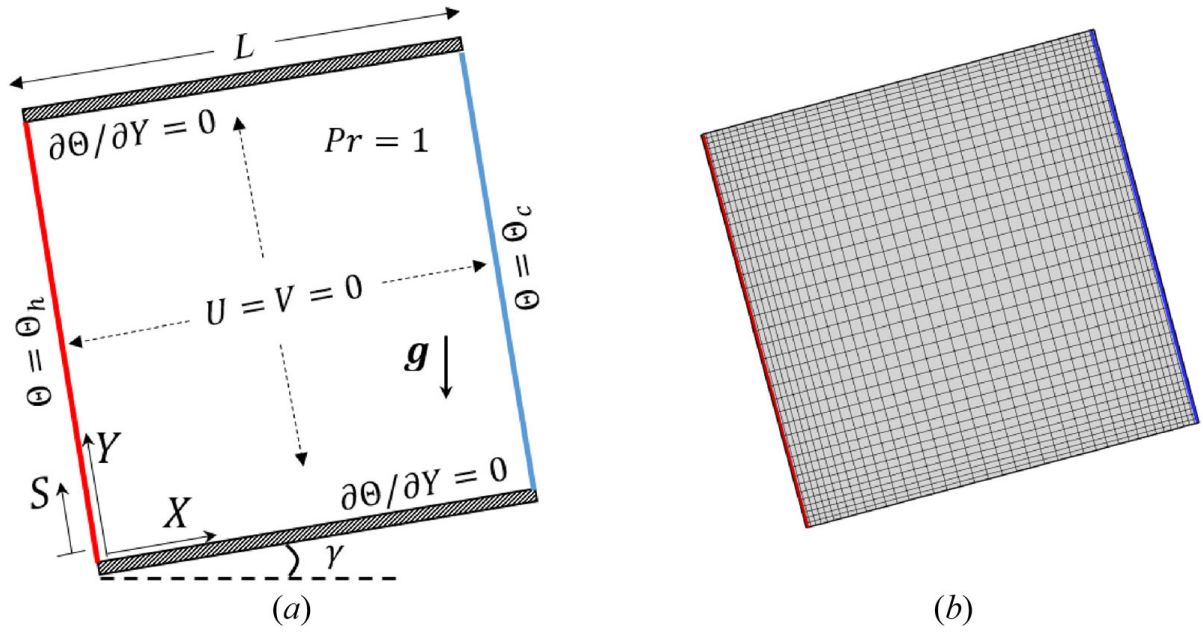

Figure 1. A schematic representation of the problem including (*a*) applied boundary conditions and (*b*) a coarse computational grid having 40 × 40 quadrilateral elements depicted at a positive leaning angle.

side length of the geometry ($L_{ref} = L$). The physical domain is meshed using quadrilateral elements. A schematic coarse mesh is shown for illustration purposes in Figure 1.

The local and average Nusselt number along the two constant-temperature surfaces are calculated from

$$Nu_{\text{loc}}(S) = -\left.\frac{\partial \Theta}{\partial \boldsymbol{n}}\right|_{\text{wall}}, \tag{13}$$

$$Nu_{\text{avg}} = \int_0^1 Nu_{\text{loc}}\ \mathrm{d}S. \tag{14}$$

In Eq. (13), $\boldsymbol{n}$ is the unit outward normal vector to the surface. The friction coefficient along the internal surfaces is calculated from

$$\boldsymbol{c_f} = -2Pr\begin{bmatrix}\tau_{xx} & \tau_{xy}\\ \tau_{yx} & \tau_{yy}\end{bmatrix}\begin{bmatrix}n_x\\ n_y\end{bmatrix} = -2Pr\begin{bmatrix}2\partial U/\partial X & \partial U/\partial Y + \partial V/\partial X\\ \partial U/\partial Y + \partial V/\partial X & 2\partial V/\partial Y\end{bmatrix}\begin{bmatrix}n_x\\ n_y\end{bmatrix}, \tag{15}$$

where n_x and n_y are the horizontal and vertical components of the wall-normal vector, respectively. The friction coefficient magnitude is defined as

$$c_f = \sqrt{(c_{f_x})^2 + (c_{f_y})^2} \tag{16}$$

where,

$$c_{f_x} = -2Pr\left[(2\partial U/\partial X)n_x + (\partial U/\partial Y + \partial V/\partial X)n_y\right], \tag{17}$$

$$c_{f_y} = -2Pr\left[(\partial U/\partial Y + \partial V/\partial X)n_x + (2\partial V/\partial Y)n_y\right]. \tag{18}$$

The governing equations are solved using a control volume finite-element method (CVFEM) solver employing a fractional step method with second order temporal accuracy (Adams Bashforth/Crank—Nicolson) for the time dependent equations. The nonlinear advection/convection terms are Discretized using both 2$^{\text{nd}}$-order upwind and central schemes, while diffusion terms are Discretized via central schemes. In CVFEM, a unique control volume (as shown in

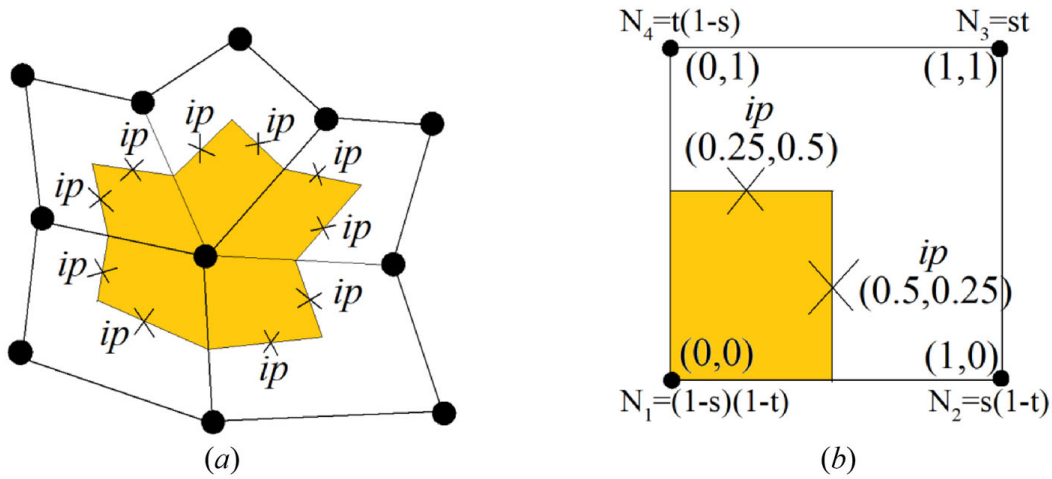

Figure 2. A schematic of unstructured quadrilateral elements: (*a*) a typical control volume associated with integration points (*b*) local coordinate (*s,t*) and bilinear shape functions in a standard element.

Figure 2(*a*)) is assigned to each node. The boundaries of each control volume are comprised of a number of planar panels and an integration point (*ip*) is assigned at the middle of each panel. Integration of the diffusion term over the control volume and applying the Gauss divergence theorem yields

$$\int_{v_p} \nabla^2 \boldsymbol{U} \mathrm{d}v = \oint_{A_p} \nabla \boldsymbol{U}_{ip} \cdot \mathrm{d}\boldsymbol{A} = \sum_{ip=1}^{n} \nabla \boldsymbol{U}_{ip} \cdot \boldsymbol{A}_{\boldsymbol{ip}}. \tag{19}$$

In Eq. (19), n is the number of integration points surrounding the main node and $\boldsymbol{A}_{\boldsymbol{ip}}$ is the normal vector surface at each *ip*. Using bilinear shape functions ($N_j(s,t)$), any parameter (such as $\boldsymbol{U}$) within the element with a local coordinate (s,t) is related to the nodal values via weighted values provided by shape functions

$$\boldsymbol{U}_{ip} = \boldsymbol{U}(s,t) = \sum_{j=1}^{4} N_j(s,t) \boldsymbol{U}_j. \tag{20}$$

The shape functions relating *ip* values to the nodal values for a quadrilateral element are shown in Figure 2(*b*). The diffusion operator may be expressed as follows

$$\mathrm{D}(\boldsymbol{U}) = \sum_{ip=1}^{n} \sum_{j=1}^{4} \omega_j \nabla N_j \cdot \boldsymbol{A}_{\boldsymbol{ip}}. \tag{21}$$

Since the bilinear shape functions are functions of their local coordinate system, their gradients with respect to the global coordinate system are calculated using the chain rule. In Eq. (21), the effect of all nodes surrounding an *ip* (such as the one shown in Figure 2(*b*)) are considered by weighted values. The diffusion operator in the energy equation is calculated in a similar fashion.

In the governing equations, nonlinear convection/advection terms are linearized using lagged values from the previous iteration. For instance, integration of the advection term over the control volume and applying Gauss divergence theorem yields

$$\int_{v_p} \boldsymbol{U} \cdot \nabla \overline{\boldsymbol{U}} \mathrm{d}v = \oint_{A_p} \boldsymbol{U}\left(\overline{\boldsymbol{U}} \cdot \boldsymbol{A}_{\boldsymbol{ip}}\right) = \sum_{ip=1}^{n} \boldsymbol{U}_{ip}\left(\overline{\boldsymbol{U}}_{\boldsymbol{ip}} \cdot \boldsymbol{A}_{\boldsymbol{ip}}\right). \tag{22}$$

Using bilinear shape functions (Eq. (20)) to relate the integral point values to the nodal values yields

Table 1. Comparison of the present calculated local and average Nusselt number by CVFEM solver (bold) with published benchmarks.

	Quantity	Present study	Davis [3]	Wan *et al.* [7]	Ashrafizadeh & Nikfar [8]
$Ra = 10^4$	Nu_{max} (at Y)	**3.548 (0.140)**	3.53 (0.143)	3.597 (0.13)	3.531 (0.139)
	Nu_{min} (at Y)	**0.589 (1.0)**	0.586 (1.0)	0.577 (1.0)	0.584 (1.0)
	Nu_{avg}	**2.23**	2.42	2.25	2.24
$Ra = 10^5$	Nu_{max} (at Y)	**7.778 (0.075)**	7.71 (0.08)	7.945 (0.08)	7.720 (0.084)
	Nu_{min} (at Y)	**0.734 (1.0)**	0.729 (1.0)	0.698 (1.0)	0.726 (1.0)
	Nu_{avg}	**4.51**	4.52	4.60	4.52
$Ra = 10^6$	Nu_{max} (at Y)	**17.633 (0.038)**	17.92 (0.038)	17.86 (0.03)	17.732 (0.039)
	Nu_{min} (at Y)	**0.996 (1.0)**	0.989 (1.0)	0.913 (1.0)	0.975 (1.0)
	Nu_{avg}	**8.82**	8.92	8.98	8.83
$Ra = 10^7$	Nu_{max} (at Y)	**40.253 (0.015)**	N. A.	38.60 (0.015)	39.457 (0.015)
	Nu_{min} (at Y)	**1.286 (1.00)**	N. A.	1.298 (1.00)	1.315 (1.00)
	Nu_{avg}	**16.51**	N. A.	16.66	16.54

$$N(\boldsymbol{U}) = \sum_{ip=1}^{n} \sum_{j=1}^{4} \boldsymbol{U}_j N_j \left(\overline{\boldsymbol{U}}_{\boldsymbol{ip}} \cdot \boldsymbol{A}_{\boldsymbol{ip}} \right). \tag{23}$$

Similarly, in Eq. (23) n is the number of ip surrounding the main node. If the lagged values in Eq. (23) (which are denoted by an overbar) disrespected of the flow direction to be approximated from nodal values within the element via weighted values from the, then the approximation is equivalent to the central scheme. Another possible Discretization is approximating lagged values considering flow direction, which is known as the upwind scheme. The nonlinear convection term in the energy equation is calculated in a similar fashion. Iterative solution procedure is stopped as soon as the maximum difference of variables during two successive iterations becomes less than 10^{-7}. Accurate performance of the used solver is already tested [39–47] but here it is further validated against refs. [3, 7, 8] in terms of the local and average Nusselt number of square cavity with zero inclination angle at four different Rayleigh number, adopting air as the working fluid ($Pr = 0.71$) in Table 1. A close agreement is observed.

Accurate performance of the CVFEM solver under the LMS approximation is also validated against ref. [48] in terms of the average Nusselt number and thermodynamic pressure at two Rayleigh numbers $Ra = 10^6$ and 10^7 at $\varepsilon = 0.6$ with air as the working fluid ($Pr = 0.71$) in two states including constant and variable properties (see Table 2). The present simulations recover published values very well, with discrepancies lower than 1.97%.

Mesh dependence is checked for the CVFEM solver in Table 3 at $Ra = 10^7$ and $Pr = 1$ under the OB approximation ($Ga = 0$) and under the GL approach at the highest Ga value in this study ($Ga = 0.6$). Results indicate that 124 nodes in each direction is enough for mesh independence for both incompressible approximations.

Mesh dependence of the CVFEM solver under the LMS approximation is also checked in Table 4 at the highest Rayleigh number $Ra = 10^7$ and $Pr = 1$ for the highest relative temperature difference ($\varepsilon = 0.3$) in this study. It is found using 124 nodes ($n_x \times n_y = 124^2$) in each direction guarantees results independence from the mesh size for the weakly compressible approach. Similar dependence is also found for the inclined cavity cases but for the sake of brevity, they are not mentioned here.

4. Comparing results under the GL and SGL approaches and computational cost

In this section, results obtained under the GL and SGL approaches are compared. In other words, it is shown the GL and SGL approaches give similar results in both transient and steady states. The mismatch in steady state solutions under the two approaches is investigated by calculation of the absolute difference in temperature and velocity magnitude in the square cavity with $\gamma = 0$ at

Table 2. Comparison of the present calculated local and average Nusselt number by CVFEM solver (bold) with published benchmarks.

	Quantity	Present study	Le Quéré *et al.* [48]	|difference|%
$Ra = 10^6,\ \varepsilon = 0.6$	P_{th}	0.858	0.856	0.23
Constant properties	Nu_{ave}	8.895	8.859	0.40
$Ra = 10^6,\ \varepsilon = 0.6$	P_{th}	0.921	0.924	0.32
Variable properties	Nu_{ave}	8.693	8.686	0.08
$Ra = 10^7,\ \varepsilon = 0.6$	P_{th}	0.920	0.922	0.21
Variable properties	Nu_{ave}	16.461	16.241	1.33

$Ra = 10^7,\ Pr = 1$ and $Ga = 0.6\ (\varepsilon = 0.3)$. The results are shown in Figures 3(*a*) and (*b*), respectively. The maximum absolute temperature and velocity magnitude differences in Figures 3(*a*) and (*b*) are approximately 0.0025 and 2.5, respectively, which ranges within 0.5% and 0.35% of the temperature and velocity magnitude values. Interestingly, the largest differences in velocity magnitude occur at top-left and bottom-right regions of the cavity. These regions correspond to where flow traveling adjacent to the hot and cold boundaries deflects horizontally. The longitudinal transport along the top and bottom walls is then perturbed, resulting in the largest temperature difference being detected in those regions.

Similar output/behavior of the GL and SGL approximations in the transient state is investigated in Figure 4 in the context of the absolute local Nusselt number and friction coefficient differences along the vertical surfaces of the square cavity with $\gamma = 0$ at $Ra = 10^7,\ Pr = 1$ and $Ga = 0.6$. Results indicate the absolute local Nusselt number difference is three orders smaller than the local Nusselt number magnitude during transient solution $(O(|\Delta Nu_{loc}|/Nu_{loc}) \sim 0.001)$. A similar comparison for the absolute local friction coefficient difference shows a value of five order smaller value, i.e. $O\left(|\Delta c_f|/c_f\right) \sim 10^{-5}$.

Computational cost and convergence histories of the GL and SGL approaches are also investigated in Figures 5(*a*) and (*b*), respectively. To compare computational cost, CPU-time is calculated at $Ra = 10^7,\ Pr = 1$ and $Ga = 0.6$ in two states in which advection/convection terms are Discretized using upwind or central schemes. Bar charts of Figure 5(*a*) shows a 17% and 11% lower computational cost for the SGL compared to the GL approximation for the central and upwind schemes, respectively. Convergence rates of the two approaches are also checked in terms of the velocity components and temperature tolerance in Figure 5(*b*). The tolerance of any scalar in this study is defined as the maximum alteration of all nodal values during two successive iterations. Results in Figure 5(*b*) indicate that both approaches have similar convergence rate and omitting density variations from the continuity equation merely simplifies the formulation and reduces the computational cost. Having demonstrated that the GL and SGL approximations exhibit identical behavior, we consider only the SGL approximation hereafter.

5. Results under the SGL, OB, and LMS approximations

In this section, results under the SGL, OB and LMS approximations are compared. Simulations are performed at $Pr = 1$ up to $Ra = 10^7\ (10^2 \leq Ra \leq 10^7)$ and $\varepsilon = 0.3\ (0 \leq \varepsilon \leq 0.3)$. It should be noted that a relative temperature difference of 0.01 is considered as a differential relative temperature difference and is representative of a OB case. Here, we extend this parameter to 30 times larger, beyond the validity of the OB approximation. Studying relative temperature differences exceeding 0.3 is beyond the scope and goals of this article. The considered range for ε gives $0 \leq Ga \leq 0.6$. For the considered range of the pertinent parameters, it is supposed that the flow field is 2 D, laminar and stable.

For a better understanding of the thermo-flow fields produced under the different approximations, absolute temperature differences of the weakly compressible approach at $Ra = 10^7$ and

Table 3. Mesh resolution study for average Nusselt number at $Ra = 10^7$ and $Pr = 1$.

	$n_x \times n_y$	31^2	62^2	124^2	248^2
OB approximation	Nu_{ave}	13.281114	13.812208	13.932074	13.932074
($Ga = 0$)	|difference|	–	0.531094	0.119866	0.000000
SGL approximation	Nu_{ave}	13.245957	13.772384	13.890921	13.890921
($Ga = 0.6$)	|difference|	–	0.526427	0.118537	0.000000

Table 4. Mesh resolution study for average Nusselt number and thermodynamic pressure at $Ra = 10^7$, $Pr = 1$, and $\varepsilon = 0.3$.

	$n_x \times n_y$	62^2	124^2	248^2
LMS approximation	P_{th}	0.9601	0.9677	0.9677
	|difference|	–	0.0076	0.000000
	Nu_{ave}	13.9613	14.0476	14.0476
	|difference|	–	0.0863	0.000000

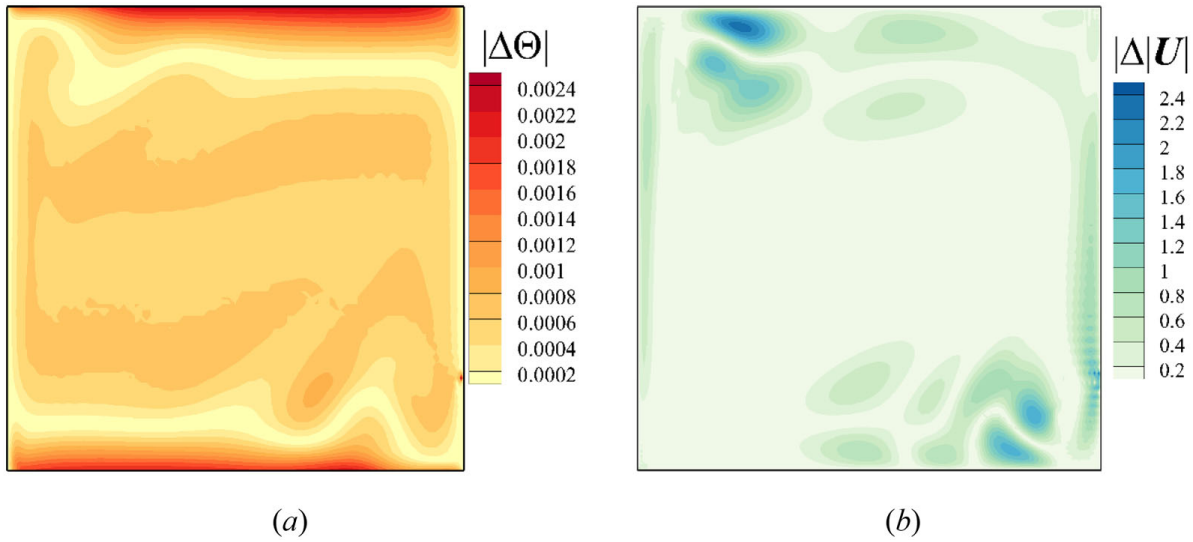

Figure 3. Comparing results under the GL and SGL approximations at $Ra = 10^7$, $Pr = 1$, and $Ga = 0.6$ for (*a*) absolute temperature difference and (*b*) absolute velocity magnitude difference.

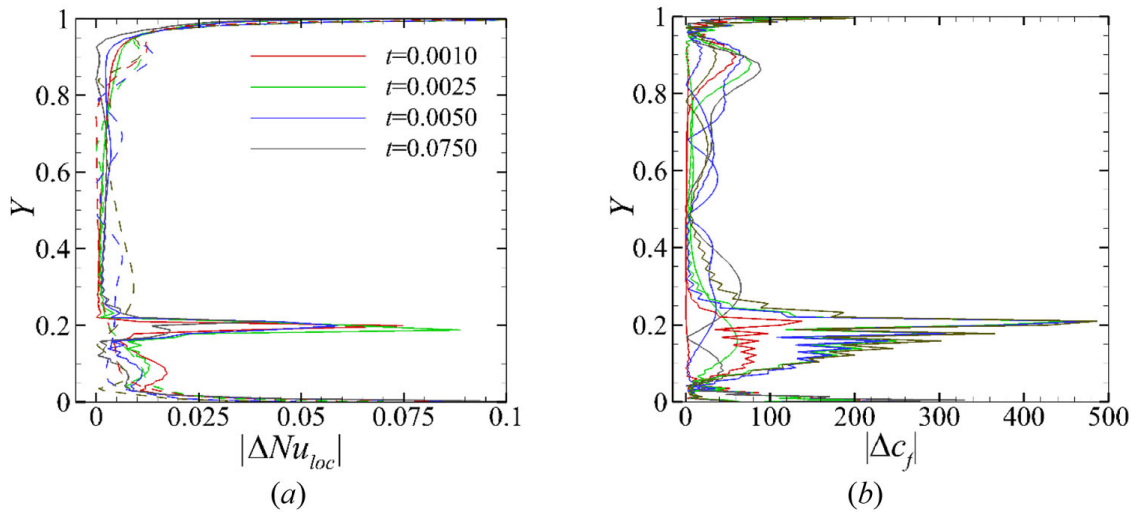

Figure 4. Comparing transient local Nusselt number and coefficient friction differences along the vertical walls of the square cavity with $\gamma = 0$ under the GL and SGL approximations at $Ra = 10^7$, $Pr = 1$, and $Ga = 0.6$: (*a*) absolute local Nusselt number differences and (*b*) absolute local coefficient friction differences. In both figures, solid lines represent data of the left (hot) wall while dashed lines represent data of the right (cold) wall.

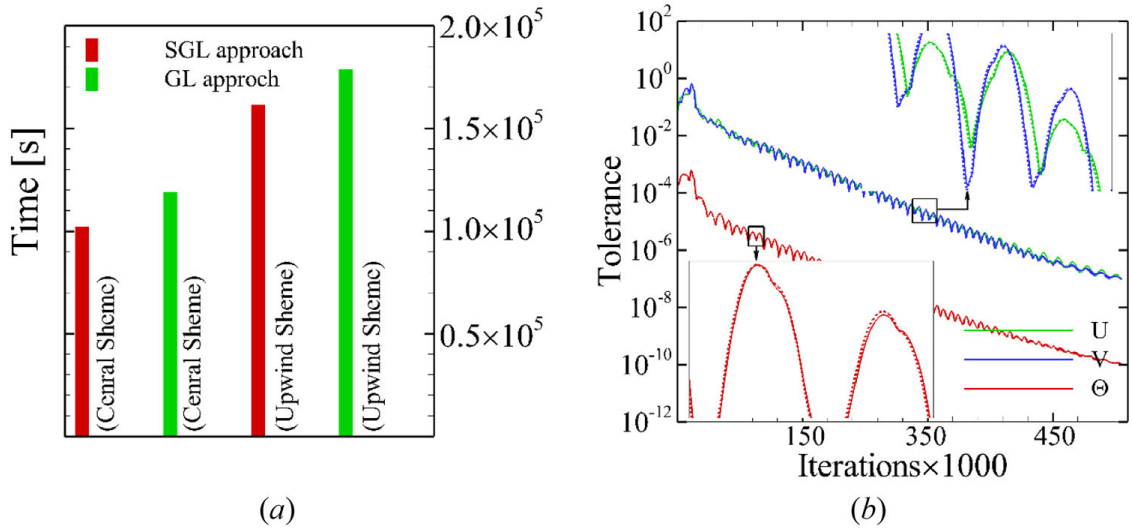

Figure 5. Comparing convergence rate and computational cost of the GL and SGL approximations at $Ra = 10^7$, $Pr = 1$, and $Ga = 0.6$: (*a*) elapsed time under the two approaches using central and upwind schemes and (*b*) convergence history. In convergence history plot, solid lines represent the GL approach while dashed lines show the SGL approach.

$\varepsilon = 0.3$ ($Ga = 0.6$) against the OB and SGL approximations are depicted in Figures 6(*a–f*). Absolute temperature differences under the different approaches shift isotherms, with larger differences found for the zero inclination angle cavity compared to the negative and positive inclination angles. In the zero inclination angle case (Figures 6(*b*) and (*e*)), the difference is largest at the top-left and bottom-right corners, while in the positive inclination angle case (Figures 6(*c*) and (f)) it is occurring almost evenly over the interior region with a focus along the two adiabatic sides. For the negative inclination angle case (Figures 6(*a*) and (*d*)), larger differences occur along the isothermal wall. Regions with smaller temperature differences may be attributed to different situations of the fluid decelerated with respect to the geometry. For instance, negligible differences of the temperature fields in the negative inclination angle case across the top-left corer may be attributed to the enforced downward flow direction by the geometry that is in conflict with the upward buoyancy-driven flow at that region. The maximum absolute temperature difference in the square cavity with $\gamma = 0$ is approximately 12% of the temperature range within the enclosure (with a slightly larger difference for the SGL approximation), reflecting a mismatch of this magnitude between the weakly compressible and incompressible approaches. A similar comparison for the negative/positive inclination angle cases shows a smaller difference approximately 5% mismatch between the compressible and incompressible approximations. The SGL approach shows a better performance in the negative inclination angle case compared to the OB approximation in the interior while both approaches show a similar deviation from the LMS approximation in the positive inclination angle case. It is expected that the mismatch between the aforementioned approaches to be augmented by increasing the relative temperature difference.

To appreciate the role of non-Boussinesq term effects in the advection/convection terms of the governing equation under the SGL approximation, the magnitude of $|\Theta((\boldsymbol{U}\cdot\nabla)\boldsymbol{U})|$ and $|\Theta((\boldsymbol{U}\cdot\nabla)\Theta)|$ under the OB approximation is portrayed for the square cavity with different inclination angels at $Ra = 10^7$ in Figures 7(*a–f*). As seen, the magnitude of the non-Boussinesq term in the momentum equation is stronger along the isothermal walls and especially at the four corners of the cavity, though weaker effects are found within the central regions of the enclosure. Stronger non-Boussinesq effects in the momentum equation along the isothermal walls may be attributed to larger velocity gradients since fluid adjacent to the wall is accelerated by buoyancy force as it reaches to the wall during circulation and decelerated as it gets close to the end of the path parallel to the isotherm wall. Stronger non-Boussinesq effects in the momentum equation at the four corners is attributed to fluid rotation to adjust its motion with respect to the geometry

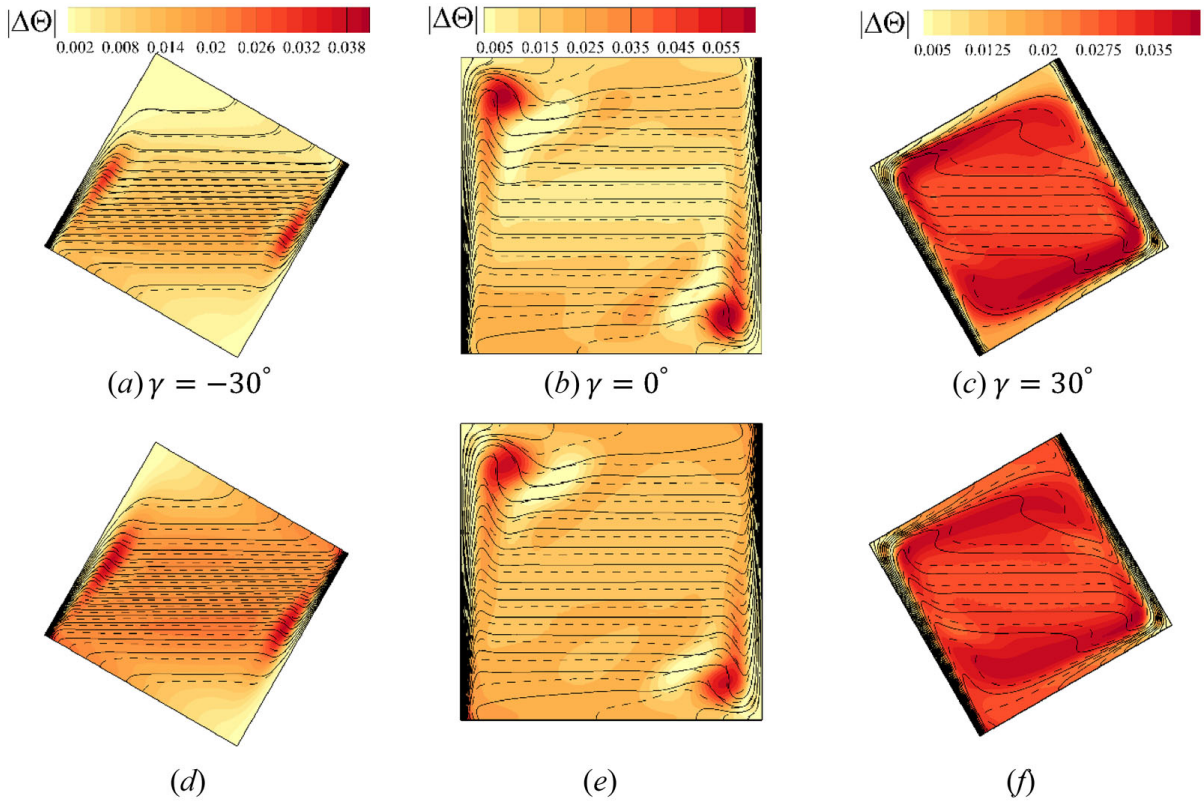

Figure 6. Results at $Ra = 10^7$, $Pr = 1$, and $\varepsilon = 0.3$ (*a, b, c*): absolute temperature difference between the SGL and LMS approximations (*d, e, f*) and absolute temperature difference between the OB and LMS approximations. Solid lines represent the LMS approximation isotherms, while dashed lines show the compared approach.

corners. It is found that the non-Boussinesq term magnitude in the momentum equation is smaller for the negative inclination angel cavity compared to the zero and positive inclinations cases. The magnitude of the non-Boussinesq term in the energy equation has a similar pattern, as it is stronger along the isothermal walls and especially at top-right and bottom-left corners. Stronger non-Boussinesq effects in the energy equation in these regions may be attributed to the larger temperature gradients. This is clear from Figure 6, where isotherm lines are accumulated across the top-right and bottom-left corners that result in larger temperature gradients across those regions. Results also indicate that, the magnitude of the non-Boussinesq term in the momentum equation ($|\Theta((\boldsymbol{U}\cdot\nabla)\boldsymbol{U})|$) is larger than the non-Boussinesq term in the energy equation ($|\Theta((\boldsymbol{U}\cdot\nabla)\Theta)|$), though, a fair comparison should be made based on the magnitude of the mentioned terms in their equations. For the square cavity with zero inclination angle at $Ra = 10^7$, the maximum dimensionless velocity magnitude obtained is approximately 715. Comparing the maximum magnitude of $|\Theta((\boldsymbol{U}\cdot\nabla)\boldsymbol{U})|$ (that is portrayed in Figure 7(*b*)) to the maximum dimensionless velocity magnitude gives a value of approximately 840. Similarly, dividing the maximum value of $|\Theta((\boldsymbol{U}\cdot\nabla)\Theta)|$ in the energy equation (that is portrayed in Figure 7(*e*)) to the maximum dimensionless temperature yields a value of approximately 480, concluding that under the Gay-Lussac approach, velocity is more affected by the corresponding non-Boussinesq term rather than temperature field. In this respect, vorticity absolute differences under the three approximations at $Ra = 10^7$ and $\varepsilon = 0.3$ are portrayed for the square cavity with different inclination angles in Figure 8. Comparing obtained results from different approaches reveals that when the buoyancy driven flow is simulated via the weakly compressible approach for large relative temperature difference, the same pattern of vorticity field is formed and the difference mainly comes from vortices (with different strengths) stretching or location shifting through the flow field. In these figures, large values of the vorticity absolute differences are primarily elongated adjacent to the isotherm walls where flow accelerates due to buoyancy force. Finally, vorticity

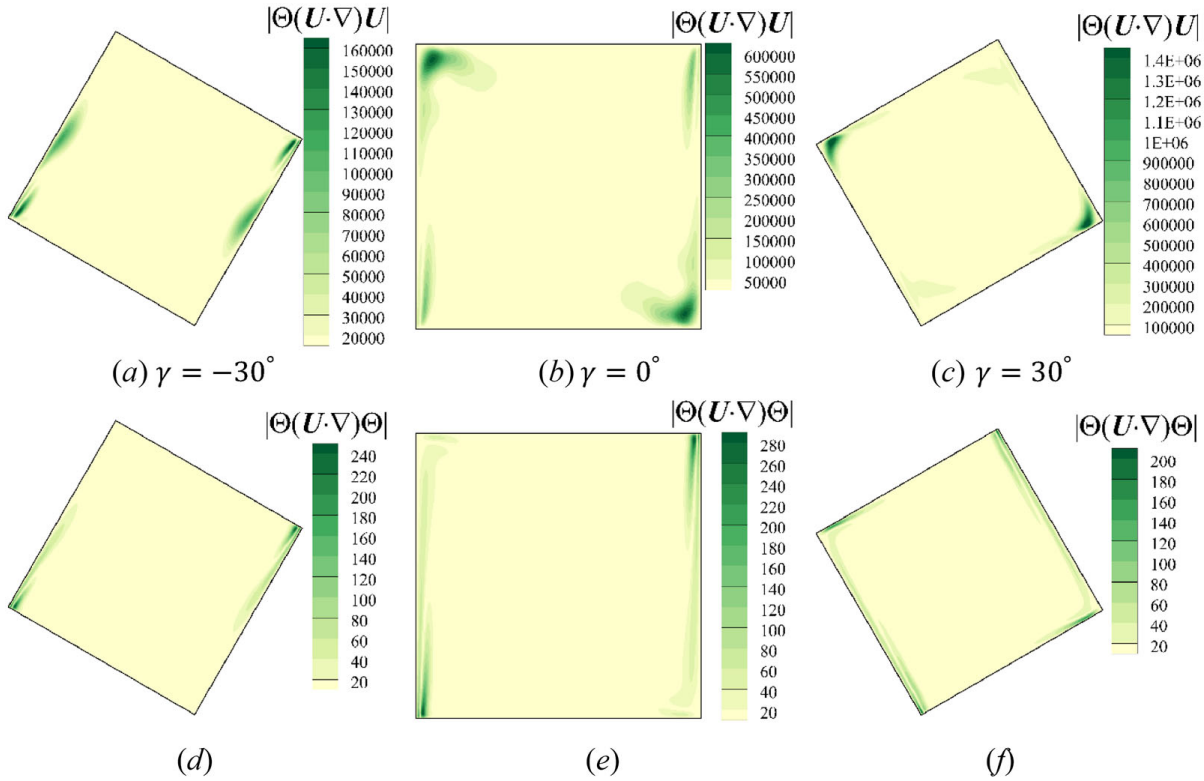

Figure 7. Magnitude of the non-OB advection/convection terms obtained from simulation under the OB approximation for square cavity with different inclination angle (*a, d*) $\gamma = -30^\circ$, (*b, e*) $\gamma = 0^\circ$, and (*c, f*) $\gamma = 30^\circ$.

differences results of different approaches indicate even larger non-Boussinesq term that results in significant modifications in the momentum equation does not create a considerable superior results for the SGL approach compared to the OB approximation.

5.1. Local Nusselt number

The local Nusselt number distribution along the isothermal walls under the different approximations are plotted in Figure 9 at $Ra = 10^7$, $Pr = 1$ and $\varepsilon = 0.3$ for square geometry with the different leaning angles. As seen, the local Nusselt number distributions versus surface length is reversed between the two isothermal walls for all cases. This may be attributed to the increasing and decreasing thermal boundary layer thickness along the isothermal walls in flow direction for the hot and cold walls, respectively. For the square cavity with zero and negative inclination angles (Figures 9(*a*) and (*b*)), there is a monotonic distribution of the local Nusselt number with a local optimum at the bottom-left and top-right corners, but for the positive inclination angle case (Figures 9(*c*)) this changes to an oscillating behavior having smaller local Nusselt number value resembling the Rayleigh–Bénard configuration. Comparing the local Nusselt number distributions along the isothermal walls for the zero and negative inclination angles cases show a clear mismatch between the incompressible and compressible approximations across the bottom-left and top-right corners while the difference is visible along almost all of the two isothermal surfaces for the positive inclination angle case. Results indicate that the SGL approach has a better performance across the bottom-left corner while the OB approximation gives more accurate results across the top-right region.

5.2. Average Nusselt number

The variations of the average Nusselt number across $10^2 \leq Ra \leq 10^7$ is studied at $\varepsilon = 0.15$ and 0.3 under different approximations in Figure 10. Average Nusselt number under the LMS

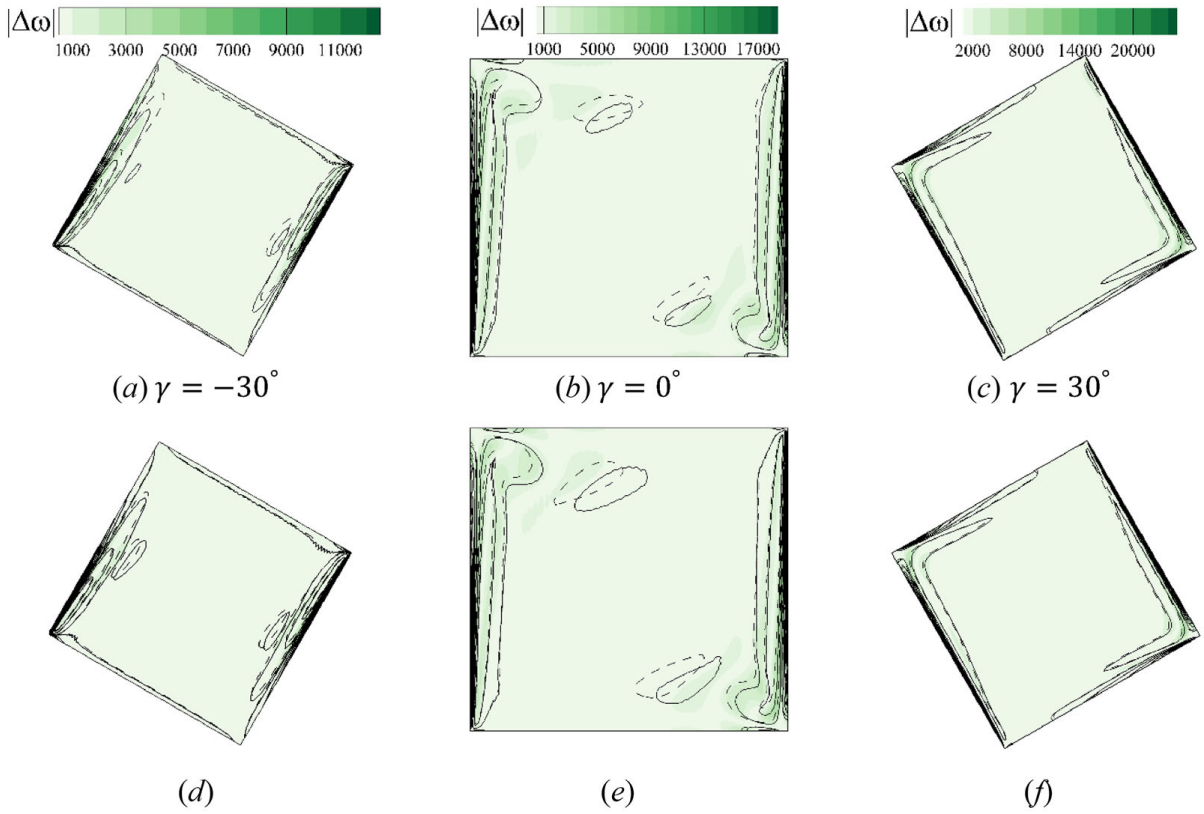

Figure 8. Absolute vorticity differences at $Ra = 10^7$, $Pr = 1$, and $\varepsilon = 0.3$: (*a-c*) SGL and LMS approximations (*d-f*) OB and LMS approximations. In all figures, solid lines represent vorticity under the LMS approximation while dashed lines show vorticity under the other approach. Minimum and maximum of contour levels are equal in each column.

approximation for different inclination angles is plotted at $\varepsilon = 0.15$ and 0.3 in Figures 10(*a*) and (*b*), respectively. As expected, the average Nusselt number increases with increasing Rayleigh number. Since the values of the average Nusselt number under the different approximations are similar, the absolute average Nusselt number differences between the LMS and the two considered incompressible approximations are plotted in separate frames in Figures 10(*c–f*). Due to negligible difference of the average Nusselt number between the OB and SGL approximations that comes from the close results of their local Nusselt number distributions, their difference are not shown here. Comparing the average Nusselt number slope versus the Rayleigh number in Figures 10(*a*) and (*b*) reveals that negative inclination angle decreases the total heat transfer rate. It is also found that a zero inclination angle square cavity has a larger average Nusselt number compared to the both positive and negative inclination angles.

For the average Nusselt number, some of the difference between the compressible and incompressible approximations are nullified by opposite behavior of the local Nusselt number distributions. For instance, in the square cavity with zero inclination angle (Figures 9(*a*) and (*b*)), the approximation that has a lower local Nusselt number distribution along $0 \leq S \leq 0.5$ has a larger value at $0.5 \leq S \leq 1$ and vice versa. This diminishes the difference of the local Nusselt number distribution and gives a smaller difference of the average Nusselt number for the compressible and incompressible approaches. However, the total differences of the average Nusselt number for both incompressible approximations increases by increasing the Rayleigh number, but it does not exceed 2 in the considered range of γ, ε and Ra in this study. Besides, by increasing the relative temperature difference, the difference of the average Nusselt number is increased. Results indicate both positive and negative inclination angles show a considerable average Nusselt number difference in the range of $Ra \geq 10^4$ with an almost linear growth rate while for the zero inclination angle case, the difference grows rapidly in the range of $Ra \geq 10^5$.

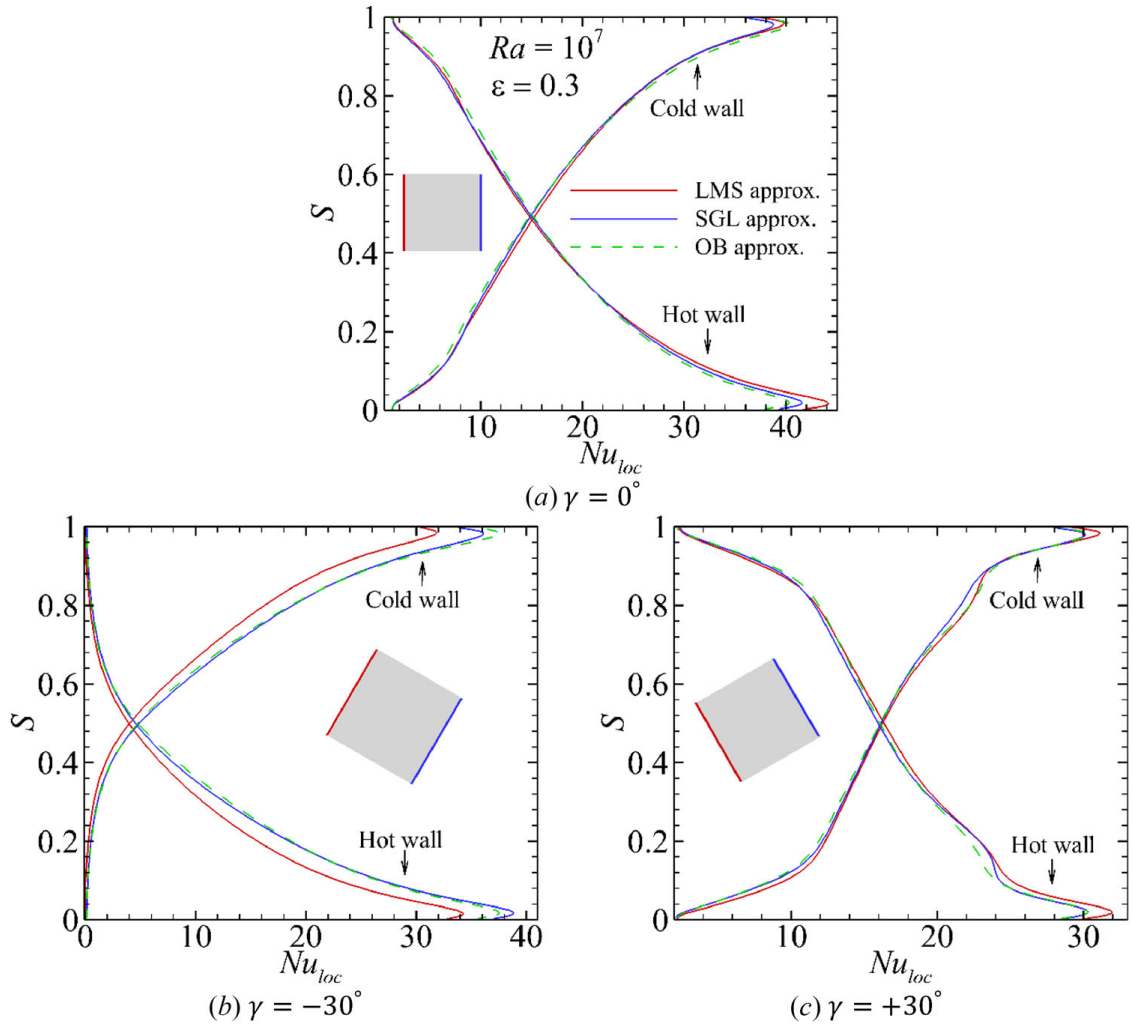

Figure 9. Local Nusselt number distribution along the isothermal walls at $Ra = 10^7$, $Pr = 1$, and $\varepsilon = 0.3$ in square with different inclination angles (*a*) $\gamma = 0^\circ$, (*b*) $\gamma = -30^\circ$, and (*c*) $\gamma = +30^\circ$.

5.3. Skin friction

Local friction coefficient along the isothermal walls is investigated at $Ra = 10^7$, $\varepsilon = 0.15$ and $\varepsilon = 0.3$ under the different approximations in Figure 11. Results show a considerable mismatch between the weakly compressible and incompressible approximations. A comparison among c_f results at $\varepsilon = 0.15$ (Figures 11(*a*), (*c*) and (*e*)) and $\varepsilon = 0.3$ (Figures 11(*b*), (*d*) and (*f*)) reveals that this discrepancy increases with an increase in the relative temperature differences. Indeed, by increasing the relative temperature difference, incompressible approximations show more deviations from the compressible approach. Presented results in Figure 11 indicate that extending the density variations to the advection/convection terms via the linear density state equation does not impose a significant impact on the local friction coefficient as c_f results of the incompressible approximations are attached together in most of the regions.

For the zero inclination angle (Figure 11(*a*)) at $\varepsilon = 0.15$, results of the local coefficient friction indicate that the SGL approach works slightly better than the OB approximation along the hot wall. By increasing the relative temperature difference to 0.3, c_f along the hot wall under the SGL approach deviates from the LMS approximation, especially over $0.55 \leq S \leq 0.85$, but it achieves a better performance than the OB approximation at $0.45 \leq S \leq 0.55$. For the cold wall, by increasing the relative temperature difference, a slightly better prediction is observed for the OB approximation in this case. For the negative inclination case (Figures 11(*c*) and (*d*)), a similar behavior is observed so that in most of the isotherm surfaces, c_f values predicted by the

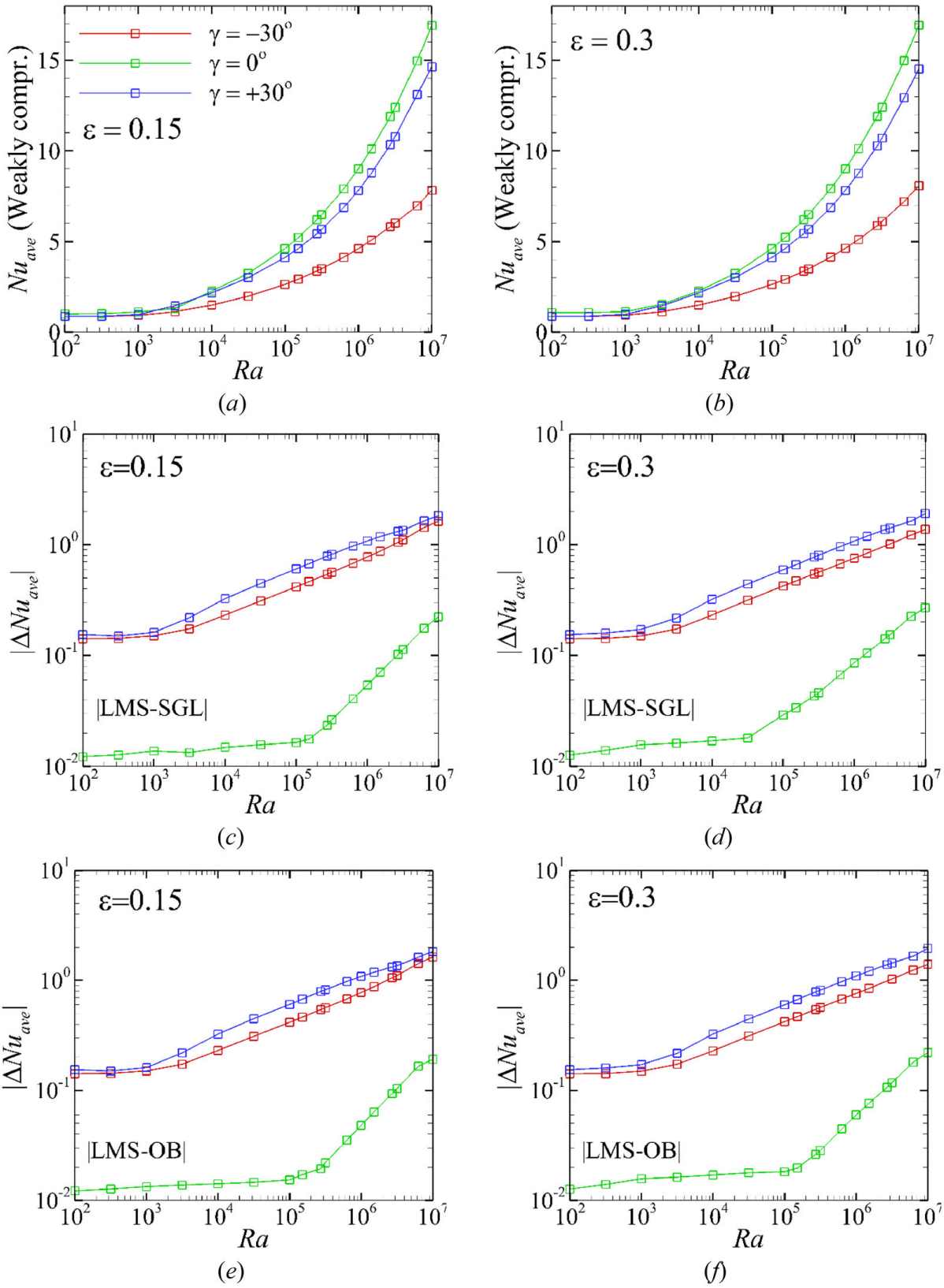

Figure 10. Average Nusselt number against Rayleigh number at $Pr = 1$ in square cavity with different inclination angles as stated: (*a*) $\varepsilon = 0.15$ and (*b*) $\varepsilon = 0.3$. Absolute average Nusselt number differences between the SGL and LMS approximations: (*c*) $\varepsilon = 0.15$ and (*d*) $\varepsilon = 0.3$. Absolute average Nusselt number differences between the OB and LMS approximations: (*e*) $\varepsilon = 0.15$ and (*f*) $\varepsilon = 0.3$.

incompressible approaches do not show a consider mismatch but as it can be seen, result under the SGL approximation deteriorate as the relative temperature difference is increased. For the

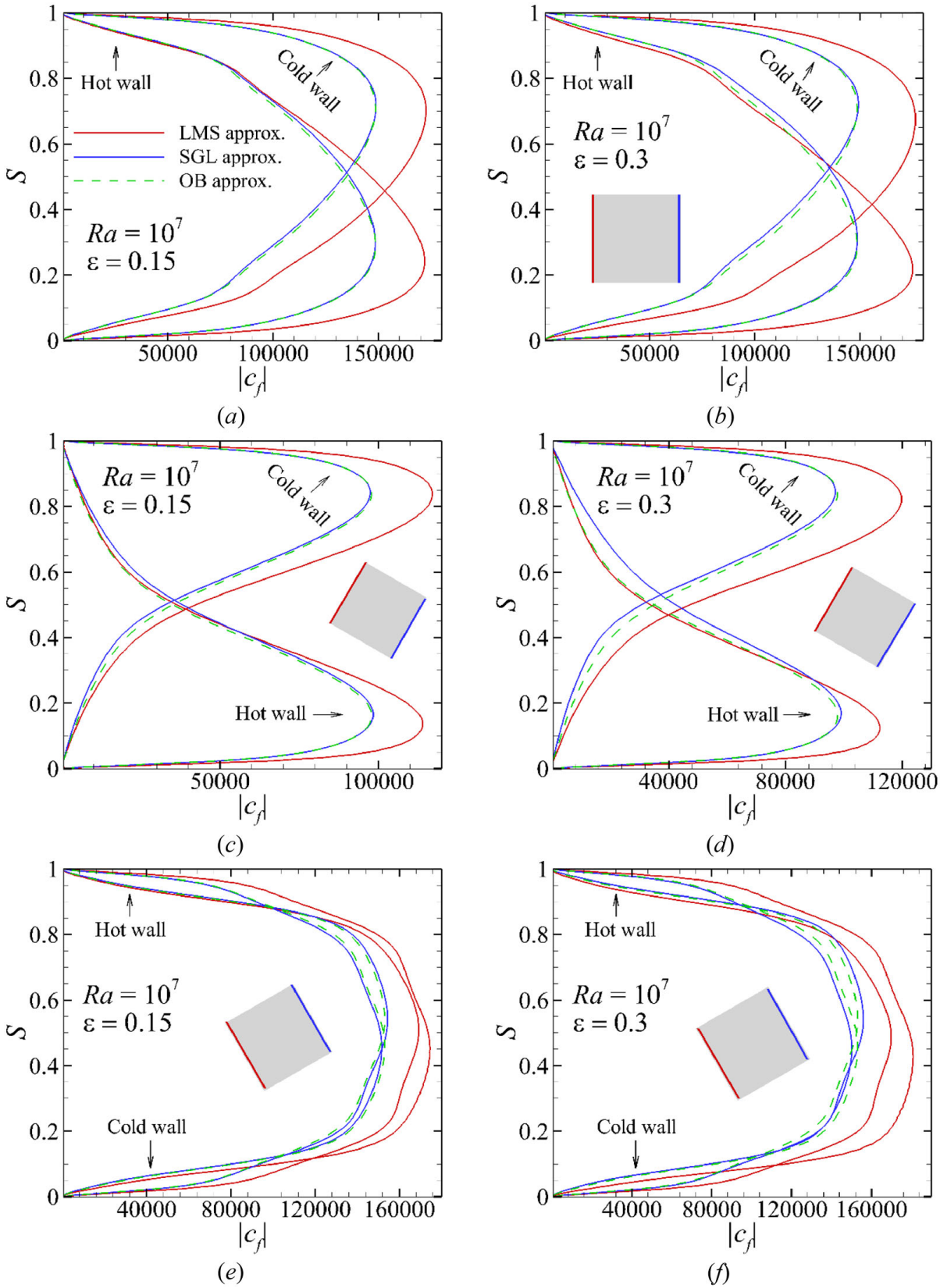

Figure 11. Local friction coefficient distributions along the isotherm walls at $Ra = 10^7$, $\varepsilon = 0.15$, and $\varepsilon = 0.3$: (*a*, *b*) zero inclination angle, (*c*, *d*) negative inclination angle ($\gamma = -30°$), and (*e*, *f*) positive inclination angle ($\gamma = 30°$).

positive inclination angle (Figures 11*e* and *f*), a better performance is observed for the SGL approach across the hot wall while the OB approximation works slightly better across the cold wall at both $\varepsilon = 0.15$ and 0.3.

6. Conclusion

In this study, a simplified and efficient form of the Gay-Lussac approach is proposed for non-Boussinesq treatment of the governing equations for the buoyancy driven flows. It is shown that removing density variations from the continuity equation brings no difference to the produced results compared to the traditional Gay-Lussac approach that is established based on considering density variations in any term of the governing equations in which density appears. This can be attributed to the density pre-factor to the velocity divergence in the mass conservation equation having no influence on the results in an incompressible framework. Results indicate that the proposed simplification reduces the computational cost of the traditional Gay-Lussac approach by 17% and 11% by applying the upwind and central schemes, respectively, while having no adverse impact on the convergence rate. Performance of the simplified Gay-Lussac approach is compared against the conventional Oberbeck—Boussinesq and weakly compressible approaches at high relative temperature differences in terms of the local and average Nusselt number and skin friction. In this respect, natural convection in square cavity with zero, negative and positive inclination angles is numerically simulated under the aforementioned approaches up to $Ra = 10^7$ at $Pr = 1$. Compared results show a considerable mismatch between the compressible and incompressible approaches at high relative temperature differences. Therefore, it is concluded the Gay-Lussac family of approaches require serious revisions to act more accurately than the Oberbeck—Boussinesq approximation at high relative temperature differences as an incompressible approach for buoyancy driven flows.

Deceleration of interest

No deceleration of interest.

Funding

This research was supported by the Australian Research Council through Discovery Project DP180102647. P. M. is supported by a Monash Graduate Scholarship and a Monash International Postgraduate Research Scholarship. The authors are also supported by time allocations on the National Computational Infrastructure (NCI) peak facility and the Pawsey Supercomputing Centre through NCMAS grants. NCI is supported by the Australian Government.

References

[1] J. Boussinesq, *Theorie Analytique de la Chaleur*. Paris: Gauthier-Villars, 1897.

[2] A. Oberbeck, "Ueber die Wärmeleitung der Flüssigkeiten bei Berücksichtigung der Strömungen infolge von Temperaturdifferenzen, "*Ann. Phys. Chem.*, vol. 243, no. 6, pp. 271–292, 1879. DOI: 10.1002/andp.18792430606.

[3] G. de Vahl Davis, "Natural convection of air in a square cavity, a benchmark numerical solution," *Int. J. Numer. Methods Fluids*, vol. 3, no. 3, pp. 249–264, 1983. DOI: 10.1002/fld.1650030305.

[4] I. V. Miroshnichenko and M. A. Sheremet, "Turbulent natural convection heat transfer in rectangular enclosures using experimental and numerical approaches: A review," *Renew. Sust. Energ. Rev.*, vol. 82, pp. 40–59, 2018. DOI: 10.1016/j.rser.2017.09.005.

[5] A. Mohamad, M. A. Sheremet, J. Taler and P. Ocłoń, "Natural convection in differentially heated enclosures subjected to variable temperature boundaries," *HFF*, vol. 29, no. 11, pp. 4130–4141, 2019. DOI: 10.1108/HFF-02-2019-0137.

[6] M. Sheremet, T. Groson and I. Pop, "MHD free convection flow in an inclined square cavity filled with both nanofluids and gyrotactic microorganisms," *HFF*, vol. 29, no. 12, pp. 4642–4659, 2019. DOI: 10.1108/HFF-03-2019-0264.

[7] D. C. Wan, B. S. V. Patnail and G. W. Wei, "A new benchmark quality solution for the buoyancy-driven cavity by discrete singular convolution," *Numer. Heat Transf. B*, vol. 40, pp. 199–228, 2001. DOI: 10.1080/104077901752379620.

[8] A. Ashrafizadeh and M. Nikfar, "On the numerical solution of generalized convection heat transfer problems via the method of proper closure equations–part II: Application to test problems," *Numer. Heat Transf. B*, vol. 70, no. 2, pp. 204–222, 2016. DOI: 10.1080/10407782.2016.1173467.

[9] S. C. Saha and M. M. K. Khan, "A review of natural convection and heat transfer in attic-shaped space," *Energy Buildings*, vol. 43, no. 10, pp. 2564–2571, 2011. DOI: 10.1016/j.enbuild.2011.06.020.

[10] O. M. Kamiyo, D. Angeli, G. S. Barozzi, M. W. Collins, V. O. S. Olunloyo and S. O. Talabi, "A comprehensive review of natural convection in triangular enclosures," *Appl. Mech. Rev.*, vol. 63, no. 6, pp. 060801, 2010. DOI: 10.1115/1.4004290.

[11] N. S. Bondareva, M. A. Sheremet, H. F. Oztop and N. Abu-Hamdeh, "Free convection in an open triangular cavity filled with a nanofluid under the effects of Brownian diffusion. thermophoresis and local heater," *J. Heat Transf. ASME*, vol. 140, no. 4, pp. 042502, 2018. DOI: 10.1115/1.4038192.

[12] M. A. Sheremet, I. Pop and A. Ishak, "Time-dependent natural convection of micropolar fluid in a wavy triangular cavity," *Int. J. Heat Mass Transf.*, vol. 105, pp. 610–622, 2017. DOI: 10.1016/j.ijheatmasstransfer.2016.09.044.

[13] Y. L. Wu, G. R. Liu and Y. T. Gu, "Application of Meshless Local Petrov-Galerkin (MLPG) Approach to Simulation of Incompressible Flow," *Numer. Heat Transf. B*, vol. 48, no. 5, pp. 459–475, 2005. DOI: 10.1080/10407790500324763.

[14] D. Angeli, G. S. Barozzi, M. W. Collins and O. M. Kamiyo, "A critical review of buoyancy-induced flow transitions in horizontal annuli," *Int. J. Therm. Sci.*, vol. 49, no. 12, pp. 2231–2241, 2010. DOI: 10.1016/j.ijthermalsci.2010.08.002.

[15] H. K. Dawood, H. A. Mohammed, and N. A. C. Sidik, K. M. Munisamy and M. A. Wahid, "Forced, natural and mixed-convection heat transfer and fluid flow in annulus: A review," *Int. Commun. Heat Mass Transf.*, vol. 62, pp. 45–47, 2015. DOI: 10.1016/j.icheatmasstransfer.2015.01.006.

[16] H. Paillere, C. Viozat, A. Kumbaro and I. Toumi, "Comparison of low Mach number models for natural convection problems," *Heat Mass Transf.*, vol. 36, no. 6, pp. 567–573, 2000. DOI: 10.1007/s002310000116.

[17] K. Szewc, J. Pozorski and A. Tanière, "Modelling of natural convection with Smoothed Particle Hydrodynamics: Non-Boussinesq formulation," *Int. J. Heat Mass Transf.*, vol. 54, no. 23-24, pp. 4807–4816, 2011. DOI: 10.1016/j.ijheatmasstransfer.2011.06.034.

[18] Q. Wang, S. Xia, R. Yan, D. Sun and Z. Wan, "Non-Oberbeck-Boussinesq effects due to large temperature differences in a differentially heated square cavity filled with air," *Int. J. Heat Mass Transf.*, vol. 128, pp. 479–491, 2019. DOI: 10.1016/j.ijheatmasstransfer.2018.06.079.

[19] J. K. Yuan, C. K. Ho and J. M. Christian, "Numerical simulation of natural convection in solar cavity receivers," *J. Solar Energy Eng.*, vol. 137, no. 3, pp. 031004, 2015. DOI: 10.1115/1.4029106.

[20] M. Niajalili, P. Mayeli, M. Naghashzadegan and A. H. Poshtiri, "Techno-economic feasibility of off-grid solar irrigation for a rice paddy in Guilan province in Iran: A case study," *Solar Energy*, vol. 150, pp. 546–557, 2017. DOI: 10.1016/j.solener.2017.05.012.

[21] J. Vierendeels, B. Merci and E. Dick, "Numerical study of natural convective heat transfer with large temperature differences," *Int. J. Numer. Methods HFF*, vol. 11, no. 4, pp. 329–341, 2001. DOI: 10.1108/09615530110389117.

[22] W. Fu, C. Li, C. Huang and J. Huang, "An investigation of a high temperature difference natural convection in a finite length channel without Bossinesq assumption," *Int. J. Heat Mass Trans.f*, vol. 52, no. 11-12, pp. 2571–2580, 2009. DOI: 10.1016/j.ijheatmasstransfer.2009.01.012.

[23] S. Busto, M. Tavelli, W. Boscheri and M. Dumbser, "Efficient high order accurate staggered semi-implicit discontinuous Galerkin methods for natural convection problems," *Comput. Fluids*, vol. 198, pp. 104399, 2020. DOI: 10.1016/j.compfluid.2019.104399.

[24] A. Bermúdez, S. Busto, M. Dumbser, J. L. Ferrín, L. Saavedra and M. E. Vázquez-Cendón, "A staggered semi-implicit hybrid FV/FE projection method for weakly compressible flows," *J. Comput. Phys.*, vol. 421, pp. 109743, 2020. DOI: 10.1016/j.jcp.2020.109743.

[25] S. Paolucci, "On the filtering of sound from the Navier-Stokes equations," Technical report, Sandia National Laboratories, no. 9, SAND 82-8257, 1982.

[26] J. Vierendeels, B. Merci and E. Dick, "A multigrid method for natural convective heat transfer with large temperature differences," *J. Comput. Appl. Math.*, vol. 168, no. 1-2, pp. 509–517, 2004. DOI: 10.1016/j.cam.2003.08.081.

[27] R. Becker and M. Braack, "Solution of a stationary benchmark problem for natural convection with large temperature difference," *Int. J. Therm. Sci.*, vol. 41, no. 5, pp. 428–439, 2002. DOI: 10.1016/S1290-0729(02)01335-2.

[28] T. Pesso and S. Piva, "Laminar natural convection in a square cavity: Low Prandtl numbers and large density differences," *Int. J. Heat Mass Transf.*, vol. 52, no. 3-4, pp. 1036–1043, 2009. DOI: 10.1016/j.ijheatmasstransfer.2008.07.005.

[29] J. M. Lopez, F. Marques and M. Avila, "The Boussinesq approximation in rapidly rotating flows," *J. Fluid Mech.*, vol. 737, pp. 56–77, 2013. DOI: 10.1017/jfm.2013.558.
[30] P. Mayeli and G. Sheard, "A new formulation for Boussinesq-type natural convection flows applied to the annulus cavity problem," *Int. J. Numer. Methods Fluids*, vol. 93, no. 3, pp. 683–702, 2021. DOI: 10.1002/fld.4904.
[31] P. Mayeli and G. Sheard, "Natural convection and entropy generation in square and skew cavities due to large temperature differences: A Gay-Lussac type vorticity stream-function approach," *Int. J. Numer. Methods Fluids*, vol. 93, no. 7, pp. 2396–2420, 2021. DOI: 10.1002/fld.4980.
[32] Y. R. Li, X. F. Yuan, C. M. Wu and Y. P. Hu, "Natural convection of water near its density maximum between horizontal cylinders," *Int. J. Heat Mass Transf.*, vol. 54, no. 11-12, pp. 2550–2559, 2011. DOI: 10.1016/j.ijheatmasstransfer.2011.02.006.
[33] E. A. Spiegel and G. Veronis, "On the Boussinesq approximation for a compressible fluid," *Astrophys. J.*, vol. 131, pp. 442–447, 1960. DOI: 10.1086/146849.
[34] J. A. Dutton and G. H. Fichtl, "Approximate equations of motion for gases and liquid," *J. Atmos. Sci.*, vol. 26, no. 2, pp. 241–254, 1969. DOI: 10.1175/1520-0469(1969)026<0241:AEOMFG>2.0.CO;2.
[35] D. D. Gray and A. Giorgini, "The validity of the Boussinesq approximation for liquids and gases," *Int. J. Heat Mass Transf.*, vol. 19, no. 5, pp. 545–551, 1976. DOI: 10.1016/0017-9310(76)90168-X.
[36] M. Pons and P. L. Quéré, "Modeling natural convection with the work of pressure-forces: A thermodynamic necessity," *Int. J. Numer. Methods HFF*, vol. 17, no. 3, pp. 322–332, 2007. DOI: 10.1108/09615530710730184.
[37] M. A. Leal, H. A. Machado and R. M. Cotta, "Integral transform solutions of transient natural convection in enclosures with variable fluid properties," *Int. J. Heat Mass Transf.*, vol. 43, no. 21, pp. 3977–3990, 2000. DOI: 10.1016/S0017-9310(00)00023-5.
[38] M. Souza, R. Miranda and H. Machado, "Natural convection in enclosures with variable fluid properties," *Int. J. Numer. Methods Heat Fluid Flow*, vol. 13, no. 8, pp. 1079–1096, 2003. DOI: 10.1108/09615530310501966.
[39] P. Mayeli, M. Nili-Ahmadabadi, M. R. Pirzadeh and P. Rahmani, "Determination of desired geometry by a novel extension of ball spine algorithm inverse method to conjugate heat transfer problems," *Comput. Fluids*, vol. 154, pp. 390–406, 2017. DOI: 10.1016/j.compfluid.2016.05.022.
[40] H. Hesami and P. Mayeli, "Development of the ball-spine algorithm for the shape optimization of ducts containing nanofluid," *Numer. Heat Transf. A*, vol. 70, no. 12, pp. 1371–1389, 2016. DOI: 10.1080/10407782.2016.1243976.
[41] M. Nikfar and P. Mayeli, "Surface shape design in different convection heat transfer problems via a novel coupled algorithm," *J. Heat Transf.-Trans. ASME*, vol. 140, no. 2, pp. 021702-1, 2018. DOI: 10.1115/1.4037581.
[42] P. Mayeli, and H. Hesami and M. H. D. F. Moghaddam, "Numerical investigation of the MHD forced convection and entropy generation in a straight duct with sinusoidal walls containing water-Al2O3 nanofluid," *Numer. Heat Transf. A*, vol. 71, no. 12, pp. 1371–1389, 2017. DOI: 10.1080/10407782.2016.1243976.
[43] P. Mayeli, H. Hesami, H. Besharati-Foumani and M. Niajalili, "Al_2O_3-Water nanofluid heat transfer and entropy generation in a ribbed channel with wavy wall in the presence of magnetic field," *Numer. Heat Transf. A*, vol. 73, no. 9, pp. 604–623, 2018. DOI: 10.1080/10407782.2018.1461494.
[44] A. Ashrafizadeh, B. Alinia and P. Mayeli, "A new co-located pressure-based discretization method for the numerical solution of incompressible Navier-Stokes equations," *Numer. Heat Transf. B*, vol. 67, no. 6, pp. 563–589, 2015. DOI: 10.1080/10407790.2014.992094.
[45] P. Mayeli and M. Nikfar, "Temperature identification of a heat source in conjugate heat transfer problems via an inverse analysis," *HFF*, vol. 29, no. 10, pp. 3994–4010, 2019. DOI: 10.1108/HFF-05-2018-0193.
[46] M. Nikfar, A. Ashrafizadeh and P. Mayeli, "Inverse shape design via a new physical-based iterative solution strategy," *Inverse Prob.Sci. Eng.*, vol. 23, no. 7, pp. 1138–1162, 2015. DOI: 10.1080/17415977.2014.973873.
[47] P. Mayeli, M. Nili-Ahmadabadi and H. Besharati-Foumani, "Inverse shape design for heat conduction problems via the ball spine algorithm," *Numer. Heat Transf. B*, vol. 69, no. 3, pp. 249–269, 2016. DOI: 10.1080/10407790.2015.1096690.
[48] P. L. Quéré, *et al.*, "Modelling of natural convection flows with large temperature differences: A benchmark problem for low Mach number solvers. Part 1. Reference solutions," *ESAIM M2AN*, vol. 39, no. 3, pp. 609–616, 2005. DOI: 10.1051/m2an:2005027.

Received: 29 May 2021 | Revised: 10 July 2021 | Accepted: 13 July 2021

DOI: 10.1002/fld.5033

RESEARCH ARTICLE

WILEY

An efficient and simplified Gay-Lussac approach in secondary variables form for the non-Boussinesq simulation of free convection problems

Peyman Mayeli | **Gregory J. Sheard**

Department of Mechanical and Aerospace Engineering, Monash University, Clayton, Victoria, Australia

Correspondence
Peyman Mayeli, Department of Mechanical and Aerospace Engineering, Monash University, Clayton, VIC 3800, Australia.
Email: peyman.mayeli@monash.edu

Funding information
National Computational Infrastructure; Australian Research Council, Grant/Award Number: DP180102647

Abstract

The Gay-Lussac (GL) approach is an incompressible-based strategy for non-Boussinesq treatment of the governing equations for free convection problems that is established based on extending the density variations beyond the gravity term. Such a strategy leads to emerging the GL parameter as a non-Boussinesq prefactor of different terms in the governing equations. In this article, the GL approach is expressed/discussed in terms of the secondary variables, that is, vorticity and stream-function, for the first time and a simplified version of this approach is proposed by removing density variations from the continuity equation. The difference of results under the simplified and traditional GL approach ranges within a maximum of 1% for different parameters. The lower computational cost of numerical solution of governing equations in the secondary variables formula and the corresponding convergence rate is scrutinized for the simplified GL approach showing around 25% lower computational cost. The performance of this approach is evaluated at high relative temperature differences against the low Mach number scheme and the Boussinesq approximations. In this respect, natural convection in an annulus cavity is numerically simulated using a CVFEM solver under the aforementioned approximations up to Rayleigh number $Ra = 10^5$ at Prandtl number $Pr = 1$ and high relative temperature differences ($\varepsilon = 0.15$ and 0.3). The largest deviations found for either the simplified GL or Boussinesq methods from the low Mach number scheme solution are less than 20% for velocity magnitude, 14% for stream function, 6% for vorticity, and 5% for temperature. Results under the three approximations are also analyzed in terms of the skin friction and local and average Nusselt number, indicating that the Gay-Lussac approach requires some revisions to act more accurately than the classical Boussinesq approximation at high relative temperature differences in natural convection problems, especially within the convection dominated regime.

KEYWORDS

annulus cavity, Gay-Lussac approximation, low Mach number scheme

1 | INTRODUCTION

Free convection related problems have myriad scientific and industrial applications, such as metallurgy processes, solar chimneys and collectors, astrophysical and geophysical phenomena, and so on.[1–5] Accurate prediction of the thermoflow fields within these systems when heat transfer mechanism is free convection dominated is of paramount importance. Traditionally, free convection problems are simulated numerically under the Boussinesq approximation that is also known as the Oberbeck–Boussinesq approximation. The Oberbeck–Boussinesq (OB) approximation is organized based on some basic assumptions: small temperature differences, negligible viscous heat dissipation in the energy equation, constant thermophysical properties of the working fluid, and small hydrostatic pressure variations across the height of the system. When these assumptions are satisfied, density variations negligibly affect the flow except the buoyancy term of the momentum equation. Using the volumetric thermal expansion coefficient, a linear state equation is derived as a function of temperature that makes the governing equations independent of explicit density variations.

The OB approximation is designed for natural convection phenomena associated by differential temperature difference featuring small order of compressibility but there are many situations, where the temperature nonuniformities generate significant density variations. In such situation, applying the classical OB approximation produces inaccurate results.[6] Literature survey indicates a few remedies that were proposed to overcome this issue. Different non-OB approximations for natural convention phenomena may be split into two major groups capturing compressible and incompressible approaches.

The first non-OB category is developed based on returning to the original essence of the natural convection phenomena by considering compressibility effects that invokes the Mach number. Generally speaking, actions toward compressible simulation of the Navier–Stokes equations is performed in two subcategories: fully compressible and weakly compressible approaches. However, the fully compressible approximation, in theory, is the optimal method for numerical simulation of free convection phenomena, but numerical complications caused by low-order compressibility ratio is a serious hindrance to its application. This approach was used by Darbandi and Hosseinizadeh,[7] Harish and Venkatasubbaiah,[8] and Busto et al..[9] The second remedy of the compressible non-OB category is the weakly compressible approach. In the weakly compressible approach that is often referred to as the low Mach number scheme (LMS), acoustic waves are filtered from the governing equation, which makes the method suitable for the compressible treatment of natural convection phenomena with small order of compressibility ratio. Under the LMS approximation, the total pressure is broken into two significant segments. The first segment is a spatially uniform pressure (known as the thermodynamic pressure) that comes from the equation of state by which the density is updated. The second segment is a local pressure (known as the hydrodynamic pressure) that acts just in the momentum equations. Armengol et al.[10] and Wan et al.[11] employed this algorithm for free convection phenomena with large temperature differences beyond the validity of the OB approximation.

The second category of the non-OB approximations rests on an incompressibility assumption. One of the non-OB strategies in this category is the Gay-Lussac (GL) approach that is established based on incorporating density variations beyond the gravity term of the momentum equations. This leads to the appearance of a dimensionless parameter, $Ga = \beta\Delta\theta$, where β is the isobaric expansion coefficient and $\Delta\theta$ a reference temperature. Following the OB approximation, a linear density state equation is employed to correlate density variations to the temperature differences. As will be shown later, Ga is equal to twice of the relative temperature difference. Under the GL approach, $(1 - Ga\Theta)$ emerges as a prefactor of different terms in the governing equations that acts as a modifier. Increasing Ga (e.g., invoking larger temperature differences) leads to an increase in deviation from the OB approximation. In Reference 12, the square cavity benchmark problem is studied by this strategy at large temperature differences. A GL-type approach is also possible by extending density variations just to one of the momentum or energy equations. For instance, Lopez et al.[13] proposed a GL-type approximation valid for rapidly rotating flows, whereby centrifugal contributions due to background rotation were captured via extension of density variations to the advection terms. Mayeli and Sheard[14,15] adopted a similar approach and showed that Ga may be cast in terms of Rayleigh, Prandtl, and Froude numbers, that is, $Ga = RaPrFr$.

Nonlinear density state relation,[16] temperature-dependent properties of the fluid[17] and also considering viscous friction and work of pressure stress terms of the energy equation (known as the thermodynamic Boussinesq model[18]) are other subcategories of the incompressible-based non-OB approximation strategies but for the sake of brevity, they are not discussed here. Different scenarios for the numerical simulation

of NC problems beyond the OB approximation in compressible and incompressible categories are reviewed in Reference 19.

The horizontal concentric annulus enclosure is a known benchmark problem in free convection related research. A comprehensive coverage was given in Kuhen and Goldstein.[20] Numerical contributions have also been made by References 20–28, where it is consistently reported that the two-dimensional solution remains time-invariant up to a Rayleigh number $Ra = 10^5$ at Prandtl numbers near unity. The interested reader is directed to the review by Reference 29.

In the present study, the annulus cavity problem is studied at high relative temperature differences under the three approximations including LMS, GL, and OB approximations. In this respect, governing equations under the GL approach are presented in secondary variable formulas (vorticity stream-function) for the first time. The following sections of the article are arranged as follows: Governing equations under the three approximations are presented in Section 2. The geometry, boundary conditions and numerical algorithms used in this work are introduced in Section 3. In Section 4, mismatches between the three approximations are interrogated via measurements of skin friction, local and average Nusselt number. A brief conclusion is given in Section 5.

2 | THE GAY-LUSSAC AND WEAKLY COMPRESSIBLE APPROACHES

Governing equations under the GL approach are extended beyond the OB approximation by taking into account density variations in any term of the governing equations in which density appears. Starting with the incompressible Navier–Stokes equations in the absence of any additional forces,

$$\begin{cases} (\rho/\rho_0)\nabla\cdot\boldsymbol{u} = 0, \\ \partial\boldsymbol{u}/\partial t^* + (\rho/\rho_0)(\boldsymbol{u}\cdot\nabla)\boldsymbol{u} = -(1/\rho_0)\nabla p + \nu\nabla^2\boldsymbol{u} + (\rho/\rho_0)\boldsymbol{e_g}, \\ \partial T/\partial t^* + (\rho/\rho_0)(\boldsymbol{u}\cdot\nabla)T = \alpha\nabla^2 T. \end{cases} \tag{1}$$

Following the OB approach, a linear density state relation ($\rho/\rho_0 = 1 - \beta\theta$) is substituted, and the following group of dimensionless parameters,

$$t = \frac{t^*\alpha}{L^2}, \boldsymbol{X} = \frac{\boldsymbol{x}}{L}, \boldsymbol{U} = \frac{\boldsymbol{u}L}{\alpha}, P = \frac{p^*L^2}{\rho\alpha^2}, \Theta = \frac{\theta}{\Delta\theta} = \frac{T - T_0}{T_h - T_c}, Ga = \beta\Delta\theta \tag{2}$$

the dimensionless form of the governing equation under the GL approximation are derived,

$$\begin{cases} (1 - Ga\boldsymbol{\Theta})\nabla\cdot\boldsymbol{U} = 0, \\ \partial\boldsymbol{U}/\partial t + (1 - Ga\boldsymbol{\Theta})(\boldsymbol{U}\cdot\nabla)\boldsymbol{U} = -\nabla P - RaPr\boldsymbol{\Theta}\boldsymbol{e_g} + Pr\nabla^2\boldsymbol{U}, \\ \partial\boldsymbol{\Theta}/\partial t + (1 - Ga\boldsymbol{\Theta})(\boldsymbol{U}\cdot\nabla)\boldsymbol{\Theta} = \nabla^2\boldsymbol{\Theta}. \end{cases} \tag{3}$$

As seen, as $Ga \to 0$ ($\Delta\theta \to 0$), the usual OB approximation is recovered. Under the GL approximation, $(1 - Ga\boldsymbol{\Theta})$ modifies different terms, and its effect becomes more pronounced by increasing Ga (and consequently $\Delta\theta$), but in practice Ga cannot exceed a specified value to avoid an unphysical (negative) density, that is,

$$\rho/\rho_0 = 1 - \beta\theta = 1 - \beta\Delta\theta\boldsymbol{\Theta} = 1 - Ga\Theta > 0. \tag{4}$$

Equation (4) indicates the maximum Ga value in practice cannot exceed 2 ($Ga_{max} = 2$) based on defined dimensionless temperature. In Section 4, it is shown that by omitting density variations from the continuity equation, a simplified Gay-Lussac (SGL) approximation is obtained that yields identical results with the traditional GL approach,

$$\begin{cases} \nabla\cdot\boldsymbol{U} = 0, \\ \partial\boldsymbol{U}/\partial t + (1 - Ga\boldsymbol{\Theta})(\boldsymbol{U}\cdot\nabla)\boldsymbol{U} = -\nabla P - RaPr\boldsymbol{\Theta}\boldsymbol{e_g} + Pr\nabla^2\boldsymbol{U}, \\ \partial\boldsymbol{\Theta}/\partial t + (1 - Ga\boldsymbol{\Theta})(\boldsymbol{U}\cdot\nabla)\boldsymbol{\Theta} = \nabla^2\boldsymbol{\Theta}. \end{cases} \tag{5}$$

For comparison purposes, the problem is also simulated under the low Mach number scheme. The dimensionless low-Mach-number governing equations[19] are,

$$\begin{cases} \frac{\partial \rho}{\partial t} + \nabla \cdot (\rho \boldsymbol{U}) = 0, \\ \frac{\partial (\rho \boldsymbol{U})}{\partial t} + \nabla \cdot (\rho \boldsymbol{U} \otimes \boldsymbol{U}) = -\nabla P + \frac{RaPr}{2\varepsilon} \rho \boldsymbol{e}_g + Pr \nabla \cdot \boldsymbol{\tau}, \\ \frac{\partial (\rho \Theta)}{\partial t} + \nabla \cdot (\rho \boldsymbol{U} \Theta) = \nabla^2 \Theta + \left(\frac{\gamma - 1}{\gamma} \right) \frac{\mathrm{d}P_{\mathrm{th}}}{\mathrm{d}t}, \\ P_{\mathrm{th}} = \rho \Theta. \end{cases} \tag{6}$$

The following parameters have been used for dimensionless analysis of Equation (6),

$$\Theta = \frac{T}{T_0}, P_{\mathrm{th}} = \frac{p_{th}}{p_0}, \rho = \frac{\rho^*}{\rho_0}, t = \frac{t^* \alpha}{L^2}, \boldsymbol{X} = \frac{\boldsymbol{x}}{L_{ref}}, \boldsymbol{U} = \frac{\boldsymbol{u} L_{ref}}{\alpha}, P = \frac{p^* L_{ref}^2}{\rho \alpha^2}. \tag{7}$$

In Equation (6), P_{th} is the spatially uniform thermodynamic pressure, ε is the relative temperature difference ($\varepsilon = \Delta\theta / 2T_0$), and γ stands for heat capacity ratio ($\gamma = c_p / c_v$). When Stokes' hypothesis is applied for the bulk viscosity, the stress tensor is expressed as follows,

$$\boldsymbol{\tau} = \nabla \boldsymbol{U} + (\nabla \boldsymbol{U})^T - 2/3 (\nabla \cdot \boldsymbol{U}) \boldsymbol{I}. \tag{8}$$

The relative temperature difference that is applied for compressible simulation of natural convection problems may be related to the GL parameter by

$$\underbrace{2\varepsilon = (T_{\mathrm{h}} - T_{\mathrm{c}}) / T_o}_{\text{Compressible}} = \underbrace{\beta \Delta\theta = Ga}_{\text{Incompressible}}. \tag{9}$$

Using the vorticity ($\omega = \partial V / \partial X - \partial U / \partial Y$) and stream-function ($U = \partial \psi / \partial Y; V = -\partial \psi / \partial X$) parameters, the secondary variables form of the governing equations under the SGL approximation become

$$\begin{cases} \frac{\partial^2 \psi}{\partial X^2} + \frac{\partial^2 \psi}{\partial Y^2} = -\omega \\ \frac{\partial \omega}{\partial t} + (1 - 2\varepsilon\Theta) \left(\frac{\partial \psi}{\partial Y} \frac{\partial \omega}{\partial X} - \frac{\partial \psi}{\partial X} \frac{\partial \omega}{\partial Y} \right) = Pr \left(\frac{\partial^2 \omega}{\partial X^2} + \frac{\partial^2 \omega}{\partial Y^2} \right) + RaPr \frac{\partial \Theta}{\partial X}, \\ \frac{\partial \Theta}{\partial t} + (1 - 2\varepsilon\Theta) \left(\frac{\partial \psi}{\partial Y} \frac{\partial \Theta}{\partial X} - \frac{\partial \psi}{\partial X} \frac{\partial \Theta}{\partial Y} \right) = \frac{\partial^2 \Theta}{\partial X^2} + \frac{\partial^2 \Theta}{\partial Y^2}. \end{cases} \tag{10}$$

Similar to the primitive variables formulas, governing equations under the OB approximation are recovered as $\varepsilon \to 0$.

3 | THE ANNULUS ENCLOSURE AND NUMERICAL CONSIDERATIONS

The concentric horizontal annulus enclosure is studied at high relative temperature differences under the three approximations. Figure 1 shows the system under investigation. r_o and r_i are respectively the outer and inner enclosure radii. To be consistent with published benchmark studies,[20–24] the aspect ratio is fixed at $r_o - r_i / r_i = 1.6$. Applied boundary conditions in both primitive and secondary variables are shown in Figure 1(A). The gap between the two cylinders is filled with a working fluid with unity Prandtl number. The outer and inner cylinders are fixed at constant cold and hot temperatures, respectively. The gap between the two cylinders in the radial direction serves as the reference length, $L_{\mathrm{ref}} = r_o - r_i$. The two-dimensional steady flow is computed at Rayleigh numbers $10 \leq Ra \leq 10^5$ and relative temperature differences of 0.15 and 0.3. The computational domain is discretized with quadrilateral elements conforming to the circular domain, as shown in Figure 1(B). Elements are distributed uniformly in azimuth and are compressed toward the inner and outer cylinder surfaces to resolve the boundary layers.

Simulations are conducted using a solver employing a control volume finite-element method (CVFEM) for spatial discretization. In CVFEM, the physical domain is covered by a series of control volumes so that a unique finite volume is

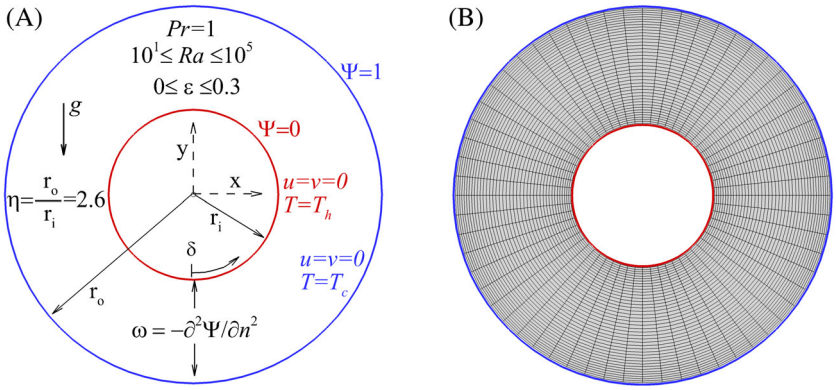

FIGURE 1 Concentric annulus enclosure. (A) Applied boundary conditions. (B) A coarse computational grid for illustration purposes [Colour figure can be viewed at wileyonlinelibrary.com]

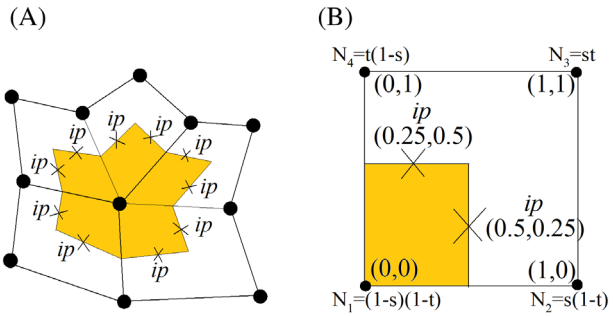

FIGURE 2 A schematic of quadrilateral elements. (A) A typical finite volume associated with integration points. (B) Local coordinate (s,t) and bilinear shape functions in a standard element [Colour figure can be viewed at wileyonlinelibrary.com]

allocated to each node as shown in Figure 2(A). Each control volume is encircled by several panels with an integration point (ip). Integration of Laplacian term over the finite volume yields

$$\int_{v_p} \nabla^2 \omega \mathrm{d}v = \oint_{A_p} \nabla \omega_{ip} \cdot \mathrm{d}\boldsymbol{A} = \sum_{ip=1}^{n} \nabla \omega_{ip} \cdot \boldsymbol{A_{ip}}. \tag{11}$$

In Equation (11), series counts for the number of ip encircling the main node where $\boldsymbol{A_{ip}}$ is corresponding to the normal vector of the surface at each ip. Under the CVFEM, bilinear shape functions ($N_j(s,t)$) are used to attribute the value of any parameter within the element to the nodal values via the weighted values,

$$\omega_{ip} = \omega(s,t) = \sum_{j=1}^{4} N_j(s,t)\omega_j. \tag{12}$$

The shape functions relating ip values to the nodal values in a quadrilateral element are shown in Figure 2(B). The Laplacian operator can be stated as follows

$$\mathrm{L}(\omega) = \sum_{ip=1}^{n}\sum_{j=1}^{4} \omega_j \nabla N_j \cdot \boldsymbol{A_{ip}}. \tag{13}$$

The effects of all nodes encircling an ip are involved in Equation (13) by weighted values that are identical to a central scheme. The Laplacian operator acts similarly in other equations.

The lagging technique is used to linearize the nonlinear terms in the governing equations. Integration of the advection term in secondary variables form over the finite volume and using data of the previous iteration for the lagged values

yields

$$\int_{v_p} (\bar{\psi}_y \omega_x - \bar{\psi}_x \omega_y) \mathrm{d}v = \oint A_p \bar{\psi}_y \omega \mathrm{d}A_x - \bar{\psi}_x \omega \mathrm{d}A_y = \oint A_p \omega (\bar{\psi}_y \mathrm{d}A_x - \bar{\psi}_x \mathrm{d}A_y) = \sum_{ip=1}^{n} \omega_{ip} (\bar{\psi}_{y_{ip}} A_{xip} - \bar{\psi}_{xip} A_{yip}). \tag{14}$$

Utilizing shape functions to approximate the integral point values to the nodal values yields

$$\mathrm{N}(\omega) = \sum_{ip=1}^{n} \sum_{j=1}^{4} \omega_j N_j (\bar{\psi}_{y_{ip}} A_{xip} - \bar{\psi}_{xip} A_{y_{ip}}). \tag{15}$$

Similarly, n in the series counts the number of ip encircling the main node in Equation (15). In linearization scheme, two storylines are possible to estimate the lagged values. In the first state, lagged values are approximated irrespective of the flow direction and weighted values determine the share of each node within the element, which leads to a central scheme. Another possible plan is estimating lagged values according to the flow direction at each ip that leads to the upwind scheme. It should be noted that velocity components are hidden in the vorticity and energy equations in terms of the stream-function, that is, $\bar{\psi}_{y_{ip}}$ and $-\bar{\psi}_{xip}$ for the horizontal and vertical components, respectively.

Solutions are advanced in time to a steady state using a second-order temporal scheme. A maximum difference of scalar values less than 10^{-7} during two successive steps is considered as the stop criteria for the iterative solution procedure. The solver has been validated in several previous studies.[30–34] A mesh resolution study was conducted on the present problem; it was determined that a mesh having 181 azimuthal and 91 radial elements provided six significant figures of accuracy for pertinent measured quantities.

In this study, natural convection in the considered geometry is studied in terms of the Nusselt number and skin friction. The local and average Nusselt numbers along the walls of the annulus enclosure are obtained from

$$Nu_{\mathrm{loc}} = -\partial \Theta / \partial \mathbf{n}|_{\mathrm{wall}} \tag{16}$$

and

$$Nu_{\mathrm{ave}} = \frac{1}{2\pi(r_i + r_o)} \left[\int_0^{2\pi r_o} Nu_{\mathrm{loc},o} \mathrm{d}s + \int_0^{2\pi r_i} Nu_{\mathrm{loc},i} \mathrm{d}s \right]. \tag{17}$$

The friction coefficient along the surface may be defined based on the dimensionless velocity

$$c_f = -\frac{\tau_w}{1/2\rho(\alpha/L)^2} = -2Pr \frac{\partial U_\delta}{\partial \boldsymbol{n}}\bigg|_{\mathrm{wall}}. \tag{18}$$

In the Cartesian coordinate system, the above fundamental definition for friction coefficient may be implemented through the following 2D shear stress tensor

$$\boldsymbol{c_f} = -2Pr \begin{bmatrix} \tau_{xx} & \tau_{xy} \\ \tau_{yx} & \tau_{yy} \end{bmatrix} \begin{bmatrix} n_x \\ n_y \end{bmatrix} = -2Pr \begin{bmatrix} 2\partial U/\partial X & \partial U/\partial Y + \partial V/\partial X \\ \partial U/\partial Y + \partial V/\partial X & 2\partial V/\partial Y \end{bmatrix} \begin{bmatrix} n_x \\ n_y \end{bmatrix}, \tag{19}$$

where n_x and n_y are the components of the wall-normal unit vector, respectively. The overall friction coefficient is then

$$c_f = \sqrt{(c_{fx})^2 + (c_{fy})^2}. \tag{20}$$

4 | ANALYZING RESULTS UNDER THE FULL AND SIMPLIFIED GAY-LUSSAC APPROACHES

In this section, it is demonstrated that the GL and SGL approaches give similar results in both transient and steady states. In other words, it is shown that the mismatch of the obtained results under the GL and SGL approaches is negligible with a reduced computational cost for the SGL approach. In this respect, the absolute difference in temperature, vorticity,

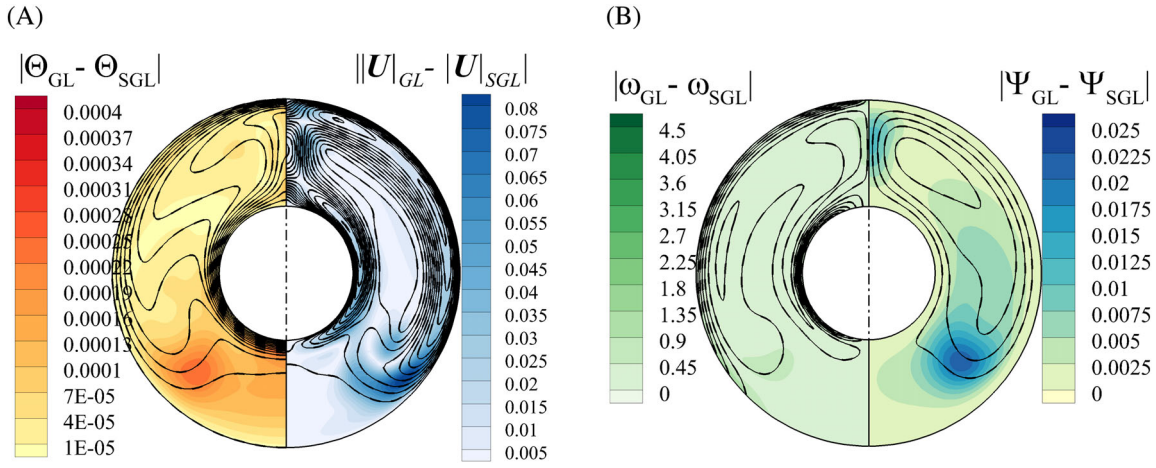

FIGURE 3 Comparing results under the GL and SGL approaches at $Ra = 10^5$, $Pr = 1$ and $Ga = 0.6$ for (A) absolute temperature and velocity magnitude difference and (B) absolute vorticity and stream-function difference. In both figures, solid and dashed lines show isovalues under the GL and SGL approximations, respectively [Colour figure can be viewed at wileyonlinelibrary.com]

stream-function and velocity magnitude at $Ra = 10^5$ and $Ga = 0.6$ ($\varepsilon = 0.3$), under the two approaches is calculated in steady state, and results are portrayed in Figure 3.

The maximum absolute temperature and velocity magnitude differences in Figure 3(A) are approximately 0.005 and 0.1, respectively, which ranges within 1% and 0.06% of the temperature and velocity magnitude values. Though the differences are very small, the largest differences in velocity magnitude are detected across the plume region and the middle height of the lower half of the enclosure adjacent to the outer cylinder. The first location corresponds to a strong free convection region where the working fluid leaves the inner hot cylinder toward a higher location close to the top cold boundary. The second location of large velocity magnitude differences corresponds to the region where the fluid becomes ready to start its vertical transport toward the highest location of the enclosure. The same difference pattern is observed for the stream-function in Figure 3(B) as expected while the vorticity difference has almost a uniform distribution over the physical domain in the same figure. The maximum absolute vorticity and stream-function differences in Figures 3(B) are approximately 5 and 0.03, respectively, which ranges within 0.14% and 0.12% of the vorticity and stream-function magnitude values.

Similar output/behavior of the GL and SGL approximations in the transient state is investigated in Figure 4 in the context of the absolute local Nusselt number and friction coefficient differences along the outer and inner cylinders at $Ra = 10^5$ and $Ga = 0.6$. Results indicate the absolute local Nusselt number difference is three orders smaller than the local Nusselt number magnitude during transient solution ($O(|\Delta Nu_{loc}|/Nu_{loc}) \sim 0.001$). A similar comparison for the absolute local friction coefficient difference shows a value of four order smaller value, that is, $O(|\Delta c_f|/c_f) \sim 10^{-4}$. Having demonstrated that the GL and SGL approximations exhibit identical behavior, we consider only the SGL approximation hereafter.

5 | ANALYZING COMPUTATIONAL COST AND CONVERGENCE HISTORIES OF THE PRIMARY AND SECONDARY VARIABLES FORMULAS

The secondary variables form of the governing equations are derived as an alternative to resolve the pressure coupling problem with the flow field. Nevertheless, the advantage of the secondary variables formula is not restricted to establish a coupling between the pressure and the velocity, but it has also a lower computational cost compared with the primary variables that are investigated in terms of the convergence rate and CPU time in this section.

To compare the computational cost of the iterative solution procedure, successive substeps at each iteration are explained for both primary and secondary variables formulas. For a consistent analysis, governing equations in both primary and secondary variables forms are advanced in time using a second-order Adams–Bashforth/Crank–Nicolson scheme in the context of a fractional step method having three substeps. For the primary variables, the first substep is

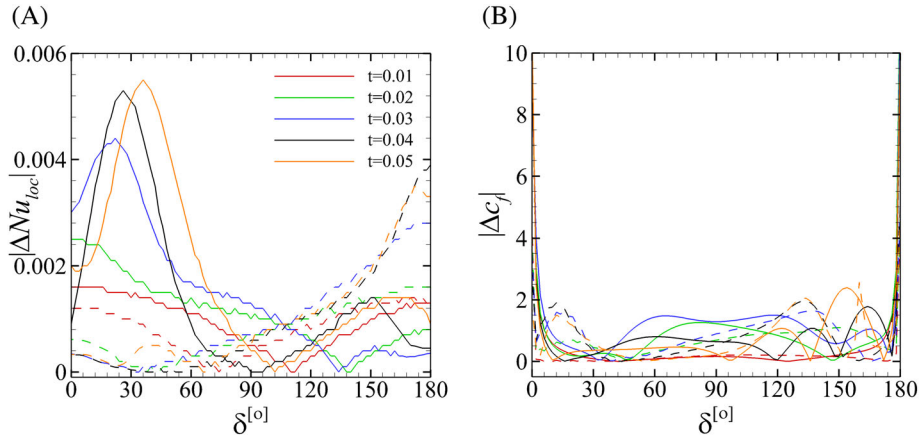

FIGURE 4 Comparing transient local Nusselt number and coefficient friction differences along the inner and outer cylinders under the GL and SGL approximations at $Ra = 10^5$, $Pr = 1$, and $Ga = 0.6$. (A) Absolute local Nusselt number differences and (B) absolute local coefficient friction differences. In both figures, solid lines represent data of the inner (hot) cylinder while dash lines represent data of the outer (cold) cylinder [Colour figure can be viewed at wileyonlinelibrary.com]

computing an intermediate velocity ($\boldsymbol{U}^*$) by solving the momentum equation in an explicit manner in the absence of the pressure term,

$$\frac{\boldsymbol{U}^* - \boldsymbol{U}^{\boldsymbol{n}}}{\Delta t} = -\frac{3}{2}(1 - 2\varepsilon\Theta^n)\mathrm{N}(\boldsymbol{U}^{\boldsymbol{n}}) + \frac{1}{2}(1 - 2\varepsilon\overline{\Theta^{n-1}})\mathrm{N}(\boldsymbol{U}^{\boldsymbol{n-1}}) + \frac{Pr}{2}\mathrm{L}(\boldsymbol{U}^{\boldsymbol{n}}) - RaPr\overline{\Theta^{n+1}}\boldsymbol{e_g}. \tag{21}$$

The second substep is applying the intermediate velocity accompanying by the pressure to the continuity equation, which yields a Poisson equation for the pressure, that is,

$$\nabla^2 P = \frac{1}{\Delta t}(\nabla \cdot \boldsymbol{U}^*). \tag{22}$$

The third substep is modifying the intermediate velocity using a pressure that satisfies a divergence-free condition for an incompressible flow field in an implicit manner,

$$\frac{\boldsymbol{U}^{\boldsymbol{n+1}} - \boldsymbol{U}^*}{\Delta t} = -\nabla P + \frac{Pr}{2}\mathrm{L}(\boldsymbol{U}^{\boldsymbol{n+1}}). \tag{23}$$

Equation (21) requires temperature information from the next time step in the buoyancy term. Thus, before updating the velocity field at each time step, the energy equation is advanced in time in the following two substeps,

$$\frac{\Theta^* - \Theta^n}{\Delta t} = -\frac{3}{2}(1 - 2\varepsilon\overline{\Theta^n})\mathrm{N}(\Theta^n) + \frac{1}{2}(1 - 2\varepsilon\overline{\Theta^{n-1}})\mathrm{N}(\Theta^{n-1}) + \frac{1}{2}\mathrm{L}(\Theta^n), \tag{24}$$

$$\frac{\Theta^{n+1} - \Theta^*}{\Delta t} = \frac{1}{2}\mathrm{L}(\Theta^{n+1}). \tag{25}$$

Similar to the primary variable, for the secondary variables formulas, the solution procedure at each time step starts with solving the energy equation in the two substeps explained by Equations (24) and (25). Then, the solution procedure continues with solving the vorticity and stream-function equations in the following substeps

$$\frac{\omega^* - \omega^n}{\Delta t} = -\frac{3}{2}(1 - 2\varepsilon\overline{\Theta^n})\mathrm{N}(\omega^n) + \frac{1}{2}(1 - 2\varepsilon\overline{\Theta^{n-1}})\mathrm{N}(\omega^{n-1}) + \frac{Pr}{2}\mathrm{L}(\omega^n) + RaPr\overline{\partial\Theta/\partial X^{n+1}}, \tag{26}$$

$$\frac{\omega^{n+1} - \omega^*}{\Delta t} = \frac{Pr}{2}\mathrm{L}(\omega^{n+1}), \tag{27}$$

$$\mathrm{D}(\psi^{n+1}) = -\overline{\omega^n}. \tag{28}$$

In general, solving Navier–Stokes and energy equations in the primary variable form with a second-order temporal accuracy requires solving seven equations for a 2D problem while the same problem may recast in five equations via the secondary variables.

Computational cost and convergence histories of the primary and secondary variables are compared in Figure 5. An inverse matrix of the Laplacian operator with appropriate boundary conditions is constructed for each of the equations that are being solved in an implicit manner to speed up the solution procedure. For instance, an inverted Laplacian matrix ($[D]^{-1}$) is multiplied by the vorticity vector at the right-hand side of Equation (28) to update the stream-function values in each iteration. CPU-time for a sample case having 121×81 elements is measured to compare the computational cost. Calculations were performed at $Ra = 10^5$ and $\epsilon = 0.3$ in two states in which the nonlinear operator acts based on upwind or central schemes. Bar charts of Figure 5(A) show an almost 25% lower computational cost for the secondary variables formulas compared with the primary one for both upwind and central schemes.

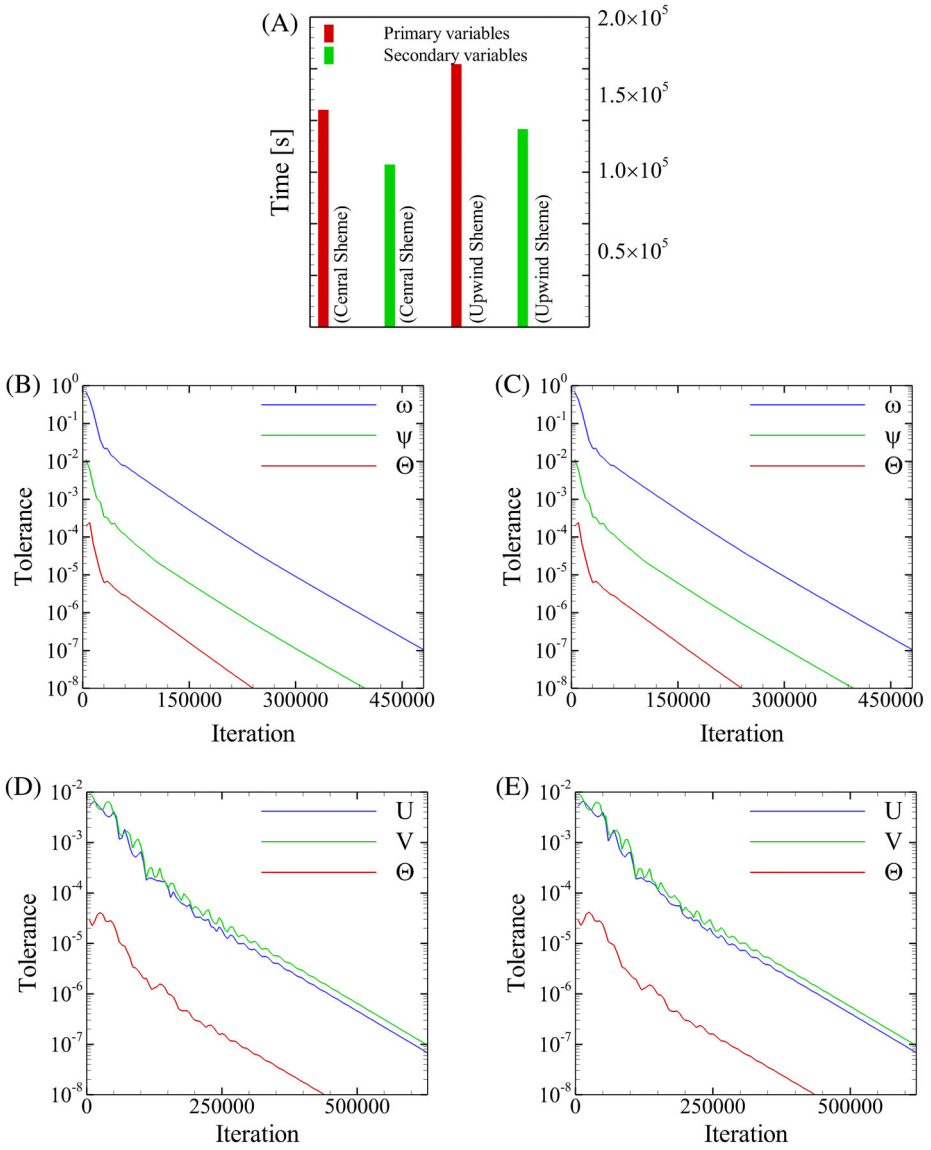

FIGURE 5 Computational cost and convergence histories of the computations at $Ra = 10^5$ and $\epsilon = 0.3$ using primitive and secondary variables. (A) CPU-time, (B) convergence rate of the secondary variables, central scheme; (C) convergence rate of the secondary variables, second-order upwind scheme; (D) convergence rate of secondary variables, second-order upwind; (E) convergence rate of the primitive variables, second-order upwind. A global time-step of 10^{-6} ($dt = 10^{-6}$) is used for calculations for all cases [Colour figure can be viewed at wileyonlinelibrary.com]

Convergence rates of the two approaches are also checked in terms of the variables tolerance during the iterative solution procedure through Figure 5(B–E). The tolerance of any parameter in this study is defined as the maximum alteration of all nodal values during two successive time-steps. Comparing convergence histories of the two approaches indicate that secondary variables form of the governing equations converges to a steady state with fewer oscillations. In addition, since both central and upwind schemes are applied in the second-order form, the differences in the convergence histories are not much different in each category.

6 | ANALYZING RESULTS UNDER THE LOW MACH NUMBER SCHEME, SIMPLIFIED GAY-LUSSAC, AND OBERBECK–BOUSSINESQ APPROXIMATIONS AT HIGH RELATIVE TEMPERATURE DIFFERENCES

Results under the three aforementioned approximations are analyzed in terms of the skin friction and local and average Nusselt number, in this section. For a deep analyze of the thermoflow fields, temperature, stream-function, velocity magnitude and vorticity fields under the LMS approximation are compared against the incompressible approaches in Figure 6(A–D), respectively, at $Ra = 10^5$ and $\varepsilon = 0.3$ ($Ga = 0.6$). It is apparent from the similar patterns traced by the solid and dashed contour lines, corresponding respectively to the weakly compressible and incompressible approaches, that both approaches correctly capture the essential thermal and kinematic features of the system. The largest deviations found for either the GL or OB methods from the LMS solution are less than 20% for velocity magnitude, 14% for stream function, 6% for vorticity and 5% for temperature. Local measurements are notoriously sensitive to small changes in the location and strength of structures within a flow; in support of the efficacy of the tested approaches, it will be shown later that integrated quantities obtained from these solutions, including Nusselt number, exhibit even smaller differences. Figure 6(D) demonstrates that the vorticity field is captured exceptionally well using both the GL and OB methods. The largest deviations are experienced in both cases within a layer of fluid just outside the boundary layer on either side of the inner cylinder. The contour lines in Figure 6(C) reveal that this layer corresponds to fast-moving fluid entrained in buoyant jets ascending around each side of the cylinder. Both the GL and OB methods produce deviations in velocity magnitude that are greatest on the outer side of these fast-moving jets. These deviations extend upward from the top of the inner cylinder, straddling the buoyant plume that rises on the vertical centerline of the cavity. The GL approach exhibits slightly stronger velocity magnitude deviations than the OB approach in the jet, while the OB approach deviates more toward the sides of the outer cylinder, in the part of the flow that descends adjacent to the cooler outer cylinder.

The most visible differences between the GL and OB methods may be found in the stream-function fields plotted in Figure 6(B). The stream-function is zero along the vertical plane of symmetry and on both cylinder surfaces, and rises in the interior of the fluid on both sides of the cavity. This reflects the circulating flow generated by the natural convective transport of heat from the inner cylinder, up to the top of the cavity, before cooling and descending adjacent to the outer cylinder toward the bottom of the cavity. Both the GL and OB approaches show the largest deviations in stream-function in the upper quadrants of the cavity, close to the core of the circulations. The GL approach exhibits deviations extending down to the side of the cylinder, outside the fast-moving jet around the inner cylinder, while the OB method is relatively weaker in that region, instead manifesting a stronger zone in the lower quadrant of the cavity.

Finally, the temperature deviations are qualitatively similar between the GL and OB approaches. The GL approach exhibits slightly larger differences within the large overturning natural convection cell. By contrast, stronger deviations are seen under the OB approach at the top of the plume near the upper surface of the outer cylinder. It becomes apparent that under high-temperature differences, neither the OB nor the GL method is universally superior; care must be taken to determine which quantity(s) of interest may be better captured by which method. The distributions of the local Nusselt number and skin friction coefficients presented in the sections to follow provide further insights as to which approach may be more suitable, depending on the governing parameter values and local features of a flow.

The magnitude of the non-OB terms in the momentum and energy equations in secondary variable formulas are portrayed in Figure 7. These are indeed the terms that are appeared by taking into account density variations beyond the gravity term. The magnitude of the non-OB term in the momentum equation, that is, $|\Theta(\partial\psi/\partial Y\partial\omega/\partial X - \partial\psi/\partial X\partial\omega/\partial Y)|$ in Figure 7(A), is larger across the upper half of the inner cylinder and end of the plume region colliding the highest height of the cavity. These are the regions that isovorticity lines are accumulated in Figure 6(D) leading to larger vorticity gradients. A similar distribution of the non-OB term in the energy equation, that is, $|\Theta(\partial\psi/\partial Y\partial\Theta/\partial X - \partial\psi/\partial X\partial\Theta/\partial Y)|$ is

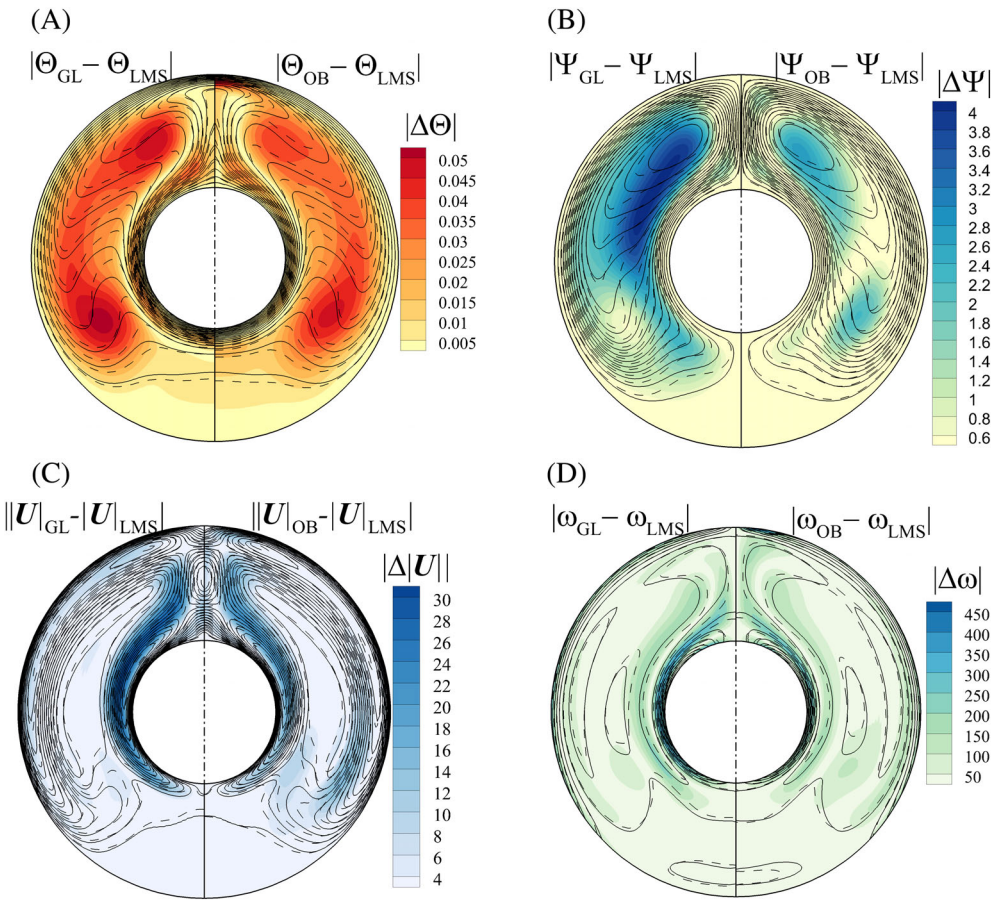

FIGURE 6 Absolute differences of results under the LMS, GL, and OB approximations at $Ra = 10^5$ and $\varepsilon = 0.3$ for (A) temperature, (B) stream-function, (C) velocity magnitude, and (D) vorticity. In all figures, the left half shows the difference between the LMS and GL approximations while the right half depicts the difference between the LMS and OB approximations. Solid lines in all figures represent the isovalues of the parameter under the LMS approximation while dash lines show the incompressible approach [Colour figure can be viewed at wileyonlinelibrary.com]

observable in Figure 7(B). Regions having larger temperature gradients amplify the non-OB term in the energy equation. Accumulation of the isotherm-lines in Figure 6(A) is in agreement with the regions having stronger non-OB term in the energy equation, however, a comparison of the result against the LMS approximation reveals that the non-OB terms are not efficiently modifying thermoflow field at larger temperature differences.

6.1 | Local Nusselt number

The local Nusselt number under the three approximations is investigated at the highest Rayleigh number ($Ra = 10^5$) and respective relative temperature differences $\varepsilon = 0.15$ and 0.3 in Figure 8(A,B), respectively. As seen, the two incompressible approaches show similar behavior, both deviating from the LMS approximation. Along the outer cylinder, the SGL approach shows more accurate results compared with the OB approximation at about $\delta \approx 170$ with $\varepsilon = 0.3$ (Figure 8(B)) compared with $\varepsilon = 0.15$ (Figure 8(A)). For the inner cylinder, there is a visible gap among the local Nusselt number values at smaller δ under the incompressible and LMS approximations that becomes more visible by increasing ε. Also by increasing ε, the SGL approach shows more deviation from the LMS approximation at about $0 \lesssim \delta \lesssim 25^{\circ}$ compared with the OB approximation.

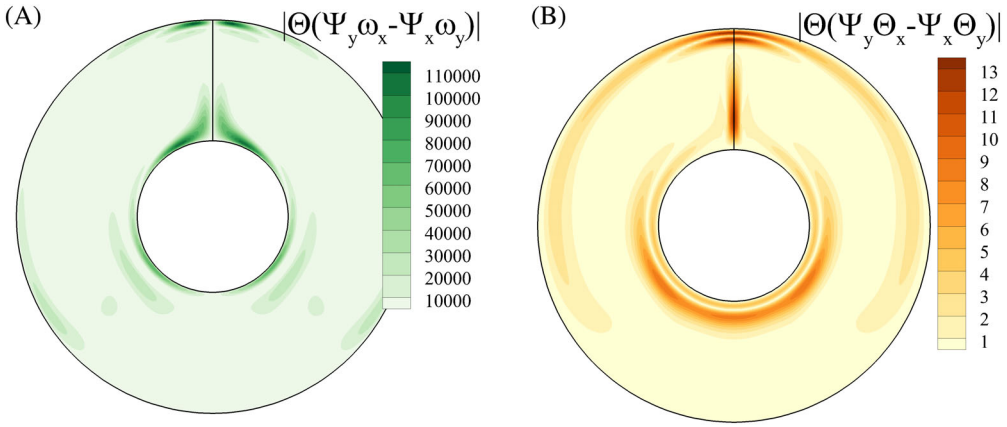

FIGURE 7 The magnitude of the non-OB terms at $Ra = 10^5$ in secondary variable form of the governing equations in (A) vorticity equation and (B) energy equation [Colour figure can be viewed at wileyonlinelibrary.com]

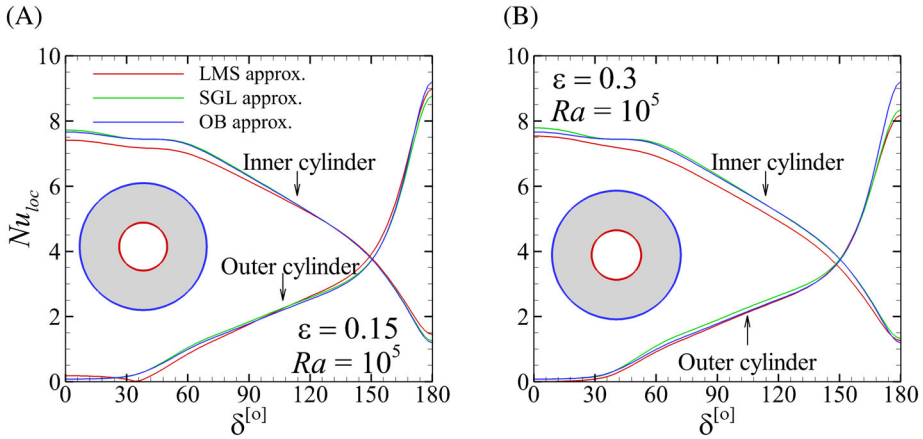

FIGURE 8 Comparing the local Nusselt number under the LMS and incompressible approximations along the inner and outer surfaces at $Ra = 10^5$ and (A) $\varepsilon = 0.15$, (B) $\varepsilon = 0.3$ [Colour figure can be viewed at wileyonlinelibrary.com]

6.2 | Average Nusselt number

The average Nusselt number was calculated from the simulations spanning $10^1 \leq Ra \leq 10^5$, and is plotted in Figure 9(A,B) for $\varepsilon = 0.15$ and 0.3, respectively. Equation (12) is evaluated by Simpson's one-third rule. Below $Ra \approx 10^2$, Nusselt number was found to be approximately constant at both relative temperature values. In this regime, thermal conduction dominates. As Rayleigh number increases to $Ra \approx 10^3$, the flow evolves into a state dominated by thermal convection, beyond which Nusselt number follows approximately to a power-law going as $Nu \sim Ra^4$.

In the low-Ra regime, the average Nusselt number is indistinguishable between the three methods. This follows from the conduction-dominated nature of this regime, where advection, convection, and buoyancy contribute negligibly to the flow, this suppressing the very components of the respective sets of governing equations that differ between the three methods. In the higher-Ra regime, the results obtained for $\varepsilon = 0.15$ are differed by a smaller amount between the three methods when compared with the results at $\varepsilon = 0.3$. Interestingly, at both $\varepsilon = 0.15$ and 0.3, the OB and SGL approximations yield almost the same results, with both slightly over-estimating the Nusselt number when compared with the LMS method. At $Ra = 10^5$ and $\varepsilon = 0.3$, respective mismatches in average Nusselt numbers of 4.8% and 4.2% for the SGL and OB approximations are found when compared with the LMS method.

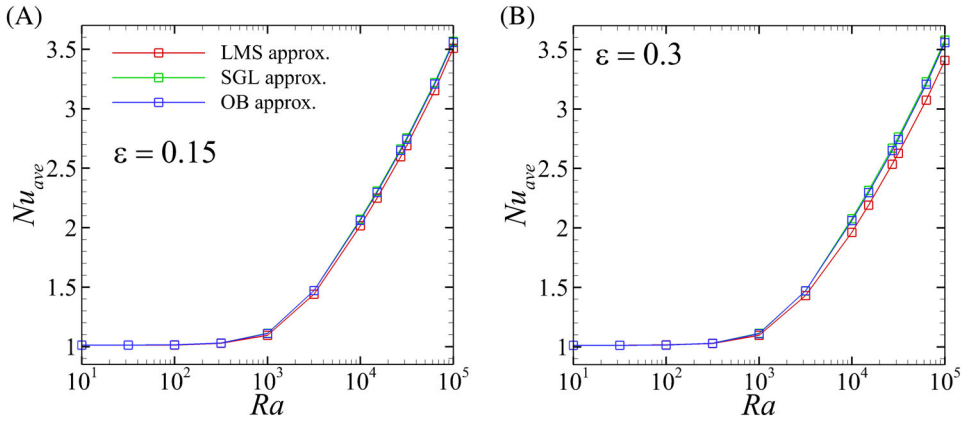

FIGURE 9 Comparing the average Nusselt number under the low Mac number scheme and two incompressible approximations at $10^1 \leq Ra \leq 10^5$ and (A) $\varepsilon = 0.15$, (B) $\varepsilon = 0.3$ [Colour figure can be viewed at wileyonlinelibrary.com]

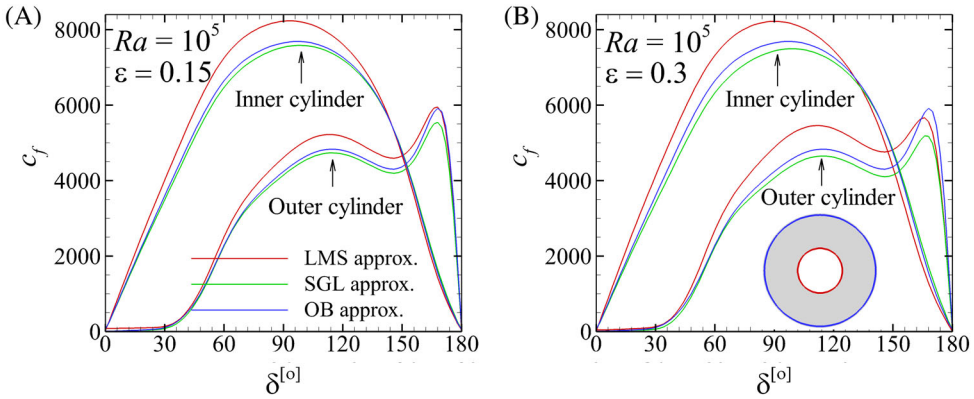

FIGURE 10 Comparing the local coefficient friction results under the two incompressible and LMS approximations along the inner and outer surfaces at $Ra = 10^5$ and (A) $\varepsilon = 0.15$, (B) $\varepsilon = 0.3$ [Colour figure can be viewed at wileyonlinelibrary.com]

6.3 | Skin shear stress

The coefficient of friction is the final considered parameter in this study. Results are plotted for the inner and outer cylinders at $Ra = 10^5$ and $\varepsilon = 0.15$ and 0.3 in Figure 10(A,B), respectively. Both incompressible approaches show a visible mismatch against the LMS approximation. For the inner (hot) cylinder, the mismatch is larger at $50 \lesssim \delta \lesssim 170$ but for the outer (cold) cylinder the mismatch is detected at $10 \lesssim \delta \lesssim 110$. The results indicate that increasing the relative temperature difference from 0.15 to 0.3 leads to the SGL approach deviating from the LMS approximation compared with the OB approximation. This deviation (also detected in the Nusselt number data) may be ascribed to the inappropriate density state equation that is used to extend density variations beyond the gravity term under the SGL approximation.

7 | CONCLUSION

Free convection in a concentric annulus enclosure is studied numerically at high relative temperature differences ($\varepsilon = 0.15$ and 0.3) up to Rayleigh number $Ra = 10^5$ and a fixed Prandtl number of unity under the low Mach number and an incompressible non-Boussinesq approximation known as the Gay-Lussac approach. The non-Boussinesq approximation is established based on extending density variations beyond the gravity term of the momentum equations. In this respect, governing equations under the Gay-Lussac approach are presented in vorticity stream-function form. The problem is also simulated under the classical Oberbeck–Boussinesq approximation and results are evaluated in terms of the absolute differences in temperature, stream-function, velocity magnitude, and vorticity fields. These comparisons

show a considerable mismatch among the compressible and incompressible approximations at high relative temperature differences, even for the applied non-Boussinesq approach. In other words, obtained results under the Gay-Lussac approach do not show a clear superiority compared with the Oberbeck–Boussinesq approximation. Results of the incompressible approaches are also compared against the weekly compressible approach in terms of the skin friction and local and average Nusselt number, confirming that the Gay-Lussac approach requires further treatments/revisions to surpass the performance of the Boussinesq approximation. Finally, a computational cost analysis confirms that solving governing equations in the presented secondary variable formulas reduces the computational cost by around 25% compared with the primary variables formulas.

ACKNOWLEDGMENTS

This research was supported by the Australian Research Council through Discovery Project DP180102647. Peyman Mayeli is supported by a Monash Graduate Scholarship and a Monash International Postgraduate Research Scholarship. The authors are also supported by time allocations on the National Computational Infrastructure (NCI) peak facility and the Pawsey Supercomputing Centre through NCMAS grants. NCI is supported by the Australian Government.

CONFLICT OF INTEREST

The authors declare no conflict of interest.

DATA AVAILABILITY STATEMENT

Data sharing is not applicable as no new data generated.

NOMENCLATURE

c_f	skin friction coefficient
Ga	Gay-Lussac parameter ($\beta\Delta\theta$)
L	Laplacian operator
L_{ref}	reference length
$\boldsymbol{n}$	unit normal vector to the surface
N	nonlinear operator
Nu_{ave}	average Nusselt number
Nu_{loc}	local Nusselt number
p^*	modified pressure
P	dimensionless pressure
P_{th}	thermodynamic pressure
Pr	Prandtl number
r	radius
Ra	Rayleigh number
T	temperature
$\boldsymbol{u}$	velocity vector
$\boldsymbol{U}$	dimensionless velocity vector
$\boldsymbol{x}$	coordinate vector
$\boldsymbol{X}$	dimensionless coordinate vector
α	thermal diffusivity
β	isobaric expansion coefficient
γ	heat capacity ratio
ε	relative temperature difference
θ	physical temperature
Θ	dimensionless temperature
ρ	density
ν	kinematic viscosity
τ_w	wall shear stress
ψ	stream-function
ω	vorticity

SUBSCRIPT

ave	average
loc	local
0	reference value

SUPERSCRIPT

n	current time-step
$n-1$	previous time-step
—	refers to a lagged value

ORCID

Peyman Mayeli https://orcid.org/0000-0003-4084-2627

REFERENCES

1. Buchberg H, Catton I, Edwards DK. Natural convection in enclosed spaces—a review of application to solar energy collection. *ASME J Heat Transf*. 1976;98(2):182-188.
2. Tonui JK, Tripanagnostopoulos Y. Performance improvement of PV/T solar collectors with natural air flow operation. *Sol Energy*. 2008;82(1):1-12.
3. Phiraphat S, Prommas R, Puangsombut W. Experimental study of natural convection in PV roof solar collector. *Int Commun Heat Mass Transf*. 2017;89:31-38.
4. Van Dam RL, Simmons CT, Hyndman DW, Wood WW. Natural free convection in porous media: first field documentation in groundwater. *Geophys Res Lett*. 2008;609:111-137. https://doi.org/10.1029/2008GL036906
5. Sparrow EM, Patankar SV, Ramadhyani S. Analysis of melting in the presence of natural convection in the melt region. *ASME J Heat Transf*. 1977;99(4):520-526.
6. Paillere H, Viozat C, Kumbaro A, Toumi I. Comparison of low Mach number models for natural convection problems. *Heat Mass Transf*. 2000;36:567-573.
7. Darbandi M, Hosseinizadeh SF. Numerical study of natural convection in vertical enclosures using a novel non-Boussinesq algorithm. *Numer Heat Transf A*. 2007;52:849-873.
8. Harish R, Venkatasubbaiah K. Numerical investigation of instability patterns and nonlinear buoyant exchange flow between enclosures by variable density approach. *Comput Fluids*. 2014;96:276-287.
9. Busto S, Tavelli M, Boscheri W, Dumbser M. Efficient high order accurate staggered semi-implicit discontinuous Galerkin methods for natural convection problems. *Comput Fluids*. 2020;198:104399.
10. Armengol JM, Bannwart FC, Xaman J, Santos RG. Effects of variable air properties on transient natural convection for large temperature differences. *Int J Therm Sci*. 2017;120:63-79.
11. Wan ZH, Wang Q, Wang B, Xia SN, Zhou Q. On non-Oberbeck–Boussinesq effects in Rayleigh–Bénard convection of air for large temperature differences. *J Fluid Mech*. 2020;889:A10.
12. Pesso T, Piva S. Laminar natural convection in a square cavity: low prandtl numbers and large density differences. *Int J Heat Mass Transf*. 2009;52(3–4):1036-1043.
13. Lopez JM, Marques F, Avila M. The Boussinesq approximation in rapidly rotating flows. *J Fluid Mech*. 2013;737(2013):56-77.
14. Mayeli P, Sheard G. A new formulation for Boussinesq-type natural convection flows applied to the annulus cavity problem. *Int J Numer Methods Fluids*. 2021;93(3):683-702.
15. Mayeli P, Sheard G. Natural convection and entropy generation in square and skew cavities due to large temperature differences: a gay-Lussac type vorticity stream-function approach. *Int J Numer Methods Fluids*. 2021;93(7):2396-2420.
16. Lee CH, Hyun JM, Kwak HS. Oscillatory enclosed buoyant convection of a fluid with the density maximum. *Int J Heat Mass Transf*. 2000;43(19):3747-3751.
17. Zhong ZY, Yang KT, Lioyd JR. Variable property effects in laminar natural convection in a square enclosure. *ASME J Heat Transf*. 1985;107:133-138.
18. Pons M, Le Quéré P. Modeling natural convection with the work of pressure-forces: a thermodynamic necessity. *Int J Numer Methods Heat Fluid Flow*. 2007;17(3):322-332.
19. Mayeli P, Sheard GJ. Buoyancy-driven flows beyond the Boussinesq approximation: a brief review. *Int Commun Heat Mass Transf*. 2021;125:105316.
20. Kuhen TH, Goldstein RJ. An experimental and theoretical study of natural convection in the annulus between horizontal concentric cylinders. *J Fluid Mech*. 1976;74(4):695-719.
21. Abu-Nada E, Masoud Z, Hijazi A. Natural convection heat transfer enhancement in horizontal concentric annuli using nanofluids. *Int Commun Heat Mass Transf*. 2008;35:657-665.
22. Ashrafizadeh A, Nikfar M. On the numerical solution of generalized convection heat transfer problems via the method of proper closure equations–part II: application to test problems. *Numer Heat Transf B*. 2016;70(2):204-222.
23. Ashorynejad HR, Mohamad AA, Sheikholeslami M. Magnetic field effects on natural convection flow of a nanofluid in a horizontal cylindrical annulus using lattice Boltzmann method. *Int J Therm Sci*. 2013;64:240-250.

24. Wu YL, Liu GR, Gu YT. Application of Meshless local Petrov-Galerkin (MLPG) approach to simulation of incompressible flow. *Numer Heat Transf B*. 2005;48(5):459-475.
25. Shadlaghani A, Farzaneh M, Shahabadi M, Tavakoli MR, Safaei MR, Mazinani I. Numerical investigation of serrated fins on natural convection from concentric and eccentric annuli with different cross sections. *J Therm Anal Calorim*. 2019;135:1429-1442.
26. Afrand M, Sina N, Teimouri H, et al. Effect of magnetic field on free convection in inclined cylindrical annulus containing molten potassium. *Int J Appl Mech*. 2015;7(4):1550052.
27. Rozati SA, Montazerifar F, Ali Akbari O, et al. Natural convection heat transfer of water/Ag nanofluid inside an elliptical enclosure with different attack angles. *Math Methods Appl Sci*. https://doi.org/10.1002/mma.7036
28. Malvandia A, Safaei MR, Kaffash MH, Ganji DD. MHD mixed convection in a vertical annulus filled with Al_2O_3–water nanofluid considering nanoparticle migration. *J Magn Magn Mater*. 2015;382:296-306.
29. Dawood HK, Mohammed HA, Sidikb NAC, Munisamy KM, Wahid MA. Forced, natural and mixed-convection heat transfer and fluid flow in annulus: a review. *Int Commun Heat Mass Transf*. 2015;62:45-47.
30. Mayeli P, Hesami H, Besharati-Foumani H, Niajalili M. Al2O3-water nanofluid heat transfer and entropy generation in a ribbed channel with wavy wall in the presence of magnetic field. *Numer Heat Transf A*. 2018;73(9):604-623.
31. Hesami H, Mayeli P. Development of the ball-spine algorithm for the shape optimization of ducts containing nanofluid. *Numer Heat Transf A*. 2016;70(12):1371-1389.
32. Mayeli P, Nikfar M. Temperature identification of a heat source in conjugate heat transfer problems via an inverse analysis. *Int J Numer Methods Heat Fluid Flow*. 2019;29(10):3994-4010.
33. Mayeli P, Nili-Ahmadabadi M, Pirzadeh MR, Rahmani P. Determination of desired geometry by a novel extension of ball spine algorithm inverse method to conjugate heat transfer problems. *Comput Fluids*. 2017;154:390-406.
34. Mayeli P, Nili-Ahmadabadi M, Besharati-Foumani H. Inverse shape design for heat conduction problems via the ball spine algorithm. *Numer Heat Transf B*. 2016;69(3):249-269.

How to cite this article: Mayeli P, Sheard GJ. An efficient and simplified Gay-Lussac approach in secondary variables form for the non-Boussinesq simulation of free convection problems. *Int J Numer Meth Fluids*. 2021;93:3264-3279. doi: 10.1002/fld.5033

2.4 Summary of the chapter

The Gay-Lussac approximation has been introduced and governing equations under this approach have been derived in both primary and secondary variables form. A simplified version of this approach has been proposed in which the density variations are removed from the continuity equation and time derivatives. It is shown that, the original and simplified versions give almost identical results with a lower computational cost for the simplified version due to simpler form of the continuity equation while the convergence rate under the two versions remains unaltered. This motivates a furthest simplification of the traditional GL approach, whereby in the next chapter the advection focused centrifugal approximation will be introduced and explored.

Chapter 3

3 Centrifugal approximation

Having previously introduced the SGL approach in chapter 2 in primary and secondary variables forms, and showing that as an incompressible approach the difference of the results under the original and simplified Gay-Lussac approaches are negligible, in this chapter an approximation referred to herein as the centrifugal approximation is introduced.

3.1 Concept of the centrifugal approximation

Under the centrifugal approximation, the density variations are extended just to the advection term in addition to the gravity term in the momentum equations. This strategy was first proposed by Lopez and co-workers [7] in the inertial frame for a Newtonian fluid, as part of their development of a buoyancy model suitable for rapidly rotating flows. The centrifugal approximation may be recognised as a GL type approach. The philosophy behind simplification of the original GL approach is to draw more attention to the term that has a significant effect in rapidly rotating flows. Under this approximation, the momentum equation may be expressed as

$$\rho_0(\partial_t + \boldsymbol{u}\cdot\nabla)\boldsymbol{u} = -\nabla p^* + \mu\nabla^2\boldsymbol{u} + \rho\boldsymbol{f} - \rho'\nabla\phi - \rho'(\boldsymbol{u}\cdot\nabla)\boldsymbol{u}. \tag{3.1}$$

In this form, the density is considered in two parts ($\rho = \rho_0 + \rho'$) including a constant reference value (ρ_0) and a perturbation part (ρ') that captures the temperature dependences, density variations due to fluid density stratification or density variations in a binary fluid with miscible species of different densities, etc. In Eq. 3.1, the $\rho\boldsymbol{f}$ term describes any additional body forces that may act on the fluid.

3.2 Governing equation under the centrifugal approximation

The same concept proposed by Mayeli and Sheard *et al.*[6] by considering a unified value/definition for the density yields,

$$\nabla\cdot\boldsymbol{u} = 0, \tag{3.2}$$

$$\frac{\partial \boldsymbol{u}}{\partial t^*} + (\rho/\rho_0)(\boldsymbol{u}\cdot\nabla)\boldsymbol{u} = -(1/\rho_0)\nabla p + \nu\nabla^2\boldsymbol{u} + (\rho/\rho_0)g\mathbf{e}_g, \tag{3.3}$$

$$\frac{\partial T}{\partial t^*} + (\boldsymbol{u}\cdot\nabla)T = \alpha\nabla^2 T. \tag{3.4}$$

Following the OB approximation and implementing a linear density state relation ($\rho/\rho_0 = 1-\beta\Delta\theta$) instead of the density ratio in the momentum equation yields,

$$\nabla\cdot\boldsymbol{u} = 0, \tag{3.5}$$

$$\frac{\partial \boldsymbol{u}}{\partial t^*} + (1-\beta\Delta\theta)(\boldsymbol{u}\cdot\nabla)\boldsymbol{u} = -(1/\rho_0)\nabla p + \nu\nabla^2\boldsymbol{u} + (1-\beta\Delta\theta)g\mathbf{e}_g, \tag{3.6}$$

$$\frac{\partial T}{\partial t^*} + (\boldsymbol{u}\cdot\nabla)T = \alpha\nabla^2 T. \tag{3.7}$$

Following the non-dimensionalisation parameters introduced in Eq. (2.9), one can derive the dimensionless form of the governing equation under the centrifugal approximation, where here the GL parameter has been replaced by its relation to Rayleigh, Prandtl and Froude numbers [6],

$$\nabla\cdot\boldsymbol{U} = 0, \tag{3.8}$$

$$\frac{\partial \boldsymbol{U}}{\partial t} + (\boldsymbol{U}\cdot\nabla)\boldsymbol{U} = -\nabla P + Pr\nabla^2\boldsymbol{U} - RaPr\Theta(\mathbf{e}_g - Fr(\boldsymbol{U}\cdot\nabla)\boldsymbol{U}), \tag{3.9}$$

$$\frac{\partial \Theta}{\partial t} + (\boldsymbol{U}\cdot\nabla)\Theta = \nabla^2\Theta. \tag{3.10}$$

As seen, the governing equations under the centrifugal approximation are consistent with the OB approximation, except for the additional inertial buoyancy term on the right hand side of the momentum equation. When expressed in this form, it is apparent that the action of this additional term is to modify the local effective direction (and strength) of buoyancy from the direction due to gravity throughout the flow. This contribution is ignored in the conventional OB approximation. Indeed, regions which are experiencing higher spatial accelerations described by $(\boldsymbol{U}\cdot\nabla)\boldsymbol{U}$ will experience deviations from the OB approximation. The strength of these deviations relative to gravity is described by Fr, with $Fr \to 0$ (and $Ga \to 0$) recovering the classical OB approximation.

The scalar formulation of the governing equations under the centrifugal approximation using secondary variables, i.e. vorticity and stream-function and the relative temperature difference are expressed as [5],

$$\nabla^2\psi = -\omega, \tag{3.11}$$

$$\frac{\partial \omega}{\partial t} + (1 - 2\varepsilon\Theta)\left(\frac{\partial \psi}{\partial Y}\frac{\partial \omega}{\partial X} - \frac{\partial \psi}{\partial X}\frac{\partial \omega}{\partial Y}\right) = Pr\nabla^2\omega + RaPr\partial\Theta/\partial X, \tag{3.12}$$

$$\frac{\partial \Theta}{\partial t} + \left(\frac{\partial \psi}{\partial Y}\frac{\partial \Theta}{\partial X} - \frac{\partial \psi}{\partial X}\frac{\partial \Theta}{\partial Y}\right) = \nabla^2\Theta. \tag{3.13}$$

3.3 Published papers

The centrifugal approximation is applied to study free convection in two benchmark problems. The primary form of the governing equations is applied for a concentric annulus geometry and the results are published in a research paper entitled "A centrifugal buoyancy formulation for Boussinesq-type natural convection flows applied to the annulus cavity problem". The secondary variables form of the centrifugal approximation is applied to square and skew cavity benchmark problems and it is published as a research paper entitled "Natural convection and entropy generation in square and skew cavities due to large temperature differences: A Gay-Lussac-type vorticity stream-function approach". Governing equations are solved using a CVFEM solver and results under the weakly compressible approach are added to the papers for comparison purposes. In both works, the centrifugal buoyancy approximation shows better performance compared to the convectional OB approximation.

Received: 3 August 2019 | Revised: 27 June 2020 | Accepted: 2 August 2020

DOI: 10.1002/fld.4904

RESEARCH ARTICLE

WILEY

A centrifugal buoyancy formulation for Boussinesq-type natural convection flows applied to the annulus cavity problem

Peyman Mayeli | **Gregory J. Sheard**

The Sheard Lab, Department of Mechanical and Aerospace Engineering, Monash University, Melbourne, Victoria, Australia

Correspondence
Peyman Mayeli, The Sheard Lab, Department of Mechanical and Aerospace Engineering, Monash University, Melbourne, VIC 3800, Australia.
Email: peyman.mayeli@monash.edu

Funding information
Australian Research Council, Grant/Award Numbers: DP180102647, DP150102920

Summary

Traditionally, the Boussinesq approximation is adopted for numerical simulation of natural convection phenomena where density variations are supposed negligible except through the gravity term of the momentum equation. In this study, a recently developed formulation based on a Boussinesq approximation is presented in which the density variations are also considered in the advection terms. Extending density-variations to the advection terms captures centrifugal effects arising from both bulk enclosure rotation and within individual vortices, and thus more accurate results are expected. In this respect, the results of the proposed formulation are compared against the conventional Boussinesq simulations and weakly compressible approximation in the concentric horizontal annulus cavity. A new relation is established which maps the magnitude of the non-Boussinesq parameter of incompressible flow to the corresponding relative temperature difference of a compressible flow simulation which is in agreement with the maximum allowed Gay-Lussac number to avoid unphysical density values. For comparison purposes, variations of different thermo-fluid parameters including average and local Nusselt number, entropy generation, and skin friction up to $Ra = 10^5$ are computed. Results obtained under the proposed approximation agree with the classical Boussinesq approximation up to $Ra = 10^3$ for large non-Boussinesq parameter corresponding to the large relative temperature difference, but at $Ra = 10^5$, computed thermo-fluid parameters via the two approaches are not identical which justifies the inclusion of large Gay-Lussac number for convection dominated regime in natural convection problems.

KEYWORDS

annulus cavity, Boussinesq approximation, control volume finite-element method, Gay-Lussac, non-Boussinesq approximation, weakly compressible

1 | INTRODUCTION

Numerical simulation of natural convection phenomena, due to their many scientific and technical applications such as solar collectors, foundry devices, geophysical and astrophysical processes, and so on,[1-5] has attracted attention of researchers over several decades. Predicting the exact behavior of such systems when natural convection is the dominant

heat transfer mechanism is of paramount importance. Typically, the Boussinesq approximation (ie, ignoring density variations except in the gravity term of the momentum equation[6]) is adopted for numerical simulation of natural convection problems. In this approach, a linear state equation is typically adopted to relate density and temperature variations via a volumetric thermal expansion coefficient.

The horizontal annulus cavity is a widely used benchmark problem in numerical heat transfer research. At low Rayleigh (Ra) numbers, diffusion is the dominant mechanism, but at higher Rayleigh numbers convection ultimately dominates the heat transfer, resulting in thin boundary layers. One of the initial works in this area was performed by Thomas and Davis,[7] while Kuhen and Goldstein[8] studied natural convection in an annulus cavity by means of both experimental and numerical simulations. Sheremet and Pop[9,10] studied this problem in the context of porous media and nanofluids. The problem has been solved by a variety of numerical methods, including finite difference,[8] finite volume,[11,12] control volume finite-element,[13,14] lattice Boltzmann,[15] and finite-element based approaches such as local Petrov-Galerkin,[16,17] Galerkin radial-basis-function,[18] differential quadrature method,[19] strongly implicit procedure,[20] and so on. Studies have shown the flow to be steady state up to at least $Ra = 10^5$[12-16] across Prandtl numbers spanning air and water.

In all of the aforementioned works, the Boussinesq approximation along with a linear relation between density and temperature variations has been adopted. This is based on the assumption that the density variations are small, confining their effect to the buoyancy term. This allows the flow field to be treated as incompressible. Note that in different situations, where the density variations under the influence of the temperature non-uniformities are significant, the classical Boussinesq approximation may produce inaccurate results. Available remedies to overcome this issue in the literature may be divided into two major categories. The first remedy is compressible solution of the governing equations. This approach was used by Vierendeels et al[21] and Becker and Braack[22] for numerical simulation of the natural convection problem at low Mach number. The second remedy is dealing with the incompressible Navier-Stokes equations accompanying with some modifications to achieve more accurate results. One approach in this category is to include the linear state relation between density and temperature to terms beyond only the gravity term, which results in the emergence of the Gay-Lussac number ($Ga = \beta\Delta\theta$) in the governing equations. This parameter describes the level of density variations caused by the temperature field. It can be shown that the Boussinesq approximation is retrieved as the Gay-Lussac number goes to zero.[23] For this approach, the difference between the Boussinesq approximation and considering the Gay-Lussac number for the Rayleigh number regime that leads to a steady state solution of the problem, was studied by Szewc et al[23] for a rectangular cavity filled with air. They reported a 4% discrepancy of the average Nusselt number between the two approaches. Lopez et al[24] described an alternative approach, for the treatment of rapidly rotating flows, whereby buoyancy effects were extended to the centrifugal part of the advection term to capture centrifugal effects in those flows.

In the context of experimental studies, some works have considered non-Boussinesq effects. These studies often emphasize the properties of the working fluid (often a liquid), and especially its viscosity that is sensitive to temperature variations. The Boussinesq approximation is developed based on small density variations assumption which implies a small temperature difference. For liquid working fluid cases, having large temperature differences between hot and cold surfaces and its effect on the viscosity along with applying the Boussinesq approximation for non-gaseous mixtures may result in inaccurate results. For instance, Valori et al[25] used water and methanol as their working fluid beyond the validity of the Boussinesq approximation in a cubical Rayleigh-Bénard convection cell. They found that the non-Boussinesq effect manifests itself as an increase of time-averaged horizontal velocity component close to the bottom wall of the cell and as a global top-bottom asymmetry of the velocity field. In another study, Manga and Weerante[26] used corn syrup as working fluid in their experimental set-up at high Prandtl and Rayleigh numbers ($10^3 \leq Pr \leq 10^6$, $10^4 \leq Ra \leq 10^8$). Corn syrup exhibits a strict viscosity dependence on temperature. They found that at their largest Rayleigh number, $Ra = 10^8$, the Nusselt number (Nu) was lower than expected, based on an extrapolation of the Nu- Ra relationship determined at lower Rayleigh numbers. A similar experimental study was also performed by Zhang et al[27] in which glycerol was used as working fluid in a square cubic cell at higher Rayleigh numbers ($10^6 \leq Ra \leq 10^9$) and lower Prandtl numbers ($10^2 \leq Pr \leq 10^3$). They presented a simplified 2-D model for the mean centre temperature based on an equation for the thermal boundary layer and compared that with the experimental results.

The idea of applying variable properties as a separate class of non-Boussinesq approximation is continued in numerical simulations as well. For example, Zhang and Cao[28] investigated the non-Boussinesq effects of natural convection in a horizontal annulus with aspect ratio of 2.0 over $10^4 \leq Ra \leq 10^6$. They reported discrepancies among obtained solutions via different approaches of variable property-based lattice Boltzmann flux solver method as an influence of the non-Boussinesq effect that is induced by partial or total variations in fluid properties on the flow instability behaviors and heat transfer characteristics.

In the present study, the work of Lopez et al[24] informs the presentation of a new form of the governing equations based on the idea of considering density variations through both the advection term (capturing centrifugal effects) as well as the gravitational term in the momentum equations for natural convection problems. This formulation is implemented into a control volume finite-element method solver and results are investigated for local and average Nusselt number, entropy generation and skin friction in a horizontal concentric annulus cavity up to $Ra = 10^5$. The rest of the article is organized as follows: Section 2 presents the aforementioned formulation, Section 3 introduces the geometry of the problem and details numerical treatment including accuracy and mesh dependency. In Section 4, the mismatch between Boussinesq and non-Boussinesq approximations is scrutinized, and conclusions are drawn in Section 5.

2 | GOVERNING EQUATIONS AND PARAMETERS

Under the classical Boussinesq approximation for buoyancy, density differences are neglected except with respect to the gravity term, but as mentioned before, one approach to extend beyond the Boussinesq approximation is elaborated in Lopez et al,[24] in which the density variations are considered through the advection terms as well as the buoyancy term. In Lopez et al,[24] the density $\rho = \rho_0 + \rho'$ comprises a constant (ρ_0) and a perturbation part (ρ') that captures the temperature dependences, density variations due to fluid density stratification or density variations in a binary fluid with miscible species of different densities, and so on. This extension produces the modified governing momentum equation in the inertial frame for a Newtonian fluid,

$$\rho_0(\partial_t + u \cdot \nabla)\boldsymbol{u} = -\nabla p^* + \mu\nabla^2\boldsymbol{u} + \rho\boldsymbol{f} - \rho'\nabla\phi - \rho'(\boldsymbol{u} \cdot \nabla)\boldsymbol{u}. \tag{1}$$

Here a modified pressure is introduced as $p^* = p + \rho_0\phi$, where ϕ is the gravitational potential whose gradient opposes the gravitational acceleration vector, that is, . $\nabla\phi = -g\boldsymbol{e}_g$, where $\boldsymbol{e}_g$ is the unit vector in the direction of gravity. In addition, the term $\rho\boldsymbol{f}$ in Equation (1) accounts for additional body forces that may act on the fluid, but this is taken as zero throughout this study. Here buoyancy effects are also considered with respect to the advection term, but a unified density is used to derive the governing equations under the proposed approximation. Starting with the steady-state incompressible momentum equation in vector form,

$$\rho(\boldsymbol{u} \cdot \nabla)\boldsymbol{u} = -\nabla p + \mu\nabla^2\boldsymbol{u} + \rho g\boldsymbol{e}_g, \tag{2}$$

and dividing Equation (2) by the reference density, ρ_0, yields

$$\frac{\rho}{\rho_0}(\boldsymbol{u} \cdot \nabla)\boldsymbol{u} = -\frac{1}{\rho_0}\nabla p + \nu\nabla^2\boldsymbol{u} + \frac{\rho}{\rho_0}g\,\boldsymbol{e}_g. \tag{3}$$

Following the Boussinesq approach, only the first term of the density state relation is taken into account. Substituting the density state relation $\rho/\rho_0 = 1 - \beta\theta$ and the modified pressure into (3) yields

$$(\boldsymbol{u} \cdot \nabla)\boldsymbol{u} = -\frac{1}{\rho_0}\nabla p^* + \nu\nabla^2\boldsymbol{u} - \beta\theta g\boldsymbol{e}_g + \beta\theta(\boldsymbol{u} \cdot \nabla)\boldsymbol{u}. \tag{4}$$

Using dimensionless quantities

$$X = \frac{x}{L}, Y = \frac{y}{L}, U = \frac{uL}{\alpha}, P = \frac{p^*L^2}{\rho\alpha^2}, \Theta = \frac{\theta}{\Delta\theta} = \frac{T - T_0}{T_h - T_c}, \tag{5}$$

one can derive the dimensionless form of the momentum equation for natural convection problems,

$$(\boldsymbol{U} \cdot \nabla)\boldsymbol{U} = -\nabla P + Pr\nabla^2\boldsymbol{U} - RaPr\Theta\boldsymbol{e}_g + Ga\Theta(\boldsymbol{U} \cdot \nabla)\boldsymbol{U}. \tag{6}$$

Equation (6) introduces the Prandtl number $Pr = \nu/\alpha$ characterising the ratio of the molecular to thermal dissipation, and the Rayleigh number $Ra = g\beta\Delta\theta{L_{\text{ref}}}^3/\nu\alpha$ characterising the ratio of buoyancy to viscous and thermal dissipation. It also reveals the Gay-Lussac number ($Ga = \beta\Delta\theta$) in the last term on the right-hand side. We restrict ourselves to modest values of Ga to avoid unphysical (negative) density under the linear density-temperature state relation. The linear density-temperature state relation in terms of dimensionless temperature and Gay-Lussac number is expressed as

$$\frac{\rho}{\rho_0} = 1 - \beta\theta = 1 - \beta\Delta\theta\Theta = 1 - Ga\Theta. \tag{7}$$

Regarding the highest dimensionless temperature in the physical domain ($\Theta_h = 0.5$), the constraint $Ga < 2$, guaranties a physical value for density. Introduction of a Froude number characterising the ratio of inertia to gravity,

$$Fr = \frac{U_{ref}^2}{gL} = \frac{(\alpha/L)^2}{gL} = \frac{\alpha^2}{gL^3},$$

permits the Gay—Lussac parameter to be expressed as $Ga = \beta\Delta\theta = FrRaPr$, and thus

$$Fr = \frac{Ga}{RaPr}, \tag{8}$$

which has a maximum value of

$$Fr_{max} = \frac{2}{RaPr} \tag{9}$$

at each given Rayleigh and Prandtl number. Using Equation (8), Equation (6) becomes

$$(\boldsymbol{U}\cdot\nabla)\boldsymbol{U} = -\nabla P + Pr\nabla^2\boldsymbol{U} - RaPr\Theta(\boldsymbol{e}_g - Fr(\boldsymbol{U}\cdot\nabla)\boldsymbol{U}). \tag{10}$$

As can be seen, Equation (10) is consistent with the momentum equation under the Boussinesq approximation, except for the additional inertial buoyancy term on the right hand side. When expressed in this form, it is apparent that the action of this additional term is to modify the effective direction (and strength) of the gravity locally throughout the flow which is ignored in the conventional Boussinesq approximation. Indeed, regions which are experiencing higher spatial accelerations (described by $(\boldsymbol{U}\cdot\nabla)\boldsymbol{U}$) will experience deviations from the Boussinesq buoyancy approximation. The strength of these deviations relative to gravity is described by Fr, with $Fr \to 0$ (and $\beta\Delta\theta \to 0$) recovering the classical Boussinesq approximation.

The effect of Fr on the buoyancy-driven flow is investigated in Section 4. Thus, under the proposed approximation, the general form of the governing equations is expressed as

$$\begin{cases} \nabla\cdot\boldsymbol{U} = 0, \\ (\boldsymbol{U}\cdot\nabla)\boldsymbol{U} = -\nabla P + Pr\nabla^2\boldsymbol{U} - RaPr\Theta(\boldsymbol{e}_g - Fr(\boldsymbol{U}\cdot\nabla)\boldsymbol{U}), \\ (\boldsymbol{U}\cdot\nabla)\Theta = \nabla^2\Theta. \end{cases} \tag{11}$$

In this formulation, large values of Ga are not considered, which would necessitate its inclusion in other terms; instead it is shown that the effect on the flow is non-negligible through advection in certain situations, such as rapid rotation.[24] The present formulation generalizes the description of centrifugal effects both globally *and* locally, and about any axis.

For comparison, results are compared to natural convection simulations under the weakly compressible approximation.[29] In this approach, due to the small compressibility ratio (identified by Mach number) in natural convection problems, acoustic waves of the fully compressible form of the Navier-Stokes equations are filtered. This approach is also known as low Mach number scheme (LMS). Aside from filtering acoustic waves, the main feature of the LMS model is splitting the total pressure into a mechanical (local) pressure that acts in the momentum equation to balance the advection with buoyancy and diffusion, and a global thermodynamic pressure that is used to update density variations during the solution procedure. Paillere et al[30] compared results of the LMS model vs fully compressible Navier-Stokes equations for both small and large temperature differences (beyond the Boussinesq approximation) and showed that the LMS model can simulate natural convection with high fidelity and negligible differences compared to the hyperbolic compressible Navier-Stokes equations. The conservative form of the governing equations under the LMS approximation are[31]

$$\begin{cases} \frac{\partial\rho^*}{\partial t^*} + \nabla\cdot(\rho\boldsymbol{u}) = 0, \\ \frac{\partial(\rho^*\boldsymbol{u})}{\partial t^*} + \nabla\cdot(\rho^*\boldsymbol{u}\otimes\boldsymbol{u}) = -\nabla p^* + \rho^*\boldsymbol{e}_g + \nabla\cdot\boldsymbol{\tau}^*, \\ \rho^* c_p\left(\frac{\partial T}{\partial t^*} + \nabla\cdot(\boldsymbol{u}T)\right) = \kappa\nabla^2 T + \frac{\mathrm{d}p_{th}}{\mathrm{d}t}, \\ p_{th} = \rho^* RT. \end{cases} \tag{12}$$

Using the non-dimensionalizations

$$X=\frac{x}{L}, Y=\frac{y}{L}, \boldsymbol{U}=\frac{\boldsymbol{u}L}{\alpha}, P=\frac{p^{*}L^{2}}{\rho\alpha^{2}}, \Theta=\frac{T}{T_{0}}, \varepsilon=\frac{T_{h}-T_{c}}{2T_{0}}, P_{\mathrm{th}}=\frac{p_{th}}{p_{0}}, t=\frac{t^{*}L}{u}, Z=\frac{R}{R_{0}}, \rho=\frac{\rho^{*}}{\rho_{0}} \tag{13}$$

the dimensionless form of Equation (12) becomes[32]

$$\begin{cases} \frac{\partial\rho}{\partial t}+\nabla\cdot(\rho\boldsymbol{U})=0, \\ \frac{\partial(\rho\boldsymbol{U})}{\partial t}+\nabla\cdot(\rho\boldsymbol{U}\otimes\boldsymbol{U})=-\nabla P+\frac{RaPr}{2\varepsilon}\rho\boldsymbol{e}_{g}+Pr\nabla\cdot\boldsymbol{\tau}, \\ \frac{\partial(\rho\Theta)}{\partial t}+\nabla\cdot(\rho\boldsymbol{U}\Theta)=\nabla^{2}\Theta+\left(\frac{\eta-1}{\eta}\right)\frac{\mathrm{d}P_{\mathrm{th}}}{\mathrm{d}t}, \\ P_{\mathrm{th}}=Z\rho\Theta. \end{cases} \tag{14}$$

In Equation (14), Pr is the Prandtl number as defined earlier, η is the heat capacity ratio ($\eta=c_{p}/c_{v}$), and P_{th} is the global dimensionless thermodynamic pressure. In this study, we only present results for an ideal diatomic gas ($Z=1$). Also, $\boldsymbol{\tau}$ is the stress tensor given in dimensionless form by

$$\boldsymbol{\tau}=\nabla\boldsymbol{U}+(\nabla\boldsymbol{U})^{T}-2/3(\nabla\cdot\boldsymbol{U})\boldsymbol{I}. \tag{15}$$

In Equation (15), Stokes' hypothesis ($\lambda=-2/3\mu$) for bulk viscosity is used. In the compressible/weakly-compressible approach, the Rayleigh number is expressed slightly differently compared to the incompressible flow, as

$$Ra=Pr\frac{g{\rho_{0}}^{2}(T_{\mathrm{h}}-T_{\mathrm{c}})L^{3}}{T_{o}{\mu_{0}}^{2}}. \tag{16}$$

Comparing incompressible and compressible Rayleigh number definitions gives an interesting relation for Froude number,

$$\underbrace{2\varepsilon=(T_{\mathrm{h}}-T_{\mathrm{c}})/T_{o}}_{\text{Compressible}}=\underbrace{\beta\Delta\theta=RaPrFr}_{\text{Incompressible}}\rightarrow Fr=2\varepsilon/RaPr. \tag{17}$$

Equation (17) is an important relation that matches the Froude number corresponding to a given relative temperature difference at each Rayleigh and Prandtl number; it additionally demonstrates the required result for isobaric and isochoric thermal expansion in gases, whereby $\alpha=1/T_{0}$. Regarding the maximum possible relative temperature difference value of unity ($\varepsilon_{\max}=1$), the maximum physical Froude number at each Rayleigh and Prandtl number is equal to $2/RaPr$ ($Fr_{\max}=2/RaPr$), which is consistent with Equation (9) for the maximum non-Boussinesq parameter value.

3 | DESCRIPTION OF THE PROBLEM

In this study, the proposed model natural convection problem is the concentric horizontal annulus cavity portrayed in Figure 1. While the symmetry of the geometry naturally lends itself to the use of polar coordinates, the present formulation is developed in a Cartesian framework to permit future generalisation to arbitrary geometries. Boundary conditions are shown in Figure 1A. The inner and outer radii of the annulus are denoted by r_{i} and r_{o}, respectively, with aspect ratio fixed at $r_{o}/r_{i}=2.6$ consistent with published benchmark studies.[8,14,16-19] The region between the two cylinders is filled with air having $Pr=0.71$. The inner and outer cylinders are kept at constant temperatures T_{h} and T_{c}, respectively, with $T_{\mathrm{h}}>T_{\mathrm{c}}$. The reference length, $L_{\mathrm{ref}}=r_{o}-r_{i}$, is equal to the radial gap between the two cylinders. Simulations are carried out for Rayleigh numbers ranging from 10^{1} to 10^{5}, within the steady-state regime for this system.[10-14]

Once the values of the thermo-fluid parameters in the physical domain are obtained, the Nusselt number, entropy generation, and friction coefficient are determined. The local and average Nusselt numbers along the walls of the annulus cavity are obtained from

$$Nu_{\mathrm{loc}}=-\partial\Theta/\partial\widetilde{r}\big|_{\mathrm{wall}} \tag{18}$$

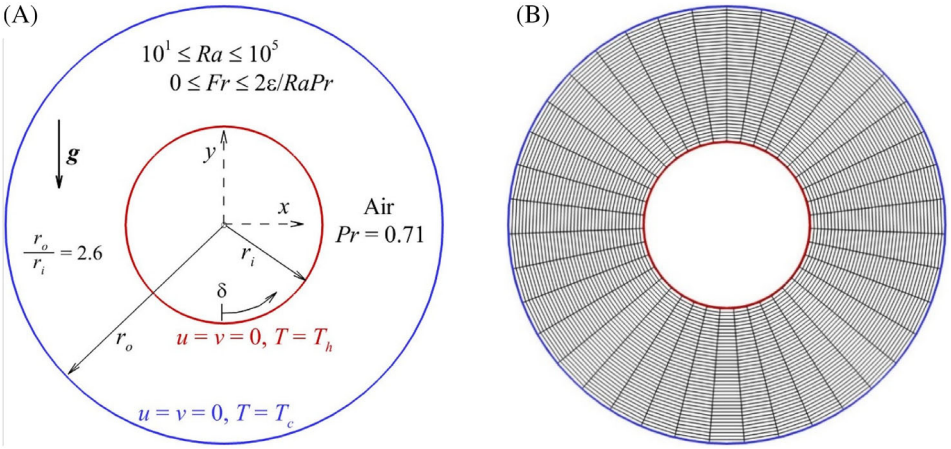

FIGURE 1 The concentric annulus of two circular cylinders. A, Schematic view and boundary conditions; B, A coarse computational grid having 40×40 computational nodes is shown for illustration purposes [Colour figure can be viewed at wileyonlinelibrary.com]

and

$$Nu_{\text{ave}} = \frac{1}{2\pi(r_i + r_o)}\left[\int_0^{2\pi r_o} Nu_{\text{loc},o}\,\mathrm{d}s + \int_0^{2\pi r_i} Nu_{\text{loc},i}\,\mathrm{d}s\right]. \tag{19}$$

The skin friction along the cylinder surfaces is related to the fluid flow via the gradient of the velocity components normal to the surface. In this study, the friction coefficient along the surface based on the dimensionless velocity is defined as

$$c_f = -\frac{\tau_w}{1/2\rho(\alpha/L)^2} = -2Pr\frac{\partial U_\delta}{\partial \boldsymbol{n}}\bigg|_{\text{wall}}. \tag{20}$$

In Equation (18), $\boldsymbol{n}$ is the unit normal vector to the surface. Since the governing equations are solved in a Cartesian coordinate system, the above fundamental definition is implemented through the 2D shear stress tensor as

$$\boldsymbol{c_f} = -2Pr\begin{bmatrix}\tau_{xx} & \tau_{xy}\\ \tau_{yx} & \tau_{yy}\end{bmatrix}\begin{bmatrix}n_x\\ n_y\end{bmatrix} = -2Pr\begin{bmatrix}2\partial U/\partial X & \partial U/\partial Y + \partial V/\partial X\\ \partial U/\partial Y + \partial V/\partial X & 2\partial V/\partial Y\end{bmatrix}\begin{bmatrix}n_x\\ n_y\end{bmatrix}, \tag{21}$$

where n_x and n_y are the horizontal and vertical components of the wall-normal vector, respectively. In this state, the friction coefficient magnitude is calculated as

$$c_f = \sqrt{(c_{f_x})^2 + (c_{f_y})^2} \tag{22}$$

where

$$c_{f_x} = -2Pr[(2\partial U/\partial X)n_x + (\partial U/\partial Y + \partial V/\partial X)n_y], \tag{23}$$

$$c_{f_y} = -2Pr[(\partial U/\partial Y + \partial V/\partial X)n_x + (2\partial V/\partial Y)n_y]. \tag{24}$$

The dimensionless local entropy generation due to heat transfer (S_θ) and fluid friction (S_ψ) are calculated as

$$S_\Theta = \left[\left(\frac{\partial \Theta}{\partial X}\right)^2 + \left(\frac{\partial \Theta}{\partial Y}\right)^2\right], \tag{25}$$

$$S_\psi = \chi\left[2\left\{\left(\frac{\partial U}{\partial X}\right)^2 + \left(\frac{\partial V}{\partial Y}\right)^2\right\} + \left(\frac{\partial U}{\partial Y} + \frac{\partial V}{\partial X}\right)^2\right], \tag{26}$$

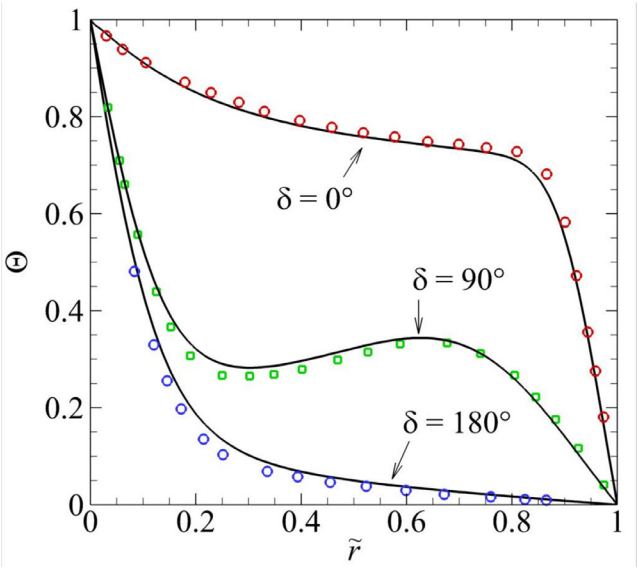

FIGURE 2 Comparison of profiles at $Ra = 5 \times 10^4$ and $Pr = 0.706$ using the present scheme (lines) and Kuhen and Goldstein[8] (symbols) at shown angles [Colour figure can be viewed at wileyonlinelibrary.com]

where in Equation (24), χ is the irreversibility distribution ratio related to the fluid friction irreversibility defined as

$$\chi = \frac{\mu T_0}{k}\left(\frac{\alpha}{L\Delta\theta}\right)^2. \tag{27}$$

The irreversibility distribution ratio assumed to be fixed and equal to 10^{-4} in this study. A similar value for χ was considered in References 33, 34. The total entropy generation due to heat transfer and fluid friction can be calculated by the summation of the local entropy generation over the physical domain via

$$S_{\Theta,\text{tot}} = \int_V S_\Theta \, \mathrm{d}v \tag{28}$$

and

$$S_{\psi,\text{tot}} = \int_V S_\psi \, \mathrm{d}v. \tag{29}$$

The relative dominance of entropy generation due to heat transfer and fluid friction is characterized by the average Bejan number (Be_{ave}), a dimensionless parameter defined as[35-37]

$$Be_{\text{ave}} = \frac{S_{\Theta,\text{tot}}}{S_{\Theta,\text{tot}} + S_{\psi,\text{tot}}}. \tag{30}$$

Values of $Be_{\text{ave}} > 0.5$ imply the dominance of the heat transfer irreversibility and $Be_{\text{ave}} < 0.5$ implies dominance of fluid friction irreversibility.

For the numerical solution of the governing equations, a control volume finite-element method (CVFEM) is used that implements the method of proper closure equation (MPCE)[38] and co-located variables. The problem is two-dimensional and steady. The advection terms are approximated by a second-order upwind scheme and the diffusion terms are discretized using a second order central differentiation scheme. Convergence criteria is considered as the maximum variation of the velocity and temperature fields over all nodes during two successive iterations less than 10^{-7}. Accurate performance of the developed solver has already been validated in References 39-46, but here it is evaluated by comparing the radial temperature profiles at three different angles including $\delta = 0^o$, 90^o, and 180° vs dimensionless radius ($\tilde{r} = r - r_i/r_o - r_i$) at $Ra = 5 \times 10^4$ for air with $Pr = 0.706$. Computed profiles are plotted in Figure 2 and are compared with the results of Kuhen and Goldstein.[8] A close agreement is observed.

TABLE 1 Comparison of the calculated average equivalent heat conductivities along the inner and outer cylinders to the available data

	Reference	$\overline{k}_{eq,i}$ (Error)	$\overline{k}_{eq,o}$ (Error)
$Ra = 10^3$	Kuhen and Goldstein[8]	1.081 (1.08%)	1.084 (1.08%)
	Ashrafizadeh and Nikfar[14]	1.082 (0.99%)	1.082 (1.26%)
	Najafi and Enjilela[16]	1.083 (0.89%)	1.093 (0.26%)
	Wu et al[17]	1.076 (1.54%)	1.087 (0.80%)
	Ho-Minh et al[18]	1.080 (1.17%)	1.079 (1.53%)
	Shu[19]	1.082 (0.99%)	1.082 (1.26%)
	Present Study	**1.092**	**1.095**
$Ra = 10^4$	Kuhen and Goldstein[8]	2.010 (0.65%)	2.005 (0.55%)
	Ashrafizadeh and Nikfar[14]	1.979 (0.89%)	1.980 (1.79%)
	Najafi and Enjilela[16]	2.022 (1.25%)	2.090 (3.66%)
	Wu et al[17]	1.998 (0.05%)	2.084 (3.36%)
	Ho-Minh et al[18]	1.967 (1.49%)	1.953 (3.13%)
	Shu[19]	1.979 (0.89%)	1.979 (1.84%)
	Present Study	**1.996**	**2.016**
$Ra = 5 \times 10^4$	Kuhen and Goldstein[8]	3.024 (0.90%)	2.973 (2.06%)
	Ashrafizadeh and Nikfar[14]	2.958 (1.29%)	2.960 (2.48%)
	Najafi and Enjilela[16]	2.932 (2.16%)	2.992 (1.43%)
	Ho-Minh et al[18]	2.946 (1.69%)	2.866 (5.58%)
	Shu[19]	2.958 (1.29%)	2.958 (2.55%)
	Present Study	**2.99**	**3.03**
$Ra = 7 \times 10^4$	Kuhen and Goldstein[8]	3.308 (2.10%)	3.226 (1.69%)
	Ashrafizadeh and Nikfar[14]	3.193 (1.44%)	3.196 (2.60%)
	Najafi and Enjilela[16]	3.208 (0.97%)	3.102 (5.47%)
	Ho-Minh et al[18]	3.182 (1.78%)	3.070 (6.44%)
	Present Study	**3.23**	**3.28**
$Ra = 10^5$	Ashrafizadeh and Nikfar[14]	3.462 (1.59%)	3.464 (1.47%)
	Najafi and Enjilela[16]	3.497 (0.59%)	3.419 (2.75%)
	Present Study	**3.518**	**3.516**

Accuracy of the solver is also evaluated by computing the equivalent inner cylinder conductivity, $\overline{k}_{eq,i}$, and the average equivalent outer cylinder conductivity, $\overline{k}_{eq,o}$, which are defined for the annulus cavity problem as

$$\overline{k}_{eq,i} = -\frac{\ln(\eta)}{2\pi(\eta-1)} \int_0^{2\pi} \left.\frac{\partial T}{\partial r}\right|_{r=r_i} d\delta, \tag{31}$$

$$\overline{k}_{eq,o} = -\frac{\eta \ln(\eta)}{2\pi(\eta-1)} \int_0^{2\pi} \left.\frac{\partial T}{\partial r}\right|_{r=r_o} d\delta. \tag{32}$$

Results of computed $\overline{k}_{eq,i}$ and $\overline{k}_{eq,o}$ are compared in Table 1 with data reported in References 8, 14, 16-19 at five different Rayleigh numbers. Calculated error percentages shows a pleasing agreement between the computational results and the available data.

A mesh dependency test was conducted, and it was found that a 181×181 computational grid achieves convergence of numerical computations to six significant figures for average Nusselt number. The mesh sensitivity analysis vs mesh

TABLE 2 Mesh sensitivity analysis at $Ra = 10^5$

No. radial nodes × No. axial nodes	$\overline{k}_{eq,i}$	$\overline{k}_{eq,o}$
91 × 91	3.489367	3.509973
121 × 91	3.509823	3.510798
151 × 121	3.517114	3.512402
181 × 151	3.518266	3.514339
181 × 181	3.518479	3.516452
361 × 361	3.518479	3.516452

refinement is presented in terms of inner and outer cylinder equivalent conductivities in Table 2. For illustration purposes, a lower-resolution mesh is shown in Figure 1B.

4 | RESULTS AND DISCUSSION

In this section, the results obtained using each of the classic Boussinesq approximation, proposed approximation and weakly compressible approach are presented. Throughout this study, Fr is altered between a small relative temperature difference representative of the Boussinesq case ($\varepsilon_B = 0.01$) and a large relative temperature difference beyond the validity of the Boussinesq approximation ($\varepsilon_{nB} = 0.2$). Both are computed by Equation (17) at a given Rayleigh and Prandtl number, that is, $2\varepsilon_B/RaPr \le Fr \le 2\varepsilon_{nB}/RaPr$, yielding a range $0.02/RaPr \le Fr \le 0.4/RaPr$ for Froude number. In all simulations reported in this article, the flows were consistently found to be symmetrical about the vertical centreline of the annulus. Also, for the investigated range of the Froude number and Rayleigh number ($10 \le Ra \le 10^5$), it is supposed that the flow field is 2D and stable. It is presently unknown when and how these flows bifurcate from the steady 2D solution branch. It would be interesting for future studies to elucidate the stability of this system.

To appreciate the role of the added term $RaPr\Theta(\,Fr(\boldsymbol{U}\cdot\nabla)\boldsymbol{U})$ in the momentum equation, simulations are conducted at $Ra = 10^5$ under the three models with $\varepsilon = 0.2$, with resulting thermo-flow fields shown in Figure 3. This corresponds to a Gay-Lussac parameter value of $Ga = \beta\Delta\theta = RaPrFr = 0.4$. The flow field corresponding to the proposed model can be seen to be slightly different at this ε from the Boussinesq solution in the upper half of the enclosure where natural convection is stronger. In the solution corresponding to the proposed model, the location of the maximum stream function has shifted slightly transversely away from the vertical centre-line. Comparing the stream-function fields in Figure 3A,B,D under the three approaches, the proposed method more closely resembles the weakly compressible result than the Boussinesq solution does. In addition, this similarity bears out in the temperature fields, particularly near the upper part of the inner cylinder, where the proposed method and weakly compressible approach exhibit a wider plume rising from the top of the inner cylinder.

Further insights into the action of the non-Boussinesq buoyancy effects may be gleaned by considering the acceleration field generated by the extra term in the momentum equation (ie, the right-most term in Equation (10). The magnitude of the non-Boussinesq acceleration field generated from the Boussinesq flow field (ie, $|\Theta((\boldsymbol{U}\cdot\nabla)\boldsymbol{U})|$) from Figure 3A is shown in Figure 3D. It shows that the non-Boussinesq accelerations are strongest at the base of the plume rising from the top of the inner cylinder, with weaker effects extending around the surface of the inner cylinder, within the plume approximately half-way between inner and outer cylinders, and near to the outer cylinder across the lower half of the domain. The magnitude of the field is close to zero in the lower regions of the cavity, which correspond to the regions of greatest similarity between the Boussinesq and non-Boussinesq cases compared in Figure 3A,B.

Finally, to understand the directionality of the action of the non-Boussinesq effect, "streamlines" (strictly, lines everywhere tangent to the acceleration vector field) of the non-Boussinesq acceleration field are plotted in Figure 3A. Notable features in this plot in the context of the distortion of the non-Boussinesq solution from its Boussinesq counterpart include the following: with the exception of the vertical centreline, the tangent lines near the inner cylinder point inward toward its surface, explaining the thinner thermal boundary layer in the non-Boussinesq case (Figure 3B); tangent lines exhibit a strong horizontal extension field approximately one-third of the distance from the top of the inner cylinder to the outer cylinder along the centreline, explaining the wider thermal plume seen in the non-Boussinesq case; above this location either side of the centreline the tangent lines point uniformly down and outward, explaining the greater spread of hotter fluid expelled by the plume near the top of the cavity in the non-Boussinesq case; tangent lines converge to a

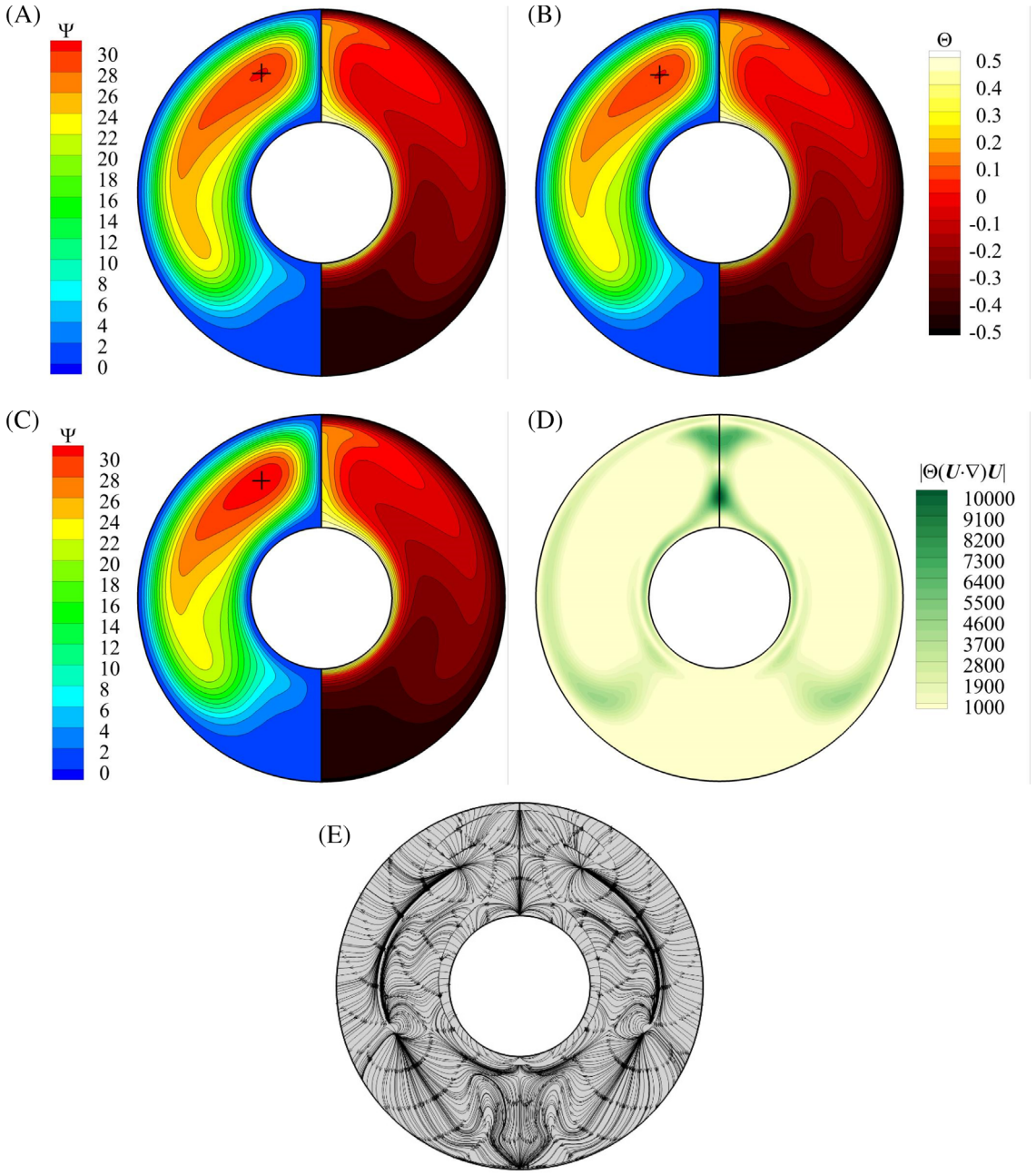

FIGURE 3 Results computed for $Pr = 0.71$, $Ra = 10^5$, and $\varepsilon = 0.2$, A, under the Boussinesq approximation; B, the proposed approximation with $Fr = 0.4/RaPr$, C, weakly compressible approach. Contours depict stream function (left half) and temperature (right half), and "+" identifies the point of maximum stream function. D, Magnitude of the acceleration vector field of the non-Boussinesq acceleration term, where light to dark shading denotes small to large magnitudes. E, "Streamlines" (lines everywhere tangent to the vector field) of the non-Boussinesq acceleration term [Colour figure can be viewed at wileyonlinelibrary.com]

sink at $(X, Y) \cong (\pm 0.53, 1.05)$ which is near to the location that the point of maximum stream-function shifts to in the non-Boussinesq case.

4.1 | Local Nusselt number

The local Nusselt number distribution along the inner cylinder is plotted in Figure 4. It should be noted that, to compensate for the different dimensionless temperature definitions between the weakly compressible and incompressible

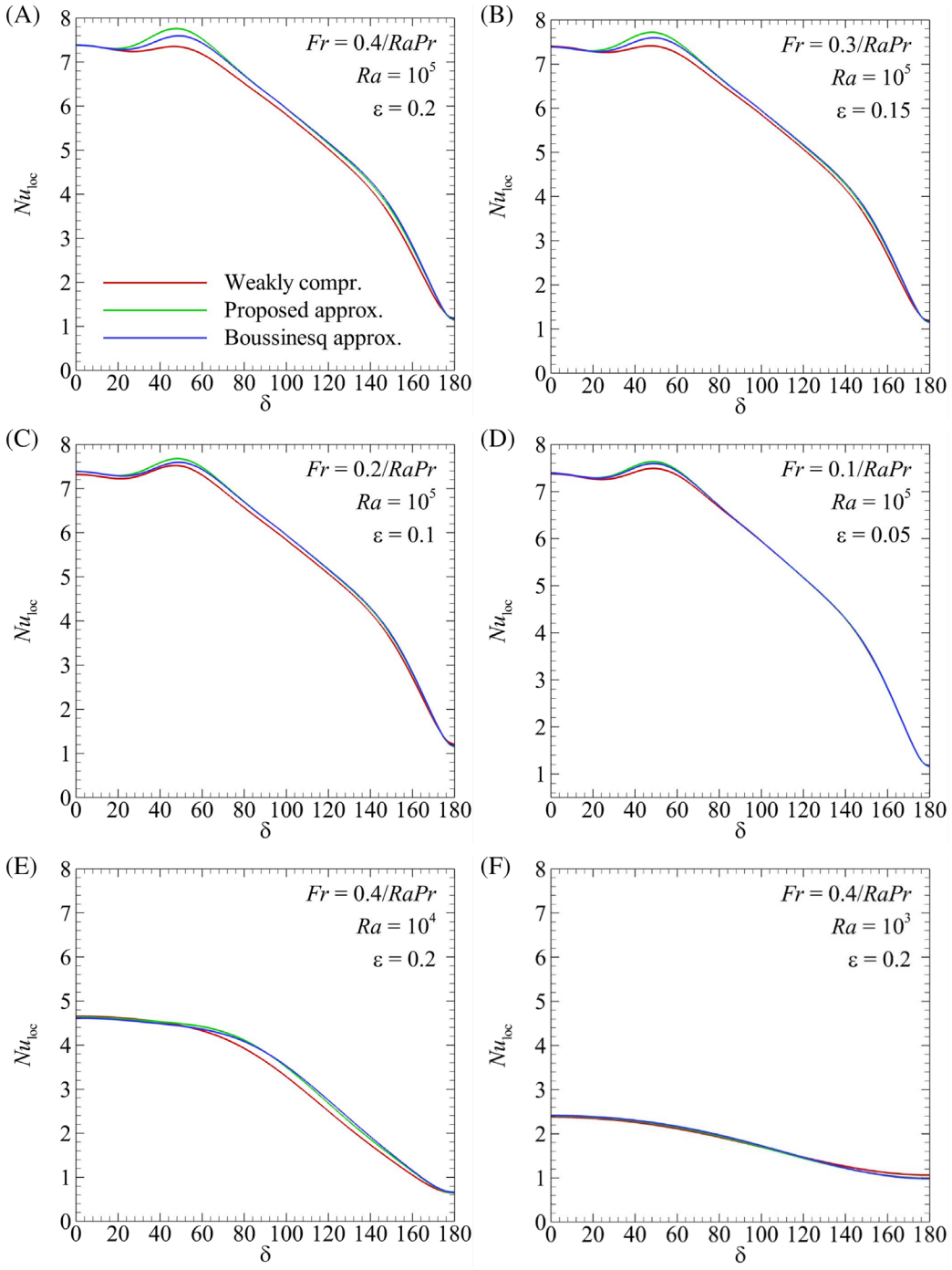

FIGURE 4 Local Nusselt number distribution along the inner cylinder for *Fr* values as stated, at $Pr = 0.71$ and, A-D, $Ra = 10^5$, E, $Ra = 10^4$, and F, $Ra = 10^3$ [Colour figure can be viewed at wileyonlinelibrary.com]

approaches, compressible Nusselt numbers are multiplied by $1/2\varepsilon$. Because of symmetry, only half of the local Nusselt number distribution is shown ($0^o \leq \delta \leq 180^o$). It was found that the mismatch of local Nusselt number distribution along both surfaces is negligible for Froude number lower than $0.1/RaPr$ ($\varepsilon = 0.05$) across the investigated range of the Rayleigh number for different approaches used in this study. Thus, for clarity, only the results of Froude number corresponding to $\varepsilon = 0.05$, 0.1, 0.15, and 0.2 are shown. For the inner cylinder, the local Nusselt number decreases from $\delta = 0^o$ to 180^o with a local peak at approximately $\delta = 50^o$. At $Ra = 10^5$, there is a considerable mismatch between computed local Nusselt number between the different approaches at Froude numbers corresponding to $\varepsilon = 0.15$ and 0.2 compared to lower Froude numbers throughout the range of angular positions. For these two Froude numbers, the local Nusselt number

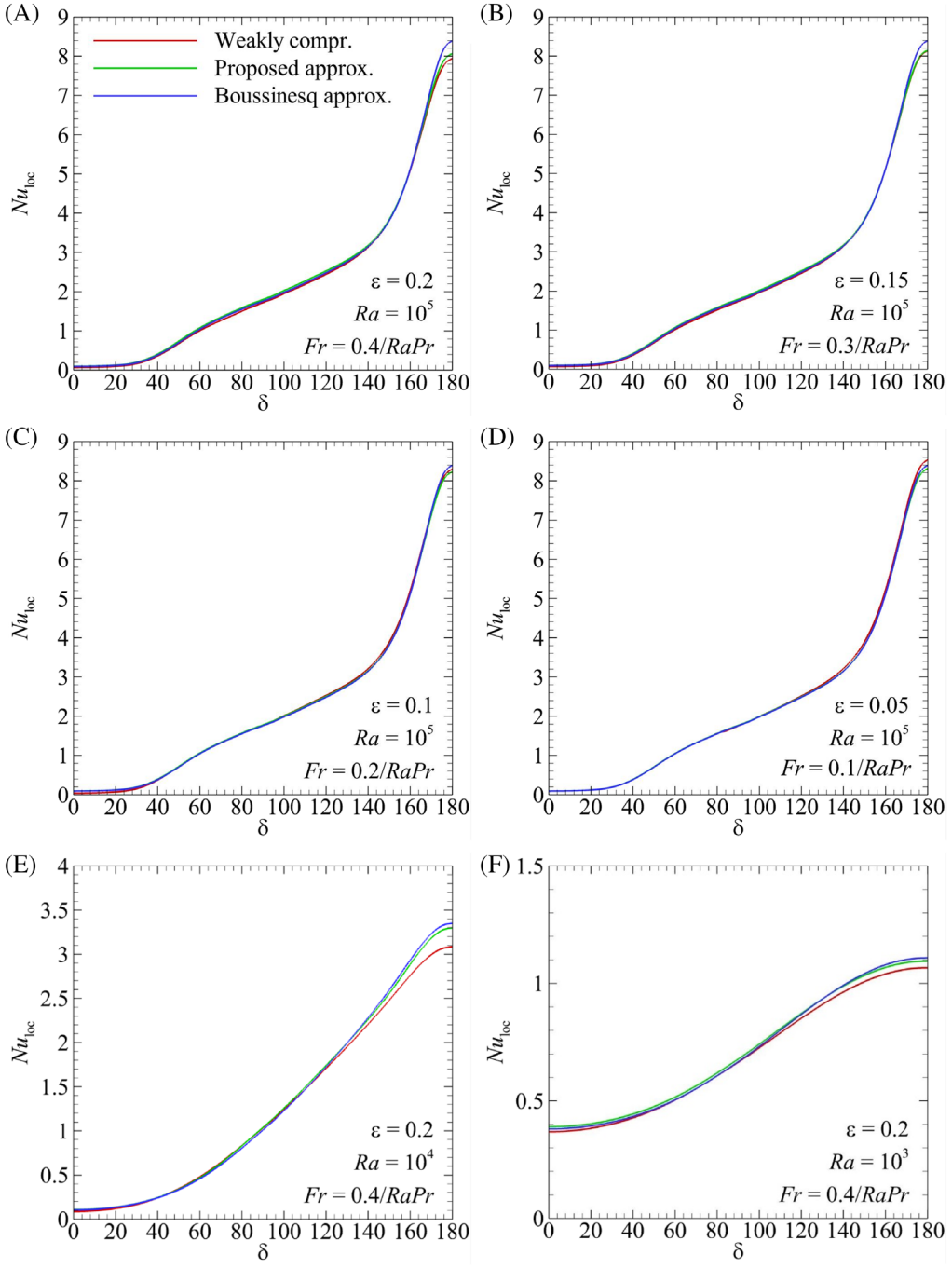

FIGURE 5 Local Nusselt number distribution along the outer cylinder for *Fr* values as shown, at $Pr = 0.71$ and, A-D, $Ra = 10^5$, E, $Ra = 10^4$, and, F, $Ra = 10^3$ [Colour figure can be viewed at wileyonlinelibrary.com]

distribution along the inner surface obtained with the weakly compressible approach shows a lower value compared to the Boussinesq and new approximations. As shown, calculated local Nusselt number distribution under the Boussinesq approximation shows less deviation from the weakly compressible approach compared to the proposed approximation. This may be attributed to the linear density state relation, which is designed for a Boussinesq case with small Gay-Lussac number ($Ga \leq 0.01$). We notice that for $\epsilon = 0.05$ both the Boussinesq and proposed approximations exhibit almost identical results to the weakly compressible approach in Figure 4D. Results from lower Rayleigh numbers, $Ra = 10^4$ and 10^3 (Figure 4E,F), show almost the same results for the three approaches used in this study even for large relative temperature difference applied in this study ($\epsilon = 0.2$), concluding that the effect of a large Gay-Lussac number is much important in convection dominated regimes in natural convection problems.

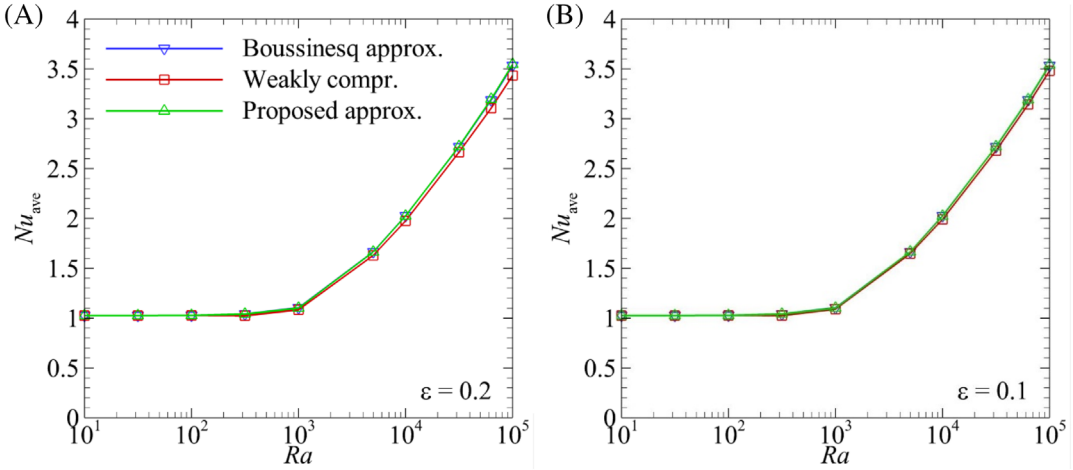

FIGURE 6 A plot of average Nusselt number against Rayleigh number for different ϵ values as shown [Colour figure can be viewed at wileyonlinelibrary.com]

Distribution of the local Nusselt number along the outer cylinder is shown in Figure 5. For the outer cylinder, the local Nusselt number increases from $\delta = 0^o$ to $\delta = 180^o$. Along this surface, distribution of the local Nusselt number for different ϵ are almost identical at $Ra = 10^5$ (Figure 5A-D). Regarding stronger natural convection along the inner hot wall where the plume forms, this negligible difference between different approaches may be attributed to the weaker natural convection effect along the outer cold cylinder. Decreasing by one order to $Ra = 10^4$ (Figure 5E), a deviation between weakly compressible and Boussinesq type approximations is formed that is annihilated by decreasing one extra order to $Ra = 10^3$ (Figure 5F). Results over $Fr \leq 0.1/RaPr$ (non-Boussinesq approximation) and $Fr = 0$ (Boussinesq approximation) yield almost the same results to the weakly compressible approach in the range of investigated Rayleigh numbers. Hence the results from small relative temperature differences are not presented here.

4.2 | Average Nusselt number

The variation in the average Nusselt number with Rayleigh number ($10 \leq Ra \leq 10^5$) for relative temperature differences $\epsilon = 0.2$ and 0.1 ($Fr = 0.4/RaPr$ and $Fr = 0.2/RaPr$, respectively) is plotted in Figure 6. In order to evaluate Equation (19), Simpson's 1/3rd rule of integration is used. As predicted, the average Nusselt number is increased by increasing the Rayleigh number. Across the computed range of Rayleigh number, obtained results for $Fr \leq 0.2/RaPr$ ($\epsilon = 0.1$) are giving similar results with a negligible difference between different approaches, which is why average Nusselt number results for $\epsilon < 0.1$ are not presented here. Figure 6 indicates that by increasing the Rayleigh number, the Boussinesq and proposed approximations start to deviate from the weekly compressible approach at around $Ra = 10^4$, where the heat transfer mechanism becomes convection dominated. Also, the difference between Boussinesq and proposed approximation across the investigated range of Rayleigh number is negligible at least up to $\epsilon = 0.2$. Both approximations show deviation from the weakly compressible approach in the convection dominated regime. Comparison of the average Nusselt number at $Ra = 10^5$ for $\epsilon = 0.2$ reveals a respective 3.25% and 2.89% mismatch between proposed and Boussinesq approximations compared to the weakly compressible approach. The slight deviation of obtained results via proposed approximation from weakly compressible in average Nusselt number at high Rayleigh number may be attributed to the linear definition of the density state relation, which is designed for small relative temperature difference.

4.3 | Skin shear stress

The next quantity to be considered is coefficient of friction over the surface of the cylinders. Results are shown for $10^3 \leq Ra \leq 10^5$ and $0.05 \leq \epsilon \leq 0.2$ in Figures 7 and 8 for the inner and outer cylinders, respectively. Since for $\epsilon \leq 0.05$ results of different approaches are hardly distinguishable, they are not presented here. For $Ra \leq 10^3$ where the heat transfer

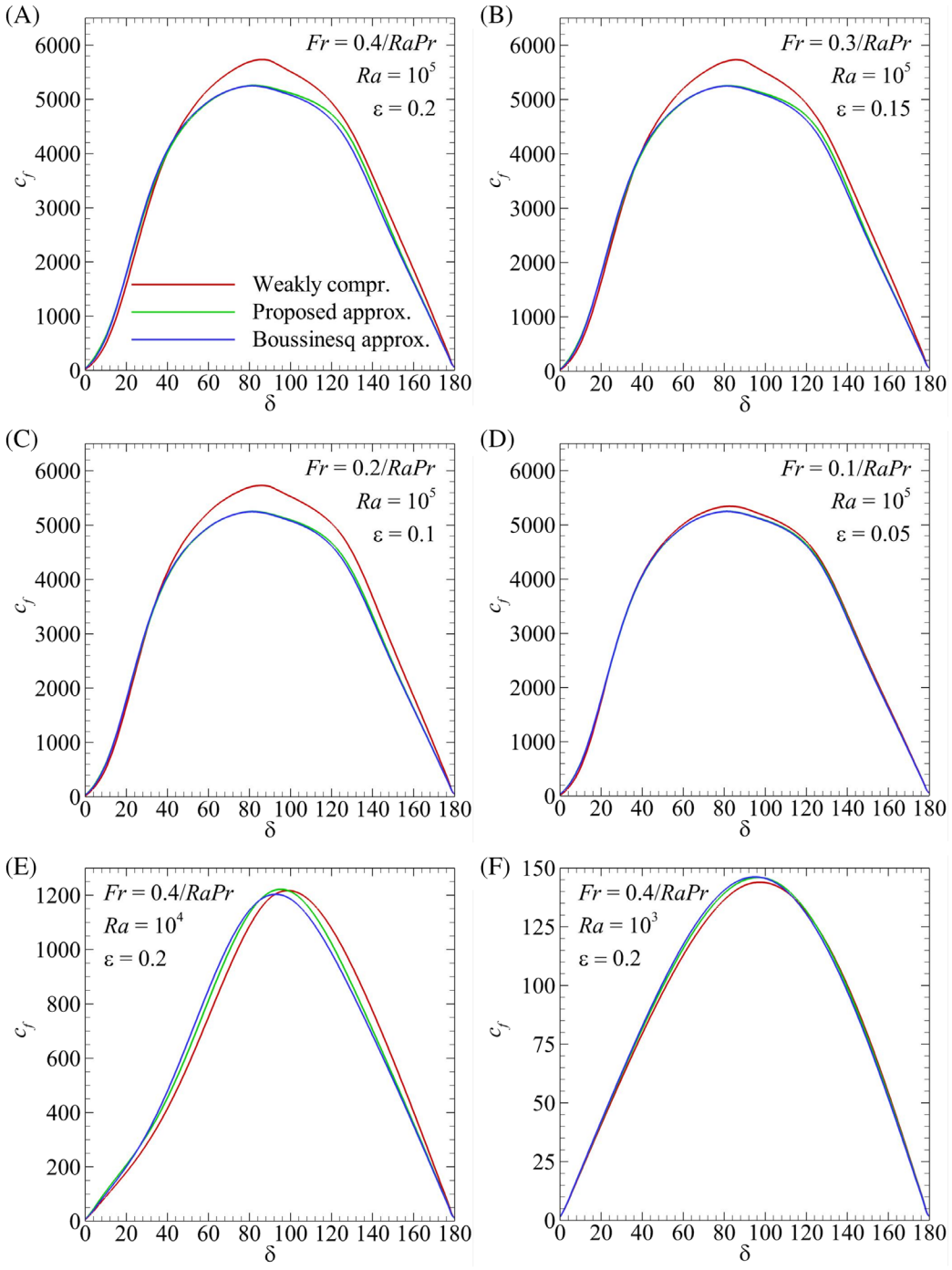

FIGURE 7 Skin friction coefficient distribution along the inner cylinder at stated *Fr* values and Rayleigh numbers, A-D, $Ra = 10^5$, E, $Ra = 10^4$, and, F, $Ra = 10^3$ [Colour figure can be viewed at wileyonlinelibrary.com]

is conduction dominated, results of the different approaches are almost identical even for large relative temperature differences. At $Ra \geq 10^4$, results of the Boussinesq and proposed approximation are not in agreement with the weakly compressible approach having $\varepsilon \geq 0.05$. A comparison of the coefficient of friction along the inner cylinder (Figure 7) reveals that the proposed approximation is giving slightly closer results to the weakly compressible approach compared to the Boussinesq approximation within the convection dominated regime (Figure 7A-D). Better performance of the proposed approximation in approximating flow field gradients becomes more evident for conduction dominated regime and large relative temperature difference (Figure 7E,F). Along the outer cylinder (Figure 8) aside from around $\delta \cong 10^o$ for convection dominated regime (Figure 8A-D), the proposed approximation is superior to the Boussinesq approximation in

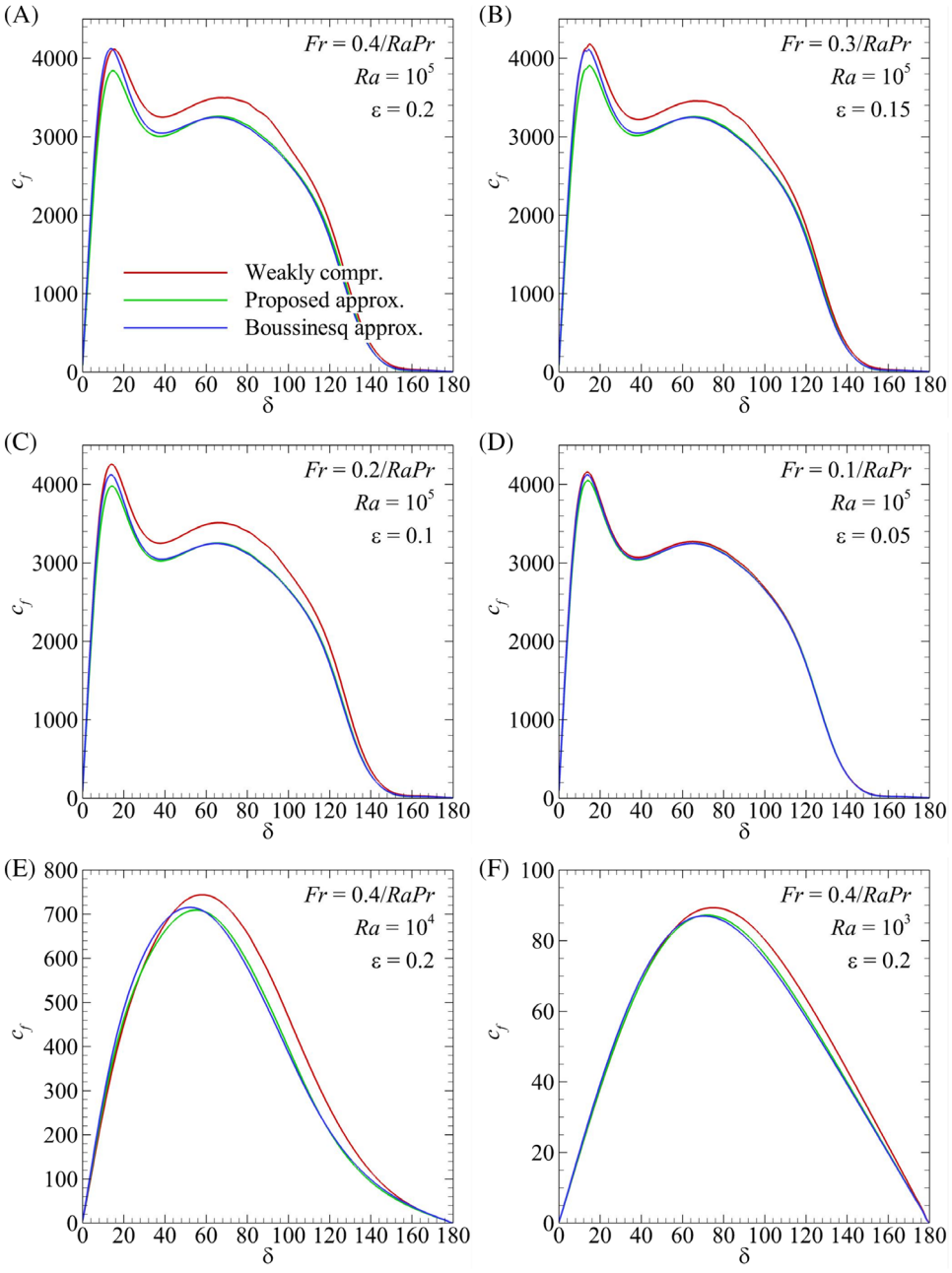

FIGURE 8 Skin friction coefficient distribution along the inner cylinder at stated *Fr* values and Rayleigh numbers, A-D, $Ra = 10^5$, E, $Ra = 10^4$, and, F, $Ra = 10^3$ [Colour figure can be viewed at wileyonlinelibrary.com]

estimating the flow field gradients. As with the inner cylinder, this is more clear as the convection effects diminish toward a conduction dominated regime especially at large ε values (Figure 7E,F). Flow-wise, better performance of the proposed approximation may be attributed to the extension of density variation to advection over the Boussinesq approximation.

4.4 | Entropy generation analysis

The dependence of the average Bejan number on the Rayleigh number will now be investigated over $10 \leq Ra \leq 10^5$ for $\varepsilon = 0.1$ and 0.2. As shown in Figure 9, by increasing the Rayleigh number, the average Bejan number is decreased. This is because by increasing the Rayleigh number, thermal convection increasingly becomes the dominant mechanism driving the flow, in turn producing thinner plum and thermal boundary layer structures, which in turn are subjected to irreversible heat transport via conduction along the steep thermal gradients. This is illustrated in the thermal fields in Figure 3. Notice the thinner thermal boundary layer on the inner cylinder and the stronger plume at $\varepsilon = 0.05$ vs $\varepsilon = 0.2$, which reflects the higher average Nusselt number (Figure 6) and lower Bejan number (Figure 9) seen at $Ra = 10^5$. Note

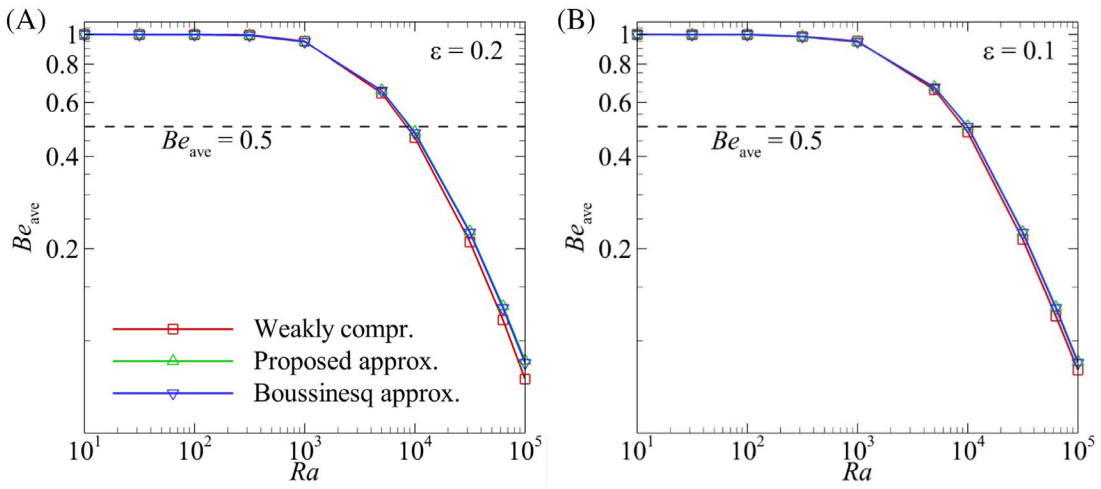

FIGURE 9 A plot of average Bejan number against Rayleigh number for two ε values as shown [Colour figure can be viewed at wileyonlinelibrary.com]

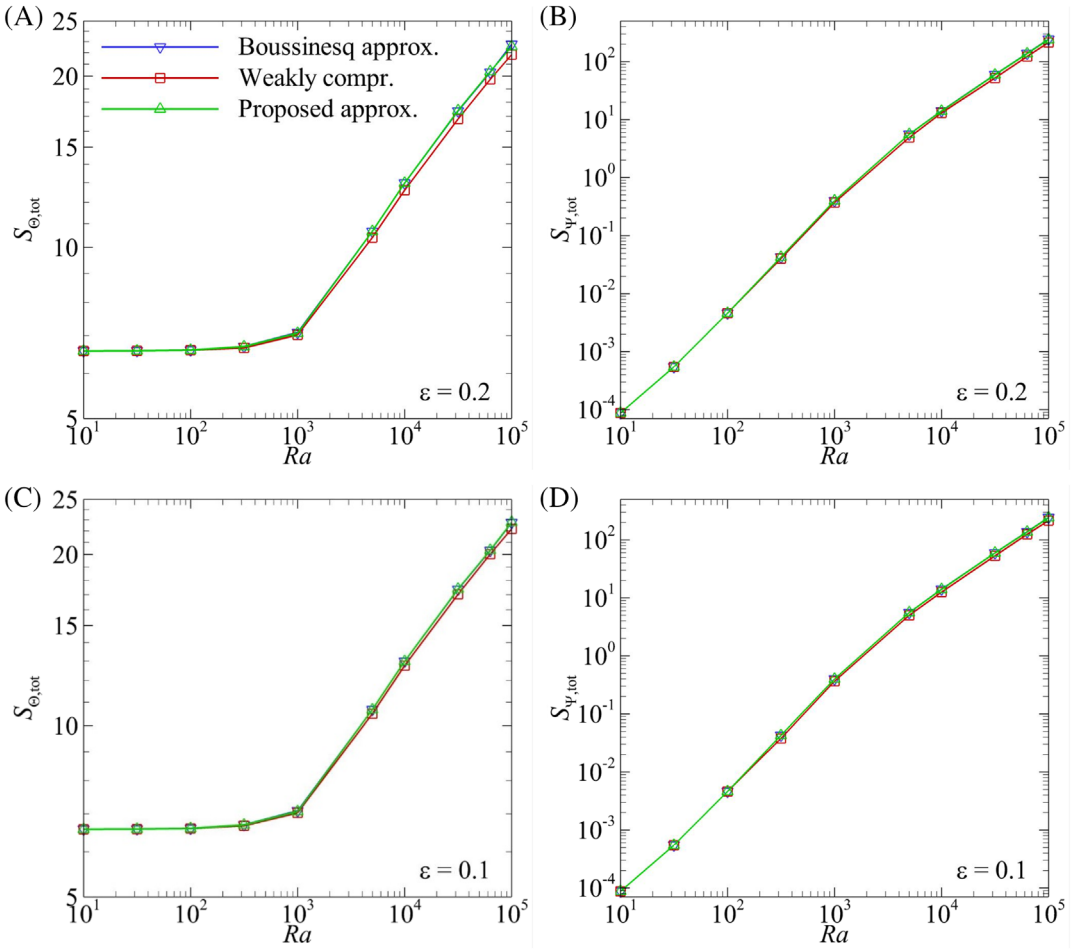

FIGURE 10 A plot of total entropy generation due to, A,C, heat transfer:$S_{\Theta,\,tot}$, B,D, fluid friction: $S_{\psi,\,tot}$ for two ε values as shown [Colour figure can be viewed at wileyonlinelibrary.com]

that, for $Ra > 10^4$, the average Bejan number is smaller than 0.5, which means that most of the irreversibility is due to convection heat transfer. For $Ra < 10^4$, where conduction is still the dominant mechanism, the average Bejan number has a value larger than 0.5, indicating that the majority of generated irreversibility is due to fluid friction.

Similar to the average Nusselt number, both the Boussinesq and proposed approximations show similar results up to $\varepsilon = 0.2$ with a negligible difference of order 10^{-3}. A noticeable mismatch between the Boussinesq type approaches and the weakly compressible approach is observed at $Ra = 10^5$. Obtained results demonstrate that the Boussinesq type approximations exhibit 6.47% and 14.93% higher values for $\varepsilon = 0.1$ and 0.2, respectively. This means that the non-Boussinesq effects have created a tendency for the flow to bias slightly toward fluid friction irreversibility rather than heat transfer irreversibility.

The rate of total entropy generation due to heat transfer ($S_{\Theta,\,\mathrm{tot}}$) and fluid friction ($S_{\psi,\,\mathrm{tot}}$) is also investigated separately over $10 \leq Ra \leq 10^5$ for $\varepsilon = 0.1$ and 0.2 in Figure 10. Irrespective of ε value, by increasing the Ryleigh number, the magnitude of both entropies is increased, but this is more evident for entropy generation due to fluid friction ($S_{\psi,\,\mathrm{tot}}$). As mentioned before, by increasing Rayleigh number, convection becomes the dominant part of the heat transfer mechanism and the share of conduction in heat transfer is decreased. This describes the continuing growth rate of entropy generation due to fluid friction in Figure 10B,D vs slow growth rate of entropy generation due to heat transfer in Figure 10A,C. In the range of investigated entropy generation up to $\varepsilon = 0.2$, the difference between Boussinesq type approximations is small, of order 10^{-3}. At $Ra = 10^5$ and $\varepsilon = 0.2$, a noticeable mismatch of 4.28% and 11.57% is observed for $S_{\Theta,\,\mathrm{tot}}$ and $S_{\psi,\,\mathrm{tot}}$, respectively.

5 | CONCLUSIONS

In this study, a new approximation is proposed for natural convention problems in Cartesian coordinates. In this formulation, Froude number is introduced, characterising deviation from the classic Boussinesq approximation. In addition, a relation is established that matches the Froude number to the relative temperature difference at a given Rayleigh and Prandtl number. The proposed formulation is applied to natural convection in a concentric horizontal annulus cavity with aspect ratio of 2.6 ($r_o/r_i = 2.6$) and results are compared in terms of the local and average Nusselt number, average Bejan number, and skin friction. Obtained results under the proposed approximation show a close agreement with the results under the Boussinesq and weakly compressible approach up to $\varepsilon = 0.05$ for this problem but as the relative temperature difference exceeds 0.05, the results from the different approximations start to deviate from each other, especially in the convection-dominated regime. Obtained results indicate that the proposed Boussinesq type model is superior in its capture of momentum, but is not necessarily better than the traditional Boussinesq approximation in its description of energy. In the context of the Gay-Lussac parameter, the present results demonstrate that the traditional Boussinesq approximation is accurate up to at least $\beta\Delta\theta = RaPrFr = O(10^{-2})$, with deviations being significant approaching values of order unity. It would, therefore, be expected that non-Boussinesq effects would be significant at higher Rayleigh numbers, small-scale systems, or for fluids having large thermal expansion coefficients. For example, ammonia and R-12 refrigerant dichlorodifluoromethane have $\beta \approx 2.5 \times 10^{-3}$ K^{-1} compared to water (2.14×10^{-4} K^{-1}), yielding Fr more than two orders of magnitude greater at the same scale. Finally, the proposed formula is applied here for the laminar regime and horizontal annulus cavity but its extension to turbulent regime and complex geometries is of interest for future studies.

ACKNOWLEDGEMENTS

This research was supported by the Australian Research Council through Discovery Projects DP150102920 and DP180102647. P. M. is supported by a Monash Graduate Scholarship and a Monash International Postgraduate Research Scholarship. The authors are also supported by time allocations on the National Computational Infrastructure (NCI) peak facility and the Pawsey Supercomputing Centre through NCMAS grants. NCI is supported by the Australian Government.

NOMENCLATURE

Be_{ave}	average Bejan number
c_f	skin friction coefficient
e_g	unit vector in gravity direction
Fr	Froude number
g	gravitational acceleration
Ga	Gay-Lussac number ($\beta\Delta\theta$)
L_{ref}	reference length

Nu_{ave}	average Nusselt number
Nu_{loc}	local Nusselt number
P	pressure
p^*	modified pressure
P	dimensionless pressure
P_{th}	thermodynamic pressure
Pr	Prandtl number
R	ideal gas constant
R	radius
r_i	inner cylinder radius
r_o	inner cylinder radius
$\widetilde{r}$	dimensionless radius
Ra	Rayleigh number
S	entropy generation
S_Θ	entropy generation due to heat transfer
S_ψ	entropy generation due to fluid friction
T	temperature
x	horizontal coordinate
X	dimensionless horizontal coordinate
y	vertical coordinate
Y	dimensionless vertical coordinate
$\boldsymbol{U}$	velocity vector
$\boldsymbol{U}$	dimensionless velocity vector
U_δ	angular dimensionless velocity vector
α	thermal diffusivity
β	volumetric thermal expansion coefficient
δ	angle along the cylinders
ϵ	relative temperature difference
θ	physical temperature
Θ	dimensionless temperature
κ	thermal conductivity
μ	kinematic dynamic viscosity
ν	kinematic viscosity
ρ	density
ρ_0	reference density
τ_w	wall shear stress
ϕ	gravitational potential
χ	irreversibility distribution ratio

SUBSCRIPT

ave	average
c	cool
h	hot
loc	local
ref	reference
tot	total

ORCID

Peyman Mayeli https://orcid.org/0000-0003-4084-2627

REFERENCES

1. Varol Y, Oztop HF. A comparative numerical study on natural convection in inclined wavy and flat-plate solar collectors. *Build Environ*. 2008;43(9):1535-1544. https://doi.org/10.1016/j.buildenv.2007.09.002.

2. Tonui JK, Tripanagnostopoulos Y. Improved PV/T solar collectors with heat extraction by forced or natural air circulation. *Renew Energy*. 2007;32(4):623-637. https://doi.org/10.1016/j.renene.2006.03.006.
3. Tonui JK, Tripanagnostopoulos Y. Performance improvement of PV/T solar collectors with natural air flow operation. *Sol Energy*. 2008;82(1):1-12. https://doi.org/10.1016/j.solener.2007.06.004.
4. Wells AJ, Worster MG. A geophysical-scale model of vertical natural convection boundary layers. *J Fluid Mech*. 2008;609:111-137. https://doi.org/10.1017/S0022112008002346.
5. Wettlaufer JS, Worster MG, Huppert HE. Natural convection during solidification of an alloy from above with application to the evolution of sea ice. *J Fluid Mech*. 1997;344:291-316. https://doi.org/10.1017/S0022112097006022.
6. Boussinesq J. *Theorie Analytique de la Chaleur, vol. II*. Gauthier-Villars; 1903.
7. Thomas RW, Davis GV. Natural convection in annular and rectangular cavities a numerical study. Paper presented at International Heat Transfer Conference 4, Paris-Versailies, France; 1970.
8. Kuhen TH, Goldstein RJ. An experimental and theoretical study of natural convection in the annulus between horizontal concentric cylinders. *J Fluid Mech*. 1976;74(4):695-719. https://doi.org/10.1017/S0022112076002012.
9. Sheremet MA, Pop I. Natural convection in a horizontal cylindrical annulus filled with a porous medium saturated by a nanofluid using Tiwari and Das' nanofluid model. *Eur Phys J Plus*. 2015;130:107 https://link.springer.com/article/10.1140/epjp/i2015-15107-4.
10. Sheremet MA, Pop I. Free convection in a porous horizontal cylindrical annulus with a nanofluid using Buongiorno's model. *Comput Fluids*. 2015;118:182-190. https://doi.org/10.1016/j.compfluid.2015.06.022.
11. Moukalled F, Acharya S. Natural convection in the annulus between concentric horizontal circular and square cylinders. *J Thermophys Heat Transf*. 1996;10(3):524-531. https://doi.org/10.2514/3.820.
12. Abu-Nada E, Masoud Z, Hijazi A. Natural convection heat transfer enhancement in horizontal concentric annuli using nanofluids. *Int Commun Heat Mass Transf*. 2008;35:657-665. https://doi.org/10.1016/j.icheatmasstransfer.2007.11.004.
13. Ashrafizadeh A, Nikfar M. On the numerical solution of generalized convection heat transfer problems via the method of proper closure equations–part I: description of the method. *Numer Heat Transf B*. 2016;70(2):187-203. https://doi.org/10.1080/10407782.2016.1173456.
14. Ashrafizadeh A, Nikfar M. On the numerical solution of generalized convection heat transfer problems via the method of proper closure equations–part II: application to test problems. *Numer Heat Transf B*. 2016;70(2):204-222. https://doi.org/10.1080/10407782.2016.1173467.
15. Ashorynejad HR, Mohamad AA, Sheikholeslami M. Magnetic field effects on natural convection flow of a nanofluid in a horizontal cylindrical annulus using lattice Boltzmann method. *Int J Therm Sci*. 2013;64:240-250. https://doi.org/10.1016/j.ijthermalsci.2012.08.006.
16. Najafi M, Enjilela V. Natural convection heat transfer at high Rayleigh numbers – extended meshless local Petrov–Galerkin (MLPG) primitive variable method. *Eng Anal Bound Elem*. 2014;44:170-184. https://doi.org/10.1016/j.enganabound.2014.01.022.
17. Wu YL, Liu GR, Gu YT. Application of meshless local Petrov-Galerkin (MLPG) approach to simulation of incompressible flow. *Numer Heat Transf B*. 2005;48(5):459-475. https://doi.org/10.1080/10407790500324763.
18. Ho-Minh D, Mai-Duy N, Tran-Cong T. A galerkin-RBF approach for the streamfunction-vorticity-temperature formulation of natural convection in 2D enclosured domains. *Comput Model Eng Sci*. 2009;44(3):219-248. https://doi.org/10.3970/cmes.2009.044.219.
19. Shu C. Application of differential quadrature method to simulate natural convection in a concentric annulus. *Int J Numer Methods Fluids*. 1999;30:977-993. https://doi.org/10.1002/(SICI)1097-0363(19990830)30:8%3C977::AID-FLD873%3E3.0.CO;2-J.
20. Pepper DW, Harris SD. Numerical simulation of natural convection in closed containers by a fully implicit method. *J Fluids Eng*. 1977;99(4):649-656. http://fluidsengineering.asmedigitalcollection.asme.org/article.aspx?articleid=1424151.
21. Vierendeels J, Merci B, Dick E. A multigrid method for natural convective heat transfer with large temperature differences. *J Comput Appl Math*. 2004;168(1–2):509-517. https://doi.org/10.1016/j.cam.2003.08.081.
22. Becker R, Braack M. Solution of a stationary benchmark problem for natural convection with large temperature difference. *Int J Therm Sci*. 2002;41(5):428-439. https://doi.org/10.1016/S1290-0729(02)01335-2.
23. Szewc K, Pozorski J, Tanière A. Modelling of natural convection with smoothed particle hydrodynamics: non-Boussinesq formulation. *Int J Heat Mass Transf*. 2011;54:4807-4816. https://doi.org/10.1016/j.ijheatmasstransfer.2011.06.034.
24. Lopez JM, Marques F, Avila M. The Boussinesq approximation in rapidly rotating flows. *J Fluid Mech*. 2013;737:56-77. https://doi.org/10.1017/jfm.2013.558.
25. Valori V, Elsinga G, Rhode M, Tummers M, Westerweel J, van der Hagen T. Experimental velocity study of non-Boussinesq Rayleigh-Bénard convection. *Phys Rev 95*. 2017;053113:1-12. https://journals.aps.org/pre/abstract/10.1103/PhysRevE.95.053113.
26. Manga M, Weeraratne D. Experimental study of non-Boussinesq Rayleigh–Bénard convection at high Rayleigh and Prandtl numbers. *Phys Fluids*. 1999;11:2969-2976. https://aip.scitation.org/doi/abs/10.1063/1.870156.
27. Zhang J, Childress S, Libchaber A. Non-Boussinesq effect: thermal convection with broken symmetry. *Phys Fluids*. 1997;9:1034-1042. https://doi.org/10.1063/1.869198.
28. Zhang Y, Cao Y. A numerical study on the non-Boussinesq effect in the natural convection in horizontal annulus. *Phys Fluids*. 2018;30:040902. https://doi.org/10.1063/1.5010864.
29. Paolucci S. On the filtering of sound from the Navier-Stokes equations, Technical report, Sandia National Laboratories. *SAND*. 1982;9:82-8257.
30. Paillere H, Viozat C, Kumbaro A, Toumi I. Comparison of low Mach number models for natural convection problems. *Heat Mass Transf*. 2000;36:567-573. https://doi.org/10.1007/s002310000116.
31. Le Quéré P, Weisman C, Paillère H, et al. Modelling of natural convection flows with large temperature differences: a benchmark problem for low Mach number solvers. Part 1. Reference solutions. *ESAIM: Math Model Numer Anal*. 2005;39(3):609-616. https://doi.org/10.1051/m2an:2005027.

32. Chenoweth DR, Paolucci S. Natural convection in an enclosed vertical air layer with large horizontal temperature differences. *JFM*. 1986;169:173-210. https://doi.org/10.1017/S0022112086000587.
33. Basak T, Kaluri RS, Balakrishnan AR. Effects of thermal boundary conditions on entropy generation during natural convection. *Numer Heat Transf A*. 2011;59(5):372-402. https://doi.org/10.1080/10407782.2011.549075.
34. Ilis GG, Mobedi M, Sunden B. Effect of aspect ratio on entropy generation in a rectangular cavity with differentially heated vertical walls. *Int Commun Heat Mass Transf*. 2008;35(6):696-703. https://doi.org/10.1016/j.icheatmasstransfer.2008.02.002.
35. Bondareva NS, Sheremet MA, Oztop HF, Abu-Hamdeh N. Entropy generation due to natural convection of a nanofluid in a partially open triangular cavity. *Adv Powder Technol*. 2017;28:244-255. https://doi-org.ezproxy.lib.monash.edu.au/10.1016/j.apt.2016.09.030.
36. Sheremet MA, Pop I, Oztop HF, Abu-Hamdeh N. Natural convection of nanofluid inside a wavy cavity with a non-uniform heating: entropy generation analysis. *Int J Numer Methods Heat Fluid Flow*. 2017;27:958-980. https://doi.org/10.1108/HFF-02-2016-0063.
37. Astanina MS, Sheremet MA, Oztop HF, Abu-Hamdeh N. MHD natural convection and entropy generation of ferrofluid in an open trapezoidal cavity partially filled with a porous medium. *Int J Mech Sci*. 2018;136:493-502. https://doi.org/10.1016/j.ijmecsci.2018.01.001.
38. Ashrafizadeh A, Alinia B, Mayeli P. A new co-located pressure-based discretization method for the numerical solution of incompressible Navier-Stokes equations. *Numer Heat Transf B: Fundament*. 2014;67(6):563-589. https://doi.org/10.1080/10407790.2014.992094.
39. Mayeli P, Nili-Ahmadabadi M, Pirzadeh MR, Rahmani P. Determination of desired geometry by a novel extension of ball spine algorithm inverse method to conjugate heat transfer problems. *Comput Fluids*. 2017;154:390-406. https://doi.org/10.1016/j.compfluid.2016.05.022.
40. Hesami H, Mayeli P. Development of the ball-spine algorithm for the shape optimization of ducts containing nanofluid. *Numer Heat Transf A*. 2016;70(12):1371-1389. https://doi.org/10.1080/10407782.2016.1243976.
41. Nikfar M, Mayeli P. Surface shape design in different convection heat transfer problems via a novel coupled algorithm. *ASME: J Heat Transf*. 2018;140(2):1-15. http://heattransfer.asmedigitalcollection.asme.org/article.aspx?articleid=2648964.
42. Mayeli P, Hesami H, Moghaddam MHDF. Numerical investigation of the MHD forced convection and entropy generation in a straight duct with sinusoidal walls containing water-Al_2O_3 nanofluid. *Numer Heat Transf A*. 2017;71(12):1371-1389. https://doi.org/10.1080/10407782.2016.1243976.
43. Mayeli P, Hesami H, Besharati-Foumani H, Niajalili M. Al_2O_3-water nanofluid heat transfer and entropy generation in a ribbed channel with wavy in the presence of magnetic field. *Numer Heat Transf A*. 2018;73(9):604-623. https://doi.org/10.1080/10407782.2018.1461494.
44. Nikfar M, Ashrafizadeh A, Mayeli P. Inverse shape design via a new physical-based iterative solution strategy. *Inverse Probl Sci Eng*. 2015;23(7):1138-1162. https://doi.org/10.1080/17415977.2014.973873.
45. Mayeli P, Nili-Ahmadabadi M, Besharati-Foumani H. Inverse shape design for heat conduction problems via the ball spine algorithm. *Numer Heat Transf B: Fundament*. 2016;69(3):249-269. https://doi.org/10.1080/10407790.2015.1096690.
46. Mayeli P, Nikfar M. Temperature identification of a heat source in conjugate heat transfer problems via an inverse analysis. *Int J Numer Methods Heat Fluid Flow*. 2019;29(10):3994-4010. https://doi.org/10.1108/HFF-05-2018-0193.

How to cite this article: Mayeli P, Sheard GJ. A centrifugal buoyancy formulation for Boussinesq-type natural convection flows applied to the annulus cavity problem. *Int J Numer Meth Fluids*. 2021;93:683–702. https://doi.org/10.1002/fld.4904

Received: 24 November 2020 | Revised: 27 February 2021 | Accepted: 28 February 2021

DOI: 10.1002/fld.4980

RESEARCH ARTICLE

WILEY

Natural convection and entropy generation in square and skew cavities due to large temperature differences: A Gay–Lussac-type vorticity stream-function approach

Peyman Mayeli | **Gregory J. Sheard**

Department of Mechanical and Aerospace Engineering, Monash University, Melbourne, Victoria, Australia

Correspondence
Peyman Mayeli, Department of Mechanical and Aerospace Engineering, Monash University, Melbourne, Vic 3800, Australia.
Email: peyman.mayeli@monash.edu

Funding information
Pawsey Supercomputing Centre through NCMAS; National Computational Infrastructure (NCI); Monash International Postgraduate Research Scholarship; Monash Graduate Scholarship; Australian Research Council through Discovery Projects, Grant/Award Numbers: DP180102647, DP150102920

Abstract

In this study, a benchmark natural convection problem is studied under a Gay–Lussac-type approximation incorporating centrifugal effects in the context of a new vorticity-stream-function approach. This approximation differs from the classic Boussinesq approximation in that density variations are considered in the advection term as well as the gravity term in the momentum equations. Such a treatment invokes Froude number as a non-Boussinesq parameter deviating results from the classic Boussinesq approximation. It is also shown how the Gay–Lussac parameter may be expressed by its equivalent relative temperature difference. Numerical simulation of natural convection in square and skewed cavities are performed up to $Ra = 10^6$ and $\varepsilon = 0.3$ at $Pr = 0.71$. Results obtained with new approximation are compared against the weakly compressible approach and the conventional Boussinesq approximation in terms of the average and local Nusselt number, coefficient of friction and entropy generation. Comparing the local Nusselt number indicates a negligible difference between Gay–Lussac type and the Boussinesq approximations even at a high relative temperature difference, with both deviating from the weakly compressible approach. Comparing coefficient friction results obtained by the Gay–Lussac-type approximation against the weakly compressible approach confirms superior numerical data in some regions of the physical domain with less deviation for rotating flows in comparison with the Boussinesq approximation. Finally, comparing the computational cost of the numerical simulation shows at least 8% less computational cost when governing equations are solved via secondary variables using a central scheme rather than primitive variables.

KEYWORDS

Gay–Lussac approximation, non-Boussinesq approximation, rotating flows, vorticity stream-function, weakly compressible approach

1 | INTRODUCTION

Traditionally, the Boussinesq approximation[1] is adopted for the numerical simulation of the natural convection problems. The simplicity of ignoring density variations except in buoyancy term and treating the flow field as incompressible while its existence is due to density variations makes the classic Boussinesq approximation popular.[2-15] Another advantage of the Boussinesq approximation that justifies its application for a broad range of the natural convection simulations is its simple implementation and accuracy of performance for problems having small temperature differences. The Boussinesq approximation, accompanied by a linear relation between density and temperature via a volumetric thermal expansion coefficient, is the basis of many numerical simulations of natural convection benchmark problems such as rectangular,[2-7] triangular[8-11] and annular[12-14] enclosed geometries.

The classic Boussinesq approximation is established based on a fundamental assumption of small density variations. Indeed, the Boussinesq approximation yields accurate results while density variations are small, whereas applying the Boussinesq approximation on cases that are featuring large density variations produces inaccurate results.[15] Such a situation may take place in foundry processes, astrophysical magnetohydrodynamic simulations[16] or solar collector systems.[17] Numerical techniques that seek to circumvent the limitations of the Boussinesq approximation are less abundant in the literature. Generally speaking, two classes of remedy are proposed to avoid the Boussinesq approximation for numerical simulation of the natural convection problems.

The first class of approaches applies the concept of compressibility that leads to introduction of the Mach number and fully compressible treatment of the Navier–Stokes equations, including acoustic waves. This strategy is seldom used for natural convection simulations due to instability caused by the small order of the compressibility ratio for density-based compressible flow solvers; examples include Vierendeels et al.,[18] Fu et al.,[19] Busto et al.,[20] and Bermúdez et al..[21] Since the order of compressibility in the natural convection problems is small, numerical simulations in this area are confined to small Mach numbers. This motivated the use of the low Mach number scheme (LMS) or weakly compressible approach. Under the LMS approximation developed by Paulucci,[22] acoustic waves are removed from the governing equation and total pressure is split into two main parts; a global (uniform) thermodynamic pressure which is obtained from the equation of state and used for updating the density variations through the solution procedure, and a local pressure which acts in the momentum equations to establish a balance among advection, buoyancy and diffusion terms. Vierendeels et al.[23] and Becker and Braack[24] employed this technique for numerical simulation of the square cavity benchmark problem with large temperature differences beyond the validity of the Boussinesq approximation.

The second class of approaches are developed in the context of the incompressible treatment of the governing equations. One such strategy is the Gay–Lussac approach, which is developed based on retaining density variations wherever density appears in the governing equations, that is, continuity and the advection/convection terms of the momentum and energy equations, respectively. Such a treatment leads to the introduction of the Gay–Lussac parameter as a product of the volumetric thermal expansion coefficient and the reference temperature difference ($\mathrm{Ga} = \beta\Delta\theta$). Under the Gay–Lussac approach, a prefactor of $(1 - \mathrm{Ga}\Theta)$ acts as a modifier on the aforementioned terms in the governing equations. The strength of this prefactor and its modification effect becomes stronger by increasing the temperature differences and consequently the Gay–Lussac parameter. It can be also shown that the Boussinesq approximation is recovered as $\mathrm{Ga} \to 0$. Pesso and Piva[25] used this strategy for the square cavity benchmark problem with large density variations. Recently, a Gay–Lussac-type approach was proposed by Lopez et al.[26] for the treatment of rapidly rotating flows, in which density variations were extended only to the centrifugal part of the advection term to capture centrifugal effects arising from background rotation in those rapidly rotating flows. Mayeli and Sheard[27] continued this approach and showed that the Gay–Lussac number may be expressed in terms of Rayleigh, Prandtl, and Froude numbers ($\mathrm{Ga} = \mathrm{RaPrFr}$) with a maximum $\mathrm{Ga}_{\max} = 2$ required to avoid an unphysical (negative) density value. Such a constraint confines the maximum physical value of the Froude number at each Rayleigh and Prandtl number to $2/\mathrm{RaPr}$ ($\mathrm{Fr}_{\max} = 2/\mathrm{RaPr}$). The study established a relation for the Gay–Lussac approach between the Froude number and the corresponding relative temperature difference (ϵ) at each Ra and Pr as $\mathrm{Fr} = 2\epsilon/\mathrm{RaPr}$.

Another incompressible-based strategy to go beyond the Boussinesq approximation is considering nonlinear terms via retention of higher terms (e.g., square and cubic terms) of the density state relation, thus extending the applicable temperature-range. Another justification of applying nonlinear density state relation comes from strange behavior of some fluids like water at temperatures close or equal to the temperature of maximum density. In this situation, the linear density state relation may not be valid anymore even for small temperature differences. For instance, the density–temperature relationship of cool water in the vicinity of 4°C does not obey a linear function. This strategy was used by Osorio et al.[28] for natural convection of water near its density inversion in an inclined square cavity.

In the Boussinesq approximation, properties of the working fluid are treated as constants, so the idea of applying variable properties (often as a function of temperature) is considered as a separate class of approximations beyond the Boussinesq approximation. However, in this approach, fundamentals of the original Boussinesq approximation are still applied. Many works have been conducted comparing this approach to the standard constant-property Boussinesq approximation. Souza et al.[29] is one example, in which all properties of the working fluid including viscosity, thermal conductivity, and heat capacity were varied as functions of temperature in a square cavity benchmark problem. They found that thermal conductivity and dynamic viscosity are the properties most sensitive to temperature variations.

In this paper, the approach of Lopez et al.[26] is adapted to a secondary-variables vorticity stream-function formulation, which is then applied to the square cavity problem. Skewed cavities are also considered for the stronger local rotations that may be invoked in the tighter corner regions. For comparison, this approximation is compared to simulations under the LMS and Boussinesq approximations, and results are compared in terms of the local and average Nusselt number, coefficient friction and entropy generation. The rest of the paper is organized as follows: Section 2 presents the aforementioned Gay–Lussac-type formulation and the LMS approximation, Section 3 introduces the geometry and boundary conditions of the problem and numerical considerations including accuracy and mesh dependency. Section 4 compares the results obtained using the three approximations, and conclusions are drawn in Section 5.

2 | GOVERNING EQUATIONS

Under the Boussinesq approximation,[1] density variations are ignored except with in the gravity term. As mentioned before, this leads to inaccurate results for problems with large density differences.[15] As mentioned earlier, a Gay–Lussac-type approach is possible through extension of density variations to the advection term of the momentum equations. In Lopez et al.,[26] the density comprises a constant (ρ_0) and a perturbation part (ρ') that captures the temperature dependences, density variations due to fluid density stratification or density variations in a binary fluid with miscible species of different densities and etc ($\rho = \rho_0 + \rho'$). Extending this decomposition from the gravity term to the full advection term produces the modified governing momentum equation in the inertial frame for a Newtonian fluid,

$$\rho_0(\partial_t + \boldsymbol{u}\cdot\nabla)\boldsymbol{u} = -\nabla p^* + \mu\nabla^2\boldsymbol{u} + \rho\boldsymbol{f} - \rho'\nabla\phi - \rho'(\boldsymbol{u}\cdot\nabla)\boldsymbol{u}. \tag{1}$$

In Equation (1), p^* is modified pressure defined as $p^* = p + \rho_0\phi$, where ϕ is the gravitational potential whose gradient opposes the gravitational acceleration vector, that is, $\nabla\phi = -g\boldsymbol{e}_g$, where $\boldsymbol{e}_g$ is the unit vector in the direction of gravity ($\boldsymbol{e}_g = \boldsymbol{g}/|\boldsymbol{g}|$). In addition, the term $\rho\boldsymbol{f}$ in Equation (1) accounts for additional body forces that may act on the fluid. Mayeli and Sheard[27] applied the same concept on the momentum equation but they used a unified definition for density. The dimensional form of the steady-state momentum equation divided by a reference density (ρ_0) in the absence of any additional body force is expressed as follows

$$(\rho/\rho_0)(\boldsymbol{u}\cdot\nabla)\boldsymbol{u} = -\frac{1}{\rho_0}\nabla p^* + \nu\nabla^2\boldsymbol{u} + (\rho/\rho_0)g\boldsymbol{e}_g. \tag{2}$$

Under the considered Gay–Lussac-type approximation, density variations are extended to the advection terms as well as gravity term. Using a linear density state equation ($\rho/\rho_0 = 1 - \beta\theta$) derived from volumetric thermal expansion coefficient definition, the momentum equation may be rewritten as follows,

$$(\boldsymbol{u}\cdot\nabla)\boldsymbol{u} = -\frac{1}{\rho_0}\nabla p^* + \nu\nabla^2\boldsymbol{u} - \beta\theta g\boldsymbol{e}_g + \beta\theta(\boldsymbol{u}\cdot\nabla)\boldsymbol{u}. \tag{3}$$

In Equation (3), a modified pressure is used which is defined as $p^* = p + \rho_0\phi$, where ϕ is the gravitational potential whose gradient opposes the gravitational acceleration vector, that is, $\nabla\phi = -g\boldsymbol{e}_g$, where $\boldsymbol{e}_g$ is the unit vector in the direction of gravity ($\boldsymbol{e}_g = \boldsymbol{g}/|\boldsymbol{g}|$). Using dimensionless quantities

$$\boldsymbol{X} = \frac{\boldsymbol{x}}{L_{\text{ref}}}, \boldsymbol{U} = \frac{\boldsymbol{u}L_{\text{ref}}}{\alpha}, P = \frac{p^*{L_{\text{ref}}}^2}{\rho_0\alpha^2}, \Theta = \frac{\theta}{\Delta\theta} = \frac{T - T_0}{T_h - T_c}, \tag{4}$$

one can derive the dimensionless form of the momentum equation for natural convection problems as follows.[25]

$$(\boldsymbol{U}\cdot\nabla)\boldsymbol{U} = -\nabla P + Pr\nabla^2\boldsymbol{U} - \mathrm{RaPr}\Theta\boldsymbol{e}_g + Ga\Theta(\boldsymbol{U}\cdot\nabla)\boldsymbol{U}. \tag{5}$$

Equation (5) introduces the Prandtl number $\mathrm{Pr} = \nu/\alpha$ characterizing the ratio of the molecular to thermal dissipation, the Rayleigh number $\mathrm{Ra} = g\beta\Delta\theta L_{\mathrm{ref}}{}^3/\nu\alpha$ characterizing the ratio of buoyancy to viscous and thermal dissipation and Gay–Lussac parameter $\mathrm{Ga} = \beta\Delta\theta$. As later be shown, the Gay–Lussac parameter may be expressed as a product of Rayleigh, Prandtl and Froude numbers, that is, Ga = FrRaPr. Thus, under this Gay–Lussac-type approximation, the dimensionless form of the governing equations in the context of the primitive variables are expressed as.[27]

$$\begin{cases} \nabla\cdot\boldsymbol{U} = 0, \\ (\boldsymbol{U}\cdot\nabla)\boldsymbol{U} = -\nabla P + Pr\nabla^2\boldsymbol{U} - \mathrm{RaPr}\Theta(\,\boldsymbol{e_g} - Fr(\boldsymbol{U}\cdot\nabla)\boldsymbol{U}), \\ (\boldsymbol{U}\cdot\nabla)\Theta = \nabla^2\Theta. \end{cases} \tag{6}$$

Equation (6) introduces Froude number $\mathrm{Fr} = U_{\mathrm{ref}}{}^2/gL$ characterizing ratio of inertial to gravitational forces. Interested readers are referred to Reference 27 for a detailed procedure of the momentum equation derivation. As can be seen, Equation (6) is consistent with the momentum equation under the Boussinesq approximation, except for the additional inertial buoyancy term on the right-hand side. When expressed in this form, it is apparent that the action of this additional term is to modify the effective direction (and strength) of the gravity locally throughout the flow which is ignored in the conventional Boussinesq approximation. Indeed, regions which are experiencing higher spatial accelerations described by $(\boldsymbol{U}\cdot\nabla)\boldsymbol{U}$, will experience deviations from the Boussinesq buoyancy approximation. The strength of these deviations relative to gravity is described by Fr, with $\mathrm{Fr}\to 0$ (and $\mathrm{Ga}\to 0$) recovering the classical Boussinesq approximation.[27] The effect of this parameter on the buoyancy-driven flow is investigated in Section 4.

Using the secondary variables, that is, vorticity ($\omega = \partial V/\partial X - \partial U/\partial Y$) and stream-function ($U = \partial\psi/\partial Y; V = -\partial\psi/\partial X$), the scalar formulation of the governing equations under mentioned Gay–Lussac-type approximation in transient form are expressed as

$$\begin{cases} \frac{\partial^2\psi}{\partial X^2} + \frac{\partial^2\psi}{\partial Y^2} = -\omega, \\ \frac{\partial\omega}{\partial t} + (1 - \mathrm{RaPrFr}\Theta)\left(\frac{\partial\psi}{\partial Y}\frac{\partial\omega}{\partial X} - \frac{\partial\psi}{\partial X}\frac{\partial\omega}{\partial Y}\right) = \mathrm{Pr}\left(\frac{\partial^2\omega}{\partial X^2} + \frac{\partial^2\omega}{\partial Y^2}\right) + \mathrm{RaPr}\frac{\partial\Theta}{\partial X}, \\ \frac{\partial\Theta}{\partial t} + \frac{\partial\psi}{\partial Y}\frac{\partial\Theta}{\partial X} - \frac{\partial\psi}{\partial X}\frac{\partial\Theta}{\partial Y} = \frac{\partial^2\Theta}{\partial X^2} + \frac{\partial^2\Theta}{\partial Y^2}, \\ \Theta(\boldsymbol{X},0) = \omega(\boldsymbol{X},0) = \psi(\boldsymbol{X},0) = 0. \end{cases} \tag{7}$$

Following the primary variables, the classical Boussinesq approximation in secondary variables are also retrieved as $Fr\to 0$.

Within this study, the square and skew-cavity cases are also simulated under the LMS approximation for comparison purpose. The dimensionless form of the governing equations under the LMS approximation are expressed as.[30]

$$\begin{cases} \frac{\partial\rho}{\partial t} + \nabla\cdot(\rho\boldsymbol{U}) = 0, \\ \frac{\partial(\rho\boldsymbol{U})}{\partial t} + \nabla\cdot(\rho\boldsymbol{U}\otimes\boldsymbol{U}) = -\nabla P + \frac{RaPr}{2\varepsilon}\rho\boldsymbol{e}_g + Pr\nabla\cdot\boldsymbol{\tau}, \\ \frac{\partial(\rho\Theta)}{\partial t} + \nabla\cdot(\rho\boldsymbol{U}\Theta) = \nabla^2\Theta + \left(\frac{\eta-1}{\eta}\right)\frac{\mathrm{d}P_{\mathrm{th}}}{\mathrm{d}t} \\ P_{\mathrm{th}} = Z\rho\Theta, \\ \Theta(\boldsymbol{X},0) = P_{\mathrm{th}}(0) = 1, \boldsymbol{U}(\boldsymbol{X},0) = 0. \end{cases} \tag{8}$$

Equation (8) has been made dimensionless using the following parameters

$$t = \frac{t^*\alpha}{L^2}, \boldsymbol{X} = \frac{\boldsymbol{x}}{L}, \boldsymbol{U} = \frac{\boldsymbol{u}L}{\alpha}, P = \frac{p^*L^2}{\rho\alpha^2}, \Theta = \frac{T}{T_0}, P_{\mathrm{th}} = \frac{p_{\mathrm{th}}}{p_0}, Z = \frac{R}{R_0}, \rho = \frac{\rho^*}{\rho_0}. \tag{9}$$

In Equation (8), Pr is the Prandtl number as defined earlier in Equation (5), ε is the relative temperature difference defined as $\varepsilon = (T_h - T_c)/2T_0$, η is the heat capacity ratio ($\eta = c_p/c_v$) and P_{th} is the global dimensionless thermodynamic pressure.

In this study, we only present results for an ideal diatomic gas ($Z = 1$). Also, $\boldsymbol{\tau}$ is the stress tensor given in dimensionless form by

$$\boldsymbol{\tau} = \nabla \boldsymbol{U} + (\nabla \boldsymbol{U})^T - 2/3(\nabla \cdot \boldsymbol{U})\boldsymbol{I}. \tag{10}$$

In Equation (9), Stokes' hypothesis is used for bulk viscosity ($\lambda = -2/3\mu$). In natural convection simulation via compressible/weakly compressible approach, the Rayleigh number is expressed slightly different compared to the incompressible flow, as

$$\mathrm{Ra} = \mathrm{Pr}\,\frac{g{\rho_0}^2(T_\mathrm{h} - T_\mathrm{c})L^3}{T_o{\mu_0}^2}. \tag{11}$$

Comparing incompressible and compressible Rayleigh number definitions gives the following relation for the Froude number corresponding to a given relative temperature difference at each Rayleigh and Prandtl as.[27]

$$\underbrace{2\varepsilon = (T_\mathrm{h} - T_\mathrm{c})/T_o}_{\text{Compressible}} = \underbrace{\beta\Delta\theta = \mathrm{RaPrFr}}_{\text{Incompressible}} \rightarrow \mathrm{Fr} = 2\varepsilon/\mathrm{RaPr}. \tag{12}$$

Another advantage of Equation (11) is expressing the Gay–Lussac parameter by its equivalent relative temperature difference definition ($2\varepsilon = \beta\Delta\theta = \mathrm{Ga}$). So, another form of the Gay–Lussac-type approach may be expressed using ε instead of Ga and/or three dominant dimensionless parameters, that is, Ra, Pr, and Fr as

$$\begin{cases} \frac{\partial^2\psi}{\partial X^2} + \frac{\partial^2\psi}{\partial Y^2} = -\omega \\ \frac{\partial\omega}{\partial t} + (1 - 2\varepsilon\Theta)\left(\frac{\partial\psi}{\partial Y}\frac{\partial\omega}{\partial X} - \frac{\partial\psi}{\partial X}\frac{\partial\omega}{\partial Y}\right) = \mathrm{Pr}\left(\frac{\partial^2\omega}{\partial X^2} + \frac{\partial^2\omega}{\partial Y^2}\right) + \mathrm{RaPr}\frac{\partial\Theta}{\partial X}, \\ \frac{\partial\Theta}{\partial t} + \frac{\partial\psi}{\partial Y}\frac{\partial\Theta}{\partial X} - \frac{\partial\psi}{\partial X}\frac{\partial\Theta}{\partial Y} = \frac{\partial^2\Theta}{\partial X^2} + \frac{\partial^2\Theta}{\partial Y^2} \\ \Theta(\boldsymbol{X}, 0) = \omega(\boldsymbol{X}, 0) = \psi(\boldsymbol{X}, 0) = 0. \end{cases} \tag{13}$$

3 | DESCRIPTION OF THE PROBLEM AND NUMERICAL APPROACH

The square and skew cavity configurations are shown in Figure 1, highlighting the thermal boundary conditions comprising adiabatic top and bottom boundaries, and hot and cold left and right boundaries, respectively. The applied boundary conditions for vorticity and stream-function are also shown. In this study, the reference length is taken to be equal to the length of the horizontal side of the geometry ($L_\mathrm{ref} = L$). Skew cavities are also defined by an skewness angle of δ. The physical domain is meshed using quadrilateral elements. A schematic coarse mesh is shown for illustration purposes in Figure 1(C),(D).

The local and average Nusselt number along the two constant temperature surfaces are calculated as

$$Nu_\mathrm{loc}(S) = -\left.\frac{\partial\Theta}{\partial n}\right|_\mathrm{wall}, \tag{14}$$

$$Nu_\mathrm{avg} = \int_0^1 Nu_\mathrm{loc}\,\mathrm{d}S. \tag{15}$$

The dimensionless local entropy generation due to heat transfer (S_θ) and fluid friction (S_ψ) are calculated as

$$S_\Theta = \left[\left(\frac{\partial\Theta}{\partial X}\right)^2 + \left(\frac{\partial\Theta}{\partial Y}\right)^2\right], \tag{16}$$

$$S_\psi = \chi\left[2\left\{\left(\frac{\partial U}{\partial X}\right)^2 + \left(\frac{\partial V}{\partial Y}\right)^2\right\} + \left(\frac{\partial U}{\partial Y} + \frac{\partial V}{\partial X}\right)^2\right]. \tag{17}$$

For compressible approach in which$\nabla \cdot \boldsymbol{U} \neq 0$, S_ψ retains the velocity divergence and must be calculated using

$$S_\psi = \chi\left[2\left\{\left(\frac{\partial U}{\partial X}\right)^2 + \left(\frac{\partial V}{\partial Y}\right)^2\right\} + \left(\frac{\partial U}{\partial Y} + \frac{\partial V}{\partial X}\right)^2 - \frac{2}{3}\left(\frac{\partial U}{\partial X} + \frac{\partial V}{\partial Y}\right)^2\right]. \tag{18}$$

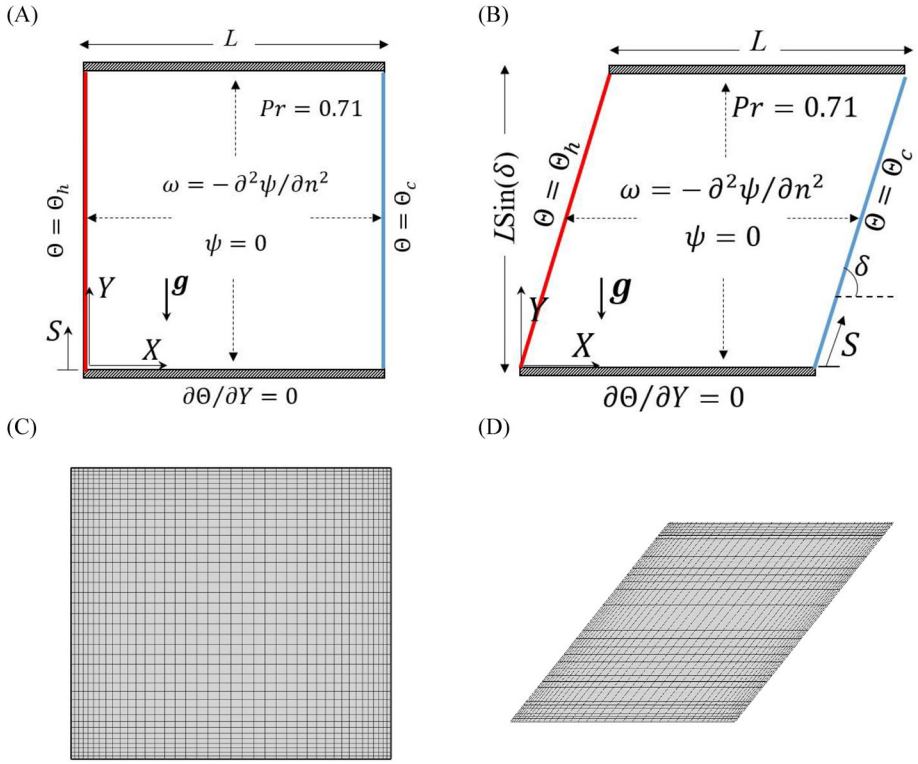

FIGURE 1 A schematic view of the problem, applied boundary conditions and used mesh, (A), Square cavity, (B), Skew cavity with skewness angle δ, (C, D), A coarse computational grid having 40×40 quadrilateral elements [Color figure can be viewed at wileyonlinelibrary.com]

In Equations (16) and (17), $\chi = \mu T_0 \alpha^2 / k(L\Delta\theta)^2$ is the irreversibility distribution ratio such that characterizes the ratio of viscous heat dissipation to heat conduction within the system. In this study, χ is taken as fixed and equal to 10^{-4} consistent with References 31–33. For context, in air at standard conditions, this corresponds to a reference length $L \sim 10^{-1}$ m and temperature difference $\Delta\theta \sim 1$ K. The total entropy generation due to heat transfer and fluid friction is calculated by the summation of the local entropy generation over the physical domain via

$$S_{\Theta,\text{tot}} = \int_V S_\Theta \, \mathrm{d}v, \tag{19}$$

$$S_{\psi,tot} = \int_V S_\psi \, \mathrm{d}v. \tag{20}$$

The relative dominance of entropy generation due to heat transfer and fluid friction is given by average Bejan number (Be_{avg}), a dimensionless parameter defined as.[34-36]

$$\text{Be}_{\text{avg}} = \frac{S_{\Theta,\text{tot}}}{S_{\Theta,\text{tot}} + S_{\psi,\text{tot}}}, \tag{21}$$

where $\text{Be}_{\text{avg}} > 0.5$ implies dominance of heat transfer irreversibility and $\text{Be}_{\text{avg}} < 0.5$ implies dominance of fluid friction irreversibility.

The skin friction along the surfaces is related to the fluid flow via the gradient of the velocity components normal to the surface. The friction coefficient along the surface based on the dimensionless velocity is defined as

$$c_f = -\frac{\tau_w}{1/2\rho(\alpha/L)^2} = -2\,\text{Pr}\,\frac{\partial U_\delta}{\partial \boldsymbol{n}}\bigg|_{\text{wall}}. \tag{22}$$

In Equation (22), $\boldsymbol{n}$ is the unit normal vector to the surface. Since the governing equations are solved in a Cartesian coordinate system, the above fundamental definition is implemented through the two-dimensional (2D) shear stress tensor as

$$\boldsymbol{c_f} = -2\,\text{Pr}\begin{bmatrix}\tau_{xx} & \tau_{xy}\\ \tau_{yx} & \tau_{yy}\end{bmatrix}\begin{bmatrix}n_x\\ n_y\end{bmatrix} = -2Pr\begin{bmatrix}2\partial U/\partial X & \partial U/\partial Y + \partial V/\partial X\\ \partial U/\partial Y + \partial V/\partial X & 2\partial V/\partial Y\end{bmatrix}\begin{bmatrix}n_x\\ n_y\end{bmatrix}, \tag{23}$$

where n_x and n_y are the horizontal and vertical components of the wall-normal vector, respectively. The friction coefficient magnitude is calculated as

$$c_f = \sqrt{(c_{f_x})^2 + (c_{f_y})^2}, \tag{24}$$

where

$$c_{f_x} = -2\,\mathrm{Pr}[(2\partial U/\partial X)n_x + (\partial U/\partial Y + \partial V/\partial X)n_y], \tag{25}$$

$$c_{f_y} = -2\,\mathrm{Pr}[(\partial U/\partial Y + \partial V/\partial X)n_x + (2\partial V/\partial Y)n_y]. \tag{26}$$

Governing equations are solved using a control volume finite-element method (CVFEM) solver with a second-order Adams Bashforth/Crank Nicolson temporal scheme for time-dependent equations having two steps. In the first step, an intermediate vorticity/temperature field is predicted using vorticity/temperature fields from the current and previous time-steps. For instance, for vorticity equation this can be shown using ω^n and ω^{n-1} as

$$\frac{\omega^* - \omega^n}{\Delta t} = -\frac{3}{2}(1 - 2\varepsilon\Theta^n)\mathrm{N}(\omega^n) + \frac{1}{2}(1 - 2\varepsilon\Theta^{n-1})\mathrm{N}(\omega^{n-1}) + \frac{Pr}{2}\mathrm{D}(\omega^n) + B^n. \tag{27}$$

In Equation (27), N and D represent the nonlinear advection and diffusion operators, respectively, and B is the buoyancy source term (i.e., $\mathrm{RaPr}\partial\Theta/\partial X$). Using intermediate vorticity (ω^*), vorticity in the next step time-step is obtained using

$$\frac{\omega^{n+1} - \omega^*}{\Delta t} = \frac{\mathrm{Pr}}{2}\mathrm{D}(\omega^{n+1}). \tag{28}$$

Equation (28) is a linear equation that is solved implicitly to update the vorticity field in each iteration. A similar procedure is applied for the energy equation to update the temperature field during iterations.

In CVFEM, a unique control volume (as shown in Figure 2(A)) is assigned to each node that its boundaries are comprised of a number of planar panels. An integration point (ip) is located at the middle of each panel, which is denoted by a × sign. Integration of diffusion term over the control volume and applying the Gauss divergence theorem yields

$$\int_{v_p} \nabla^2\omega \mathrm{d}v = \oint_{A_p} \nabla\omega_{\mathrm{ip}} \cdot \mathrm{d}\boldsymbol{A} = \sum_{\mathrm{ip}=1}^{n} \nabla\omega_{\mathrm{ip}} \cdot \boldsymbol{A}_{\mathrm{ip}}. \tag{29}$$

In Equation (29), n is the number of integration points surrounding the main node and $\boldsymbol{A}_{\mathrm{ip}}$ is the normal vector surface at each ip. Using bilinear shape functions ($N_j(s, t)$), any parameter (such as ω) within the element with a local coordinate (s,t) is related to the nodal values via weighted values provided by shape functions

$$\omega_{ip} = \omega(s, t) = \sum_{j=1}^{4} N_j(s, t)\omega_j. \tag{30}$$

For quadrilateral elements, the four shape functions relating *ip* values to the nodal values are shown in Figure 2(B). Thus, the diffusion term may be expressed as follows

$$D(\omega) = \sum_{\mathrm{ip}=1}^{n} \sum_{j=1}^{4} \omega_j \nabla N_j \cdot \boldsymbol{A}_{\mathrm{ip}}. \tag{31}$$

Since the bilinear shape functions are functions of their local coordinate system, their gradients with respect to global coordinate system are calculated using the chain rule. In Equation (31), the effect of all nodes surrounding an ip (such as the one shown in Figure 2(B)) are considered by weighted values that is equivalent to a central scheme. The diffusion operator in energy and stream function equations is calculated in a similar fashion.

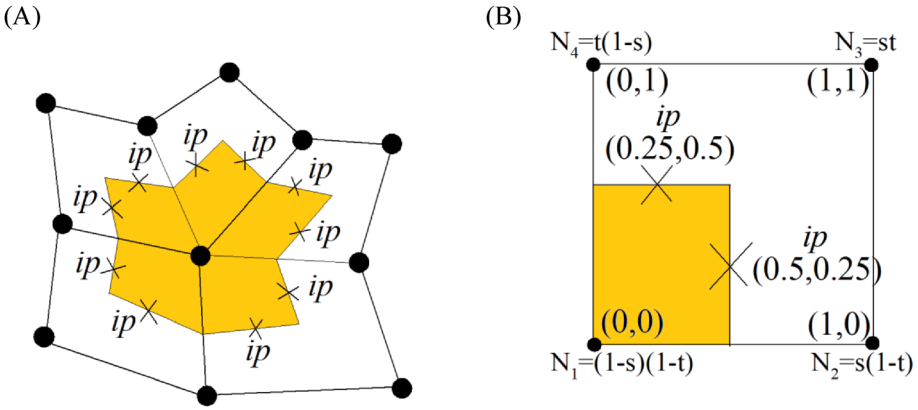

FIGURE 2 A schematic of unstructured quadrilateral elements, (A), a typical control volume associated with integration points, (B), Local coordinate (s,t) and bilinear shape functions in a standard element [Color figure can be viewed at wileyonlinelibrary.com]

	Quantity	Present study	Davis[2]	Wan et al.[6]	Ashrafizadeh and Nikfar[7]
$Ra = 10^4$	Nu_{max} (at Y)	**3.548 (0.140)**	3.53 (0.143)	3.597 (0.13)	3.531 (0.139)
	Nu_{min} (at Y)	**0.589 (1.0)**	0.586 (1.0)	0.577 (1.0)	0.584 (1.0)
	Nu_{avg}	**2.23**	2.42	2.25	2.24
$Ra = 10^5$	Nu_{max} (at Y)	**7.778 (0.075)**	7.71 (0.08)	7.945 (0.08)	7.720 (0.084)
	Nu_{min} (at Y)	**0.734 (1.0)**	0.729 (1.0)	0.698 (1.0)	0.726 (1.0)
	Nu_{avg}	**4.51**	4.52	4.60	4.52
$Ra = 10^6$	Nu_{max} (at Y)	**17.633 (0.038)**	17.92 (0.038)	17.86 (0.03)	17.732 (0.039)
	Nu_{min} (at Y)	**0.996 (1.0)**	0.989 (1.0)	0.913 (1.0)	0.975 (1.0)
	Nu_{avg}	**8.82**	8.92	8.98	8.83

TABLE 1 Comparison of the present calculated local and average Nusselt number by control volume finite-element method solver (bold) with published benchmarks

In the governing equations, non-linear terms are linearised using lagged values from the previous iteration. Integration of the advection term over the control volume and applying Gauss divergence theorem yields

$$\int_{v_p} (\overline{\psi_y}\omega_x - \overline{\psi_x}\omega_y)\mathrm{d}v = \oint_{A_p} \overline{\psi_y}\omega \mathrm{d}A_x - \overline{\psi_x}\omega \mathrm{d}A_y = \oint_{A_p} \omega(\overline{\psi_y}\mathrm{d}A_x - \overline{\psi_x}\mathrm{d}A_y) = \sum_{\mathrm{ip}=1}^{n} \omega_{\mathrm{ip}}(\overline{\psi_{y_{\mathrm{ip}}}}A_{x\mathrm{ip}} - \overline{\psi_{x_{ip}}}A_{y_{\mathrm{ip}}}). \tag{32}$$

Using bilinear shape functions (Equation (30)) to relate the integral point values to the nodal values yields

$$\mathrm{N}(\omega) = \sum_{\mathrm{ip}=1}^{n} \sum_{j=1}^{4} \omega_j N_j(\overline{\psi_{y_{\mathrm{ip}}}}A_{x\mathrm{ip}} - \overline{\psi_{x\mathrm{ip}}}A_{y_{\mathrm{ip}}}). \tag{33}$$

Similarly, in Equation (33) n is the number of ip surrounding the main node. In Equation (33), it is possible to approximate lagged values simply from the nodes within the element by weighted values (that are provided by shape functions based on local coordinate at each ip) which leads to a central scheme. Another possible scenario is approximating lagged values based on flow direction that is known as the upwind scheme. It should be noted that $\overline{\psi_{y_{\mathrm{ip}}}}$ and $-\overline{\psi_{x_{\mathrm{ip}}}}$ in vorticity and energy equations are indeed the velocity components that are expressed in the context of stream-function. The convection term in energy equation is calculated in a similar fashion. Iterative solution procedure is stopped as soon as the maximum difference of scalar values during two successive iterations becomes less than 10^{-7}. Accurate performance of the CVFEM solver is already tested in previous works[37-45] but here in Table 1 it is further validated against References 2, 6, 7 in terms of the local and average Nusselt number at three different Rayleigh numbers, adopting air as the working fluid (Pr = 0.71). A close agreement is observed.

Accurate performance of the CVFEM solver under the LMS approximation is also validated against Reference 46 in terms of average Nusselt number and thermodynamic pressure at Ra = 10^6 and $\varepsilon = 0.6$ with air as the working

TABLE 2 Comparison of the present calculated local and average Nusselt number by control volume finite-element method solver (bold) with published benchmarks

	Quantity	Present study	Le Quéré et al.[44]
$Ra = 10^6$, $\varepsilon = 0.6$ Constant properties	P_{th}	0.858	0.856
	Nu_{avg}	8.895	8.859
$Ra = 10^6$, $\varepsilon = 0.6$ Variable properties	P_{th}	0.921	0.924
	Nu_{avg}	8.693	8.686

TABLE 3 Mesh resolution study for average Nusselt and Bejan numbers at $Ra = 10^6$ and $Pr = 0.71$

	$n_x \times n_y$	31^2	61^2	121^2	241^2
Boussinesq approximation (Fr = 0)	Nu_{avg}	8.695134	8.811059	8.827201	8.827201
	|difference|	—	0.115925	0.016142	0.000000
	Be_{avg}	0.029368	0.026270	0.025471	0.025471
	|difference|	—	0.003098	7.99e-4	0.000000
Gay–Lussac-type approximation (Fr = 0.6/RaPr)	Nu_{avg}	8.654427	8.790351	8.816621	8.8166
	|difference|	—	0.135923	0.026270	0.000000
	Be_{avg}	0.029308	0.026222	0.025424	0.025424
	|difference|	—	0.003086	7.98e-4	0.000000

TABLE 4 Mesh resolution study for average Nusselt number and thermodynamic pressure at $Ra = 10^6$, $Pr = 0.71$, and $\varepsilon = 0.3$

	$n_x \times n_y$	31^2	61^2	121^2	241^2
LMS approximation	P_{th}	0.961124	0.964295	0.966286	0.966286
	|difference|	—	0.003171	0.001991	0.000000
	Nu_{avg}	8.992231	8.904211	8.854831	8.854831
	|difference|	—	0.088020	0.049379	0.000000

fluid ($Pr = 0.71$) in two states including constant and variable properties (see Table 2). The present simulations recover published values very well, with discrepancies lower than 0.41%.

Mesh dependence is checked for the CVFEM solver in Table 3 at the highest Rayleigh number $Ra = 10^6$ and $Pr = 0.71$ under the Boussinesq approximation ($Fr = 0$) and the highest Froude number under the Gay–Lussac-type approximation in this study ($Fr = 0.6/RaPr$). It is found that 121 nodes in each direction guarantees mesh independence for both of the Boussinesq and Gay–Lussac-type approximations.

Mesh dependence of the CVFEM solver under the LMS approximation is also checked in Table 4 at the highest Rayleigh number $Ra = 10^6$ and $Pr = 0.71$ for the highest relative temperature difference ($\varepsilon = 0.3$) in this study. It is found using 121 nodes ($n_x \times n_y = 121^2$) in each direction guarantees results independence from the mesh size for the weakly compressible approach. Similar dependence is also found for the skew cavity cases but for the sake of brevity, they are not mentioned here.

4 | RESULTS AND DISCUSSION

In this section, the results of three approximations are presented. Simulations are performed at $Pr = 0.71$ (consistent with air) up to $Ra = 10^6$ ($10 \leq Ra \leq 10^6$) and $\varepsilon = 0.3$ ($0 \leq \varepsilon \leq 0.3$). It should be noted that, a relative temperature difference of 0.01 is considered as a differential relative temperature difference and is representative of a Boussinesq case.[29] Here, we extend this parameter to 30 times larger, beyond the validity of the Boussinesq approximation. Studying relative temperature differences exceeding 0.3 is beyond the scope and goals of this paper. Based on Equation (12) and according to the

considered range of ε, Froude number ranges over $0 \leq \mathrm{Fr} \leq 0.6/\mathrm{RaPr}$ throughout this study. For the investigated range of the Froude and Rayleigh numbers at $\mathrm{Pr} = 0.71$, it is supposed that the flow field is 2D, laminar and stable.

For a better understanding of the produced thermo-flow field under the different approximations, absolute temperature differences of the weakly compressible approach at $\mathrm{Ra} = 10^6$ and $\varepsilon = 0.3$ (the highest Rayleigh number and relative temperature difference in this study) against the Gay–Lussac-type approximation with $\mathrm{Fr} = 0.6/\mathrm{RaPr}$ and the Boussinesq approximation ($\mathrm{Fr} = 0$) are depicted in Figures 3(A)–(F). Absolute temperature differences under the different approaches shift isotherms, with a larger differences found for the left-inclined skew cavity ($\delta = 150^\circ$) compared to the square cavity and right-inclined skew cavity ($\delta = 30^\circ$). In the square cavity, the difference is largest at the top-left and bottom-right corners while in the right-inclined skew cavity it is occurring almost evenly over the interior region. Large temperature differences for left-inclined skew cavities may be attributed to the reaction of accelerated fluid which is faced with an acute angle to rotate. The maximum absolute temperature difference in the square cavity in Figure 3(B),(E) (with a larger difference for the Gay–Lussac-type approximation) is approximately 10% of the temperature range within the enclosure, reflecting a mismatch of this magnitude between the weakly compressible and incompressible approaches. A similar comparison for the right-inclined skew cavity shows a smaller about 7% mismatch (Figure 3(A), (D)) while the largest mismatch of about 20% is found for the left-inclined skew cavity (Figure 3(C),(F)). It is clear that the mismatch between the aforementioned approaches augments by increasing the relative temperature difference and consequently the non-Boussinesq parameter (i.e., Froude number). To appreciate the role of extra term effects in the momentum equation of the Gay–Lussac-type approximation, the magnitude of $\Theta(\psi_y \omega_x - \psi_x \omega_y)$ under the Boussinesq approximation is portrayed for the square cavity and skew cavities with $\delta = 30^\circ$ and 150° at $\mathrm{Ra} = 10^6$ in Figures 3(G),(I). As seen, the magnitude of the non-Boussinesq acceleration is stronger along the isothermal walls and especially at four corners of the cavity, though weaker effects are found within the central regions of the enclosure. Stronger non-Boussinesq effects along the isothermal walls may be attributed to larger velocity gradients since fluid adjacent to the wall is accelerated by buoyancy force as it reaches to the wall during circulation and decelerated as it gets close to the end of the path parallel to the isotherm wall. Stronger non-Boussinesq effects at the four corners are attributed to fluid rotation to adjust its motion with respect to the geometry corners. Non-Boussinesq term magnitude is smaller for skew cavities compared to the square cavity but its magnitude is stronger in the left-inclined ($\delta = 150^\circ$) versus the right-inclined cavity ($\delta = 30^\circ$) skew cavity. Smaller magnitude of the non-Boussinesq term in skew cavities is due to a weaker thermally driven flow in skew cavity having smaller stream-function compared to square cavity as shown in the next figures (Figures 4(A), (C), 5(A), C, 6(A) and (C)).

Stream-function and vorticity absolute differences fields under the three approximations at $\mathrm{Ra} = 10^6$ and $\varepsilon = 0.3$ are portrayed for square and skew cavities with $\delta = 30^\circ$ and 150° in Figures 4, 5, and 6, respectively. In Figures 4(A), (C), 5(A), (C), 6(A) and (C), the general structure of the stream-function under the weakly compressible approach is considerably different compared to the Gay–Lussac and Boussinesq approximations in both square and skew geometries. Under the incompressible approximations, stream-functions have a twin core with almost equal strength but under the weakly compressible approximation, stream-function has one central core with a stronger circulation. In the square cavity, the location of the minimum stream-function obtained from incompressible simulations have shifted their place to a higher level toward the vertical centre-line compared to the obtained results under the weakly compressible approximation. The exact quantitative distance between the minimum stream-function locations is obtained equal to 0.1893 and 0.2048 length units for the Gay–Lussac-type and Boussinesq approximations, respectively. For the right skewed cavity with $\delta = 30^\circ$ (Figure 5), a stronger circulation is observed for the left main core under the weakly compressible approximation which is so close to the minimum stream-function location when governing equations are treated under Gay–Lussac approximation. In this case, the distances of the minimum stream-function location are obtained equal to 0.0144 and 0.2970 length units for the Gay–Lussac-type and Boussinesq approximations, respectively. Finally, a visible inclined distance is observed for left skewed cavity with $\delta = 150^\circ$ under different approximations, which is presented in Figure 6. In this case, the distances of the minimum stream-function location are obtained equal to 0.2362 and 0.2688 unit of dimensionless length for the Gay–Lussac and Boussinesq approximations, respectively. In general, obtained absolute stream-function differences show more deviation from the compressible simulation for the Gay–Lussac compared to the Boussinesq approximation with a concentration on four corners, but it predicts the minimum stream-function location more accurately than the Boussinesq approximation.

Obtained vorticity fields are presented under the different approximations in Figures 4(B), (D), 5(B), (D), 6(B) and (D). Comparing obtained results from different approaches reveals that when the buoyancy driven flow is simulated via weakly compressible approach for large relative temperature difference, the same pattern of vorticity field is formed and the difference mainly comes from vortexes (with different strengths) stretching or location shifting through the flow field.

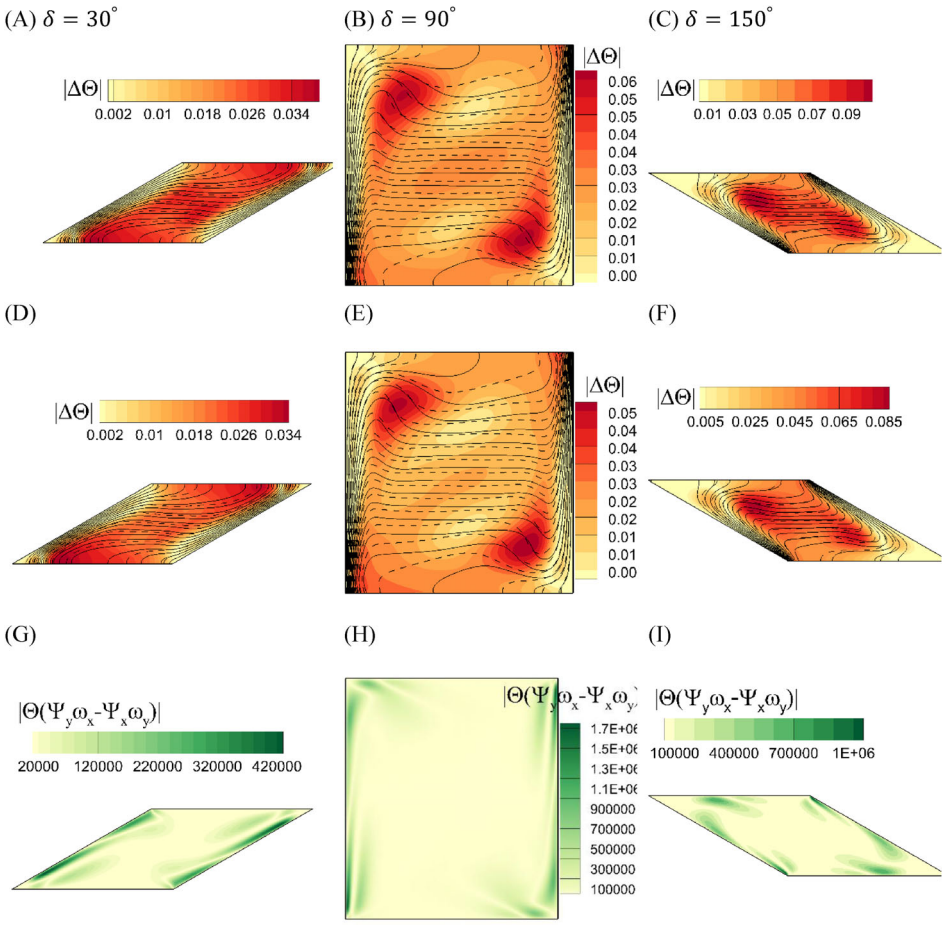

FIGURE 3 Results at $Ra = 10^6$, $Pr = 0.71$, and $\varepsilon = 0.3$, (A-C) Absolute temperature difference field between the Gay–Lussac-type and LMS approximations, (D–F) Absolute temperature difference field between the Boussinesq and LMS approximations. (G–I) Magnitude of the acceleration vector field of the non-Boussinesq acceleration term, that is, $|\Theta(\psi_y\omega_x - \psi_x\omega_y)|$ obtained from simulation under the Boussinesq approximation. In temperature difference fields, solid lines represent the LMS approximation isotherms lines at $Fr = 0.6/RaPr$ while dashed lines show the other approach [Color figure can be viewed at wileyonlinelibrary.com]

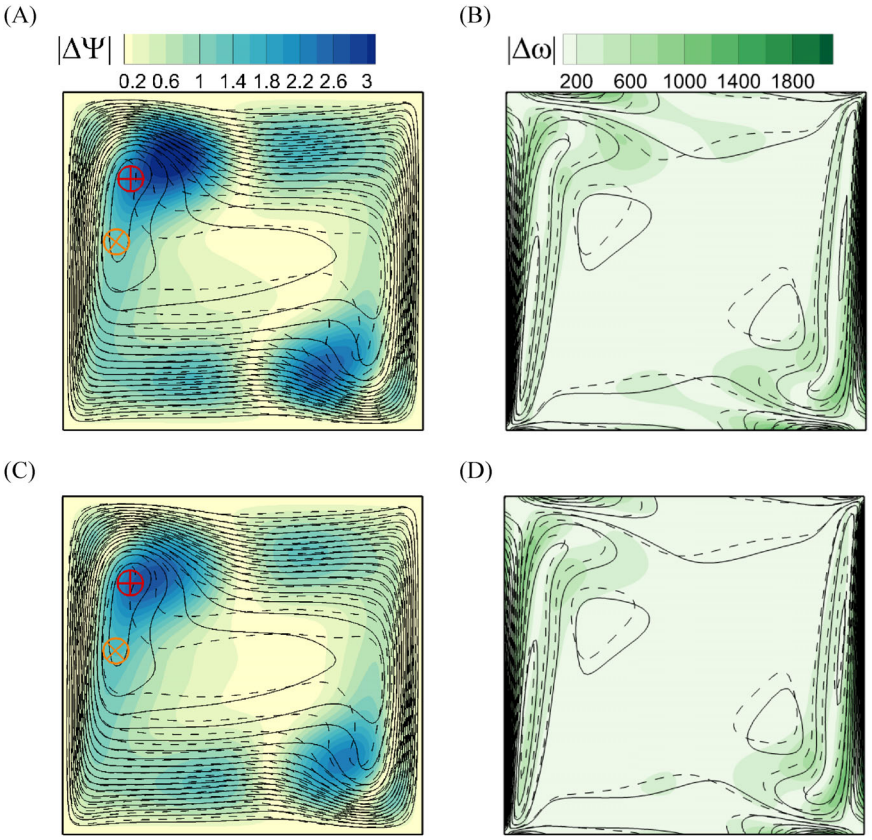

FIGURE 4 Vorticity and stream-function absolute differences in square cavity at $Ra = 10^6$ and $\varepsilon = 0.3$, (A, B) LMS and Gay–Lussac approximations, (C,D) LMS and Boussinesq approximations. "⊕" and "⊗" signs identify the point of the minimum stream-function under the LMS and incompressible approaches, respectively. In (A, C) solid and dashed lines show stream-functions under the LMS and incompressible approximations, respectively, while in (B, D) solid and dashed lines show vorticity fields under the LMS and incompressible approximations, respectively [Color figure can be viewed at wileyonlinelibrary.com]

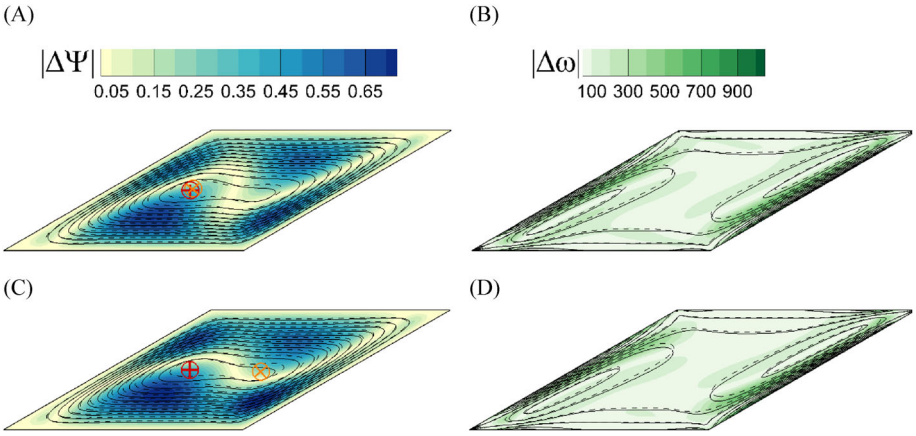

FIGURE 5 Vorticity and stream-function absolute differences in skew cavity with $\delta = 30^{\circ}$ at $\mathrm{Ra} = 10^6$ and $\varepsilon = 0.3$, (A, B), LMS and Gay–Lussac-type approximations, (C,D) LMS and Boussinesq approximations. "⊕" and "⊗" signs identify the point of the minimum stream-function under the LMS and incompressible approaches, respectively. In (A, C) solid and dashed lines show stream-functions under the LMS and incompressible approximations, respectively, while in (B, D) solid and dashed lines show vorticity fields under the LMS and incompressible approximations, respectively [Color figure can be viewed at wileyonlinelibrary.com]

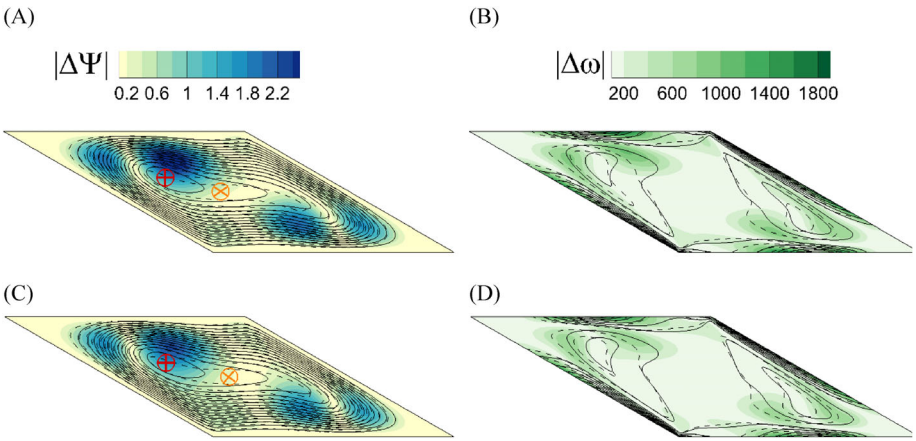

FIGURE 6 Vorticity and stream-function absolute differences in skew cavity with $\delta = 150^{\circ}$ at $\mathrm{Ra} = 10^6$ and $\varepsilon = 0.3$, (A, B) LMS and Gay–Lussac-type approximations, (C, D) LMS and Boussinesq approximations. "⊕" and "⊗" signs identify the point of the minimum stream-function under the LMS and incompressible approaches, respectively. In (A, C) solid and dashed lines show stream-functions under the LMS and incompressible approximations, respectively, while in (B, D) solid and dashed lines show vorticity fields under the LMS and incompressible approximations, respectively [Color figure can be viewed at wileyonlinelibrary.com]

In mentioned figures, large values of the vorticity absolute differences are mainly elongated adjacent to the isotherm walls where flow accelerates due to buoyancy force. For square and left skewed cavities, large values of vorticity absolute differences are also observed when accelerated rotating flow reaches to horizontal adiabatic surface.

A comparison of the temperature and velocity magnitude differences in the square cavity during transient solution is performed in Figures 7 and 8, respectively. Results of comparing transient temperature fields indicate that the Boussinesq approximation shows more deviation at the initial time of the transient solution but as the time goes on, this difference becomes less noticeable. In addition, results of the transient absolute temperature difference fields indicate that the two main cores of the temperature differences in Figure 3(B),(E) are first generated across the frontiers progressing hot and cold temperatures at the top-left and bottom right regions and then circulated in the flow direction. Comparing the values of $|\Delta\Theta|$ in steady (Figure 3) and transient (Figure 7) states reveals the absolute temperature difference between the compressible and incompressible approaches is larger in transient state compared to the steady-state solution. Comparing velocity magnitude during transient solution in Figure 8 shows a negligible difference between the Gay–Lussac type and the Boussinesq approximations against the LMS approximation. Results of the transient velocity magnitude difference

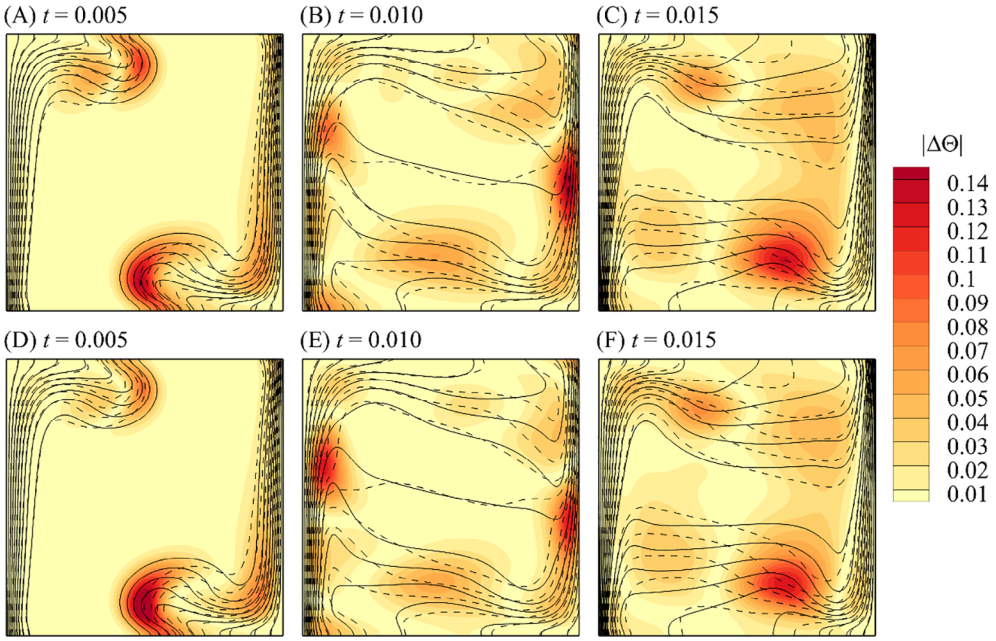

FIGURE 7 Absolute temperature difference field at different time as stated between, (A–C) The Gay–Lussac-type and LMS approximations, (D–F) The Boussinesq and LMS approximations. Solid and dashed lines show isotherms lines under the LMS and incompressible approximations, respectively [Color figure can be viewed at wileyonlinelibrary.com]

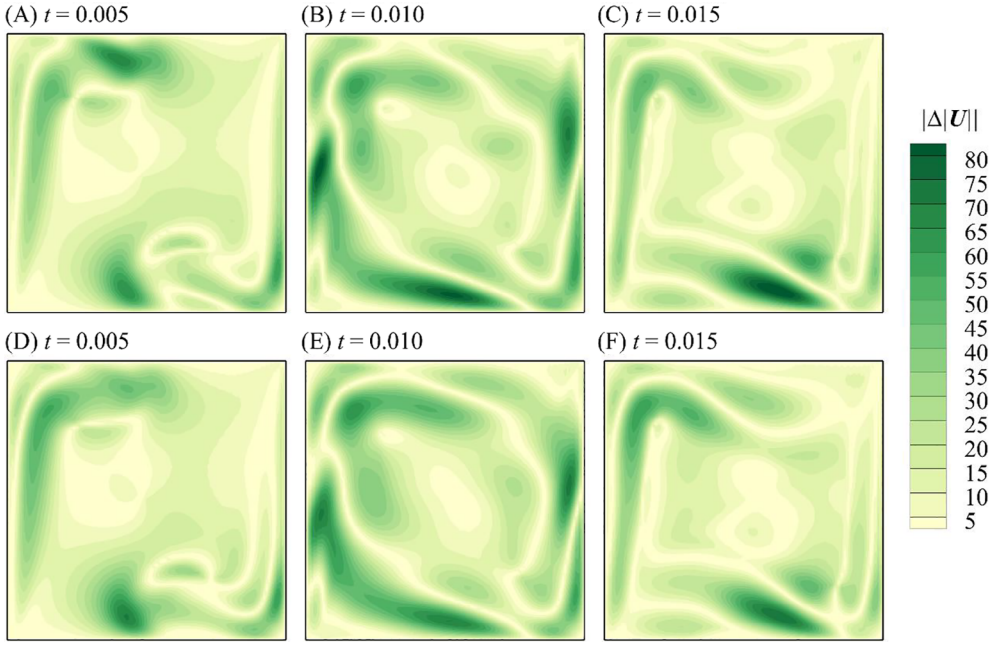

FIGURE 8 Absolute velocity magnitude difference at different time as stated between, (A–C) The Gay–Lussac-type and LMS approximations, (D–F) The Boussinesq and LMS approximations. Solid and dashed lines show isotherms lines under the LMS and incompressible approximations, respectively [Color figure can be viewed at wileyonlinelibrary.com]

indicate at the initial time of the solution (Figure 8(A),(D)), the difference mainly occurs in the regions close to the vertical walls affected by the buoyancy forces, but as the temperature field evolves toward the steady-state solution, the propagated velocity magnitude differences (Figure 8(B),(D)), concentrate mainly at the bottom-right and top-left corners (Figure 8(C),(F)).

4.1 | Local Nusselt number

The local Nusselt number distribution along the isothermal walls under the different approximations are plotted in Figure 9 at $Ra = 10^6$, $Pr = 0.71$, and $\varepsilon = 0.3$ for different geometries. As seen, the local Nusselt number distributions versus surface length is reversal for two isothermal walls. This may be attributed to the increasing and decreasing thermal boundary layer thickness along the isothermal walls in flow direction for the left and right walls, respectively. For

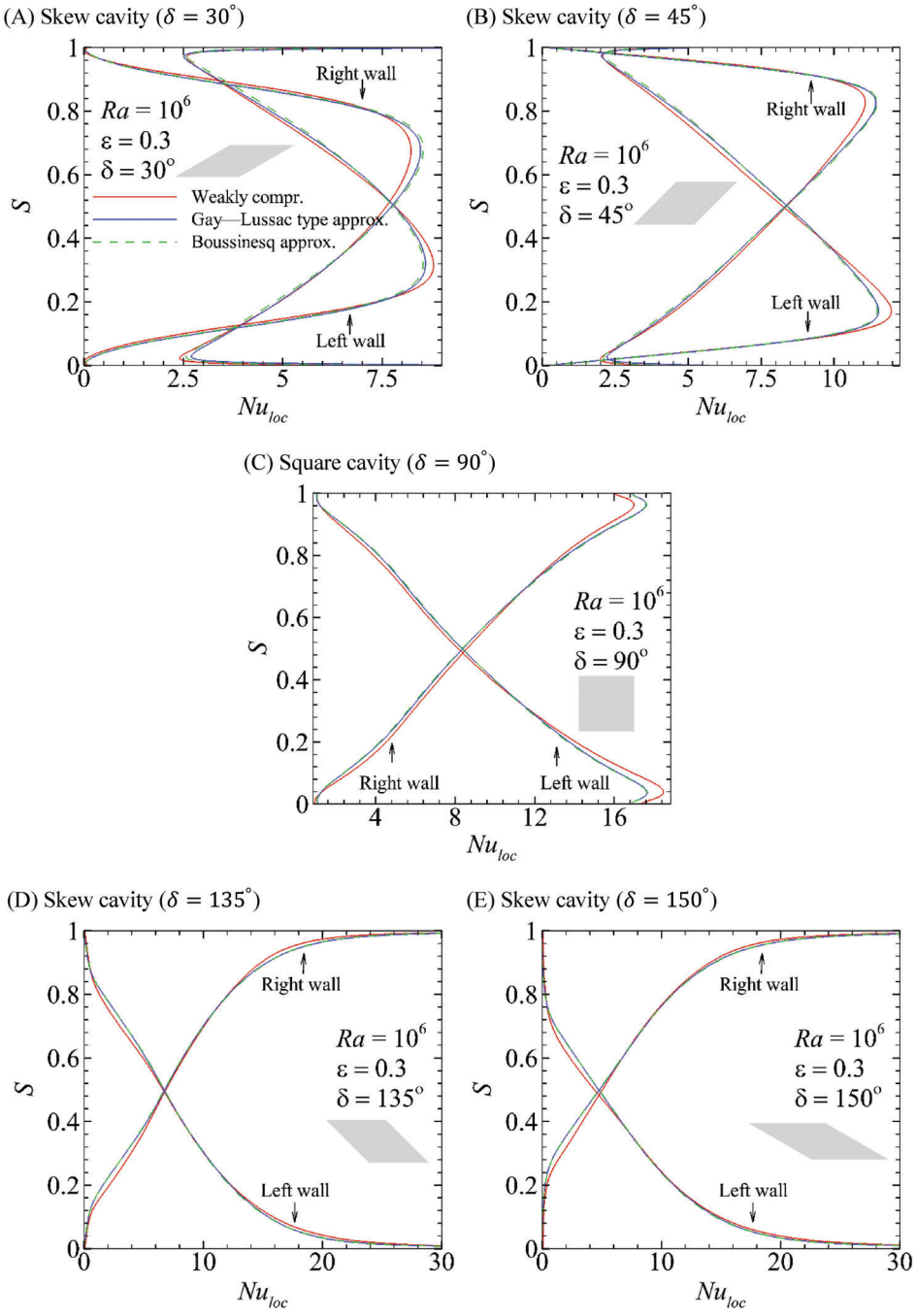

FIGURE 9 Local Nusselt number distribution along the isothermal walls at Ra = 10^6, Pr = 0.71, and $\varepsilon = 0.3$ in square and skew cavities with δ values as stated, (A) $\delta = 30^{\circ}$, (B) $\delta = 45^{\circ}$, (C) $\delta = 90^{\circ}$, (D) $\delta = 135^{\circ}$ and (E) $\delta = 150^{\circ}$ [Color figure can be viewed at wileyonlinelibrary.com]

the square cavity, there is a monotonic distribution of the local Nusselt number with a local optimum at bottom-left and top-right corners but for the right skewed cavity ($\delta = 30^{\circ}$ and 45°) this changes to a sharp oscillating behavior having smaller local Nusselt number with an optimum location at the middle height of the isothermal walls. For the left skewed cavity ($\delta = 135^{\circ}$ and 150°), there is a decreasing and increasing distribution of the local Nusselt number with no optimum location. Indeed, local Nusselt number distribution in the left-skewed cavity mimics behavior of natural convection along a vertical plate in free space. Comparing local Nusselt number distributions along the isothermal walls show a clear mismatch between incompressible and compressible approximations with slightly closer results to the compressible approach for the Gay–Lussac approximation. For the square and right skew cavities, the mismatch is more visible around the optimum location of the local Nusselt number distributions but for the left skewed cavity, the mismatch mostly occurs at the top-left and bottom-right regions. Since the difference of the local Nusselt number distributions becomes smaller by decreasing the relative temperature difference, results for the lower values of this parameter are not presented for the sake of brevity.

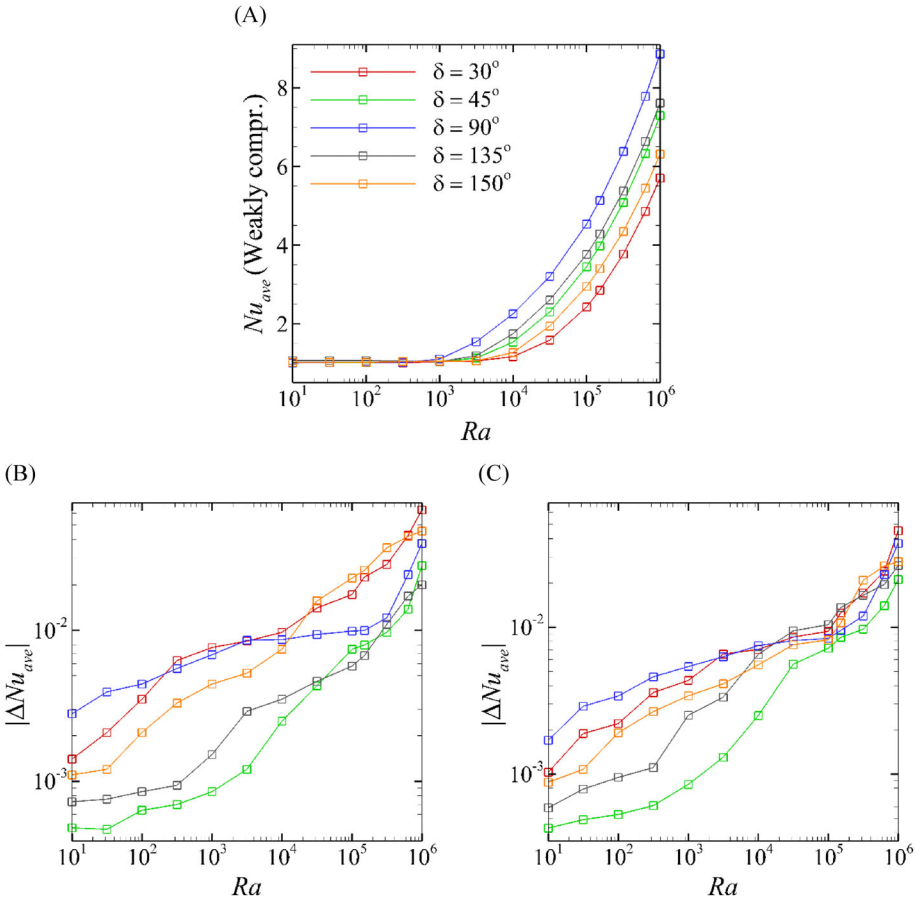

FIGURE 10 A plot of average Nusselt number against Rayleigh number at Pr = 0.71 and $\varepsilon = 0.3$ in square and skew cavities with δ values as stated, (A) Average Nusselt number for different skewness angles under the LMS approximation, (B) Absolute average Nusselt number differences between the Gay–Lussac and LMS approximations, (C) Absolute average Nusselt number differences between the Boussinesq and LMS approximations [Color figure can be viewed at wileyonlinelibrary.com]

4.2 | Average Nusselt number

The variations of the average Nusselt number across $10^1 \leq \mathrm{Ra} \leq 10^6$ is studied at the highest relative temperature difference in this study ($\varepsilon = 0.3$) under the different approximations in Figure 10. Average Nusselt number under the LMS approximation for different geometries ($\delta = 30^\circ$, 45°, 90°, 135°, and 150°) is plotted in Figure 10(A). As expected, the average Nusselt number augments by increasing the Rayleigh number. Since the values of the average Nusselt number under the different approximations are so close together, the absolute average Nusselt number differences between the LMS and two incompressible approximations are plotted in Figure 10(B),(C). Negligible differences between the average Nusselt numbers of compressible and incompressible approximations stems from opposite behavior of the local Nusselt number distributions. For instance, in square cavity problem (Figure 9(C)), the approximation that has a lower local Nusselt number distribution along $0 \leq S \leq 0.5$ has a larger value at $0.5 \leq S \leq 1$ and vice versa. This nullifies the difference of the local Nusselt number distribution and gives a small difference of the average Nusselt number for compressible and incompressible approaches. However, the total differences of the average Nusselt number for both incompressible approximations increases by increasing the Rayleigh number, but it never exceeds 10^{-1} in considered range of ε and Ra in this study. The small difference of the average Nusselt number between the Boussinesq and Gay–Lussac approximations comes from close results of the local Nusselt number distribution for this two approaches as they are almost attached together up to $\varepsilon = 0.3$ in all presented local Nusselt number distribution in Figure 9. Finally, comparing the average Nusselt number slope versus the Rayleigh number in Figure 10(A) reveals that, skewing cavity decreases the total rate heat transfer. Reduction of the average Nusselt number is more sensible for the right-skewed cavity compared to the left one.

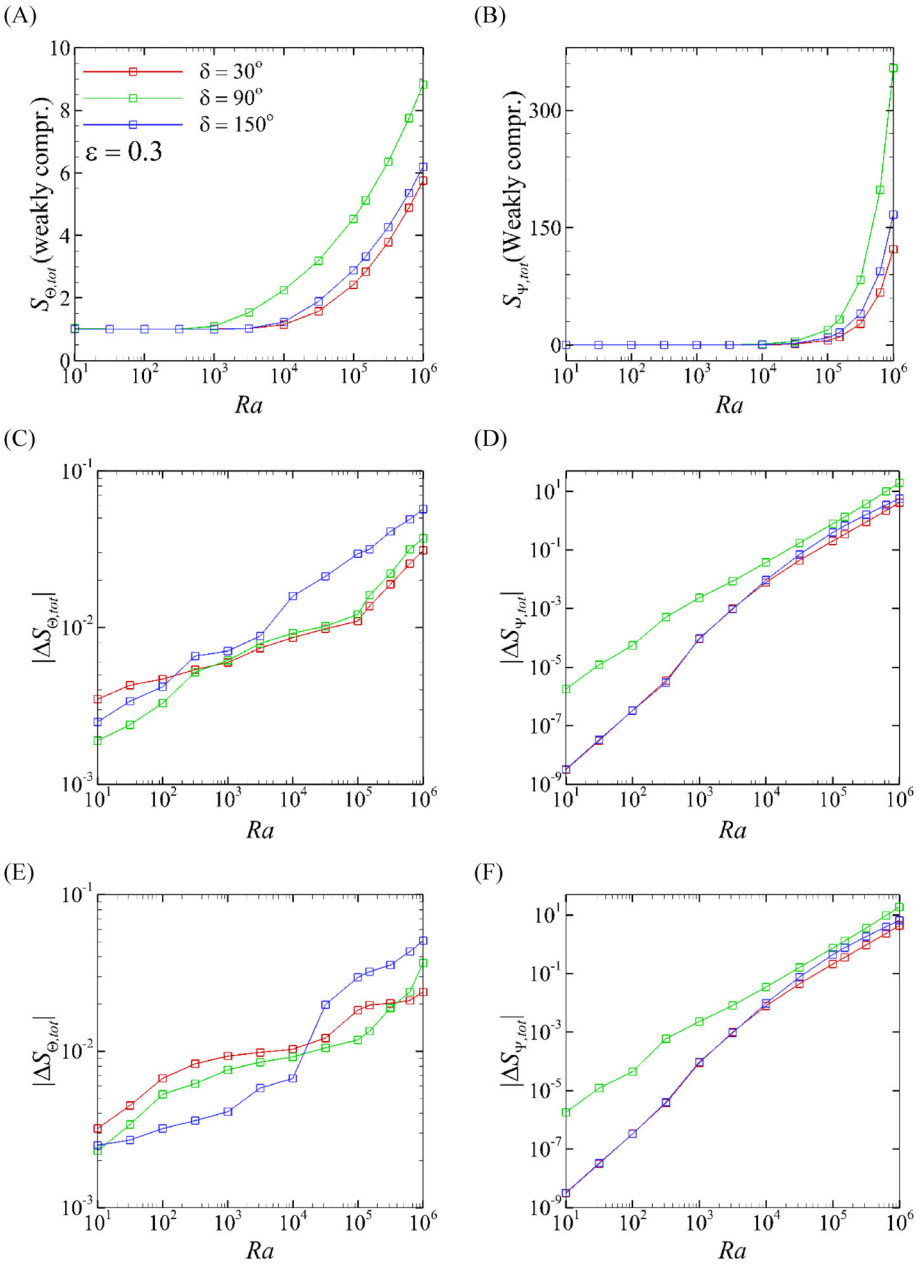

FIGURE 11 A plot of total entropy generation due to heat transfer ($S_{\Theta,\,tot}$) and fluid friction ($S_{\psi,\,tot}$) against the Rayleigh number at Pr = 0.71 and ε = 0.3, (A) $S_{\Theta,\,tot}$ under the LMS approximation at three different angles, (B) $S_{\psi,\,tot}$ under the LMS approximation at three different angles, (C) Absolute difference of $S_{\Theta,\,tot}$ between the Gay–Lussac and LMS approximations, (D) Absolute difference of $S_{\psi,\,tot}$ between the Gay–Lussac and LMS approximations, (E) Absolute difference of $S_{\Theta,\,tot}$ between the Boussinesq and LMS approximations, (F) Absolute difference of the $S_{\psi,\,tot}$ between the Boussinesq and LMS approximations [Color figure can be viewed at wileyonlinelibrary.com]

4.3 | Entropy generation

Total entropy generation due to heat transfer ($S_{\Theta,\,tot}$) and fluid friction ($S_{\psi,\,tot}$) is investigated over $10^1 \leq Ra \leq 10^6$ at $\varepsilon = 0.3$ for three different geometries (square cavity and skew cavity with $\delta = 30^\circ$ and $\delta = 150^\circ$) in Figure 11. Similar to previous section, results are plotted for the LMS approximation as reference solution in Figure 11(A),(B) and the difference of compressible and incompressible approximations are plotted in Figure 11(C)–(F). Comparing results in Figure 11(A), (B) indicate that, the growth rate of $S_{\psi,\,tot}$ is much faster than $S_{\Theta,\,tot}$. Indeed, the magnitude of $S_{\Theta,\,tot}$ for $Ra \leq 10^3$ is at least two order larger than $S_{\psi,\,tot}$. This means for all geometries at least up to $Ra = 10^3$, most of the irreversibility is due to heat transfer. For $Ra \geq 10^4$ the growth rate of $S_{\Theta,\,tot}$ versus Rayleigh number remains almost constant (linear growth rate) while $S_{\psi,\,tot}$ shows an exponential growth rate. Larger magnitude of $S_{\psi,\,tot}$ compared to the $S_{\Theta,\,tot}$ for $Ra \geq 10^4$ indicates that most of the irreversibilities at this range of the Rayleigh number is due to fluid friction. Comparing heat transfer and fluid friction irreversibilities of the compressible and incompressible approaches shows a negligible difference for $S_{\Theta,\,tot}$ for both incompressible approximations in Figure 11(C), (E) across the investigated range of the Rayleigh number while a clear mismatch is observable for $S_{\psi,\,tot}$ at $Ra \geq 10^5$ in Figure 11(D), (F). This mismatch may be attributed

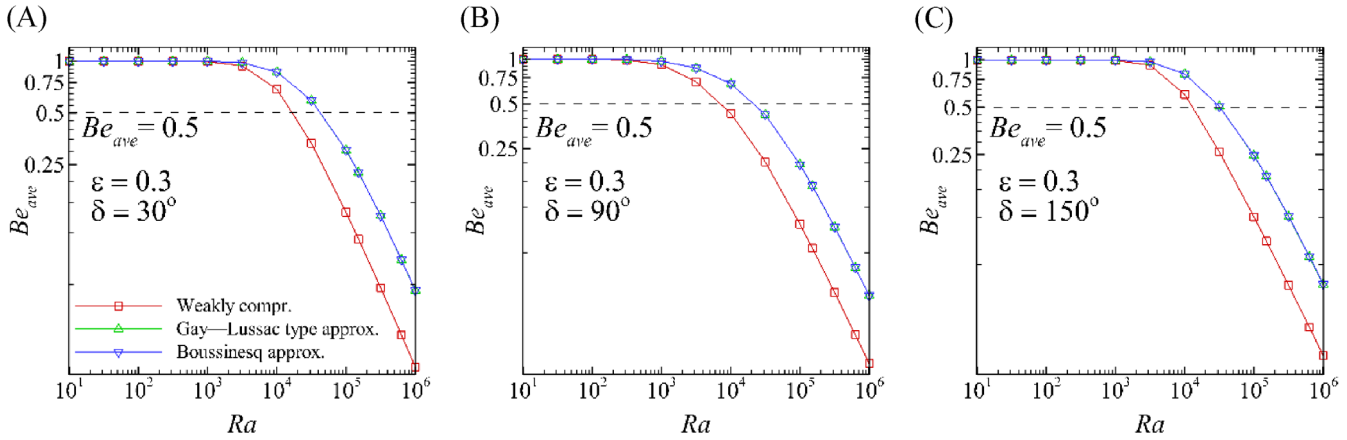

FIGURE 12 A plot of average Bejan number against Rayleigh number at $\varepsilon = 0.3$ in different geometries, (A) Right skew cavity ($\delta = 30^{\circ}$), (B) Square cavity, (C) Left skew cavity ($\delta = 150^{\circ}$) [Color figure can be viewed at wileyonlinelibrary.com]

to the divergence free flow field of incompressible approximation, which removes the last term of Equation (18). The difference of $S_{\Theta,\,\mathrm{tot}}$ and $S_{\psi,\,\mathrm{tot}}$ between the Boussinesq and Gay–Lussac-type approximations is also negligible in investigated range of Ra and ε. Finally, obtained results for $S_{\Theta,\,\mathrm{tot}}$ in different geometries plotted in Figures 11(A) show almost a similar trend for square and skew cavities with a sooner start of $S_{\Theta,\,\mathrm{tot}}$ growth versus Ra in square cavity. Results of $S_{\psi,\,\mathrm{tot}}$ in Figures 11(B) indicates skewing cavity causes delay to start of the exponential growth rate of this parameter, which is in agreement with later start of $\mathrm{Nu_{ave}}$ growth versus Ra for skew cavity compared to the square cavity in Figure 10.

Variations of the average Bejan number is investigated over $10^1 \leq \mathrm{Ra} \leq 10^6$ at $\varepsilon = 0.3$ for three different geometries in Figure 12. As seen, by increasing the Rayleigh number, the average Bejan number is decreased. This is because by increasing the Rayleigh number, thermal convection increasingly becomes the dominant mechanism driving the flow. The interesting feature of the average Bejan number is its transition to a value lower than 0.5 which indicates transition of dominant heat transfer mechanism from conduction to convection. Obtained average Bejan number in square cavity (Figure 12(B)) at $\mathrm{Ra} = 10^4$ under the LMS approximation shows a value less than 0.5, while incompressible approximations are showing values larger than 0.5 which means when temperature differences are large enough, the real heat transfer mechanism is convection dominated while incompressible approaches are approximating that as a conduction dominated regime. For skew cavities, this is occurring at higher Rayleigh number. In other words, incompressible approaches show a delay in predicting convection dominated regime at large temperature differences as the difference of the average Bejan number under different approximations becomes less in high Rayleigh numbers. As seen in Figure 12, $\mathrm{Be_{ave}}$ values versus Ra, start to deviate between compressible and incompressible approaches at $\mathrm{Ra} = 10^3$ for all geometries. Finally, similar to the average Nusselt number, both incompressible approximations are showing almost identical results for average Bejan number across investigated ranges of ε and Ra.

4.4 | Coefficient friction

Local coefficient friction along the isothermal walls is investigated for square and skew cavities ($\delta = 30^{\circ}$ and 150°) at $\mathrm{Ra} = 10^6$, $\varepsilon = 0.15$ and $\varepsilon = 0.3$ under different approximations in Figure 13. Results are showing a considerable mismatch between the weakly compressible approach and incompressible approximations. A comparison among C_f results at $\varepsilon = 0.15$ (Figure 13(A), (C), and (E)) and $\varepsilon = 0.3$ (Figure 13(B), (D) and (F)) reveals that this discrepancy augments by increasing the relative temperature differences. Indeed, by increasing the relative temperature difference, incompressible approximations show more deviations from the compressible approach. Presented results in Figure 13 indicate that extending the density variations to the advection term does not impose a significant impact on the local coefficient friction as C_f results of incompressible approximations are attached together in most of the regions. For the square cavity (Figure 13(C), (D)), the Gay–Lussac-type approximation is predicting slightly more accurate distribution of C_f with a visible difference around the maximum location of this parameter along the right wall at around $S \cong 0.3$ while the Boussinesq

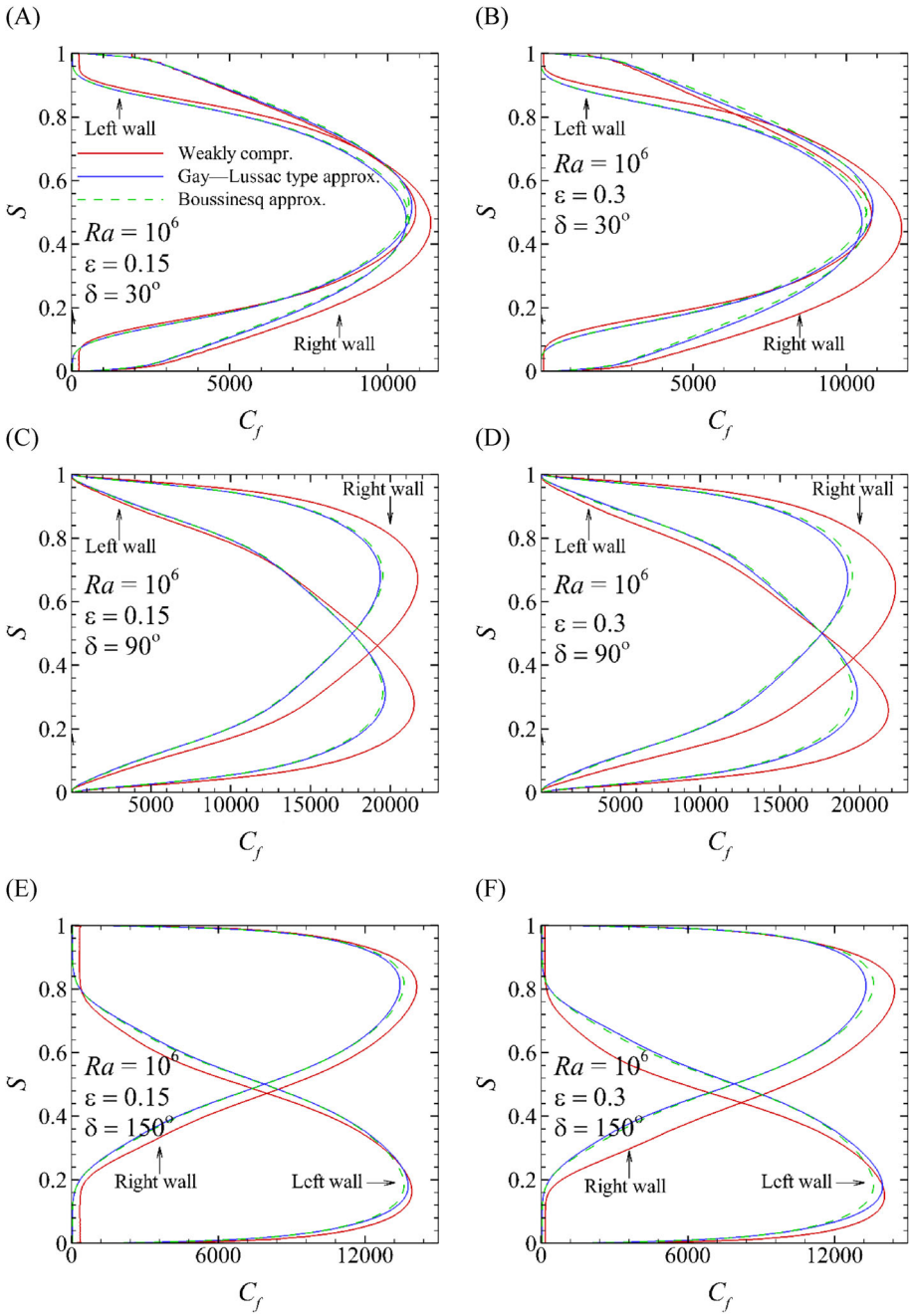

FIGURE 13 Local coefficient friction distributions along the isotherm walls at Ra = 10^6, $\varepsilon = 0.15$, and $\varepsilon = 0.3$ as stated, (A, B) Square cavity, (C, D) Right skew cavity ($\delta = 30^\circ$), (E, F) Left skew cavity ($\delta = 150^\circ$) [Color figure can be viewed at wileyonlinelibrary.com]

approximation is showing slightly more accurate distribution of C_f around the maximum location of this parameter along the left wall at around $S \cong 0.7$. This scenario is also valid for both of the right (Figure 13(A),(B)) and left (Figure 13(E),(F)) skew cavities with different locations of maximum differences.

Local coefficient friction along the horizontal adiabatic walls is also plotted for mentioned geometries at Ra = 10^6, $\varepsilon = 0.15$ and $\varepsilon = 0.3$ under different approximations in Figure 14. X_T and X_B in Figure 14(C)–(F) refer to the top and bottom horizontal adiabatic walls of the skew cavity, respectively. Presented results in Figure 14 show more deviation between the Boussinesq and Gay–Lussac-type approximations both deviating from the weakly compressible approach. In square cavity (Figure 14(C) and (D)), Gay–Lussac-type approximation is giving more accurate C_f results along the bottom wall at around $X \cong 0.85$ while the Boussinesq approximation is giving closer results to LMS approximation along the top wall at around $X \cong 0.2$. In rest of the regions, C_f results of the Boussinesq approximation lays between LMS and Gay-Lussac type approximations which means it is working better than the Gay–Lussac-type approximation in this part. This behavior is more clear at $\varepsilon = 0.3$ compared to the $\varepsilon = 0.15$. C_f results of incompressible approaches for right skew cavity with $\delta = 30^\circ$ (Figure 14(A),(B)) do not show much difference at $\varepsilon = 0.15$ but superior prediction of the Gay-Lussac

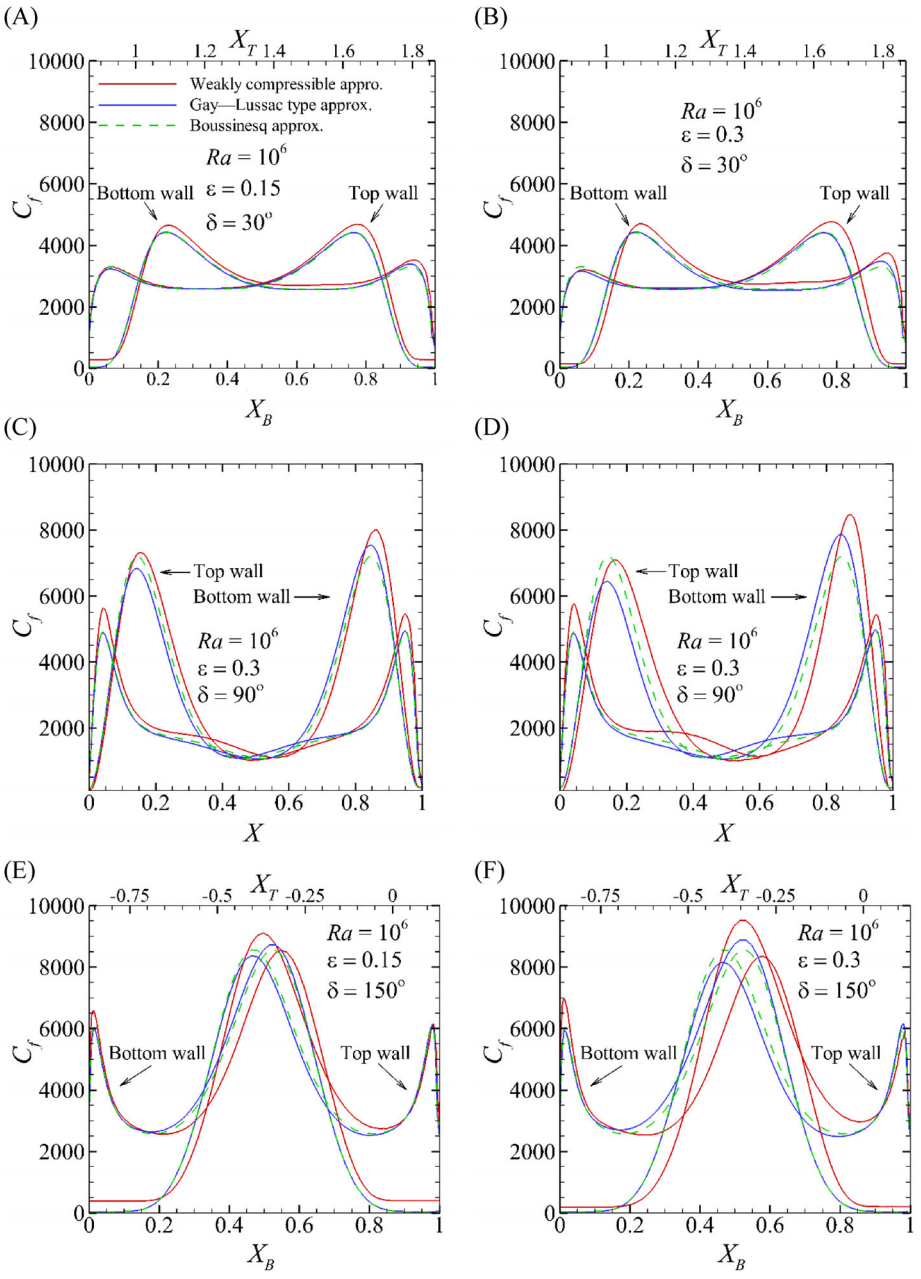

FIGURE 14 Local coefficient friction distributions along the horizontal adiabatic walls at Ra = 10^6, $\varepsilon = 0.15$, and $\varepsilon = 0.3$, (A, B), Square cavity, (C, D), Right skew cavity ($\delta = 30^\circ$), (E, F), Left skew cavity ($\delta = 150^\circ$) [Color figure can be viewed at wileyonlinelibrary.com]

type approximation in predicting maximum C_f at down-right region is clear. By increasing the relative temperature difference to 0.3, the difference of incompressible approximations becomes clear. Similar to the square cavity, C_f results of the Boussinesq approximation lays between two other approaches along the bottom wall but still superior prediction of C_f along the bottom wall at around $X_B \cong 0.95$ is valid. Increasing the relative temperature difference to 0.3 pushes the C_f results of the Gay-Lussac type approximation between two other approaches along the top wall in this geometry. Finally, for the left skew cavity with $\delta = 150^\circ$ (Figure 14(E),(F)), the difference of the C_f results along the horizontal adiabatic walls is clear between incompressible approximations for both of $\varepsilon = 0.15$ and 0.3. In this geometry, predicted C_f results along the top wall by the Gay-Lussac type approximations is more accurate up to $X_T \cong 0.4$ while after that Boussinesq approximation is showing closer results to the LMS approximation. In addition, predicted C_f results along the bottom wall by the Gay-Lussac type approximations is more accurate up to $X_B \cong 0.2$ while after that Boussinesq approximation is working better up to $X_B \cong 0.6$ where the Gay–Lussac-type approximation recovers its greater performance after that up to $X_B \cong 0.65$. For $X_B > 0.65$, C_f values of incompressible approximations are attached and they show almost no difference.

4.5 | Computational cost and convergence rate analysis

In this section, the advantage of solving equation in secondary variables form is discussed in the context of the computational cost and convergence rate. Whole of the numerical solution procedure using second-order Adams–Bashforth/Crank–Nicolson temporal scheme may be summarized in five successive steps through Equations (29)–(33) that is explained in brief in Section 3:

$$\psi^{n+1} = -[\mathrm{D}]^{-1} \times \omega^{n}. \tag{34}$$

$$\omega^{*} = \omega^{n} + \Delta t \left(-\frac{3}{2}(1 - 2\varepsilon\overline{\overline{\Theta^{n}}})\underbrace{N(\omega^{n})}_{\substack{\text{Central}\\ \text{Upwind}}} + \frac{1}{2}(1 - 2\varepsilon\overline{\overline{\Theta^{n-1}}})\underbrace{N(\omega^{n-1})}_{\substack{\text{Central}\\ \text{Upwind}}} + (\mathrm{Pr}/2)\underbrace{\mathrm{D}(\omega^{n})}_{\text{Central}} + \mathrm{Ra.\,Pr}.\overline{\overline{(\partial\Theta/\partial X)^{n}}} \right). \tag{35}$$

$$\omega^{n+1} = -[(\mathrm{Pr}/2)\mathrm{D} - (1/\Delta t)I]^{-1} \times (1/\Delta t)\omega^{*}. \tag{36}$$

$$\Theta^{*} = \Theta^{n} + \Delta t \left(-\frac{3}{2}\underbrace{N(\Theta^{n})}_{\text{Central/Upwind}} + \frac{1}{2}\underbrace{N(\Theta^{n-1})}_{\text{Central/Upwind}} + \frac{1}{2}\underbrace{D(\Theta^{n})}_{\text{Central}} \right). \tag{37}$$

$$\Theta^{n+1} = -[(1/2)D - (1/\Delta t)I]^{-1} \times (1/\Delta t)\Theta^{*} \tag{38}$$

These equations regarding boundary conditions are solved in a loop until the maximum difference of scalar variables satisfy stop criteria which is defined in Section 3 as 10^{-7}. Among three equations in the secondary variables form, the stream function equation is the only linear equation (Poisson equation) which its solution in each iteration is straightforward. To make the solution procedure as fast as possible, inverse matrix of Laplacian operator ($[D]^{-1}$) with a zero Dirichlet boundary condition for stream-function along the walls of the cavity is constructed by CVFEM solver and it is multiplied by the vorticity vector in each iteration to update stream function field. For two other nonlinear equations, that is, vorticity and energy equations, two possible scenarios are considered in which, the nonlinear advection and convection terms are discretized via upwind or central schemes. This is a benefit of solving governing equations in secondary variables form to approximate the nonlinear terms in vorticity and energy equations by central scheme even for convection-dominated regimes. In other words, applying central scheme for primitive variables at convection-advection dominated regimes will lead to diverging solution procedure. The diffusion terms due to their elliptical nature are discretized using central scheme. In addition, temperature prefactor, that is, $(1 - 2\varepsilon\Theta)$ and source term of vorticity equation (which are shown by an overbar) are lagged from the current and last update of the temperature fields. Similar to the stream function equation, an inverse Laplacian matrix is constructed for correction steps of the vorticity and energy equations, that is, Equations (31) and (33) to accelerate the solution procedure.

For comparison purposes, required computational time and convergence rate is shown in Figure 15 for square cavity at $\mathrm{Ra} = 10^{2}$ and $\varepsilon = 0.3$ for a mesh file having 10 k elements. This Rayleigh number lays in conduction dominated regime and it is possible to apply both upwind and central schemes for nonlinear terms of the governing equations in primitive variables. Another reason to pick this low Rayleigh number is obtaining the minimum computational time due to applying different approaches since required iterations (and consequently computational time) is increased by increasing the Rayleigh number. CPU-time of submitted jobs for all cases are measured by Monash University super-computer facilities (MonARCH). Obtained CPU-time show a 8.5% less and a 3.4% more computational cost for central and second-order-upwind schemes, respectively, when governing equations are solved via secondary variables rather than primitive variables. It should be noted that two momentum equations in secondary variable form are merged to one vorticity equation. In other words, in secondary variables form, one less equation is solved. As mentioned earlier, this is the *minimum* difference as required iterations and consequently computational time increases at higher Rayleigh numbers. In Figure 15(A), required CPU-time for upwind scheme is considerably more than central scheme. This is due to higher computational cost of determining flow direction and nodes located at upstream to approximate fluxes at each integration point. Presented data in Figure 15(A) suggests that upwind scheme is not suitable/recommended for the numerical solution of the governing equations in secondary variables form.

Convergence rates of the different schemes are compared in Figures 15(B)–(F) for different schemes in both secondary and primitive variables. Obtained results indicate that primitive variables in both cases (upwind and central schemes)

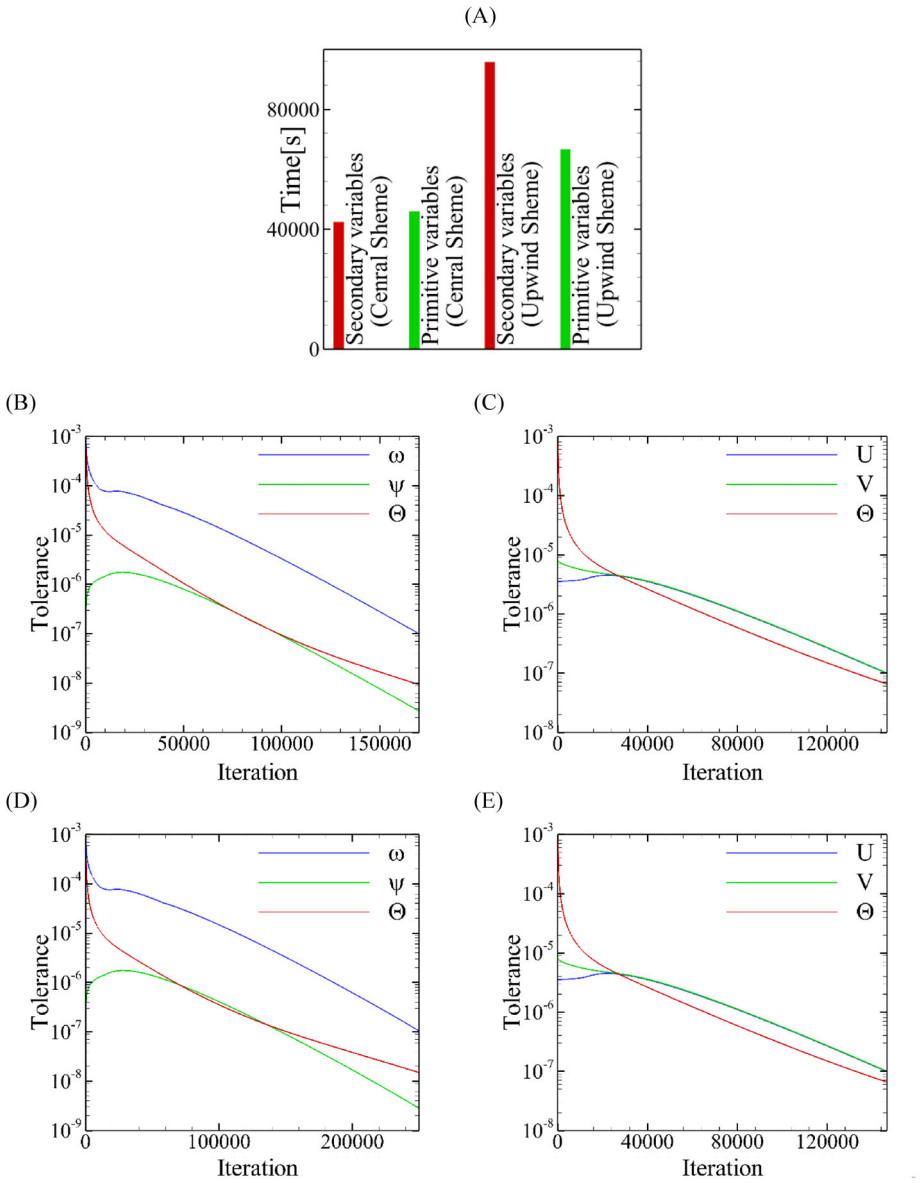

FIGURE 15 Computational cost and convergence rate of the computations for square cavity at $Ra = 10^2$ and $\varepsilon = 0.3$ using primitive and secondary variables, (A) CPU-time, (B) convergence rate of the secondary variables; central scheme, (C) convergence rate of the primitive variables; central scheme, (D) convergence rate of secondary variables; second-order upwind, (E) convergence rate of the primitive variables; second-order upwind. For all cases, a global time-step of 10^{-6} ($dt = 10^{-6}$) is used for calculations [Color figure can be viewed at wileyonlinelibrary.com]

have faster convergence rate but lower computational cost of secondary variables causes the solution procedure to be finalized before than primitive variables.

5 | CONCLUSION

In this paper, a new secondary-variable formulation for natural convection is applied to the square and skew cavity benchmark problems up to $Ra = 10^6$ and $\varepsilon = 0.3$ at $Pr = 6.14$. The formulation is derived based on considering density variations in the advection term of the momentum equations in addition to the gravity term, offering an improved description of convection in rapidly rotating regions of the flow. A Froude number proportional to the relative temperature difference is derived describing the deviation from the Boussinesq approximation. It is also shown that the Gay–Lussac parameter (also relating to deviation from the Boussinesq approximation) may be expressed by an equivalent relative temperature difference. Comparing stream-function fields for a physically meaningful range of the relative temperature difference versus both a weakly compressible approach and the Boussinesq approximation indicates that the new formulation gives consistent and slightly superior flow-related data. Results obtained for local Nusselt number distribution from the proposed formulation shows that the Gay–Lussac-type approximations still require modifications to yield accurate results comparable to the compressible approach. However, for considered problems in this study, a reversal of the local Nusselt

number distributions along the two isothermal walls nullifies the mismatch of the average Nusselt number between the compressible and incompressible solutions. An entropy generation analysis indicates that both of the Boussinesq and Gay–Lussac-type approximations show a considerable mismatch of Bejan number at middle Rayleigh number and high relative temperature differences. However, this mismatch becomes less at high Rayleigh numbers. Comparing coefficient friction results of the weakly compressible and incompressible approximations at high-relative temperature differences indicate that extending the density variations to the advection terms does not significantly increase the quality of flow field in all regions compared to the Boussinesq approximation. Finally, a computational cost analysis indicates that primitive variables have faster convergence rate but applying a central scheme for nonlinear terms and one less equation in the secondary variable form leads to the less computational cost.

ACKNOWLEDGEMENTS

This research was supported by the Australian Research Council through Discovery Projects DP150102920 and DP180102647. Peyman Mayeli is supported by a Monash Graduate Scholarship and a Monash International Postgraduate Research Scholarship. The authors are also supported by time allocations on the National Computational Infrastructure (NCI) peak facility and the Pawsey Supercomputing Centre through NCMAS grants. NCI is supported by the Australian Government.

NOMENCLATURE

B	buoyancy term
$\mathrm{Be}_{\mathrm{ave}}$	average Bejan number
c_f	skin friction coefficient
D	diffusion operator
e_g	unit vector in gravity direction
Fr	Froude number
g	gravitational acceleration
Ga	Gay–Lussac number ($\beta\Delta\theta$)
L_{ref}	reference length
$\mathrm{Nu}_{\mathrm{ave}}$	average Nusselt number
$\mathrm{Nu}_{\mathrm{loc}}$	local Nusselt number
p	pressure
p^*	modified pressure
P	dimensionless pressure
P_{th}	thermodynamic pressure
Pr	Prandtl number
R	ideal gas constant
Ra	Rayleigh number
S	surface
S_Θ	entropy generation due to heat transfer
S_ψ	entropy generation due to fluid friction
T	temperature
$\boldsymbol{x}$	coordinate vector
$\boldsymbol{X}$	dimensionless coordinate vector
$\boldsymbol{u}$	velocity vector
$\boldsymbol{U}$	dimensionless velocity vector
α	thermal diffusivity
β	isobaric expansion coefficient
δ	angle of skew cavity
ε	relative temperature difference
θ	physical temperature
Θ	dimensionless temperature
μ	dynamic viscosity
ν	kinematic viscosity
ρ	density

ρ_0	reference density
τ_w	wall shear stress
ϕ	gravitational potential
χ	irreversibility distribution ratio
ψ	stream-function
ω	vorticity

SUBSCRIPT

ave	average
c	cool
h	hot
loc	local
ref	reference
tot	total

SUPERSCRIPT

n	current time-step
$n-1$	previous time-step
$-$	refers to a lagged value

DATA AVAILABILITY STATEMENT

Data sharing is not applicable to this article as no new data were created in this study.

ORCID

Peyman Mayeli https://orcid.org/0000-0003-4084-2627

REFERENCES

1. Boussinesq J. *Theorie Analytique de la Chaleur*. Vol II. Paris: Gauthier-Villars; 1903.
2. de Vahl Davis G. Natural convection of air in a square cavity, a benchmark numerical solution. *Int J Numer Methods Fluids*. 1983;3:249-264. https://doi.org/10.1002/fld.1650030305.
3. Lage JL, Bejan A. The Ra-Pr domain of laminar convection in an enclosure heated from the side. *Numer Heat Transf A*. 1991;19:21-41. https://doi.org/10.1080/10407789108944836.
4. Mohamad A, Sheremet MA, Taler J, Ocłoń P. Natural convection in differentially heated enclosures subjected to variable temperature boundaries. *Int J Numer Methods Heat Fluid Flow*. 2019;29(11):4130-4141. https://doi.org/10.1108/HFF-02-2019-0137.
5. Shermet M, Groson T, Pop I. MHD free convection flow in an inclined square cavity filled with both nanofluids and gyrotactic microorganisms. *Int J Numer Methods Heat Fluid Flow*. 2019;29(12):4642-4659. https://doi.org/10.1108/HFF-03-2019-0264.
6. Wan DC, Patnail BSV, Wei GW. A new benchmark quality solution for the buoyancy-driven cavity by discrete singular convolution. *Numer Heat Transf B*. 2001;40:199-228. https://doi.org/10.1080/104077901752379620.
7. Ashrafizadeh A, Nikfar M. On the numerical solution of generalized convection heat transfer problems via the method of proper closure equations–Part II: application to test problems. *Numer Heat Transf B*. 2016;70(2):204-222. https://doi.org/10.1080/10407782.2016.1173467.
8. Bondareva NS, Sheremet MA, Oztop HF, Abu-Hamdeh N. Free convection in an open triangular cavity filled with a nanofluid under the effects of Brownian diffusion. thermophoresis and local heater. *J Heat Transf T ASME*. 2018;140(4):042502. https://doi.org/10.1115/1.4038192.
9. Varol Y, Koca A, Oztop HF. Natural convection in a triangle enclosure with flush mounted heater on the wall. *Int Comm Heat Mass Transf*. 2006;33(8):951-958. https://doi.org/10.1016/j.icheatmasstransfer.2006.05.003.
10. Rahman MM, Alam MS, Al-Salti N, Eltayeb IA. Hydromagnetic natural convective heat transfer flow in an isosceles triangular cavity filled with nanofluid using two-component nonhomogeneous model. *Int J Therm Sci*. 2016;107:272-288. https://doi.org/10.1016/j.ijthermalsci.2016.04.009.
11. Bhowmick S, Xu F, Zhang X, Saha SC. Natural convection and heat transfer in a valley shaped cavity filled with initially stratified water. *Int J Therm Sci*. 2018;128:59-69. https://doi.org/10.1016/j.ijthermalsci.2018.02.019.
12. Wu YL, Liu GR, Gu YT. Application of meshless local Petrov-Galerkin (MLPG) approach to simulation of incompressible flow. *Numer Heat Transf B*. 2005;48(5):459-475. https://doi.org/10.1080/10407790500324763.
13. Abu-Nada E, Masoud Z, Hijazi A. Natural convection heat transfer enhancement in horizontal concentric annuli using nanofluids. *Int Comm Heat Mass Transf*. 2008;35:657-665. https://doi.org/10.1016/j.icheatmasstransfer.2007.11.004.
14. Ashorynejad HR, Mohamad AA, Sheikholeslami M. Magnetic field effects on natural convection flow of a nanofluid in a horizontal cylindrical annulus using lattice Boltzmann method. *Int J Therm Sci*. 2013;64:240-250. https://doi.org/10.1016/j.ijthermalsci.2012.08.006.

15. Paillere H, Viozat C, Kumbaro A, Toumi I. Comparison of low mach number models for natural convection problems. *Heat Mass Transf*. 2000;36:567-573. https://doi.org/10.1007/s002310000116.
16. Szewc K, Pozorski J, Tanière A. Modelling of natural convection with smoothed particle hydrodynamics: non-Boussinesq formulation. *Int J Heat Mass Transf*. 2011;54:4807-4816. https://doi.org/10.1016/j.ijheatmasstransfer.2011.06.034.
17. Niajalili H, Mayeli P, Naghashzadegan M, Poshtiri AH. Techno-economic feasibility of off-grid solar irrigation for a rice paddy in Guilan province in Iran: a case study. *Sol Energy*. 2017;150:456-557. https://doi.org/10.1016/j.solener.2017.05.012.
18. Vierendeels J, Merci B, Dick E. Numerical study of natural convective heat transfer with large temperature differences. *In J Numer Methods Heat Fluid Flow*. 2001;11(4):329-341. https://doi.org/10.1108/09615530110389117.
19. Fu W, Li C, Huang C, Huang J. An investigation of a high temperature difference natural convection in a finite length channel without Bossinesq assumption. *Int J Heat Mass Transf*. 2009;52:2571-2580. https://doi.org/10.1016/j.ijheatmasstransfer.2009.01.012.
20. S. Busto, M. Tavelli, W. Boscheri, M. Dumbser, Efficient high order accurate staggered semi-implicit discontinuous Galerkin methods for natural convection problems. *Comput Fluids*. 2020;198:104399. https://doi.org/10.1016/j.compfluid.2019.104399.
21. Bermúdez A, Busto S, Dumbser M, Ferrín JL, Saavedra L, Vázquez-Cendón ME. A staggered semi-implicit hybrid FV/FE projection method for weakly compressible flows. *J Comput Phy*. 2020;421:109743. https://doi.org/10.1016/j.jcp.2020.109743.
22. Paolucci S. *On the Filtering of Sound from the Navier-Stokes Equations, Technical Report SAND 82–8257*. Vol 9. Livermore, CA: Sandia National Laboratories; 1982.
23. Vierendeels J, Merci B, Dick E. A multigrid method for natural convective heat transfer with large temperature differences. *J Comput Appl Math*. 2004;168(1–2):509-517. https://doi.org/10.1016/j.cam.2003.08.081.
24. Becker R, Braack M. Solution of a stationary benchmark problem for natural convection with large temperature difference. *Int J Therm Sci*. 2002;41(5):428-439. https://doi.org/10.1016/S1290-0729(02)01335-2.
25. Pesso T, Piva S. Laminar natural convection in a square cavity: low Prandtl numbers and large density differences. *Int J Heat Mass Transf*. 2009;52(3–4):1036-1043. https://doi.org/10.1016/j.ijheatmasstransfer.2008.07.005.
26. Lopez JM, Marques F, Avila M. The Boussinesq approximation in rapidly rotating flows. *J Fluid Mech*. 2013;737:56-77. https://doi.org/10.1017/jfm.2013.558.
27. Mayeli P, Sheard G. A new formulation for Boussinesq-type natural convection flows applied to the annulus cavity problem. *Int J Numer Methods Fluids*. 2020;93(3):683-702. https://doi.org/10.1002/fld.4904.
28. Osorio A, Avila R, Cervantes J. On the natural convection of water near its density inversion in an inclined square cavity. *Int J Heat Mass Transf*. 2004;47(19–20):4491-4495. https://doi.org/10.1016/j.ijheatmasstransfer.2004.06.003.
29. Souza M, Miranda R, Machado H. Natural convection in enclosures with variable fluid properties. *Int J Numer Methods Heat Fluid Flow*. 2003;13(8):1079-1096. https://doi.org/10.1108/09615530310501966.
30. Chenoweth DR, Paolucci S. Natural convection in an enclosed vertical air layer with large horizontal temperature differences. *JFM*. 1986;169:173-210. https://doi.org/10.1017/S0022112086000587.
31. Basak T, Kaluri RS, Balakrishnan AR. Effects of thermal boundary conditions on entropy generation during natural convection. *Numer Heat Transf A*. 2011;59(5):372-402. https://doi.org/10.1080/10407782.2011.549075.
32. Ilis GG, Mobedi M, Sunden B. Effect of aspect ratio on entropy generation in a rectangular cavity with differentially heated vertical walls. *Int Comm Heat Mass Transf*. 2008;35(6):696-703. https://doi.org/10.1016/j.icheatmasstransfer.2008.02.002.
33. Nayak RK, Bhattacharyya S, Pop I. Heat transfer and entropy generation in mixed convection of a nanofluid within an inclined skewed cavity. *Int Comm Heat Mass Transf*. 2016;102:596-609. https://doi.org/10.1016/j.ijheatmasstransfer.2016.06.049.
34. Bondareva NS, Sheremet MA, Oztop HF, Abu-Hamdeh N. Entropy generation due to natural convection of a nanofluid in a partially open triangular cavity. *Adv Powder Technol*. 2017;28:244-255. https://doi.org/10.1016/j.apt.2016.09.030.
35. Sheremet MA, Pop I, Oztop HF, Abu-Hamdeh N. Natural convection of nanofluid inside a wavy cavity with a non-uniform heating: entropy generation analysis. *In J Numer Methods Heat Fluid Flow*. 2017;27:958-980. https://doi.org/10.1108/HFF-02-2016-0063.
36. Astanina MS, Sheremet MA, Oztop HF, Abu-Hamdeh N. MHD natural convection and entropy generation of ferrofluid in an open trapezoidal cavity partially filled with a porous medium. *Int J Mech Sci*. 2018;136:493-502. https://doi.org/10.1016/j.ijmecsci.2018.01.001.
37. Mayeli P, Nili-Ahmadabadi M, Pirzadeh MR, Rahmani P. Determination of desired geometry by a novel extension of ball spine algorithm inverse method to conjugate heat transfer problems. *Comput Fluids*. 2017;154:390-406. https://doi.org/10.1016/j.compfluid.2016.05.022.
38. Hesami H, Mayeli P. Development of the ball-spine algorithm for the shape optimization of ducts containing nanofluid. *Numer Heat Transf A*. 2016;70(12):1371-1389. https://doi.org/10.1080/10407782.2016.1243976.
39. Nikfar M, Mayeli P. Surface shape design in different convection heat transfer problems via a novel coupled algorithm. *J Heat Transf-Trans ASME*. 2018;140(2):021702-1-021702-15. https://doi.org/10.1115/1.4037581.
40. Mayeli P, Hesami H, Moghaddam MHDF. Numerical investigation of the MHD forced convection and entropy generation in a straight duct with sinusoidal walls containing water-Al2O3 nanofluid. *Numer Heat Transf A*. 2017;71(12):1371-1389. https://doi.org/10.1080/10407782.2016.1243976.
41. Mayeli P, Hesami H, Besharati-Foumani H, Niajalili M. Al_2O_3-water nanofluid heat transfer and entropy generation in a ribbed channel with wavy wall in the presence of magnetic field. *Numer Heat Transf A*. 2018;73(9):604-623. https://doi.org/10.1080/10407782.2018.1461494.
42. Ashrafizadeh A, Alinia B, Mayeli P. A new co-located pressure-based discretization method for the numerical solution of incompressible Navier-stokes equations. *Numer Heat Transf B*. 2015;67(6):563-589. https://doi.org/10.1080/10407790.2014.992094.
43. Mayeli P, Nikfar M. Temperature identification of a heat source in conjugate heat transfer problems via an inverse analysis. *Int J Numer Methods Heat Fluid Flow*. 2019;29(10):3994-4010. https://doi.org/10.1108/HFF-05-2018-0193.

44. Nikfar M, Ashrafizadeh A, Mayeli P. Inverse shape design via a new physical-based iterative solution strategy. *Inverse Probl Eng*. 2015;23(7):1138-1162. https://doi.org/10.1080/17415977.2014.973873.
45. Mayeli P, Sheard G. Studying the natural convection problem in a square cavity by a new vorticity-stream-function approach. Paper presented at: Proceedings of the 22nd Australasian Fluid Mechanics Conference; December 7–10, 2020; The University of Queensland, Brisbane, Australia. https://doi.org/10.14264/b2c1622
46. Le Quéré P, Weisman C, Paillère H, et al. Modelling of natural convection flows with large temperature differences: a benchmark problem for low mach number solvers Part 1 reference solutions. *ESAIM Math Modell Numer Anal*. 2005;39(3):609-616. https://doi.org/10.1051/m2an:2005027.

How to cite this article: Mayeli P, Sheard GJ. Natural convection and entropy generation in square and skew cavities due to large temperature differences: A Gay–Lussac-type vorticity stream-function approach. *Int J Numer Meth Fluids*. 2021;1–25. https://doi.org/10.1002/fld.4980

3.4 Summary of the chapter

The centrifugal approximation has been introduced as a GL type approximation and governing equations under this approach were derived in primary and secondary variables form. Under the centrifugal approximation, density variations are extended to the advection term as well as the gravity term of the momentum equation to capture rotation related effects in buoyancy-driven flows. In comparison with the weakly compressible approach as a robust strategy for natural convection problems, it is found that the centrifugal approximation demonstrates improved accuracy over the conventional OB approximation. The centrifugal approximation will be used for stability analysis purposes in the next two chapters.

Chapter 4

4 Linear stability analysis of horizontal convection under the centrifugal approximation

Horizontal convection (HC) refers to natural convection in which fluid motion is invoked by non-uniform buoyancy along a horizontal buoyancy. The interest of studying this phenomenon comes from its contribution in scientific applications such as Earth's oceanic [8] and atmospheric [9] flow patterns, and the insights that it provides for industrial processes such as glass melting [10]. Numerical simulation of this phenomenon is often performed over an enclosure with different thermal boundary conditions. In this thesis, simulations and stability analyses are conducted in a relatively shallow enclosure with an aspect ratio of height to length of 0.16 at a fixed unity Prandtl number. A linear temperature distribution is imposed along the bottom boundary while other surfaces are thermally insulated. A schematic of the HC problem showing the applied boundary conditions are shown in Fig. 4.1.

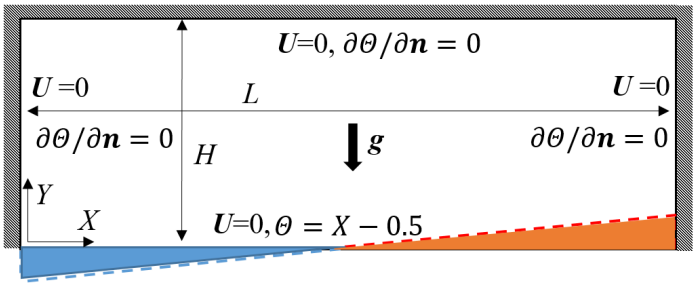

Figure 4.1: A schematic of the HC problem and boundary conditions in a rectangular enclosure.

In HC system, fluid is energised over the warming section so that it rise up around the bottom-right region but since the fluid vertical motion is restricted by the enclosure horizontal borders, an overturning circulation forms. In other words, the imposed non-uniform heating over the horizontal forcing boundary leads to overturning of the fluid for all Rayleigh numbers [11]. The scope for local rotations in the horizontal convection systems particularly exacerbates by the significant scale separations between the boundary layer and plume regions and the bulk overturning structure at higher Rayleigh numbers [12], which motivates the employment of the centrifugal approximation for investigations in this chapter.

4.1 Linearised Navier—Stokes equations under the centrifugal approximation

To conduct a linear stability analysis, the first step is deriving the linearised Navier–Stokes equations under the centrifugal approximation. Since the continuity and energy equations under the centrifugal and OB approximations are the same, it remains to derive the linearised momentum equation under this approximation. This is performed by adding an infinitesimal perturbation $(\epsilon \boldsymbol{U}', \epsilon P')$ to the velocity and pressure in the governing equations and retaining terms of order ϵ. The full derivation is provided in Appendix A. The result is ultimately,

$$\begin{aligned} \frac{\partial \boldsymbol{U}'}{\partial t} + (1 - Ga\Theta)[(\boldsymbol{U}' \cdot \nabla)\boldsymbol{U} + (\boldsymbol{U} \cdot \nabla)\boldsymbol{U}'] = -\nabla P' + Pr\nabla^2 \boldsymbol{U}' \\ -RaPr\Theta(\mathbf{e}_g - Fr(\boldsymbol{U}' \cdot \nabla)\boldsymbol{U}'). \end{aligned} \tag{4.1}$$

In Eq. (4.1), the ϵ prefactors have been factored out, and prime signed characters represent the perturbations while remaining symbols represent the base flow. Eq. (4.1) accompanied by the linearsied continuity,

$$\nabla \cdot \boldsymbol{U}' = 0, \tag{4.2}$$

and the linearsied energy equation,

$$\frac{\partial \Theta'}{\partial t} + (\boldsymbol{U} \cdot \nabla)\Theta' + (\boldsymbol{U}' \cdot \nabla)\Theta = \nabla^2 \Theta', \tag{4.3}$$

are evolved over time interval τ,

$$\hat{Q}(t + \tau) = A(\tau)\hat{Q}, \tag{4.4}$$

and the stability of the flow field is determined by finding the growth rate of the perturbations in the context of solving an eigenvalue problem,

$$A(\tau)\hat{Q}_k = \mu_k \hat{Q}_k, \tag{4.5}$$

where $\hat{Q}_k = (\hat{U}, \hat{V}, \hat{W}, \hat{\Theta})^T$ and μ_k are the k_{th} eigenvector and eigenvalue of the operator. Also, the hat values are single phase-locked spanwise Fourier mode. The eigenvalues μ_k

relate to the exponential growth rate σ and angular frequency ω of the corresponding eigenvector field through $\mu = \exp(\sigma + i\omega)$. Stability is determined by the magnitude of the leading eigenvalue (i.e. the eigenvalue having the largest absolute value), with $|\mu| = 1$ corresponding to neutral stability, while $|\mu| > 1$ and $|\mu| < 1$ respectively represent unstable and stable scenarios. As the base flows are time-invariant in this study, the analysis may proceed with an arbitrarily selected time interval. Stability analysis is performed by determining the leading eigenmode magnitude across a broad domain of wavenumbers (here $0 \leq k \leq 70$ was found to be sufficient to find σ_{max}). In addition, the instability mode may either be synchronous ($\omega = 0$) or oscillatory ($\omega \neq 0$).

4.2 Published paper

Governing equations under the centrifugal approximation are spatially discretised using a high-order nodal spectral-element method and evolved in time using a third-order backward differentiation scheme [13]. Temperature fields in the conduction and convection-dominated regimes accompanied by the linear stability analysis results has been published as a research paper entitled "Linear stability analysis of horizontal convection under a Gay-Lussac type approximation". The published paper also covers stability results predicted by direct numerical simulations (DNS).

International Journal of Heat and Mass Transfer 182 (2022) 121929

Contents lists available at ScienceDirect

International Journal of Heat and Mass Transfer

journal homepage: www.elsevier.com/locate/hmt

Linear stability analysis of horizontal convection under a Gay-Lussac type approximation

Peyman Mayeli*, Tzekih Tsai, Gregory J. Sheard

Department of Mechanical and Aerospace Engineering, Monash University, VIC 3800, Australia.

ARTICLE INFO

Article history:
Received 4 July 2021
Revised 20 August 2021
Accepted 1 September 2021

Keywords:
Gay-Lussac approximation
Non-Boussinesq approximation
Horizontal convection
Linear stability analysis

ABSTRACT

A linear stability analysis is conducted for horizontal natural convection under a Gay-Lussac (GL) type approximation in a relatively shallow enclosure cavity. The GL type approximation is developed based on extending density variations to the advection term as well as gravity term through the momentum equation. Such a treatment invokes the GL parameter ($Ga = \beta\Delta\theta$) as the non-Boussinesq parameter with a physical value ranging $0 \leq Ga \leq 2$, characterising deviation from the classic Boussinesq approximation. Results are compared against the Boussinesq approximation in terms of the Nusselt number and skin friction. Extreme values of Ga are found to produce a counter-rotating convection cell at the hot end of the enclosure at higher Rayleigh numbers - a feature absent from Boussinesq natural convection modeling. For stability analysis purposes, linearized perturbation equations under the GL type approximation are derived and solved to characterise the breakdown of the steady two-dimensional solution to infinitesimal three-dimensional disturbances. Stability results predict that the flow remains stable up to $Ra_{cr1} = 6.46 \times 10^8$ for the Boussinesq case ($Ga = 0$), and then with increasing Ga the flow briefly stabilises to $Ga \cong 0.2$, then becomes progressively more unstable with futher increases in Ga, yielding a critical Rayleigh number $Ra_{cr2} = 4.23 \times 10^8$ at $Ga_{max} = 2$. Three-dimensional transition is predicted to be via an oscillatory instability mode of the steady base flow having a spanwise wavelength that increases as Rayleigh number increases. 3D-DNS simulations verify the linear stability analysis predictions in terms of growth rate, and elucidate the mode shapes achieved at saturation.

1. Introduction

Horizontal convection (HC) is a distinct class of NC in which the fluid is heated unevenly across a horizontal boundary. Due to HC contribution in scientific applications such as earth's oceanic [1-3] and atmospheric [4-6] flow patterns and the insight that it provides for the industrial processes such as glass melting [7-8], this class of NC has attracted the attention of researchers during the recent decade. As an idealised representation of myriad natural convection systems, numerical simulation of HC is often performed within enclosed domains, such as square and rectangular wall-heated enclosures with buoyancy supplied either from the upper or lower horizontal boundary. For instance, oceanic circulation constitutes transportation of warm fluids from the tropical regions to high latitudes, where it cools and sinks, subsequently before an up-welling flow across the ocean basin completes the flow path [9].

Recent decades have seen a resurgence of horizontal convection research. Chiu-Webster et al. [8], studied the HC for very viscous fluids in rectangular cavities with aspect ratios ranging $0.01 \leq A \leq 2$ up to $Ra = 10^{10}$ and reported Rossby's [10] famous one-fifth power scaling of the average Nusselt number ($Nu_{ave} \sim Ra^{1/5}$) for HC. A similar study was performed by Sheard & King [11] for several aspect ratios ranging $0.16 \leq A \leq 2$ up to $Ra = 10^{10}$ at $Pr = 6.14$. They reported aspect ratio dependence of Nu_{ave} and boundary layer thickness at low Ra, whereas these become independent of aspect ratio for higher Ra once convection becomes the most dominant part of the heat transfer mechanism. Hossain et al. [12] analysed HC for very small aspect ratios ranging $0.001 \leq A \leq 0.16$ relevant to oceanic scale at $Pr = 6.14$ up to $Ra = 10^{12}$. They found that the transition from the diffusion-dominated regime to convection-dominated regime scales with A^{-4}, whereas the corresponding average Nusselt number at the threshold was proportional to A itself. Tsai et al. [13] studied linear stability analysis of HC in a rather shallow rectangular cavity with an aspect ratio of 0.16 under the OB approximation. Their computations indicate that the flow field remains stable up to $Ra = 3.2 \times 10^8$ for the Prandtl number spanning $0.1 \leq Pr \leq 10$. Tsai et al. [14] also conducted stability analysis of HC with different temperature profiles for the heating

* Corresponding author.
E-mail addresses: peyman.mayeli@monash.edu (P. Mayeli), Tzekih.Tsai@monash.edu (T. Tsai), Greg.Sheard@monash.edu (G.J. Sheard).

https://doi.org/10.1016/j.ijheatmasstransfer.2021.121929
0017-9310/

Nomenclature

A	Height to length aspect ratio
c_f	skin friction coefficient
e_g	unit vector in gravity direction
Fr	Froude number
g	gravity
Ga	Gay-Lussac parameter ($\beta\Delta\theta$)
H	height of the cavity
k	spanwise wavenumber
L	length of the cavity
N_f	Number of Fourier modes
Nu	Nusselt number
p	pressure
p^*	modified pressure
P	dimensionless pressure
Pr	Prandtl number
Ra	Rayleigh number
T	Temperature
x	coordinate vector
X	dimensionless coordinate vector
u	velocity vector
U	dimensionless velocity vector
$\hat{U}$	eigenmode
α	thermal diffusivity
β	isobaric expansion coefficient
θ	physical temperature
Θ	dimensionless temperature
μ	kinematic viscosity
μ	eigenvalue
ν	kinematic viscosity
ρ	density
ρ_0	reference density
τ_w	wall shear stress
ϕ	gravitational potential

Subscript

ave	average
c	cool
h	hot
loc	local
tot	total
ref	reference

part of the geometry. They found that transition from steady to time-periodic convection occurs through a supercritical bifurcation across all imposed temperature profiles, with the step profile being the most unstable one. Linear stability analysis of HC under the OB approximation is also performed by Passaggia et al. [15] for a step temperature distribution along the horizontal surface in a cavity with A = 0.25 at Pr = 1. They considered Dirichlet and free-slip boundary conditions for their simulations and reported the critical Rayleigh number equal to 2×10^7 and 1.7×10^8, respectively. Lyubimov et al. [16] studied the Rayleigh-Bénard-Marangoni system with horizontal temperature gradient under a weakly compressible type approach in which the momentum and continuity equations were considered compressible while the energy equation is treated as incompressible.

In all of these aforementioned works, HC was analysed under the Oberbeck–Boussinesq (OB) approximation, which is restricted by different assumptions such as small temperature differences. A review of different scenarios for non-OB simulation of natural convection related problems can be found in Ref. 17. One of the incompressible-based strategies to go beyond the OB approximation is the Gay-Lussac (GL) approach, which is developed based on considering density variations beyond the buoyancy term of the momentum equations, i.e. continuity and the advection/convection terms of the momentum and energy equations, respectively. An emergent feature of this approach is the GL parameter comprising the product of the volumetric thermal expansion coefficient (β) and the reference temperature difference ($\Delta\theta$). Pesso & Piva [18] used this strategy for the square cavity benchmark problem with large density variations. Recently, a GL-type approach was proposed by Lopez et al. [19] for non-OB treatment of rapidly rotating flows, in which density variations were extended only to the centrifugal part of the advection term to capture centrifugal effects arising from background rotation in those rapidly rotating flows. Mayeli & Sheard [20-21] continued this approach and showed that the GL parameter may be also expressed in terms of the Rayleigh, Prandtl, and Froude numbers (Ga = RaPrFr) with a maximum value ($Ga_{max} = 2$) to avoid an unphysical density value.

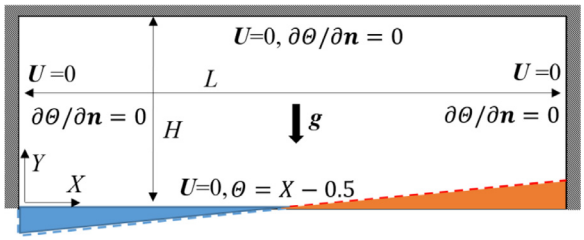

Fig. 1. A schematic of the HC problem and boundary conditions in a rectangular enclosure.

The aim of this study is to investigate the effects of the GL modification to buoyancy on the dynamics, heat transfer and linear stability of horizontal convection flow. The rest of the paper is organized as follows. In section 2, geometry and boundary conditions are described. In section 3, the non-OB approximation is demonstrated, and linearized perturbation equations under the GL type approximation are presented. Section 4 deals with the temperature difference, local Nusselt number and friction coefficient results obtained from the GL and OB approximations. Stability analysis results are presented and compared against the DNS results in Section 5. Finally, conclusions are drawn in Section 6.

2. Horizontal convection problem and boundary conditions

The GL-type approximation is applied for the HC problem in a rectangular enclosure with a fixed aspect ratio A = H/L = 0.16. A schematic of the problem associated with boundary conditions is shown in Fig. 1. In this problem, a linear temperature distribution is applied along the bottom wall while other surfaces are thermally isolated (zero temperature gradient normal to the walls), and the fluid is taken to have a constant Prandtl number Pr = 1, applicable to fluids including air. Therefore, the fluid is cooled and heated up along the left and right side of the bottom wall, respectively, and a counter-clockwise circulation is formed due to a buoyancy-driven flow. A no-slip boundary condition is imposed on all boundaries for the velocity.

3. Governing equations under the Gay-Lussac approximation and numerical consideartions

The GL approximation is an incompressible based strategy that follows the fundamentals of the OB approximation including negligible viscous heat dissipation, constant thermophysical properties, small temperature differences, and small hydrostatic pressure variations compared to thermodynamic presseure variations. However

under the GL approximation for buoyancy-driven flows, in contrast to the OB approximation in which the density variations are restricted to the gravity term, density variations are extended beyond the gravity term. Derivation of the governing equations under the GL approach begins with dividing the incompressible Navier–Stokes equations plus an advection-diffusion transport equation for temperature, taking density ρ to be variable, and dividing the equations by a reference density (ρ_0) in the absence of additional body forces and neglecting viscous heat dissipation in the energy equation,

$$\nabla \cdot \mathrm{u} = 0 \tag{1}$$

$$(\rho/\rho_0)\partial \mathrm{u}/\partial \mathrm{t}^* + (\rho/\rho_0)(\mathrm{u}\cdot\nabla)\mathrm{u} = -(1/\rho_0)\nabla \mathrm{p} + \nu\nabla^2\mathrm{u} + (\rho/\rho_0)\mathrm{e_g} \tag{2}$$

$$(\rho/\rho_0)\partial \mathrm{T}/\partial \mathrm{t}^* + (\rho/\rho_0)(\mathrm{u}\cdot\nabla)\mathrm{T} = \alpha\nabla^2\mathrm{T}. \tag{3}$$

Consistent with conventional application of the OB approximation, a linear state relation $\rho/\rho_0 = 1-\beta\theta$ connecting density to temperature is adopted. The dimensionless form of the governing mass conservation, momentum and temperature transport equations under the GL approximation may be written as

$$\nabla \cdot \mathrm{U} = 0 \tag{4}$$

$$(1-\mathrm{Ga}\Theta)\partial \mathrm{U}/\partial \mathrm{t} + (1-\mathrm{Ga}\Theta)(\mathrm{U}\cdot\nabla)\mathrm{U} = -\nabla \mathrm{P} + \mathrm{Pr}\,\nabla^2\mathrm{U} - \mathrm{RaPr}\Theta\mathrm{e_g} \tag{5}$$

$$(1-\mathrm{Ga}\Theta)\partial \Theta/\partial \mathrm{t} + (1-\mathrm{Ga}\Theta)(\mathrm{U}\cdot\nabla)\Theta = \nabla^2\Theta. \tag{6}$$

Here dimensionless symbols include velocity U, time t, pressure P and temperature Θ. These have respectively been non-dimensionalised by

$$\mathrm{t} = \frac{\mathrm{t}^*\alpha}{\mathrm{L}^2}, \mathrm{X} = \frac{\mathrm{x}}{\mathrm{L}},\ \mathrm{Y} = \frac{\mathrm{y}}{\mathrm{L}},\ \mathrm{U} = \frac{\mathrm{uL}}{\alpha}, \mathrm{P} = \frac{\mathrm{p}^*\mathrm{L}^2}{\rho\alpha^2},\ \Theta = \frac{\theta}{\Delta\theta} = \frac{\mathrm{T}-\mathrm{T}_0}{\mathrm{T}_h-\mathrm{T}_c}. \tag{7}$$

Eqs. (4-6) introduce the Gay-Lussac parameter $\mathrm{Ga} = \beta\Delta\theta$ that is twice of the relative temperature difference ($\mathrm{Ga} = 2\varepsilon$), a Rayleigh number characterising the ratio of buoyancy to viscous dissipation, $\mathrm{Ra} = \mathrm{g}\beta\Delta\theta\mathrm{L_{ref}}^3/\nu\alpha$, and the Prandtl number characterising the ratio of viscous to thermal dissipation, $\mathrm{Pr} = \nu/\alpha$. The Gay-Lussac paramter is equivalent to the Boussinesq parameter describing the relative density difference [22]. As it will be shown later, under this approach the Gay-Lussac paramter should not exceed a specified range for a physical density value. It should be noted that, since in the considered range of Ra and Ga at a fixed $\mathrm{Pr} = 1$, the base flow remains steady, non-Boussinesq effects are not considered in the transient terms. Also, $\mathrm{e_g}$ is the unit vector in the direction of gravity ($\mathrm{e_g} = \mathrm{g}/|\mathrm{g}|$).

It may be seen that as $\mathrm{Ga} \to 0$ ($\Delta\theta \to 0$), the governing equations under the conventional Boussinesq approximation are recovered. In the present formulation, $(1-\mathrm{Ga}\Theta)$ acts as a pre-factor on different terms and its effect becomes more important by increasing the reference temperature difference. In practice, Ga cannot exceed a specified value to avoid an unphysical (negative) density,

$$\rho/\rho_0 = 1-\beta\theta = 1-\beta\Delta\theta\Theta = 1-\mathrm{Ga}\Theta > 0. \tag{8}$$

Based on the defined dimensionless temperature, here the maximum Ga cannot exceed 2 ($\mathrm{Ga_{max}} = 2$). As mentioned earlier, Ga is a product of Rayleigh, Prandtl, and Froude numbers ($\mathrm{Ga} = \mathrm{RaPrFr}$), where Fr is the Froude number ($\mathrm{Fr} = \alpha^2/\mathrm{gL}^3$) characterising the ratio of inertia to gravity. It can be shown that, ignoring $(1-\mathrm{Ga}\Theta)$ prefactor from the continuity equation simplifies the the full GL approach as an incompressible based strategy and reduces the computational cost while the final results under two approaches are almost identical [23-24]. The simplified GL approach follows the same fundamentals of the Boussinesq approximation as mentioned earlier and physical range of the Gay-Lussac paramter. In this study, we follow the idea proposed by Lopez et al. [19], where a GL-type approximation was applied to the momentum advection term to capture centrifugal effects in rotating flows. Ignoring density variations in the momentum time derivative and thermal convection terms simplifies the GL approximation [20-21] to,

$$\nabla \cdot \mathrm{U} = 0 \tag{9}$$

$$\partial \mathrm{U}/\partial \mathrm{t} + (\mathrm{U}\cdot\nabla)\mathrm{U} = -\nabla \mathrm{P} + \mathrm{Pr}\,\nabla^2\mathrm{U} - \mathrm{RaPr}\Theta(\,\mathrm{e_g} - \mathrm{Fr}(\mathrm{U}\cdot\nabla)\mathrm{U}) \tag{10}$$

$$\partial \Theta/\partial \mathrm{t} + (\mathrm{U}\cdot\nabla)\Theta = \nabla^2\Theta. \tag{11}$$

Eq. (10) is consistent with the momentum equation under the OB approximation, except for the additional inertial buoyancy term on the right-hand side of the momentum equation. When expressed in this form, it is apparent that the action of this additional term is to modify the effective direction (and strength) of the gravity locally throughout the flow, which is ignored in the conventional Boussinesq approximation. Indeed, regions that are experiencing higher spatial accelerations described by $(\mathrm{U}\cdot\nabla)\mathrm{U}$, will experience deviations from the OB buoyancy approximation. The strength of these deviations relative to gravity is described by Fr, with $\mathrm{Fr} \to 0$ (hence $\mathrm{Ga} \to 0$) recovering the classical OB approximation.

The linearised Navier–Stokes equations under the GL-type approximation are derived in the conventional fashion, whereby velocity, pressure and temperature are decomposed into a 2D base flow and infinitesimal fluctuating disturbance component, i.e. $U = U_{2D} + U'$, $P = P_{2D} + P'$ and $\Theta = \Theta_{2D} + \Theta'$, where constant $|\varepsilon| << 1$. These decompositions are substituted into Eqs. (9) to (11), and retention of terms of order $O(\varepsilon)$ reveals the following equations,

$$\nabla \cdot \mathrm{U}' = 0, \tag{12}$$

$$\begin{aligned}\partial \mathrm{U}'/\partial \mathrm{t} &= \left[1-\mathrm{RaPrFr}\bar{\Theta}\right]\left((\bar{\mathrm{U}}\cdot\nabla)\mathrm{U}' + (\mathrm{U}'\cdot\nabla)\bar{\mathrm{U}}\right)\\ &= -\nabla \mathrm{P}' + \mathrm{Pr}\,\nabla^2\mathrm{U}' - \mathrm{RaPr}\Theta'\left(\mathrm{e_g} - \mathrm{Fr}\left(\bar{\mathrm{U}}\cdot\nabla\right)\bar{\mathrm{U}}\right),\end{aligned} \tag{13}$$

$$\partial \Theta'/\partial \mathrm{t} = -\left[\left(\bar{\mathrm{U}}\cdot\nabla\right)\Theta' + \left(\mathrm{U}'\cdot\nabla\right)\bar{\Theta}\right] + \nabla^2\Theta'. \tag{14}$$

A further important additional simplification is possible thanks to the invariance of the geometry in the spanwise direction. The flow variables may be represented as Fourier series in the z-direction, and a consequence of the linearization of Eqs. (12–14) is that each Fourier mode couples only with the 2D base flow, not other modes. It is therefore efficient to evolve individual 2D Fourier modes using the same spatial discretisation as used for the base flow, rather than evolving a full three-dimensional perturbation field. The dimensionless spanwise-periodic wavelength of an individual perturbation field, $\lambda = 2\pi/\mathrm{k}$, where k is the spanwise wavenumber characterising the perturbation. This reduces an evolution of a three-dimensional perturbation field to a set of 2D evolutions, with k emerging as an additional parameter to Rayleigh number, Froude number and Prandtl number. By defining $\mathrm{A}(\tau)$ to represent the linear evolution operator for time integration of a perturbation field comprising a single phase-locked spanwise Fourier mode $\hat{\mathrm{Q}} = (\hat{\mathrm{U}}, \hat{\mathrm{V}}, \hat{\mathrm{W}}, \hat{\Theta})^{\mathrm{T}}$ over time interval τ, i.e.

$$\hat{\mathrm{Q}}(\mathrm{t}+\tau) = \mathrm{A}(\tau)\hat{\mathrm{Q}}, \tag{15}$$

an eigenvalue problem may then be constructed as

$$\mathrm{A}(\tau)\hat{\mathrm{Q}}_\mathrm{k} = \mu_\mathrm{k}\hat{\mathrm{Q}}_\mathrm{k}, \tag{16}$$

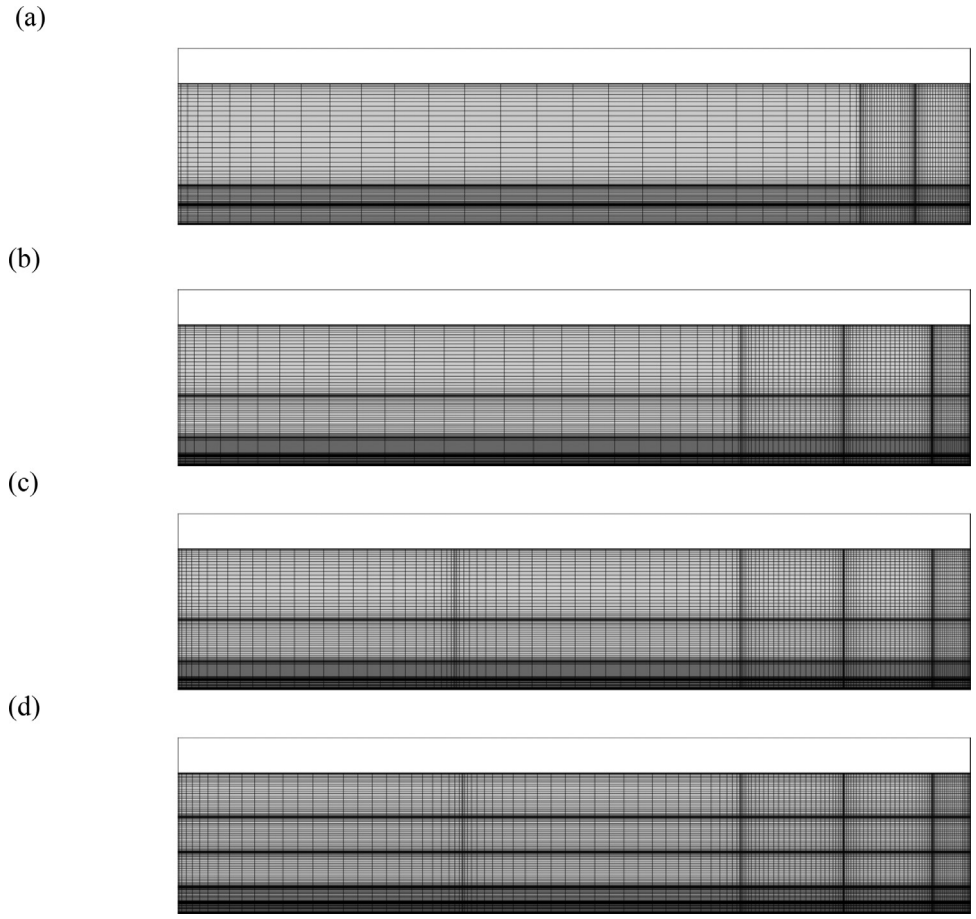

Fig. 2. Meshes having (a) 9 (b) 16 (c) 20 and (d) 25 elements, with intra-element grids displayed over the 30 × 30 quadrature points.

having complex eigenvalues μ_k and eigenvectors $\hat{Q}_k$. The eigenvalues μ_k relate to the exponential growth rate σ and angular frequency ω through $\mu = \exp[(\sigma + i\omega)\tau]$. Stability is determined by the magnitude of the leading eigenvalue, with $|\mu| = 1$ corresponding to neutral stability, while $|\mu| > 1$ and $|\mu| < 1$ respectively represent unstable and stable scenarios. As the base flows are time-invariant in this study, the analysis may proceed with an arbitrarily selected time interval τ. Stability analysis is performed by determining the leading eigenmode magnitude across a broad domain of wavenumbers ($0 \leq k \leq 70$). The bifurcation may be either synchronous ($\omega = 0$) or oscillatory ($\omega \neq 0$). Combinations of Ra and Ga are sought corresponding to neutral stability, i.e. $\sigma_{max} = 0$.

The eigenmodes for the stability analysis are computed using an implicitly restarted Arnoldi method [25-26] implemented through the ARPACK eigenvalue solver [27]. The present solver has been implemented and validated previously in [11-14].

The governing equations are spatially discretised using a high-order nodal spectral-element method and evolved in time using a third-order backward differentiation scheme [28]. The present code has been validated and employed in several natural convection problems [11-14]. To explore the mesh independence of the solutions, several meshes were constructed having different numbers of elements. In each mesh, elements were concentrated in the region where spatial flow variations are expected to be greatest: towards the heated end of the bottom boundary where buoyancy enters the flow. In each case, element polynomials of order $P = 30$ were adopted. The mesh independency is checked in terms of L_2 norm (taken here as the domain integral of the velocity magnitude) in Table 1 at $Ra = 4 \times 10^8$ and $Ga = 2$, with the meshes used being shown in Fig. 2. These parameters were chosen as they are expected to represent a taxing case to resolve. The computed L_2 norms obtained once the flows settled to their equilibrium states (see Table 1) indicate that the 20-element mesh resolves the flow to a high accuracy, and this resolution is used hereafter.

Table 1
Mesh resolution study of HC problem at $Ra = 4 \times 10^8$ and $Ga = 2$ with the different number of elements and a high order of Lagrangian polynomial (P=30).

Number of elements	L_2norm	$\lvert Difference\rvert(\%)$
9	21557.9175562921	2.096
16	21557.9627504395	6×10^{-5}
20	21557.9774402941	2×10^{-7}
25	21557.9775014154	–

A similar test was performed for the mesh having 20 elements and different orders of polynomials from $P = 20$ to 40 and it was found that, a polynomial of order $P = 30$ is sufficient for the mesh independency purposes.

Once the thermo-flow field is obtained, results are compared in terms of the local Nusselt number and skin friction. Since the flow the is thermally isolated from three sides in this study, local Nusselt number along the bottom horizontal wall is calculated as follow

$$Nu_{loc} = \left| \frac{\partial \Theta}{\partial Y} |_{wall} \right|. \quad (17)$$

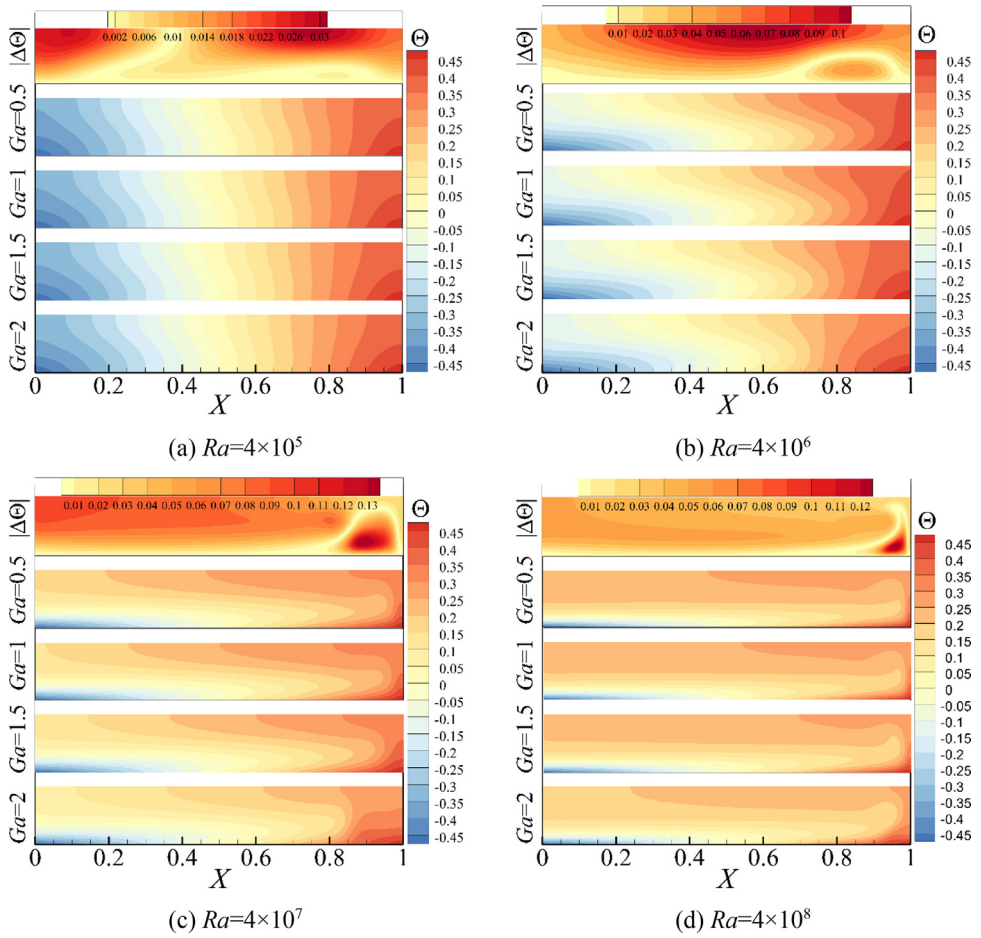

Fig. 3. Comparison of temperature fields at different Ra and Ga values, as stated. The top frame of each plot shows the absolute temperature difference between the Ga = 2 and Ga = 0 cases.

The friction coefficient along the surface based on the dimensionless velocity is defined as

$$c_f = -2\,\mathrm{Pr}\begin{bmatrix}\tau_{xx} & \tau_{xy}\\ \tau_{yx} & \tau_{yy}\end{bmatrix}\begin{bmatrix}n_x\\ n_y\end{bmatrix} = -2\mathrm{Pr}\begin{bmatrix}2\partial U/\partial X & \partial U/\partial Y+\partial V/\partial X\\ \partial U/\partial Y+\partial V/\partial X & 2\partial V/\partial Y\end{bmatrix}\begin{bmatrix}n_x\\ n_y\end{bmatrix}. \quad (18)$$

In Eq. (18), n_x and n_y are the normal vector of the surface in horizontal and vertical directions, respectively. The magnitude of friction coefficient is calculated as

$$c_f = \sqrt{(c_{fx})^2 + (c_{fy})^2} \quad (19)$$

4. Analysing thermo-flow field at different Gay-Lussac parameter values

Results of HC under the GL-type and OB approximations are analysed in this section. A qualitative comparison is performed by depicting the dimensionless temperature fields at different Ra and Ga starting from Ga_{max} at the bottom frame of each plot in Fig. 3. By decreasing Ga, the temperature field is evolved so that results under the OB approximation (Ga = 0) are retrieved. The top frame in each figure shows the absolute temperature difference between the GL-type approximation with $Ga_{max} = 2$ and results under the OB approximation (Ga = 0). At $Ra = 4 \times 10^5$ (Fig. 3a) conduction is still the dominant heat transfer mechanism, and temperature fields corresponding to different Ga values do not show a significant mismatch. In this state, the absolute temperature difference is observed mostly occurring along the top surface with a maximum value around 0.03 ($\Delta\Theta_{max} = 0.03$). As the Rayleigh number increases, the magnitude of the absolute temperature difference is also augmented in the top frame. Results start to show the centrifugal effects in Fig. 3b at $Ra = 4 \times 10^6$, where convection starts to become the dominant heat transfer mechanism and the effect of different Ga values is sensible across the bottom-right corner of the cavity. A comparison among temperature fields in Fig. 3b reveals that, under the GL-type approximation, by decreasing Ga value, isotherm-lines show less deformation in the horizontal direction, and most of the difference occurs in the vertical direction. Most of the temperature difference at this Rayleigh number still occurs along the top side with a maximum value of around 0.1 ($\Delta\Theta_{max} \cong 0.1$). At $Ra = 4 \times 10^7$ (Fig. 3c) where the flow is convection dominated, a thin thermal boundary layer is formed along the bottom side, and the effect of different Ga values is apparent on the temperature field, especially at the rising plume region across the bottom-right corner. Results indicate increasing Ga (and consequently the reference temperature difference) has a damping effect on the formation of the rising plume in convection-dominated regime. In other words, lower values of Ga let a broader area to be affected by the warming section of the bottom surface. At this Rayleigh number, large values of the temperature differences shift their location toward the bottom-right corner; however, apparent temperature differences along the top side are observable. Results at $Ra = 4 \times 10^8$ are presented in Fig. 3d. A significant difference among the temperature fields corresponding to the different Ga values is evident in this plot. Results

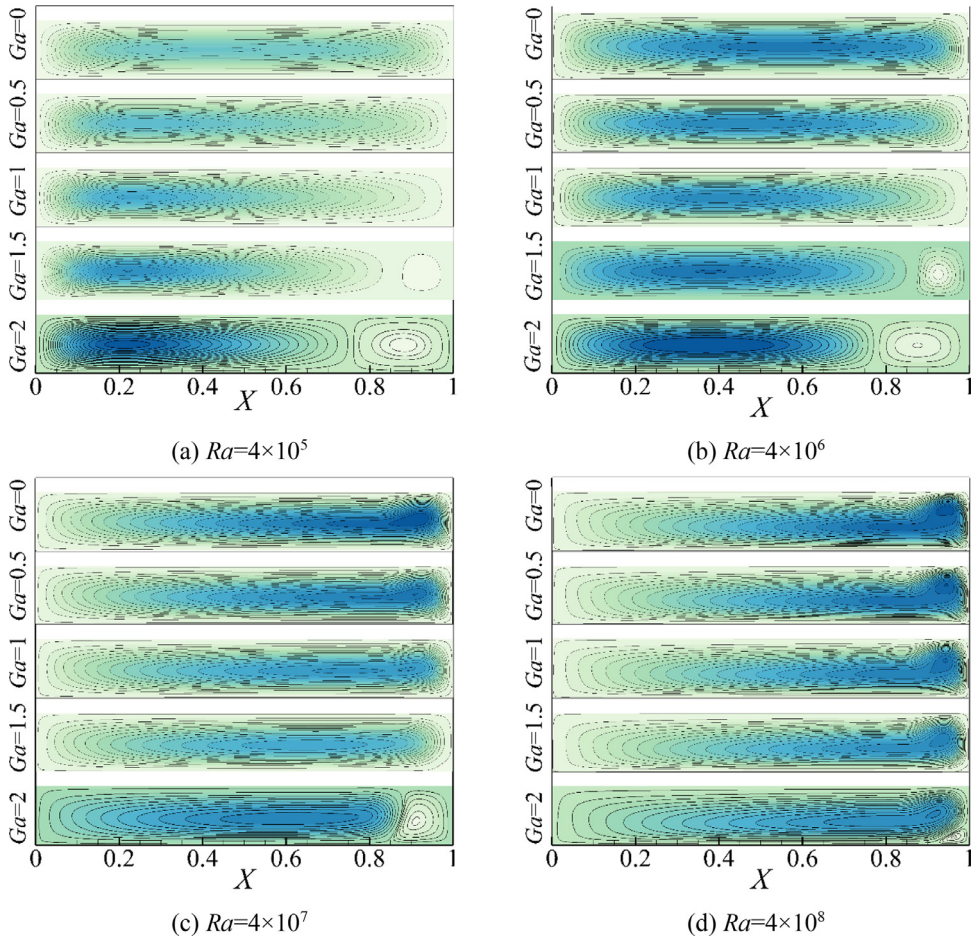

Fig. 4. A comparison of stream-function at different Ra and Ga values, as stated. The top frame of each plot shows the absolute temperature difference between Ga = 2 and Ga = 0. Dark to light shaded contours show respective maximum and minimum values of stream-function. The minimum and maximum of each figure's legend are set equal together.

indicate that, under the GL-type approximation, a thicker thermal boundary layer is formed along the horizontal bottom wall compared to the OB approximation. The damping effects of the larger Ga on the rising plume region are also visible in this figure. The maximum absolute difference at this high Rayleigh number is about 0.12, which concerning the maximum dimensionless temperature shows about 24% mismatch between Ga_{max} and Ga = 0 ($|\Delta\Theta|/\Theta_{max} = 0.24$).

In Fig. 4, stream-functions at different Ga and Ra are presented. In condution-dominated regime (Fig. 4a and b), two separate regions are distinguishable at the right half of the cavity for large GL parameters (Ga = 2 and 1.5) that are turned to smaller regions in the convection dominated regime (Fig. 4c and d). As seen, for small and moderate Ga (Ga = 0, 0.5, 1), up to $Ra = 4 \times 10^6$ there is an asymmetric distribution of the stream-function inside the geometry but by increasing the Rayleigh number, a stronger circulation forms across the top-right region of the enclosure, reflecting the plume effect to generate a strong circulation across this region.

4.1. Local Nusselt number

The local Nusselt number results at different Ra and Ga along the bottom wall are presented in Fig. 5. In general, the local Nusselt number is increased by increasing the Rayleigh number, as expected. At $Ra = 4 \times 10^5$ (Fig. 5a), the local Nusselt number has an almost symmetric distribution along both cooling and heating sections of the bottom wall, and it does not show sensitivity to Ga alteration. This behavior is attributed to a conduction-dominated regime at this Rayleigh number. As the Rayleigh is increased to $Ra = 4 \times 10^6$ (Fig. 5b), a clear mismatch among Nu_{loc} corresponding to different Ga values is visible. In this figure, the local Nusselt number undulates along the bottom wall so that its value for the higher Ga has a larger value only over of $0.3 \leq X \leq 0.65$.

In the convection-dominated regime (Fig. 5c and d), the local Nusselt number exhibits a linearly decreasing trend over the left part of the base, while over the right part, a linearly increasing trend is seen up to a maximum, before a significant deficit is produced. The linear regions are consistent with the formation of a convective boundary layer adjacent to the bottom surface. The significant reduction in the value of the local maximum in Nu_{loc} and the leftward shift in its horizontal location with increasing Ga underpins the local impact of centrifugal effects in the buoyancy supply region at the right side of the enclosure. This is underscored by this region containing the largest absolute differences in temperature between Ga = 0 and 2 cases, as shown earlier in Fig. 3(c,d). In this region, the horizontally convecting flow gains buoyancy and erupts vertically into the side-wall plume. This is a region comprising both rotation and thermal gradients inciting centrifugal effects.

4.2. Skin shear stress

The shear stress values across the horizontal boundaries are investigated in Fig. 6 in this section. The solid and dashed-lines show

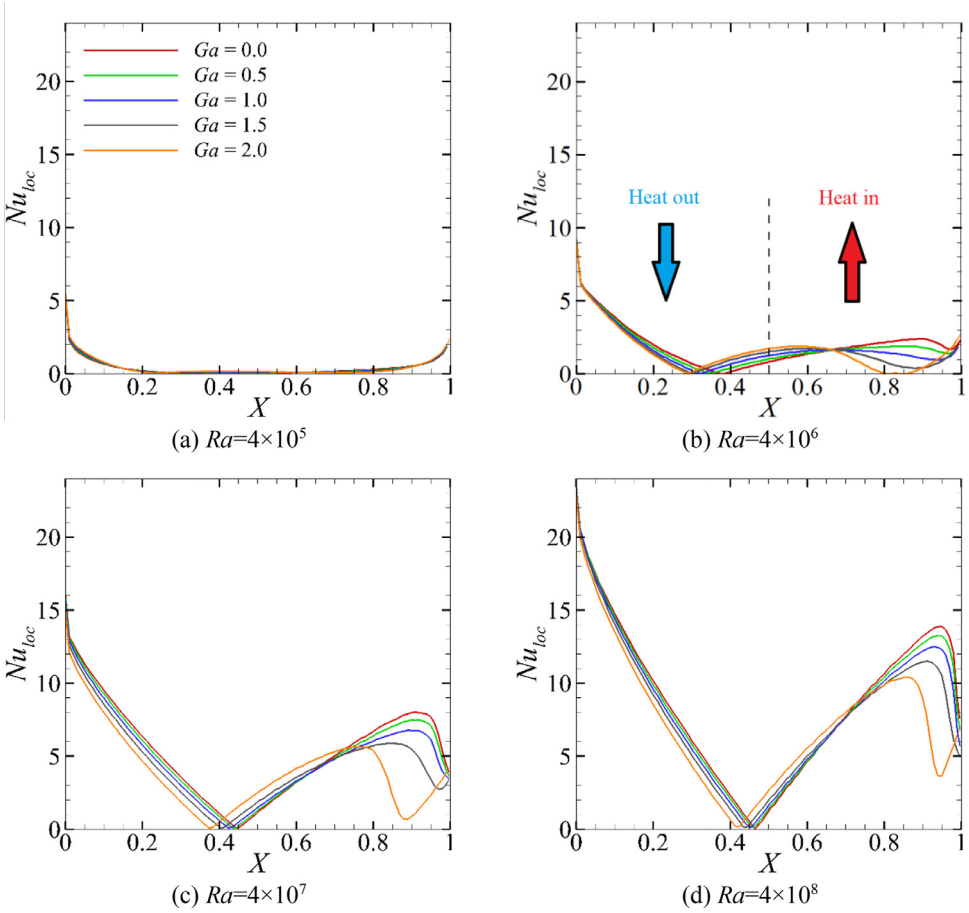

Fig. 5. The local Nusselt number distribution along the bottom surface at different Ra and Ga values as stated. Fig. 5b shows the cooling and heating sections along the bottom side.

the magnitude of the friction coefficient Eq. (19) along the bottom and top walls, respectively. In general, c_f is increased by increasing the Rayleigh number, as expected.

Results of the conduction dominated regime at $Ra = 4 \times 10^5$ (Fig. 6a) indicates c_f has a symmetric distribution along both surfaces at $Ga = 0$, but as the Ga is increased, a linear distribution is obtained for the c_f with a more considerable value along the bottom surface and a local maximum approximately at $X \cong 0.175$ for both surfaces at moderate Ga values ($Ga = 0.5$ & 1). A second local maximum is observed approximately at $X \cong 0.9$ for large Ga values ($Ga = 1.5$ & 2). Local maxima of the c_f along both horizontal surfaces at $Ga = 1.5$ and 2 may be attributed to the second core which is formed at high reference temperature differences (two bottom frames of Fig. 4a). A similar trend is observable for c_f distribution at $Ra = 4 \times 10^6$ in Fig. 6b. At $Ra = 4 \times 10^7$ (Figs. 6c) and $Ra = 4 \times 10^8$ (Fig. 6d), the general behavior of c_f distribution becomes reverse for the bottom wall so that a more symmetric distribution of the c_f is obtained by increasing Ga value. Another exciting feature of the c_f distribution at the convection-dominated regime is the large magnitude of this parameter along the top wall approximately at $X \cong 0.9$, which decreases by increasing Ga value. In other words, both of the Fig. 6c and d indicate that at convection dominated regime, the strong rising plume creates a large c_f value across the top-right region. Finally, the strange behavior of the c_f distribution at the bottom-right corner is attributed to the emergence of a counter-rotating cell (two bottom frames of Fig. 4c and d) at a high Ga value that is observable at convection-dominated regime. This feature is absent from simulations employing the conventional Boussinesq model ($Ga = 0$).

5. Stability analysis

Attention is now turned to the stability of these flows to small three-dimensional disturbances, and the effects of varying Rayleigh number, spanwise wavenumber and GL parameter at a fixed Prandtl number, $Pr = 1$. The precision of the eigenvalue μ and eigenmode $\hat{U}$ produced by subspace iteration is defined by the residual

$$R = \left\| A\hat{U} - \mu\hat{U} \right\| \tag{20}$$

where $\|\cdot\|$ is the vector norm. Obtaining the leading eigenvalue and the corresponding eigenmode at each wavenumber relies on an iterative process which is ceased as soon as $Res < 10^{-7}$ is achieved. Nevertheless, the eigenmodes are resolution-dependent. A mesh resolution study for the eigenvalue computations across wave number $0 \le k \le 70$ with different number of elements provided in Fig. 2 with a high polynomial degree of 30 within each element ($N_p = 30$) is performed. The absolute difference of the leading eigenvalues obtained from different mesh resolutions having 16, 20, and 25 elements are checked at $Ra = 4 \times 10^8$ with $Ga = 2$ and $Ra = 6.5 \times 10^8$ with $Ga = 0$. It is found that a mesh resolution having 20 elements (Fig. 2c) has enough accuracy for the eigenvalue problem as the maximum difference of the converged leading eigenvalues for the mentioned resolution was less than 0.03% compared to a higher resolution having 25 elements (Fig. 2d) for both cases.

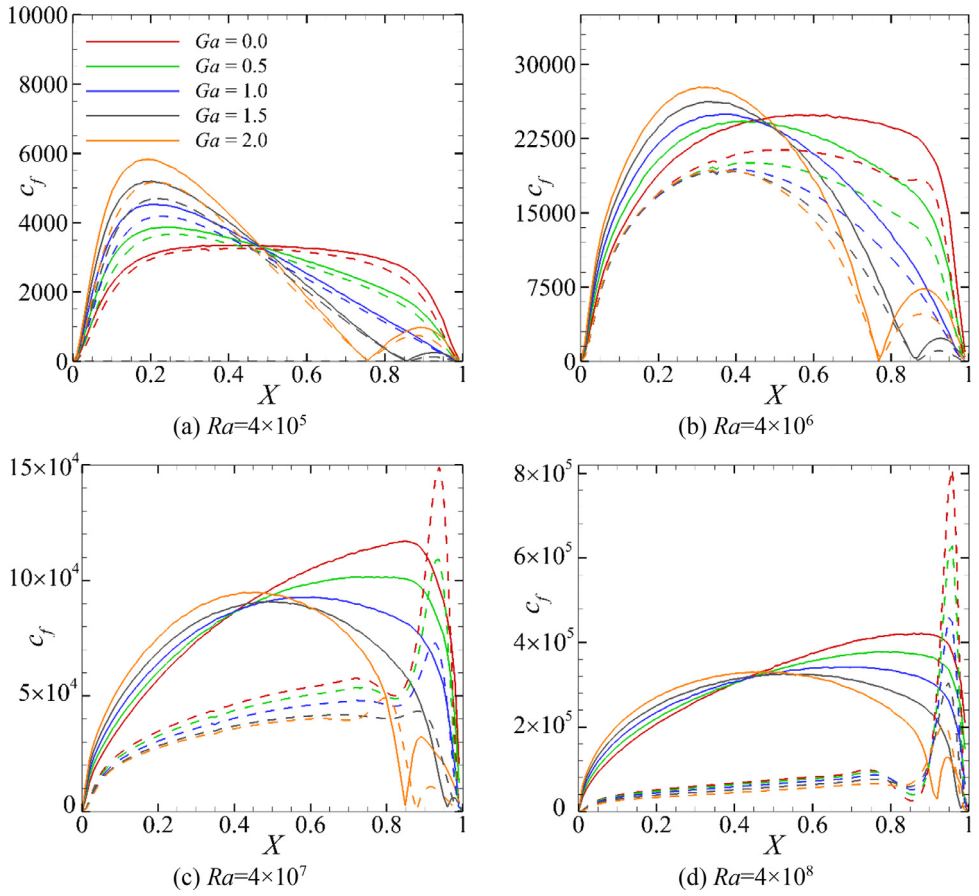

Fig. 6. Distribution of the c_f along the bottom (solid-lines) and top (dash-lines) surfaces at different Ra and Ga as stated.

5.1. Growth rates and stable regions under the Gay-Lussac type approximation

Under the GL approximation at each Ra, there exists a critical (maximum) Ga value that beyond which the flow becomes unstable. On the other hand, the Ga value is restricted to a maximum value to avoid an unphysical density ($Ga_{max} = 2$) as explained earlier in Eq. 5. Besides, the maximum Ga value is also proportional to the maximum physical Froude number at each Rayleigh and Prandtl ($Fr_{max} = Ga_{max}/RaPr$). In this respect, calculations are performed at Ga_{max} to find the primary critical Rayleigh number at which the flow becomes unstable for the first time. Thereafter, by increasing the Rayleigh number, the critical Ga value that beyond which the flow becomes unstable to 3D infinitesimal disturbances is sought. Predicted growth rates at Ga_{max} and $10^2 \leq Ra \leq 4.5 \times 10^8$ and spanwise wavenumber $0 \leq k \leq 70$ are presented in Fig. 7. The presented growth rates of disturbances in Fig. 7a and b indicate the flow remains unconditionally stable for any physical Ga value up to $Ra \leq 4 \times 10^8$. The growth rates result in Fig. 7a also indicate that the leading stable eigenvalue has a real mode for all wavenumbers up to $Ra = 10^6$. As seen, the growth rate of the leading eigenmode decreases monotonically by increasing the wavenumber in conduction dominated regime (Fig. 7a). Stability results in Fig. 7b indicate that as the Rayleigh number exceeds from 10^8, some of the leading eigenvalues turn into complex-conjugate pairs for $k \geq 32$. The growth rate results at $Ra \geq 10^8$ in Fig. 8b show a conjugate leading eigenvalue for $k \geq 16$. As seen in Fig. 7b, by increasing the Rayleigh number from 10^8 to 4×10^8, the solid lines (which connect dominant leading eigenvalues) are forming a local maximum close to the neutral stability limit ($\sigma = 0$). In Fig. 7c, the Rayleigh number is delicately increased from 4.1×10^8 to 4.5×10^8 by a small increment rate to find the primary critical Rayleigh that first produces $\sigma = 0$ and the corresponding wavenumber at which this occurs. Stability results in Fig. 7c indicate the solid-line of connecting leading eigenvalues intersects with the neutral stability line somewhere between $Ra = 4.2 \times 10^8$ and $Ra = 4.3 \times 10^8$ and $42 < k < 44$. The critical Rayleigh number at Ga_{max} is interpolated between the maximum leading eigenvalues equal to $Ra_{cr1} = 4.23 \times 10^8$ and $k_{cr1} = 43.66$. Stability results at interpolated primary critical Rayleigh number intersecting the neutral stability line ($\sigma = 0$) are checked and approved in Fig. 7d. In Fig. 7c and d ($Ra > 4 \times 10^8$), a local maximum is also observed at around $k \cong 36$, but the corresponding mode always remains in the stable region ($\sigma < 0$).

After finding the primary critical Rayleigh number, stability results are pursued at higher Rayleigh numbers. For the sake of brevity, a few stability results are presented in Fig. 8. For instance, at $Ra = 4.75 \times 10^8$ (Fig. 8a), the critical Ga value corresponding to the neutral stability occurs close to $Ga = 1.5$ while by increasing the Rayleigh number to 5×10^8 in Fig. 8b, the critical Ga value is close to 1.3. The critical Ga value intersecting $\sigma = 0$ is interpolated between two stable and unstable Ga values at each Rayleigh number. Monotonic decreasing rate of the critical Ga value by increasing the Rayleigh number with an increment rate of 0.25×10^8 continues up to $Ra = 6.25 \times 10^8$ (see Fig. 8c & d). By increasing the Rayleigh number, another local maximum is observed at around $k \cong 20$ but this mode is completely in the stable region ($\sigma < 0$). Presented stability results with $Ga = 0$ in Fig. 8e indicate the flow is unstable for $Ra \geq 6.50 \times 10^8$ with $Ga = 0$. The secondary critical Rayleigh number is interpolated equal to $Ra_{cr2} =$

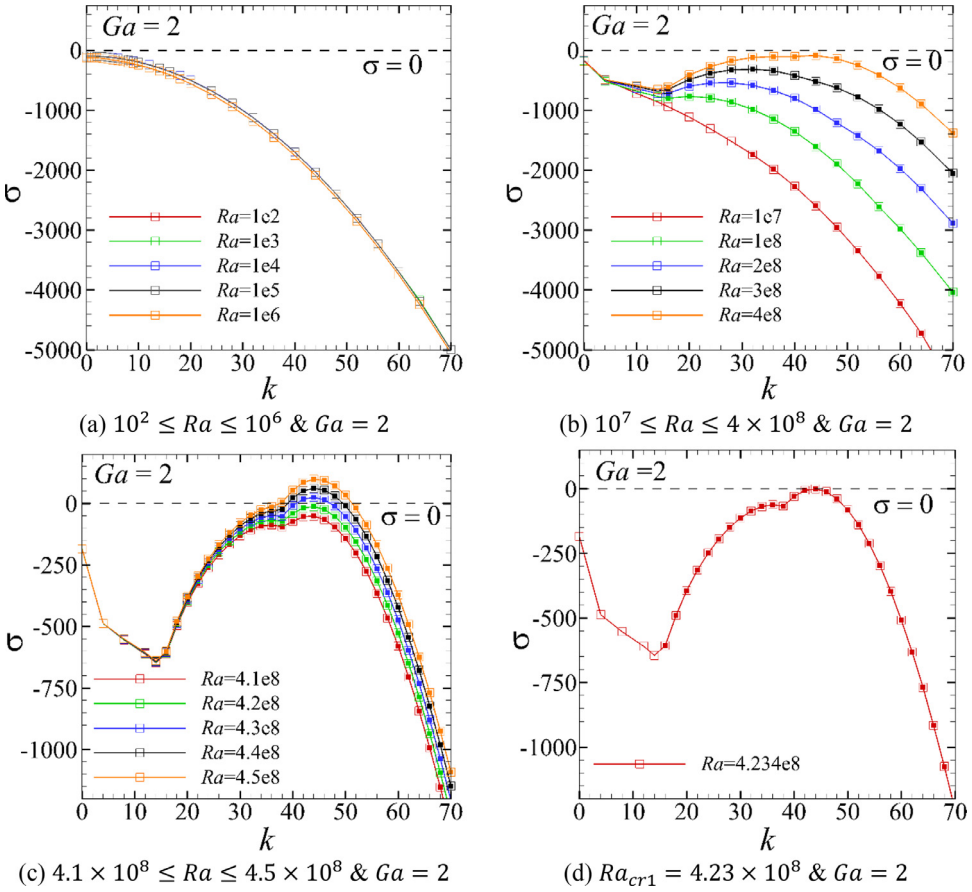

(a) $10^2 \leq Ra \leq 10^6$ & $Ga = 2$ (b) $10^7 \leq Ra \leq 4 \times 10^8$ & $Ga = 2$

(c) $4.1 \times 10^8 \leq Ra \leq 4.5 \times 10^8$ & $Ga = 2$ (d) $Ra_{cr1} = 4.23 \times 10^8$ & $Ga = 2$

Fig. 7. Growth rates of leading eigenmodes at Ga_{max} as a function of spanwise wavenumber for (a) $10^2 \leq Ra \leq 10^6$ (b) $10^7 \leq Ra \leq 4 \times 10^8$ (c) $4.1 \times 10^8 \leq Ra \leq 4.5 \times 10^8$ (d) $Ra = 4.23 \times 10^8$. Hollow symbols represent real leading eigenvalues, while solid symbols represent complex-conjugate pairs of non-real leading eigenvalues. Solid lines connect successive dominant leading eigenvalues.

Table 2
Leading eigenmodes components at $\mathrm{Ra} = 6.5 \times 10^8$ for two different Ga values.

Ga	*Growthrate*(σ)	Angular frequency (ω)
0.15	0.462378	0.997515
0.20	0.438864	0.988598
0.25	0.417707	0.982405
0.30	0.533818	0.998714

6.46×10^8. The growth rate of the perturbations versus wavenumber at the Ra_{cr2} with $\mathrm{Ga} = 0$ is plotted in Fig. 8f, and it is found that at $\mathrm{k}_{cr} = 59.91$ it produces $\sigma = 0$.

An interesting feature is found over a small range of non-zero Ga. A small stable region at $\mathrm{Ra} = 6.50 \times 10^8$ for $0.13 \leq \mathrm{Ga} \leq 0.31$ is detected, above the critical Rayleigh number at both smaller and larger Ga. The growth rates predicted over this range are portrayed in Fig. 9a over the local $\mathrm{Ga} - \mathrm{Ra}$ parameter space. The critical wavenumber can be seen to decrease monotonically from $\mathrm{k}_{cr} = 59.1$ at $\mathrm{Ga} = 0$ down to $\mathrm{k}_{cr} \cong 54$ by $\mathrm{Ga} = 0.5$. This increasing spanwise wavelength with increasing Ga correlates with the observed widening of the sidewall structures in these flows at Ga is increased (ref. Fig. 3(c,d) and 4(c,d) in particular). This stable region vanishes by $\mathrm{Ra} = 6.51 \times 10^8$, as can be seen in Fig. 9b. This behaviour implies a complicated interplay between multiple mechanisms underlying this global stability behaviour. Nevertheless, analysis of the real and imaginary parts of the eigenmodes along the locus of maximum growth, showing only slight but monotonic variation with Ga (see Table 2) suggests that this is the result of a single instability mode, rather than an overlap between distinct modes.

Plots of the critical Rayleigh number and corresponding dominant spanwise wavenumber as functions of Ga are shown in Fig. 10. The neutral stability curve intersects with $Ga = 0$ at the secondary critical Rayleigh number, i.e. $Ra_{cr2} = 6.46 \times 10^8$. The local maximum in Ra_{cr} at $Ga \cong 0.2$ corresponds to the stabilised region identified in Fig. 9. The dominant wavenumber trend in Fig. 10b extends the observed progressive decrease with increasing Ga described previously in reference to Fig. 9; here reducing to below $k_{cr} = 44$ by $Ga = 0.2$.

Fig. 11 shows the marginal stability curves for three Ga values including $Ga = 0$, 1 and 2. The marginal curves are obtained by interpolating $\sigma(k, Ra)$ to zero growth rate for each Ra. As seen, an increase in Ga, the peak of the neutral stability curve shifts to lower wavenumbers, consistent with the aforementioned trends in Fig. 10. This reinforces that flow with a higher Ga value is less stable than a smaller Ga value.

5.2. Instability mode structure

The structure of the eigenvector fields for the neutrally stable leading instability mode at $\mathrm{Ga} = 0$, 1 and 2 will now be considered for further insight into the three-dimensional stability of these flows. It should be remembered that these fields depict the amplitude of the sinusoidal z-variation of the three-dimensional disturbance; hence these represent a slice through the perturbation at a fixed z-value. Three-dimensionality appears at the rising plume region and extends upward with the

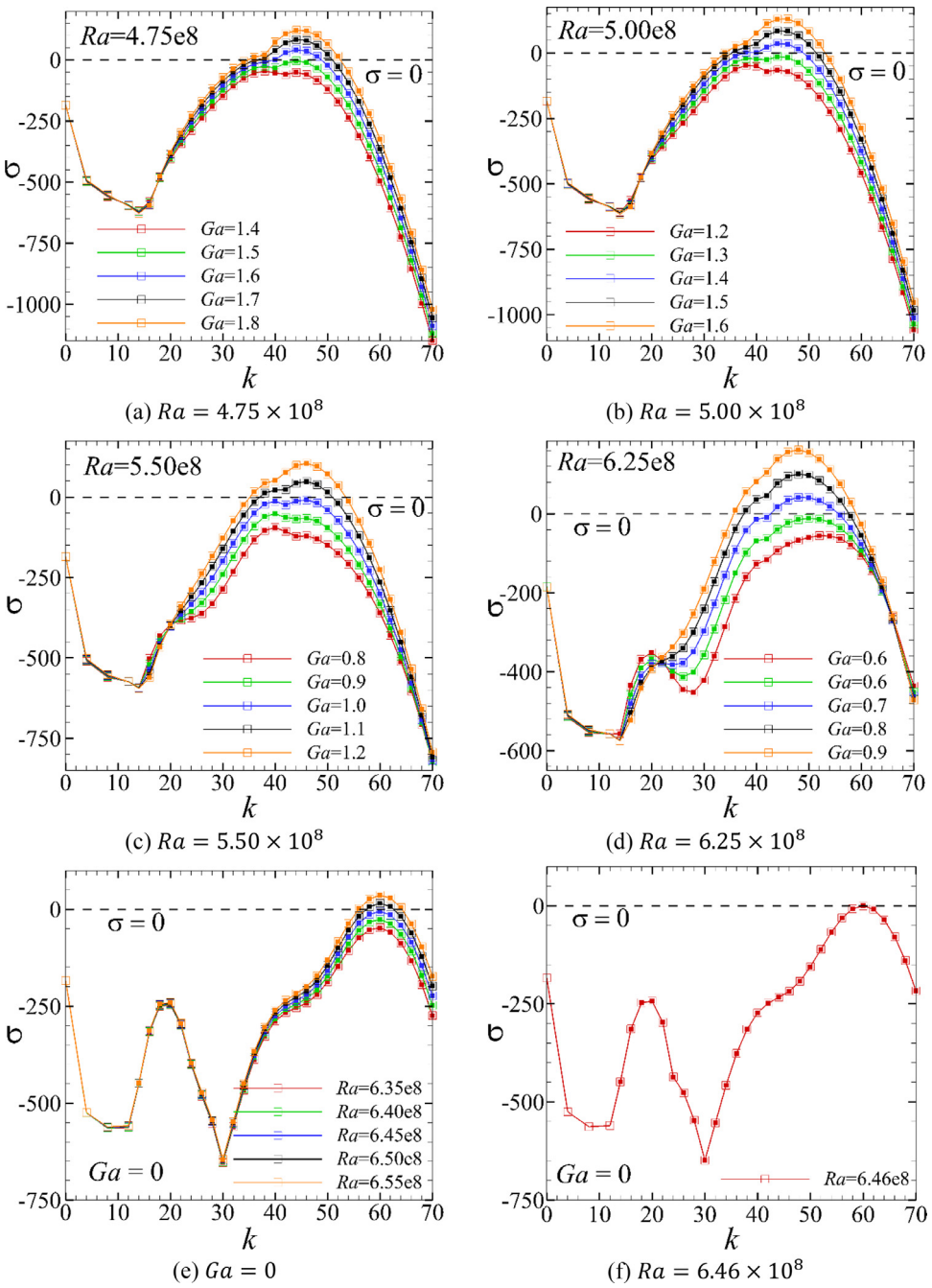

Fig. 8. Growth rates of leading eigenmodes after primary critical Rayleigh number as a function of spanwise wavenumber for (a) Ra = 4.75 $\times 10^8$ (b) Ra = 5.00 $\times 10^8$ (c) Ra = 5.50 $\times 10^8$ (d) Ra = 6.25 $\times 10^8$ (e) Ga = 0 (f) Ra = 6.46 $\times 10^8$. Hollow symbols represent real leading eigenvalues, while solid symbols represent complex-conjugate pairs of non-real leading eigenvalues. Solid lines connect successive dominant leading eigenvalues.

traversing concerning the top-right corner of the geometry as shown by the spanwise velocity component in Fig. 12. Strong spanwise velocities across the rising plume region are consistent with a mechanism involving centrifugal instability in this region. A similar counter-rotating vortices at Ga = 0 was seen in Passagia et al. [38].

5.3. Eigenvalue spectra evolution from stable to an unstable region

Thus far, only the leading eigenmode at any (Ra, Ga, k) combination has been considered. Eigenspectra containing several of the leading eigenvalues will now be considered to visualise the excursion of the leading eigenvalue as neutral stability is traversed. Fig. 13 shows the eigenvalue spectra for a representative sample case at Ra = 5 $\times 10^8$ with Ga = 1.1, 1.2, 1.3 and 1.4 and k = 44.75 (See Fig. 8b for the context on this chosen set of parameters). Stability results at this Rayleigh number and different GL parameter is already presented in Fig. 5b. The dashed-line circle in this figure indicates the onset of instability ($|\mu| = 1$). As seen, the leading eigenvalues are two complex pairs that by increasing Ga value, the first leading pair moves to the outside of the unit neutral stability circle. As seen in Fig. 13a, there are two closely grouped complex-conjugate pairs of eigenvalues, and as Ga increases the real part of the leading eigenvalue diminishes so that the faster-growing eigenmode departs rapidly from its subdominant counterpart, departing the unit circle as Ga is increased to 1.4.

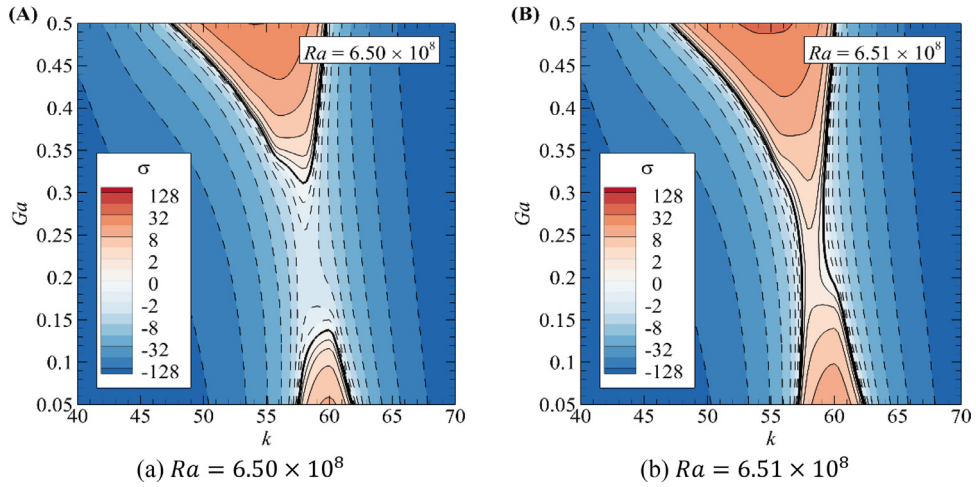

Fig. 9. Growth rate contour of the leading eigenmodes at wave number ranging $40 \leq k \leq 70$ after the secondary critical Rayleigh number as a function of GL parameter for (a) $Ra = 6.50 \times 10^8$ (b) $Ra = 6.51 \times 10^8$. The thick black line represents growth rate corresponding to neutral stability.

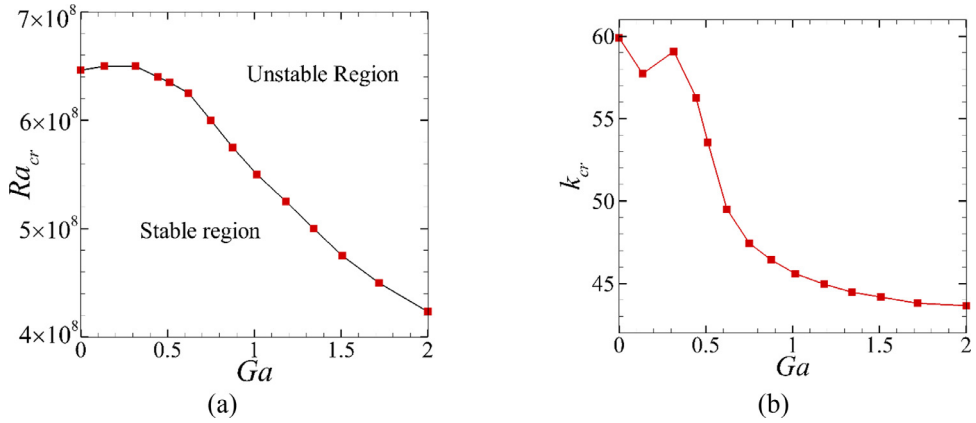

Fig. 10. Stability results for the critical (a) Rayleigh number at different Ga and (b) wavenumber at different Ga. All modes are oscillatory, in both plots.

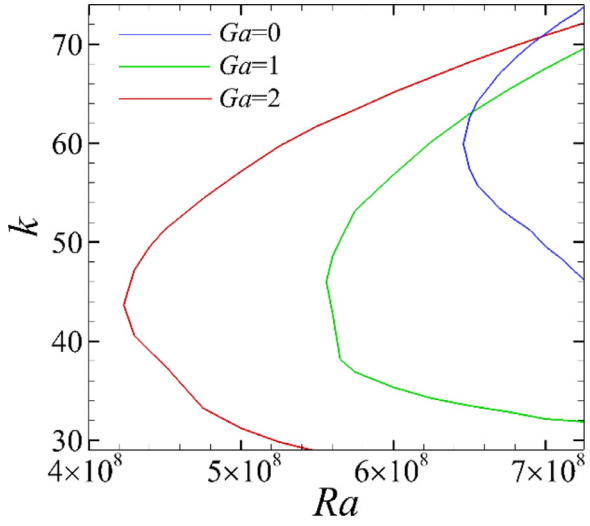

Fig. 11. Marginal stability curves for HC with Ga = 0, 1 and 2. Regions on the right of the curves represent flow conditions that are linearly unstable to 3D perturbations for that particular Ga.

The eigenvector fields corresponding to the leading eigenmode from Fig. 13(a) and (d) are visualised in Fig. 14 via plots of the spanwise vorticity, velocity and temperature perturbation fields at $Ra = 5 \times 10^8$. Fig. 14a depicts the eigenfield at Ga = 1.1, close to the onset of instability, while Fig. 15b depicts the same quantities for an unstable field (Ga = 1.4). At the lower Ga i.e. Ga = 1.1, the spanwise vorticity and velocity fields indicate that the disturbance is strongest in the region of the flow where the buoyant plume ascending along the right-hand (hot) end of the enclosure is deflected leftward by the top boundary. On the othr hand, at Ga = 1.4 the spanwise vorticity field indicates that destabilisation of the flow has advanced upstream, with disturbance vorticity structures extending the length of the right side-wall plume.

5.4. Nonlinear stability analysis to the three-dimensional state via DNS

This section presents 3D direct numerical simulation (DNS) to assess/evaluate the linear stability analysis predictions. The 3D algorithm exploits the geometry's spanwise homogeneity, combining the two-dimensional spectral-element discretisation in the x–y plane with a Fourier spectral method in the third direction normal to the x–y plane with periodic boundary conditions. Tests were conducted to determine the dependence of the computed three-dimensional solutions on the number of applied Fourier modes. In these tests, the spanwise wavenumber was selected to match a linear instability mode above the critical Rayleigh number at Ga = 0, 1, and 2. A superposition of the 2D base flow and 3D eigenvector field of the predicted linear instability was used as an initial condition. The flow was then integrated forward in time until it saturated, at which point measurements of the domain inte-

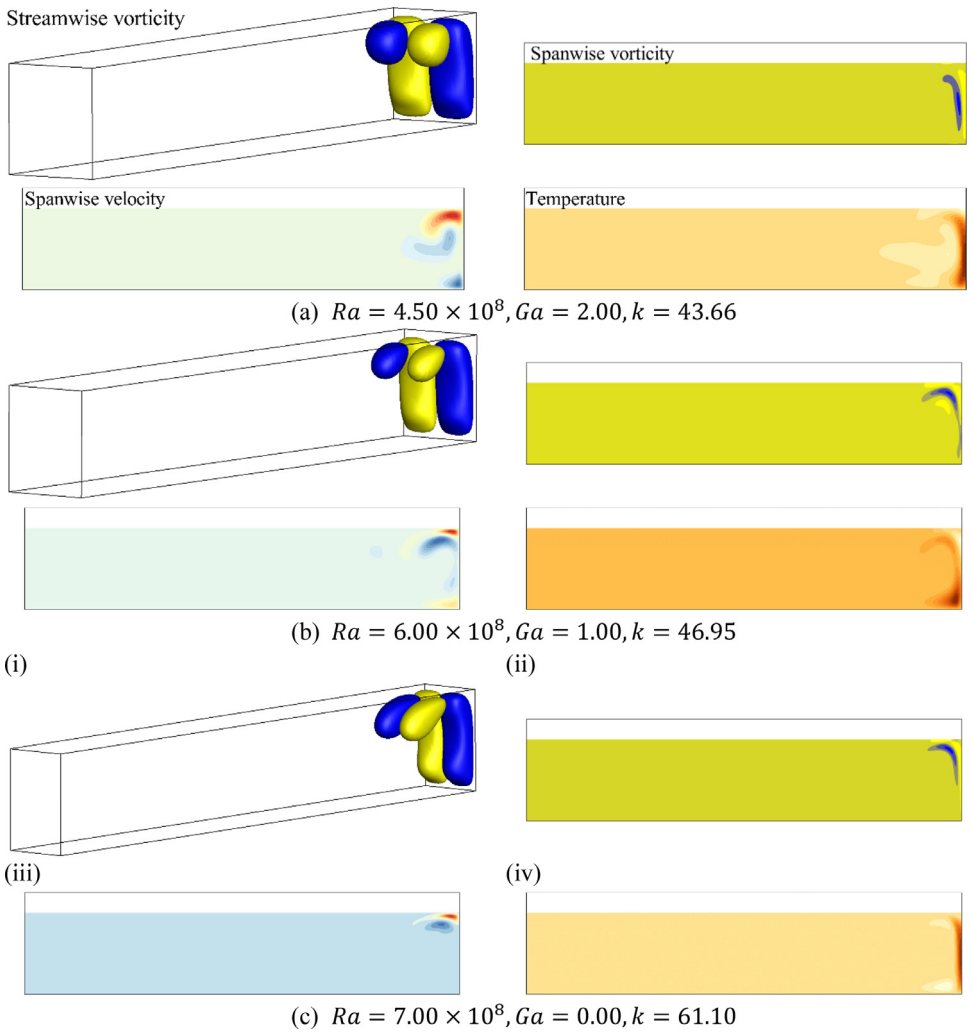

Fig. 12. (Colour online) Visualisation of the real part of leading eigenmodes at (a) Ra = 4.50 $\times 10^8$ and Ga = 2 with 43.66 (b) Ra = 6.00 $\times 10^8$ and Ga = 1 with k = 46.95 (c) Ra = 7.00 $\times 10^8$ and Ga = 0 with k = 61.10 consisting of three-dimensional visualisation of the streamwise (X-component of) vorticity, spanwise (z-component of) vorticity, spanwise velocity and temperature.

Table 3
Convergence of the saturated three-dimensional DNS solution with the number of Fourier modes included in the simulation (N_f) for a test case having Ra = 5 $\times 10^8$ and Ga = 2 with k = 45.51.

Number of Fourier modes	$\int \lvert w \rvert d\Omega$	$\lvert Difference \rvert (\%)$
2	0.188811	14.39
4	0.165055	0.20
8	0.165401	0.02
16	0.165437	–

gral of absolute velocity in the third dimension (|w|) was taken. Results of the different number of employed Fourier modes are reported in Table 3, demonstrating that the solution having 8 Fourier modes has converged to within at least four significant figures to the result obtained with 16 modes. This is supposed sufficient to capture the nonlinear growth behaviour and the mode's saturated state, so 8 Fourier modes are employed hereafter.

3D simulations were performed at Ga = 0 and 2. Rayleigh numbers are considered higher than the critical Rayleigh number corresponding to these Ga values. The spanwise wavenumbers in both cases are set to the maximum growth rate of the corresponding linear instability eigenmode. Fig. 15a and b show the time history of the spanwise velocity in three-dimensional simulations for Ra = 5 $\times 10^8$ with Ga = 2 and Ra = 7.25 $\times 10^8$ with Ga = 0, respectively. The oscillatory behaviour in Fig. 15 agrees well with the complex leading eigenmodes predicted by the linear stability analysis in Figs. 7-9. Comparing amplitude of the oscillations for the two mentioned cases indicates the flow transition to 3D periodic behaviour occurs later for a larger Ga value. In other words, flow field corresponding to a smaller Ga value faster becomes saturated to 3D periodic behaviour. In addition, comparing amplitude results indicate that the flow field with a larger Ga value has a larger amplitude of oscillations.

The growth rate of the perturbations can be calculated using the time history of energy sepctrum of the dominant Fourier mode used for w-velocity in the DNS simulation. In other words, the growth rate was obtained from the 3D DNS by finding the slope between two points in the linear growth regime from the time history of the logarithm of the kinetic energy in the first non-zero-wavenumber spanwise Fourier mode. Table 4 shows obtained growth rates via 3D-DNS and the linear stability analysis for three cases, which shows a sound agreement between two methods for three considered cases.

Fig. 16 shows 3D isosurface plots of streamwise vorticity for the cases reported in the Table 4, comparing the predicted 3D eigen-

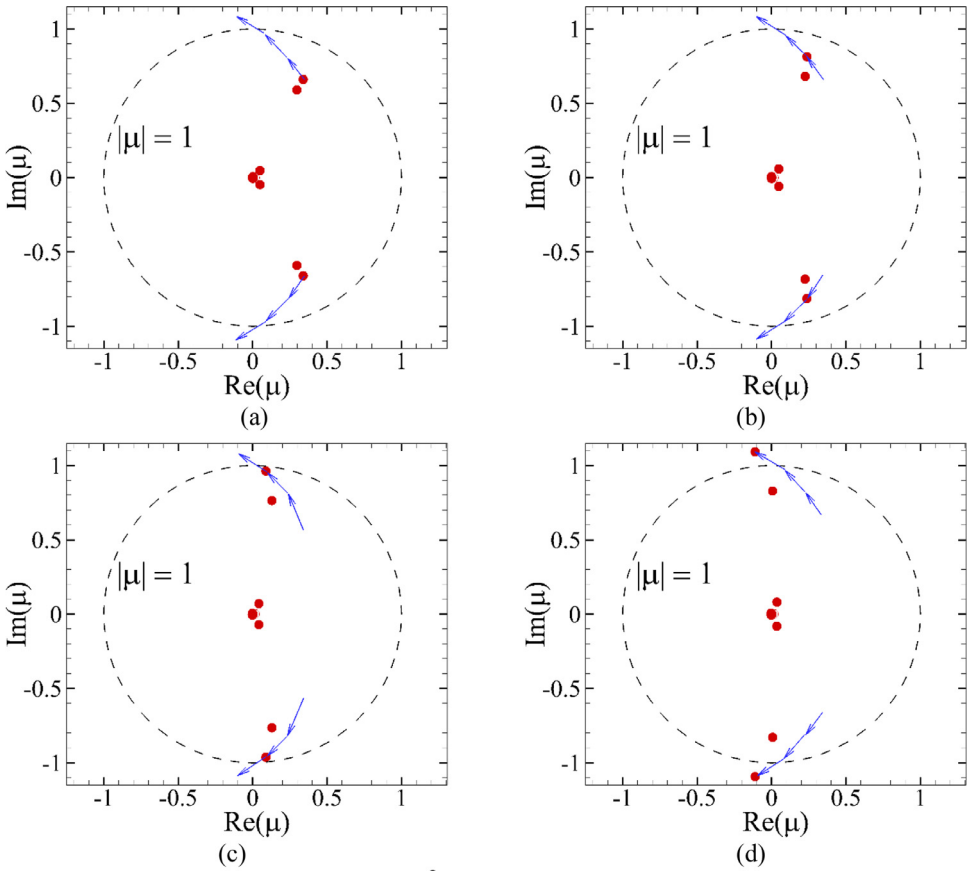

Fig. 13. Eigenvalue spectra at Ra = 5 × 10^8 with k = 44.75 and (a) Ga = 1.1, (b) 1.2, (c) 1.3, (d) 1.4. Blue arrows in each figure show the trajectory of the leading eigenmode by increasing Ga.

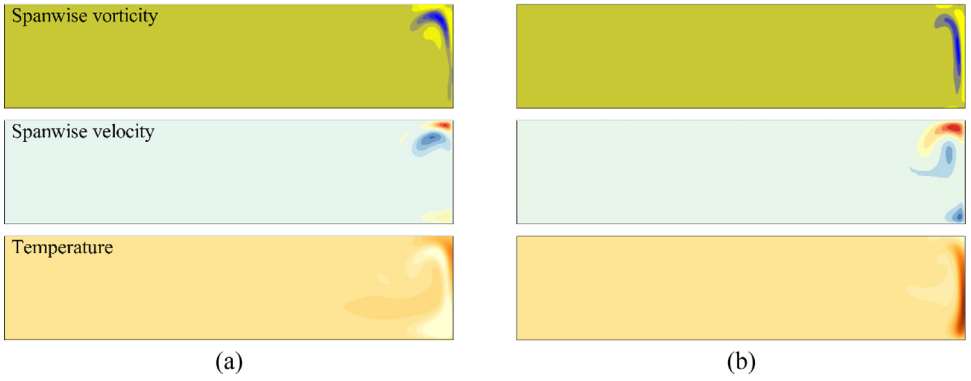

Fig. 14. Evolution of eigenvector field consisting spanwise (z-component of) vorticity and velocity and temperature at Ra = 5 × 10^8 with k = 44.75 (a) Ga = 1.1 (b) Ga = 1.4.

Table 4
Comparison between the growth rates calculated from linear stability analysis (LSA) and three-dimensional DNS.

Ga	Ra	Ra_{cr}	Ra/Ra_{cr}	k	σ(LSA)	σ(DNS)
2.00	5.00 × 10^8	4.23e8	1.18	45.51	2.72 × 10^2	2.64 × 10^2
1.01	6.50 × 10^8	5.50e8	1.18	48.25	3.15 × 10^2	3.06 × 10^2
0.00	7.25 × 10^8	6.46e8	1.12	61.63	3.23 × 10^2	3.37 × 10^2

mode in each case with the actual 3D state produced once the flow saturates following instability growth. The streamwise vorticity from the linear stability analysis (Fig. 16a-c(i)) has a good resemblance to that obtained from the three-dimensional DNS (Fig. 16a, b, c(ii)). The great agreement between the predicted eigenmode structure and the resulting saturated 3D structure verifies that the linear stability analysis provides meaningful predictions of the 3D nature of the flow. The Rayleigh numbers in Fig. 16a-c are 18% and 12% higher than the critical Rayleigh numbers for Ga = 2, 1, and 0, respectively. All three cases produce non-zero Fourier mode energy at saturation of magnitude 10^{-2} relative to the base flow energy, which is very small. The smaller the disturbance energy relative to the base flow energy, the closer the saturated state will be to the predicted infinitesimal eigenmode because the contribution of nonlinear terms is weaker that explains why a modest number (8) of Fourier modes was sufficient to resolve these 3D solutions.

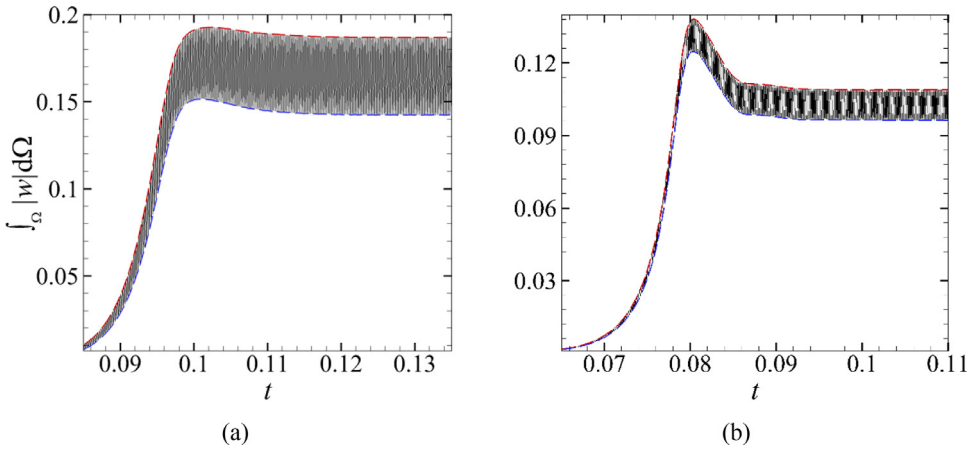

Fig. 15. Time histories of $\int |w| d\Omega$ for (a) Ga = 2 and Ra = 5.00 $\times 10^8$ with k = 45.51 and (b) Ga = 0 and Ra = 7.25 $\times 10^8$ with k = 61.63. The blue and red dashed lines demark the envelope of the oscillation of the signal.

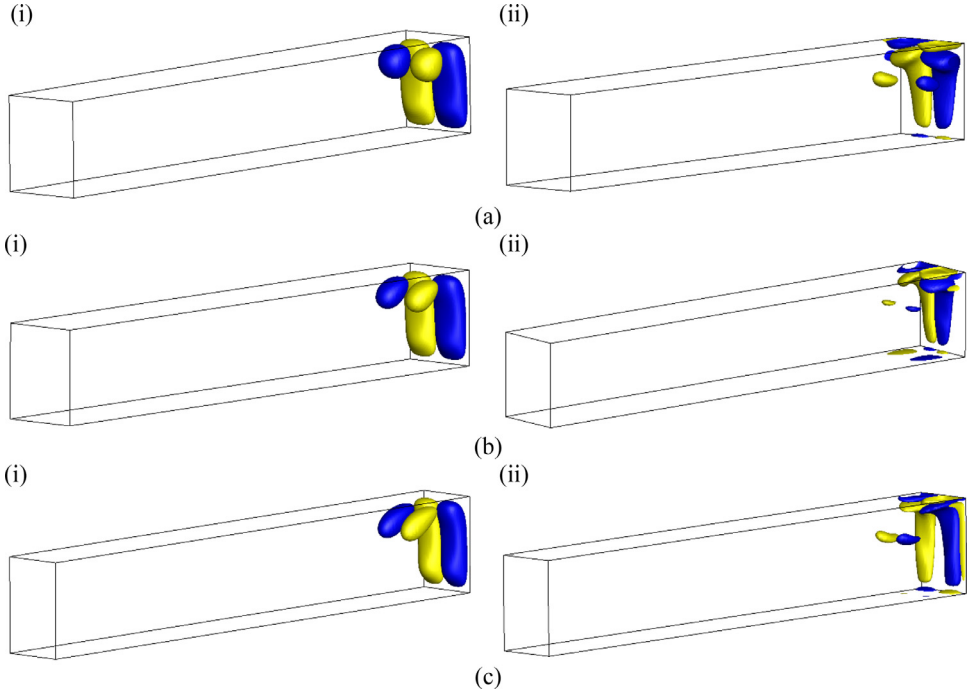

Fig. 16. Visualisation of the three-dimensional disturbances via isosurface plots of the (streamwise) x-component of vorticity for (a) Ra = 5.00 $\times 10^8$, Ga = 2, k = 45.51 (b) Ra = 6.50 $\times 10^8$, Ga = 1.01, k = 48.25 (c) Ra = 7.25 $\times 10^8$, Ga = 0, k = 61.63. In each case (i) shows the leading eigenmode predicted by the linear stability analysis and (ii) shows the saturated state of a three-dimensional DNS solution. The saturated solution in all cases is oscillatory.

6. Conclusion

Horizontal natural convection in a rectangular enclosure having an aspect ratio of height to length of 0.16 is analysed under a non-Boussinesq approximation at a Prandtl number Pr = 1. Considered non-Boussinesq approximation is a Gay-Lussac type approach under which the density variations are extended to the advection term as well as the gravity term of the momentum equation offering an improved description of rotating buoyancy-driven flows. Such a treatment inserts the Gay-Lussac parameter to the governing equations with a maximum value of 2 to avoid an unphysical density value. Many linear stability analysis were conducted to determine the critical Gay-Lussac parameters at different Rayleigh numbers that beyond which the flow becomes unstable to 3D infinitesimal disturbances. Results indicate that the flow remains unconditionally stable to any physical Gay-Lussac parameter up to the primary critical Rayleigh number which is found equal to $Ra_{cr} = 4.23 \times 10^8$. Indeed, at the primary critical Rayleigh number, the buoyancy-driven flow becomes unstable for the first time when the Gay-Lussac parameter is set to its maximum physical value. By increasing the Rayleigh number, the required Gay-Lussac parameter for an unstable buoyancy-driven flow decreases almost monotonically so that when the Gay-Lussac parameter is set to its minimum value i.e. zero, the flow field becomes unstable at the secondary critical Rayleigh number which is found equal to $Ra_{cr} = 6.46 \times 10^8$. The spanwise wavelength of the perturbations corresponding to the leading modes at the primary and secondary critical Rayleigh numbers found equal to k = 43.66 and 59.91, respectively. The stability analysis results predict that all three-dimensional transitions are via an oscillatory instability mode of the steady flow and the spanwise wavelength of the perturbations increases by increasing the Rayleigh number. Some 3D-DNS were also conducted that confirm reported stability thresholds for HC with a maximum discrepancy of 4%.

Declaration of Competing Interest

No deceleration of interest.

CRediT authorship contribution statement

Peyman Mayeli: Writing – original draft, Methodology, Conceptualization, Investigation. **Tzekih Tsai:** Writing – review & editing. **Gregory J. Sheard:** Writing – review & editing.

Acknowledgments

This research was supported by the Australian Research Council through Discovery Project DP180102647. P. M. is supported by a Monash Graduate Scholarship and a Monash International Postgraduate Research Scholarship. The authors are also supported by time allocations on the National Computational Infrastructure (NCI) peak facility and the Pawsey Supercomputing Centre through NCMAS grants. NCI is supported by the Australian Government.

References

[1] R.N. Anderson, M.A. Hobart, M.G. Langseth, Geothermal convection through oceanic crust and sediments in the Indian ocean, Science 204 (4395) (1979) 828–832.
[2] K. Brayn, M.D. Cox, A numerical investigation of the oceanic general circulation, Tellus 19 (1) (1967) 54–80.
[3] J. Yang, R. N. Edwards, J. W. Molson, Fracture-induced hydrothermal convection in the oceanic crust and the interpretation of heat-flow data, Geophys. Res. Lett., 23 (9) 929-932.
[4] S.D. King, D.L. Anderson, Edge-driven convection, Earth Planet. Sci. Lett. 160 (1998) 289–296.
[5] B.J. Foley, D. Bercovici, W. Landuyt, The conditions for plate tectonics on super-Earths: Inferences from convection models with damage, Earth Planet. Sci. Lett. 331-332 (2012) 281–290.
[6] G.O. Hughes, R.W. Griffiths, Horizontal convection, Annu. Rev. Fluid Mech 40 (2008) 185–208.
[7] H.J.J. Gramberg, P.D. Howell, J.R. Ockendon, Convection by a horizontal thermal gradient, J. Fluid Mech. 586 (2007) 41–57.
[8] S. Chiu-Webster, E.J. Hinch, J.R. Lister, Very viscous horizontal convection, J. Fluid Mech. 611 (2008) 395–426.
[9] F. Paparella, Turbulence, horizontal convection, and the Ocean's meridional overturning circulation, Math. Paradigm. Climate Sci. 15 (2016) 15–32.
[10] H.T. Rossby, On thermal convection driven by non-uniform heating from below: an experimental study, Deep Sea Res. Oceanogr. Abs. 12 (1) (1965) 9–10.
[11] G.J. Sheard, M. P.King, Horizontal convection: Effect of aspect ratio on Rayleigh number scaling and stability, Appl. Math. Model. 35 (4) (2011) 1647–1655.
[12] S. Hossain, T. Vo, G.J. Sheard, Horizontal convection in shallow enclosures scales with height, not length, at low Rayleigh numbers, Int. Comm. J. Heat Mass Transf. 109 (2018) 104308.
[13] T.K. Tsai, W.K. Hussam, A. Fouras, G.J. Sheard, The origin of instability in enclosed horizontally driven convection, Int. J. Heat Mass Transf. 94 (2016) 509–515.
[14] T.K. Tsai, W.K. Hussam, M.P. King, G.J. Sheard, Transitions and scaling in horizontal convection driven by different temperature profiles, Int. J. Therm. Sci. 148 (2020) 106166.
[15] P.Y. Passaggia, A. Scotti, B. White, Transition and turbulence in horizontal convection: linear stability analysis, J. Fluid Mech. 821 (2017) 31–58.
[16] D.V. Lyubimov, T.P. Lyubimova, N.I. Lobov, J.I.D. Alexander, Rayleigh-Benard–Marangoni convection in a weakly non-Boussinesq fluid layer with a deformable surface, Phys. Fluids 30 (2018) 024103.
[17] P. Mayeli, G.J. Sheard, Buoyancy-driven flows beyond the Boussinesq approximation: a brief review, Int. Commun. Heat Mass Transf 125 (2021) 105316.
[18] T. Pesso, S. Piva, Laminar natural convection in a square cavity: Low Prandtl numbers and large density differences, Int. J. Heat Mass Transf. 52 (3-4) (2009) 1036–1043.
[19] J.M. Lopez, F. Marques, M. Avila, The Boussinesq approximation in rapidly rotating flows, J. Fluid Mech. 737 (2013) 56–77 2013.
[20] P. Mayeli, G. Sheard, A new formulation for Boussinesq-type natural convection flows applied to the annulus cavity problem, Int. J. Numer. Methods Fluids 93 (3) (2020) 683–702.
[21] P. Mayeli, G. Sheard, Natural convection and entropy generation in square and skew cavities due to large temperature differences: a Gay-Lussac type vorticity stream-function approach, Int. J. Numer. Methods Fluids 93 (7) (2020) 2396–2420.
[22] A. Dixon, A stability analysis for interfacial waves using a Zakharov equation, J. Fluid Mech. 214 (1990) 185–210 2013.
[23] P. Mayeli, G. Sheard, An efficient and simplified Gay-Lussac approach in secondary variables form for the Non-Boussinesq simulation of free convection problems. Int. J. Numer. Method. Fluids (Published online). doi:10.1002/fld.5033.
[24] P. Mayeli, G. Sheard, A simplified and efficient Gay-Lussac approach for non-Boussinesq treatment of natural convection problems. Numer. Heat Transfer, Part B: Fundamentals (Published online). doi:10.1080/10407790.2021.1946310
[25] D. Barkley, R.D. Henderson, Three-dimensional Floquet stability analysis of the wake of a circular cylinder, J. Fluid Mech. 322 (1996) 215–242.
[26] H.M. Blackburn, J.M. Lopez, On three-dimensional quasiperiodic Floquet instabilities of two-dimensional bluff body wakes, Phys. Fluids 15 (8) (2003) L57–L60.
[27] R. Lehoucq, D. Sorensen, C. Yang, ARPACK Users' Guide, Soc. Ind. Appl. Math. (1998).
[28] G.E. Karniadakis, M. Israeli, S.A. Orszag, High-order splitting methods for the incompressible Navier–Stokes equations, J. Comput. Phys 97 (2) (1991) 414–443.

4.3 Analysing flow patterns at different Gay-Lussac parameters under the centrifugal buoyancy approximation

In this and next sections, the findings of studies on HC that are not published in the paper are discussed. This includes the effect of the GL parameter on the buoyancy-driven flow patterns in the conduction and convection-dominated regimes which is investigated in this section, and the nature of the transitions to an unstable mode via Stuart–Landau analysis that is investigated in the next section.

The effect of the different GL parameters on the flow pattern are investigated in the context of vorticity fields in Fig. 4.2. Frames of each figure show the results corresponding to specified GL parameters as stated, and the top frame of each figure shows the difference of the voritcy fields between the minimum and maximum GL parameter at the same Rayleigh number. At $Ra = 4 \times 10^5$ (Fig. 4.2a), there is a main vorticity core that has more strength (and consequently stronger circulation) close to the cooling section over the left half of the enclosure. This core becomes stronger and compressed toward the cooling section by increasing Ga. The difference between the vorticity fields at the top frame of this figure is of order $O(10^2)$ and has almost a symmetric distribution with larger difference along the four sides except for four corners. By increasing the Rayleigh number to $Ra = 4 \times 10^6$ (Fig. 4.2b), there is a similar but stronger overturning circulation that is stretched over the physical domain. Similar to the previous state, by increasing Ga this circulation becomes concentrated toward the cooling section with a slightly more strength in its central region. At this Rayleigh number, the difference has a symmetric distribution of order $O(10^2)$ along a horizontal line in the middle of the physical domain and the difference comes from contraction of the main core toward the cooling section by increasing Ga.

At $Ra = 4 \times 10^7$ (Fig. 4.2c), there is an overturning clockwise circulation in the plume region at $Ga = 0, 0.5, 1$ and 1.5, and a strong counter-clockwise circulation over the bottom side due to strong thermal boundary layer. The interaction of the fluid circulation over the plume region with the horizontal and vertical sides creates two circulations across the top-right corner of the enclosure. Interestingly, at $Ga = 2$ the main core has shifted to left with a lower strength. The difference of the vorticity fields at $Ga = 2$ and $Ga = 0$ at this Rayleigh number is of order $O(10^4)$ and as it can be seen, it mainly comes from shifting the main circulation core to left at $Ga = 2$ relative to its position at $Ga = 0$.

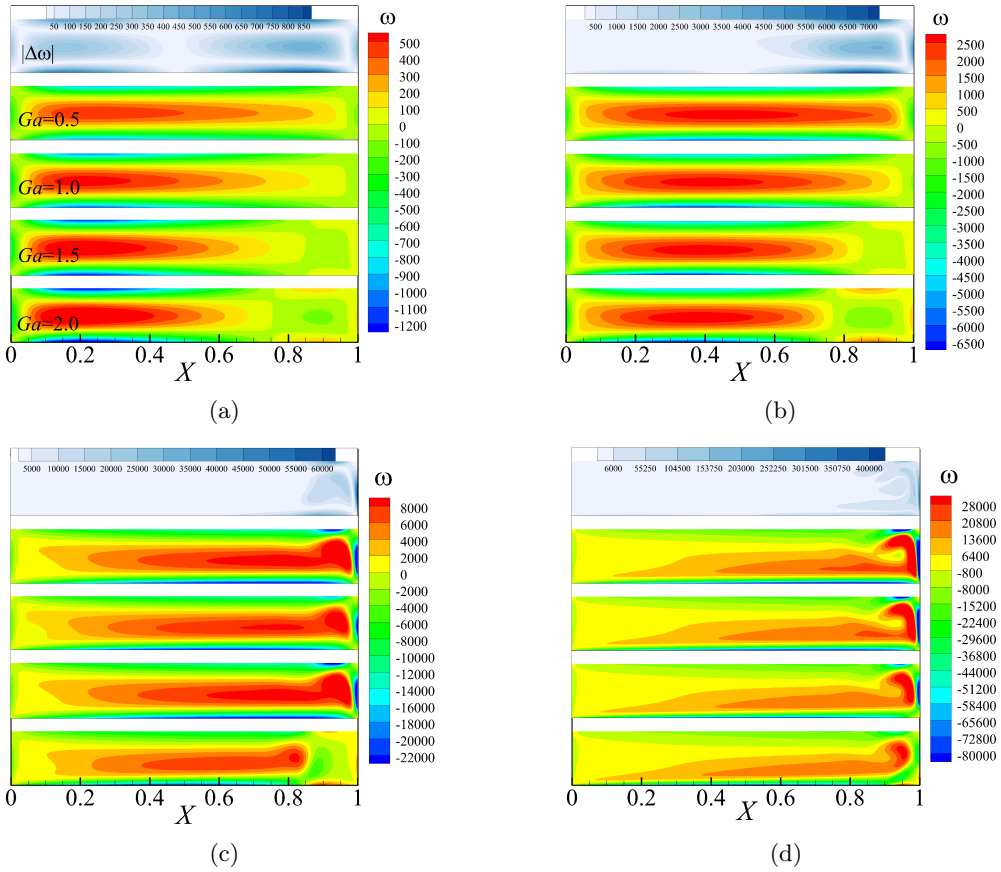

Figure 4.2: Comparison of vorticity fields at different GL parameter values as stated and (a) $Ra = 4 \times 10^5$, (b) $Ra = 4 \times 10^6$, (c) $Ra = 4 \times 10^7$, (d) $Ra = 4 \times 10^8$. The top frame of each plot shows the absolute vorticity difference between the $Ga = 2$ and $Ga = 0$ (OB) cases. The minimum and maximum of the legends for the frames (except the top one) in each figure are set equal together.

Finally, at $Ra = 4 \times 10^8$ an overturning plume in the heating region is clearly visible. The flow pattern is similar to the previous investigated Rayleigh number but here the fluid is energised enough to rise up and form a strong circulation across the top-right region. The strength of the circulations in the plume region has weakened by increasing the GL parameter. At $Ga = 0.5, 1$ and 1.5, the plume interaction with the vertical and horizontal sides has created the two clockwise vortices adjacent to the top-right corner but at $Ga = 2$, these vortices are annihilated. In addition, the strength of the circulation over the thermal boundary layer across the bottom side is decreased by increasing the GL parameter. The difference of the vorticity fields at this Rayleigh number is of order $O(10^5)$ and it mainly happens across $X \gtrsim 0.75$. More analysis of the HC thermo-flow fields may be found in the published papers.

4.4 Nature of the transition to an unstable mode

In this section, the emergence of non-linear effects on a growing instability mode is investigated via a Stuart–Landau stability analysis. This model approximates the evolution of a complex amplitude as [14],

$$\frac{\mathrm{d}A}{\mathrm{d}t} = (\sigma + i\omega)A - l(1 + ic)|A|^2 A + ..., \tag{4.6}$$

where $A(t)$ is the complex amplitude of an evolving signal as a function of time. Also σ and ω are the linear growth rate and angular frequency, respectively. Coefficients l and c describe the nonlinear departure of the mode evolution from the linear regime. Higher-order terms are truncated from the right hand side of the Eq. 4.6. Considering a $|A|\exp(i\phi)$ form for $A(t)$ where $|A|$ and ϕ are the magnitude and phase angle of the complex amplitude signal, respectively, Eq. 4.6 may be decomposed into real and imaginary components as follows,

$$\frac{\mathrm{d}(\log(A))}{\mathrm{d}t} = \sigma - l|A|^2 + ..., \tag{4.7}$$

$$\frac{\mathrm{d}\phi}{\mathrm{d}t} = \omega - lc|A|^2 + ... \tag{4.8}$$

A plot of $\mathrm{d}(\log(A))/\mathrm{d}t$ against $|A|^2$ will therefore recover the linear growth rate of instability at $|A|^2 = 0$. The nature and behaviour of flow near a transition from stable to an unstable mode in the linear stability analysis is found by the slope of $\mathrm{d}(\log(A))/\mathrm{d}t$ against $|A|^2$ in the vicinity of $|A|^2 = 0$. A positive slope ($l < 0$) indicates a subcritical bifurcation, while a negative slope ($l > 0$) corresponds to a supercritical bifurcation. A subcritical bifurcation permits bi-stability, or hysteresis, in the vicinity of the transition, whereas a supercritical bifurcation is non-hysteretic. This technique has extensively used for external flows over bluff-bodies such as toroidal bodies [15], cylinder with square cross-section flow [16] and internal flows such as flow around a 180-degree sharp bend [17] as well as flows in enclosed domains such as flow over differential-disk rotating systems [18].

For the Stuart–Landau stability analysis, the amplitude measure is taken as the envelope of oscillating w-velocity integral time history computed from DNS simulations are considered as a given signal. This is performed for two cases as shown in Fig. 4.3 at $Ra = 5 \times 10^8$ with $Ga = 2$ and $Ra = 7.25 \times 10^8$ with $Ga = 0$. For both cases,

the spanwise wavenumbers are set to the maximum growth rate of the corresponding linear instability eigenmode across the investigated wavenumbers. Considered Rayleigh numbers for two cases are 18 and 12% higher than the critical Rayleigh number at $Ga = 2$ and 0, respectively. Stability results under the Stuart–Landau model are presented in Figs. 4.3 in the context of the time derivative of the amplitude logarithm against the square of the amplitude. The nearly linear variation with a negative slope towards small $|A|^2$ close to the vertical axis shown in the plots indicates that transition occurs through a supercritical bifurcation. Calculated growth rates of the perturbations for the three Ga values via DNS simulations are also reported in table 4.1 and compared against the calculated growth rates from the Stuart–Landau model. A close agreement is observed.

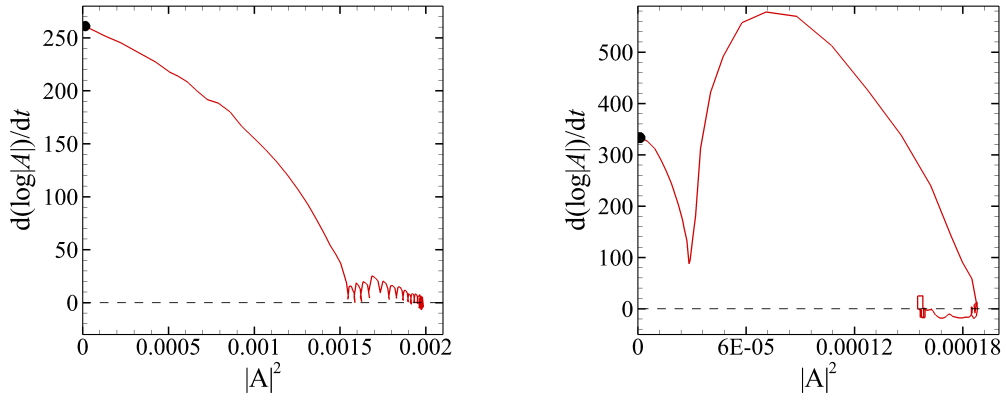

Figure 4.3: Time derivative of the amplitude logarithm of $\int |w| \mathrm{d}\omega$ against the square of the amplitude oscillations for (a) $Ra = 5 \times 10^8$and $Ga = 2$ with $k = 45.51$ (b) $Ra = 7.25 \times 10^8$and $Ga = 0$ with $k = 61.63$. The solid black circles represent the growth rate predicted by the Stuart–Landau model.

Table 4.1: Comparison between the growth rates calculated from Stuart–Landau (SL) modeling and three-dimensional DNS.

Ga	Ra	Ra_{cr}	Ra/Ra_{cr}	k	σ(SL)	σ(DNS)
2	5.00×10^8	1.23×10^8	1.18	45.51	2.72×10^2	2.64×10^2
1	6.50×10^8	5.50×10^8	1.18	48.25	3.15×10^2	3.06×10^2
0	7.25×10^8	6.46×10^8	1.12	61.63	3.23×10^2	3.37×10^2

4.5 Summary of the chapter

Horizontal convection was studied in a rectangular enclosure having an aspect ratio of height to length of 0.16 under the centrifugal approximation at unit Prandtl number. Different temperature and flow fields are investigated at different GL parameters. A

new linearsied momentum equation is derived for the linear stability analysis purposes regarding the extension of density variations to the advection term of the momentum equation beyond the gravity term. Many linear stability analysis were conducted and it is found that, from $Ra_{cr,1} = 4.23 \times 10^8$, there is a maximum GL parameter at each Rayleigh number that beyond which the buoyancy-driven flow becomes unstable to 3D infinitesimal disturbances. By increasing the Rayleigh number, the required GL parameter for an unstable buoyancy-driven flow decreases almost monotonically so that when the GL parameter is set to its minimum value (i.e. zero), the flow field becomes unstable at the secondary critical Rayleigh number which is found equal to $Ra_{cr,2} = 4.23 \times 10^8$. The stability analysis results predict that, all three-dimensional transitions are via an oscillatory instability mode of the steady flow and the spanwise wavelength of the perturbations increases by increasing the Rayleigh number. Some 3D-DNS were also conducted that confirm reported stability thresholds for horizontal convection with a maximum discrepancy of 4%. Stuart–Landau modeling of the non-linear departure from a growing linear stability mode was also conducted and it was consistently found that the evolution occurs through a supercritical bifurcation.

Chapter 5

5 Local stability analysis and evolution of heat transfer mechanism

In this chapter, average Nusselt number is scaled against the Rayleigh number at different GL parameters. Then heat transfer mechanism evolution from conduction to convection is investigated via entropy generation analysis. Results of the entropy generation analysis are prepared as a draft entitled "An entropy generation analysis of horizontal convection under the centrifugal buoyancy approximation" which is under review currently. An Orr–Sommerfeld type stability analysis is conducted to determine the longitudinal and transverse roll instabilities precedence at different Rayleigh numbers and GL parameters.

5.1 Scaling of the Nusselt number at different GL parameters

In this section, Ga-dependence of the average Nusselt number is investigated. The average Nusselt number is defined as,

$$Nu_{avg} = \frac{1}{L}\int Nu_{loc}\ \mathrm{d}X, \tag{5.1}$$

where the local Nusselt number along the bottom horizontal boundary is calculated as,

$$Nu_{loc} = \left|\frac{\partial\Theta}{\partial Y}\right|. \tag{5.2}$$

The average Nusselt number at different GL parameters including $Ga = 0, 0.5, 1, 1.5$ and 2 is plotted in Fig. 5.1a up to $Ra = 5 \times 10^8$. Results indicate that, Nu_{avg} remains almost constant up to $Ra \approx 10^5$ and it is increased by increasing the Rayleigh number from $Ra \approx 10^6$. As seen, there is a clear mismatch among Nu_{avg} values corresponding to different Ga in the convection-dominated regime so that, by increasing the GL parameter, Nu_{avg} is decreased. Calculations show around 17% difference in Nu_{avg} between $Ga = 0$ and 2 at $Ra = 5 \times 10^8$.

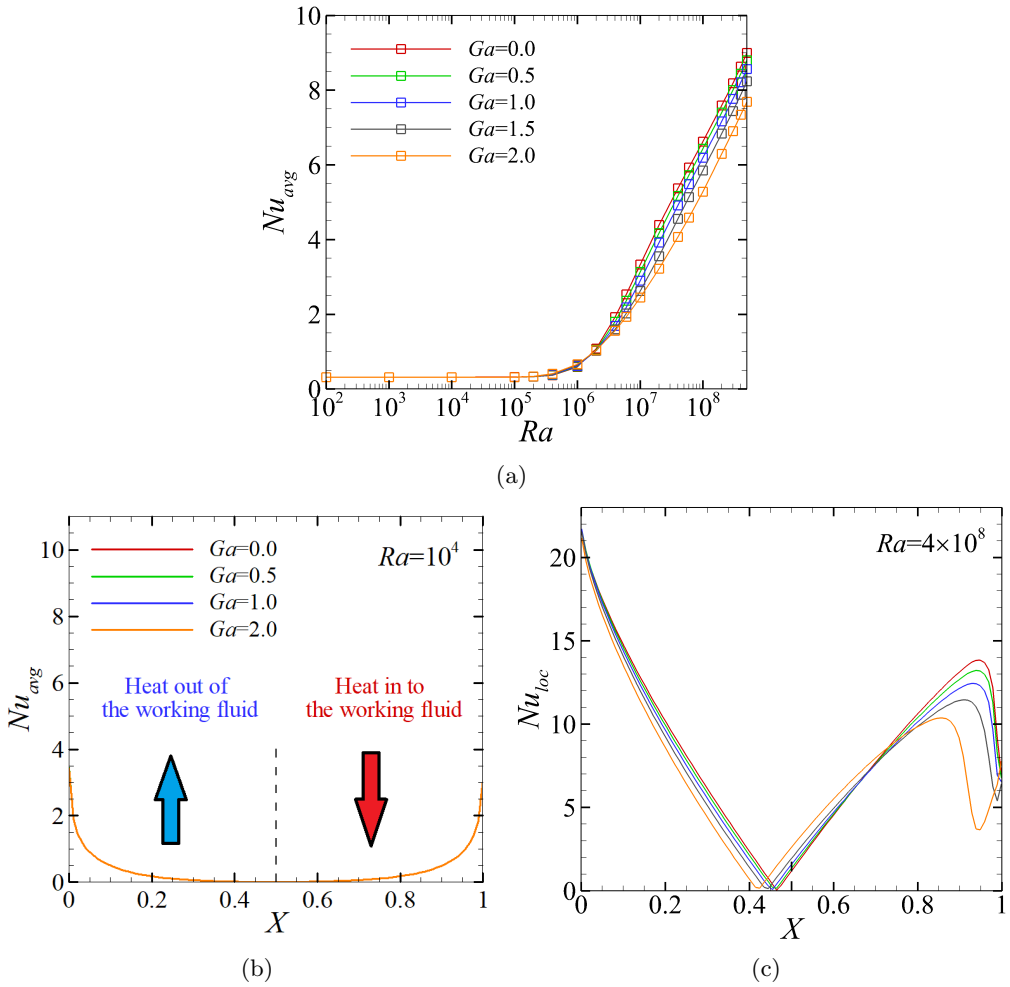

Figure 5.1: Nusselt number at different GL parameters (a) Average Nusselt number against the Rayleigh number (b, c) Local Nusselt number over the bottom surface at two different Rayleigh numbers as stated.

At $Ga = 0$, the average Nusselt number follows $Nu \sim Ra^{0.206}$ while for $Ga = 2$ the average Nusselt number scales with $Nu \sim Ra^{0.257}$. Scaling of the average Nusselt number against the Rayleigh number in the convection dominated regime is reported in table. 5.1 for different GL parameters. Nu_{avg} correlation at $Ga = 0$ is consistent with the Rossby's 1/5 scaling [19] for the average Nusselt number.

Table 5.1: Power-law scaling of the average Nusselt number $Nu_{avg} \sim Ra^n$ in the convection-dominated regime at different GL parameters.

Ga	0	0.5	1	1.5	2
n	0.206	0.214	0.223	0.238	0.257

Lower Nu_{avg} values at higher Ga is attributed to the local Nusselt number behaviour that is plotted for different GL parameters in two cases in Figs. 5.1b and 5.1c. In

the conduction-dominated regime, $Ra = 10^4$ for example (Fig. 5.1b), Nu_{loc} along the bottom surface is symmetric and there is almost no difference among different GL parameters. However, in the convection-dominated regime, $Ra = 4 \times 10^8$ for instance (Fig. 5.1c), Nu_{loc} is decreased by increasing Ga value except for a small range of $0.45 \lesssim X \lesssim 0.75$.

5.2 Governing equations for entropy generation analysis

Entropy generation analysis is an effective technique that can distinguish the evolution of heat transfer mechanism from conduction to convection both locally and globally. This is performed by measuring the entropy generation due to viscous and thermal dissipation in the context of the Bejan number, where the viscous contribution is associated with convective motions in the fluids [20]. Indeed, heat transfer processes inevitably encounter irreversible loss of useful work via dissipative processes that generate entropy. Understanding the sources of entropy generation in heat transfer may therefore provide insights permitting the improvement of efficiency in systems featuring such heat transfer processes. For incompressible fluids in the absence of internal heating, local volumetric entropy generation [20] (here normalised by $T_0^2 L^2/k\Delta\Theta^2$) may be expressed as,

$$S''' = S_\Theta + \chi S_\psi \tag{5.3}$$

where respective contributions due to thermal conduction and viscous friction are,

$$S_\Theta = \left[(\frac{\partial \Theta}{\partial X})^2 + (\frac{\partial \Theta}{\partial Y})^2 \right], \tag{5.4}$$

$$\chi S_\psi = \chi \left[2\{ (\frac{\partial U}{\partial X})^2 + (\frac{\partial V}{\partial Y})^2 \} + (\frac{\partial U}{\partial X} + \frac{\partial V}{\partial Y})^2 \right], \tag{5.5}$$

and the irreversibility distribution ratio is $\chi = \mu T_0 \alpha^2 / k L^2 \Delta\Theta^2$. The irreversibility factor may be also expressed as,

$$\chi = \mu u_0^2 \times \frac{1}{k\Delta\Theta} \times \frac{T_0}{\Delta\Theta} = u_0 \times \frac{\mu u_0/L}{k\Delta\Theta/L} \times \frac{T_0}{\Delta\Theta} = \frac{u_0 \tau_w}{q_{cond.}} \times \frac{T_0}{\Delta\Theta}, \tag{5.6}$$

or in other words,

$$\chi = \frac{q_{visc.dissip.}}{q_{cond.}} \times \frac{1}{Ga} = \frac{Br}{Ga}. \tag{5.7}$$

Eq. 5.5 is a novel expression of the irreversibility distribution ratio that introduces

the Brinkman number characterising the ratio of the viscous heat dissipation to heat conduction within the system. Typically, a small value is employed for the irreversibility distribution ratio. Considering $\chi = 10^{-4}$ (consistent with refs. [21, 22]) under the Boussinesq approximation with relative temperature difference $\varepsilon = 0.01$ ($Ga = 0.02$), gives $Br = 2 \times 10^{-5}$. In this study, we alter the irreversibility distribution corresponding to different GL parameters at a fixed $Br = 2 \times 10^{-5}$.

The ratio of entropy generation due to thermal conduction to total entropy generation yields the local Bejan number $Be_{loc} = S_\Theta/(S_\Theta + \chi S_\psi)$ from which the mean over the enclosure is calculated as $Be_{avg} = (L/H) \int Be_{loc}\, \mathrm{d}\Omega$. In entropy generation analysis, $Be > 0.5$ corresponds to scenarios where entropy generation is dominated by dissipation via thermal conduction, whereas $Be < 0.5$ corresponds to scenarios where entropy generation is dominated by viscous friction, correlating with convective heat transport.

5.3 Published paper

The entropy generation analysis is performed over $10^2 \leq Ra \leq 5 \times 10^8$ at $Ga = 0, 0.5, 1, 1.5$ and 2. Results covering variation of the average Bejan number and total irreversibilities due to thermal conduction and viscous dissipation against Rayleigh number that all together reflect heat transfer mechanism evolution from conduction to convection-dominated regime, are presented in the following published paper.

International Communications in Heat and Mass Transfer 133 (2022) 105923

Contents lists available at ScienceDirect

International Communications in Heat and Mass Transfer

journal homepage: www.elsevier.com/locate/ichmt

An entropy generation analysis of horizontal convection under the centrifugal buoyancy approximation

Peyman Mayeli *, Gregory J. Sheard

Department of Mechanical and Aerospace Engineering, Monash University, VIC 3800, Australia

ARTICLE INFO

Keywords:
Horizontal convection
Centrifugal buoyancy approximation
Gay-Lussac parameter
Entropy generation analysis

ABSTRACT

An entropy generation analysis is conducted for horizontal convection under the centrifugal buoyancy and the Boussinesq approximations in a relatively shallow enclosure at a fixed Prandtl number of unity to characterise irreversible losses across the conduction and convection-dominated regimes using the Bejan number (Be). A variable irreversibility distribution factor is expressed for the entropy generation analysis as a ratio of the Brinkman number (Br) and the Gay-Lussac (Ga) parameter for the first time. Governing equations are solved numerically using a high-order nodal spectral-element method. Calculations are performed at a fixed $Br = 2 \times 10^{-5}$ over the physical range of the Gay-Lussac parameter $0 \leq Ga \leq 2$ up to $Ra = 5 \times 10^8$. As expected, increasing the Rayleigh number shifts the flow toward a convection-dominated regime; however it is found that increasing the Gay-Lussac parameter draws the heat transfer mechanism back to a conduction-dominated state. In other words, advection related buoyancy effects act to keep the buoyancy-driven flow in conduction-dominated regime. The entropy generation analysis indicates that at $Ga \gtrsim 0.5$ conduction and convection are in balance at $Ra \approx 6 \times 10^5$, while under the conventional Boussinesq approximation ($Ga = 0$), heat transfer is convection-dominated. The transition of the average Bejan number from conduction to convection-dominated regime follows closely to a reciprocal scaling against Rayleigh number $Be_{ave} \sim Ra^{-1}$ when $Ga = 0$ but the same process scales with $Be_{ave} \sim Ra^{-0.5}$ relation at $Ga = 2$.

1. Introduction

Horizontal convection (HC) refers to natural convection in which fluid motion is invoked by non-uniform buoyancy long a horizontal buoyancy. In HC, the fluid is overturning at any Rayleigh number due to horizontal non-uniformity in buoyancy [1]. This type of convection is of interest due to its contribution in geological applications such as oceanic [2] and atmospheric [3] flow patterns as well as industrial application such as glass melting [4].

Some studies have been conducted for HC. One of the pioneering studies in HC is Rossby's $Nu \sim Ra^{1/5}$ scaling [5] in the convection dominated regime. The same scaling for the average Nusselt number against the Rayleigh number is reported up to $Ra = O(10^9)$ by Siggers et al. [6] and Sheard and King [7]. Shishkina et al. [8] adapted the scaling theory developed by Grossmann and Lohse [9] for Rayleigh–Bénard convection to a HC system where global averaged kinetic and thermal dissipation rates are decomposed into boundary layer and bulk contributions. Their theory verifies Rossby's scaling [5], characterised by the thermal boundary layer being thicker than the kinetic layer, and both thermal and kinetic dissipation being dominant in the boundary layers. A fairly comprehensive review about different aspect of HC has been provided by Hughes and Griffiths [10].

In the literature, HC systems have been studied under the classical Boussinesq approximation where density differences are considered only in the gravity term. This assumption impedes application to problems featuring large temperature differences, rapid rotation, etc. [11]. One approach that extends this treatment is the Gay-Lussac (Ga) approach in which the density variations are reintroduced wherever density appears in the governing equations [12–14]. The Gay-Lussac parameter $Ga = \beta \Delta\theta$, as a product of temperature difference and isobaric expansion coefficient emerges from this treatment. The centrifugal approximation [15–16] is a subcategory of the Gay-Lussac approach in which the density variations are extended to the advection terms of the momentum equation as well as the gravity term. This approach is suitable for flows having either localised or global rapid rotation. The interested reader is directed to a recent review of buoyancy models within and outside the Boussinesq approximation [17]. More recently, Mayeli et al. [18] studied HC under the centrifugal buoyancy approximation, finding that in the range of $4.23 \times 10^8 \leq Ra \leq 6.5 \times 10^8$

* Corresponding author.
E-mail addresses: Peyman.Mayeli@monash.edu (P. Mayeli), Greg.Sheard@monash.edu (G.J. Sheard).

https://doi.org/10.1016/j.icheatmasstransfer.2022.105923

Available online 16 February 2022

Nomenclature

Be_{ave}	average Bejan number
Be_{loc}	local Bejan number
Br	Brinkman number
e_g	unit vector in gravity direction
g	gravitational acceleration (m/s^2)
Ga	Gay-Lussac parameter ($\beta\Delta\theta$)
k	thermal conductivity ($W/m.K$)
L_{ref}	reference length (m)
n	normal vector of the surface
p	Pressure (Pa)
p^*	modified pressure
P	dimensionless pressure
Pr	Prandtl number
q	Heat (W)
$q_{cond.}$	conducted heat
$q_{visc.\ dissip.}$	dissipated heat due to viscosity
Ra	Rayleigh number
S_Θ	entropy generation due to heat transfer
S_ψ	entropy generation due to fluid friction
T	Temperature (K)
x	Cartesian coordinate (m)
X	dimensionless Cartesian coordinate
u	velocity vector (m/s)
U	dimensionless velocity vector
α	thermal diffusivity (m^2/s)
β	isobaric expansion coefficient ($1/K$)
θ	physical temperature (K)
$\Delta\theta$	reference temperature difference (K)
Θ	dimensionless temperature
ε	relative temperature difference
μ	dynamic viscosity ($Pa.s$)
ρ	density (kg/m^3)
ρ_0	reference density (kg/m^3)
τ_w	wall shear stress (Pa)
χ	irreversibility distribution ratio

Subscript

ave	average
c	cold
h	hot
loc	local
tot	total
0	a reference value

there exists a physical Ga that beyond which the buoyancy-driven flow becomes unstable.

In this study, the centrifugal approximation provides the basis for an entropy generation analysis in HC. A literature survey indicates that entropy generation analysis has not been applied to any HC problem before, but there are a vast number of studies in which different thermo-flow fields have been analyzed in terms of entropy generation. Interested readers are referred to the recent review paper [19] for a detailed discussion of entropy generation of nanofluid and hybrid nanofluid flow in thermal systems. In ref. 19 it is concluded that for microchannel systems, entropy generation decreases with decreasing nanoparticle size or increasing concentration. Also for open cavities, the entropy generation decreases by increasing both the Hartmann number and volume fraction at horizontal magnetic field, thus application direction of magnetic field is important to minimize the entropy generation.

Tayebi et al. [20–23] performed entropy generation analysis of natural convection in different setups such as square cavity with a conducting hollow cylinder [20] concluding that inserting a hollow conducting cylinder plays an important role in controlling flow characteristic and irreversibilities within the cavity. An entropy generation analysis in an annular enclosure fitted with fins under magnetic field effects [21], led to concluding irreversibility related to thermo-effects is predominant at low Rayleigh numbers, while at high Rayleigh numbers, the irreversibility due to heat transfer is no longer the main contributor of overall entropy production. Their results indicate that the in the presence of magnetic, increase the share of heat transfer irreversibility in total entropy generation. Tayebi and Oztop [22] investigated free convection in horizontal confocal elliptic cylinders filled with Al_2O_3-Cu/water hybrid nanofluid. An important contribution of their work was finding the average Bejan number is not affected by the addition of hybrid nanoparticles. Tayebi et al. [23] studied free convection in annular elliptical cavity filled with Al_2O_3-Cu/water hybrid nanofluid with an internal heat generator/absorber. They found that in the case of heat absorption, reduction of the average Bejan number by increasing Rayleigh number is more gradually and adding nanoparticles doesn't apply much effect on the average Bejan number. Dutta et al. [24] analysed free convection heat transfer in a rhombic enclosure using Cu-water working nanofluid under the magnetic field effects. Findings of their study indicates that the rate of total entropy generation has a revers relation with Hartman number and leaning angles of the geometry.

Many entropy generation analysis is also preformed in the sister class of free convection i.e. mixed convection under the Boussinesq approximation. Alsabery et al. [25] studied entropy generation analysis in an enclosure with wavy horizontal walls having different number of undulations and a rotating cylinder at the center of chamber. They found that for different number of undulations, the Bejan number is the highest for the case involving a nearly stationary inner cylinder. Hussein [26] performed an entropy generation analysis due to the transient mixed convection in a 3D right-angle triangular cavity concluding that the flow field inside the cavity is influenced significantly with the direction of the moving wall. It is also found that the Bejan number decreases as the Richardson number increases. Al-Rashed et al. [27] conducted an entropy generation analysis in a 3D heated up cubical open cavity containing a central isothermal block using vorticity-velocity approach. Their simulations were performed over Richardson number 0.01–100 and percentage of Al_2O_3 nanoparticles 1–5%, concluding that the thermal entropy generation increases by increasing the concentration of nanoparticles for all Richardson numbers, but the variation of viscous entropy generation with concentrations depends on Richardson number value. Ghachem and co-workers [28] performed a numerical simulation of 3D double-diffusive free convection and studied irreversibility effects in a solar distiller. They found that all kinds of entropy generations present a minimum value when buoyancy forces due to density and concentration differences are equal. They reported total entropy rises considerably by increasing buoyancy forces ratio. Hussein et al. [29] studied unsteady laminar 3D natural convection and entropy generation in an inclined cubical trapezoidal air-filled cavity for $10^3 \leq Ra \leq 10^5$ and different inclination angle from 0^o to 180^o. They found that the inclination angle has almost no effect on the total entropy generation in conduction-dominated regime. Al-Rashed, et al. [30] investigated entropy generation for air in a 3D cubical cavity with partially active vertical walls and four different arrangements of heating and cooling section up to $Ra = 10^6$. They found that the arrangements of heating and cooling regions have a significant effect on the entropy generation. They also reported cases corresponding to minimum and maximum Bejan number among four considered cases for their study.

Entropy generation is also investigated for buoyancy-driven flows in porous medium. For instance, Dutta et al. [31] surveyed variation of

entropy generation in a porous quadrantal enclosure with non-uniform thermal condition. Their findings indicates entropy generation due to heat transfer is the significant contributor of irreversibility at low values of Darcy number, while for larger values of Darcy number and Rayleigh number viscous dissipation becomes dominant part of total entropy generation. A similar study is also performed on a porous rhombic enclosure [32]. Bhardwaj et al. [33] studied free convection in a porous triangular enclosure with a wavy vertical wall using vorticity stream-function approach. Their numerical results indicates that by increasing the Darcy number, conduction dominates heat transfer mechanism. They also reported that entropy generation in the presence of undulations is significantly higher compared to the situation with a flat wall, while irreversibilities due to heat transfer is almost equal for both scenarios.

In all aforementioned works [20–33], the Boussinesq approximation for buoyancy-driven flows serves as a fundamental assumption for governing equation. In this study, findings of the stability analysis of HC under the centrifugal buoyancy approximation [18] are extended by determining different conduction and convection-dominated regimes and the effect of Ga on the local and global entropy generation. In the next section, the governing equations under the centrifugal approximation are introduced. Section 3 deals with the numerical set up and treatment of the irreversibility distribution ratio. Results are presented in Section 4, and in Section 5, a short conclusion is drawn.

2. Governing equations under the centrifugal buoyancy approximation

The centrifugal approximation follows fundamentals of the classic Boussinesq approximation but it extends the density variations to the advection term in addition to gravity term of the momentum equation, offering an improved description of rotation in a buoyancy-driven flow [15–16]. The dimensional form of the governing equations under the centrifugal approximation may be expressed as,

$$\nabla\bullet\mathrm{u} = 0, \tag{1}$$

$$\partial u/\partial t^{*} + (\rho/\rho_0)(u\bullet\nabla)\mathrm{u} = -(1/\rho_0)\nabla\mathrm{p} + \nu\nabla^2\mathrm{u} + (\rho/\rho_0)\mathrm{ge_g}, \tag{2}$$

$$\partial T/\partial t^{*} + (u\bullet\nabla)\mathrm{T} = \alpha\nabla^2\mathrm{T}, \tag{3}$$

where using the following non-dimensionlised quantities,

$$t = \frac{t^{*}\alpha}{L^2}, X = \frac{x}{L_{ref}}, U = \frac{uL_{ref}}{\alpha}, P = \frac{p^{*}{L_{ref}}^2}{\rho\alpha^2}, \Theta = \frac{\theta}{\Delta\theta} = \frac{T - T_0}{T_h - T_c}, Ga = \beta\Delta\theta, \tag{4}$$

accompanied by a linear density state relation ($\rho/\rho_0 = 1 - \beta\theta$), yields the dimensionless form of the governing equations,

$$\nabla\bullet\mathrm{U} = 0, \tag{5}$$

$$\partial U/\partial t + (U\bullet\nabla)\mathrm{U} = -\nabla\ \mathrm{P} + \mathrm{Pr}\nabla^2\mathrm{U} - \mathrm{RaPr}\Theta\mathrm{e_g} + \mathrm{Ga}\Theta(\mathrm{U}\bullet\nabla)\mathrm{U}, \tag{6}$$

$$\partial\Theta/\partial t + (U\bullet\nabla)\Theta = \nabla^2\Theta, \tag{7}$$

that are solved by considering the following boundary conditions,

$$U = 0 \text{ on } Y = 0, 0.16 \text{ and } -0.5 \le X \le 0.5, \tag{8}$$

$$U = 0 \text{ on } X = -0.5, 0.5 \text{ and } 0 \le Y \le 0.16, \tag{9}$$

$$\Theta = X - 0.5 \text{ on } Y = 0 \text{ and } -0.5 \le X \le 0.5, \tag{10}$$

$$\partial\Theta/\partial n = 0 \text{ on } Y = 0.16 \text{ and } -0.5 \le X \le 0.5, \tag{11}$$

$$\partial\Theta/\partial n = 0 \text{ on } X = -0.5, 0.5 \text{ and } 0 \le Y \le 0.16. \tag{12}$$

Eqs. (5)–(7) introduce the Gay-Lussac parameter $Ga = \beta\Delta\theta$ (incidentally being twice the relative temperature difference, $Ga = 2\varepsilon$), a Rayleigh number characterising the ratio of buoyancy to thermal and viscous dissipation, $Ra = g\beta\Delta\theta{L_{\mathrm{ref}}}^3/\nu\alpha$, and the Prandtl number characterising the ratio of viscous to thermal dissipation, $Pr = \nu/\alpha$. In Eq. (4) $T_0 = 0.5(T_h - T_c)$ and the reference length is equal to the horizontal length of HC system. In addition, p^{*} is a modified pressured that absorbs the hydrostatic pressure effects i.e. $p^{*} = p + \rho_0\phi$, where ϕ is the gravitational potential.

The centrifugal approximation is consistent with the conventional Boussinesq approximation, except for the additional inertial buoyancy term on the right-hand side of the momentum equation arising as a consequence of extending the density variations beyond the gravity term. Ga also appears in the dimensionless form of the density state relation,

$$\rho/\rho_0 = 1 - \beta\theta = 1 - \beta\Delta\theta\Theta = 1 - Ga\Theta. \tag{13}$$

and its range is limited to $0 \le Ga \le 2$ to avoid negative density ratios.

3. Problem description and numerical setup

The centrifugal approximation is applied to HC problem in a rectangular enclosure with a fixed aspect ratio $A = H/L = 0.16$. An invariant unit Prandtl number $Pr = 1$ is considered, applicable to fluids including air and steam. A schematic of the enclosure and applied boundary conditions is presented in Fig. 1a. A linear temperature variation is applied along the bottom boundary while other surfaces are thermally insulated. This configuration cools and heats the fluid over the left and right regions of the bottom boundary, respectively. This buoyancy imbalance leads to the formation of a counter clock-wise overturning circulation. For this problem, it is supposed that the buoyancy-driven flow is 2D and laminar and the working fluid circulating inside the enclosure is Newtonian. In the considered range of the dominant parameters ($0 \le Ga \le 2$, $Pr = 1$ and $10^2 \le Ra \le 5 \times 10^8$), all flow simulations lead to a steady-state solution.

Eqs. (1)–(3) are solved using a high-order nodal spectral-element method with time integration via a third-order backward differentiation scheme. In spectral-element method, physical domain is discretised by overlapping elements and a continuous Galerkin method is applied that leads to a weak form of the governing equations. For high accuracy purposes, an orthonormal basis function such as Legendre polynomials is used in the Galerkin formulation and resultant equations are integrated over space using Gaussian quadrature formula (Gauss-Lobatto-Legendre). Indeed, spectral-element method combines the accuracy of spectral methods with the geometrical flexibility of finite elements that yields an efficient computational method in which the error decreases exponentially as the order of approximating polynomial increases.

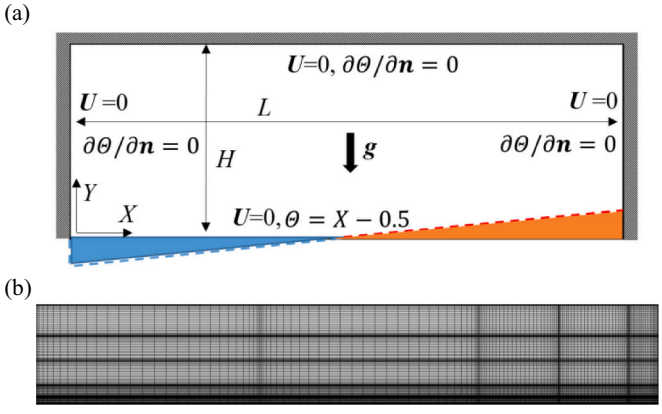

Fig. 1. (a) A schematic depiction of the horizontal convection problem showing the imposed boundary conditions, (b) The mesh showing interior quadrature points within the 5 × 4 spectral elements.

Meshing the physical geometry is performed so that resolution is concentrated toward the bottom boundary and towards the heating section where buoyancy is expected to produce plume structures. This is performed with a small number of elements having a high polynomial order 30. The mesh independency is checked in terms of an L_2 norm (defined as the integral of the velocity magnitude over the physical domain) and it is found that over the considered parameter range is less than 2×10^{-7}% [18].

Entropy generation analysis is an effective technique that can distinguish the evolution of heat transfer mechanism from conduction to convection both locally and globally. This is performed by measuring the entropy generation due to viscous and thermal dissipation in the context of the Bejan number, where the viscous contribution is associated with convective motions in the fluids [34]. Indeed, heat transfer processes inevitably encounter irreversible loss of useful work via dissipative processes that generate entropy. Understanding the sources of entropy generation in heat transfer may therefore provide insights permitting the improvement of efficiency in systems featuring such heat transfer processes. Following Ref. 34, for incompressible fluids in the absence of internal heating, local volumetric entropy generation (here normalised by $T_0^2 L^2/k\Delta\theta^2$) may be expressed as,

$$S^{'''} = S_\Theta + \chi S_\psi \tag{14}$$

where the respective contributions due to thermal conduction and viscous friction are [34]

$$S_\Theta = \left[\left(\frac{\partial \Theta}{\partial X}\right)^2 + \left(\frac{\partial \Theta}{\partial Y}\right)^2\right], \tag{15}$$

$$\chi S_\psi = \chi\left[2\left\{\left(\frac{\partial U}{\partial X}\right)^2 + \left(\frac{\partial V}{\partial Y}\right)^2\right\} + \left(\frac{\partial U}{\partial Y} + \frac{\partial V}{\partial X}\right)^2\right], \tag{16}$$

and the irreversibility distribution ratio is $\chi = \mu T_0 \alpha^2/kL^2\Delta\theta^2$. The irreversibility factor may be also expressed as,

$$\chi = \mu {u_0}^2 \times \frac{1}{(k\Delta\theta)} \times \left(\frac{T_0}{\Delta\theta}\right) = u_0 \frac{(\mu u_0)}{(k\Delta\theta)} \times \left(\frac{T_0}{\Delta\theta}\right) = u_0 \frac{\left(\frac{\mu u_0}{L}\right)}{\left(\frac{k\Delta\theta}{L}\right)} \times \left(\frac{T_0}{\Delta\theta}\right)$$

$$= \frac{(u_0 \tau_w)}{(q_{cond})} \times \left(\frac{T_0}{\Delta\theta}\right),$$

or in other words,

$$\chi = \frac{q_{visc.dissip.}}{q_{cond.}} \times \frac{1}{Ga} = \frac{Br}{Ga}. \tag{17}$$

Eq. (17) demonstrates that the irreversibility distribution ratio may be expressed in terms of the Brinkman number characterising the ratio of the viscous heat dissipation to heat conduction within the system. Typically, a small value is employed for the irreversibility distribution ratio. Considering $\chi = 10^{-4}$ (consistent with refs. [26, 28, 30]) under the Boussinesq approximation with relative temperature difference $\varepsilon = 0.01$ ($Ga = 0.02$), gives $Br = 2 \times 10^{-5}$. In this study, we alter the irreversibility distribution corresponding to different Ga at a fixed $Br = 2 \times 10^{-5}$.

The ratio of entropy generation due to thermal conduction to total entropy generation yields the local Bejan number,

$$Be_{loc} = \frac{S_\Theta}{S_\Theta + \chi S_\psi}, \tag{18}$$

from which the mean over the enclosure is obtained from

$$Be_{\text{ave}} = \frac{L}{H}\int_\Omega Be_{\text{loc}}\, d\Omega. \tag{19}$$

In entropy generation analysis, $Be > 0.5$ corresponds to scenarios where entropy generation is dominated by dissipation via thermal conduction, whereas $Be < 0.5$ corresponds to scenarios where entropy generation is dominated by viscous friction, correlating with convective heat transport.

4. Entropy generation analysis

For the entropy generation analysis in this study, calculations are performed over $10^2 \le Ra \le 5 \times 10^8$ at $Ga = 0$, 0.5, 1, 1.5 and 2. Sections 4.1 and 4.2, deal with the global and local irreversibilities, respectively, as well as the average and local Bejan number,

4.1. The effect of the Gay-Lussac parameter on the total irreversibilities and the average Bejan number

The effects of the different Ga on the $S_{\Theta tot}$, $\chi S_{\psi tot}$ and Be_{ave} are investigated in Fig. 2. Here, $S_{\Theta tot}$ and $\chi S_{\psi tot}$ refer to the integral of local S_Θ and χS_ψ over the physical domain, respectively. For entropy generation due to thermal diffusion, two regions are detected in Fig. 2a; in which up to $Ra \approx 10^6$, $S_{\Theta tot}$ remains constant, while in the second region $10^6 \lesssim Ra \le 5 \times 10^8$, it grows almost linearly. It should be noted that, the increase in $S_{\Theta tot}$ is modest being only approximately 30 times larger at $Ra = 5 \times 10^8$ than at $Ra = 10^2$ for different Ga. As seen, entropy generation due to thermal diffusion grows faster for the smaller Ga in the second region.

For entropy generation due to fluid friction (Fig. 2b), two regions are detectable. $\chi S_{\psi tot}$ increases quadratically with Ra up to $Ra \approx 10^6$ for all Ga. Subsequently, there is a linear power law correlation in the range of $10^7 \le Ra \le 5 \times 10^8$ at $Ga = 0$. This slope decreases slightly as Ga is increased, to an exponent of approximately 0.9.

Variation of the average Bejan number against Rayleigh number is presented in Fig. 2c. A feature of this figure is the intersection of the average Bejan number at different Ga with $Be_{ave} = 0.5$ that indicates conduction and convection are in balance with respect to heat transfer. At $Ga = 0$, this occurs at $Ra \approx 4 \times 10^4$, but by increasing Ga, the corresponding Rayleigh number shifts to a higher value. In other words, higher Ga tends to delay the migration from conduction to convection-dominated regime. For instance, at $Ga = 2$ intersection with $Be_{ave} = 0.5$ occurs at $Ra \approx 7 \times 10^5$. Beyond the $Be_{ave} = 0.5$ crossing, at $Ga = 0$ the average Bejan number follows closely to a reciprocal ($Be_{ave} \sim Ra^{-1}$) scaling. However, the same process occurs with a softer $Be_{ave} \sim Ra^{-0.5}$ relation at $Ga = 2$. In general, as Rayleigh number is increased into the convection-dominated regime, the average Bejan number decreases. This behaviour comes from the Bejan number definition as it is defined as the ratio of entropy generation due to thermal conduction to total entropy generation as the summation of the thermal conduction and viscous dissipation irreversibilities. Higher Rayleigh numbers are associated with stronger buoyancy forces that generates larger velocity gradients and consequently larger irreversibilities due to fluid friction that yields smaller Bejan number.

Results demonstrate that the effect of the Ga on the average Bejan number is negligible in the conduction dominated regime ($Ra \lesssim 10^4$), but it becomes significant in the fully convection-dominated regime, so much so that the difference of Be_{ave} at the largest calculated Rayleigh number at $Ra = 5 \times 10^8$ is around 95% between $Ga = 0$ and 2. Finally, in the fully convection-dominated regime ($Ra \ge 10^7$), the average Bejan number at $Ga = 0$ correlates close to $Be_{ave} \sim Ra^{-1/3}$, however this ratio decreases with increasing Ga such that a $Be_{ave} \sim Ra^{-0.3}$ relation is obtained by $Ga = 2$. A scaling of $Ra^{-1/3}$ is not unfamiliar in the context of horizontal convection. In HC, Nusselt number scales as the reciprocal HC boundary layer thickness. Siggers et al. [6] performed a variational analysis that revealed a lower bound on the scaling of the horizontal convection boundary layer thickness with Rayleigh number as $Ra^{-1/3}$. Separately, Shishkina et al. [8] developed a theory for the scaling of heat transport in horizontal convection based on an analysis of respective rates of thermal and kinetic dissipation in both the boundary layer and the interior. They proposed a Nusselt number regime scaling as $Nu \sim Ra^{1/}$

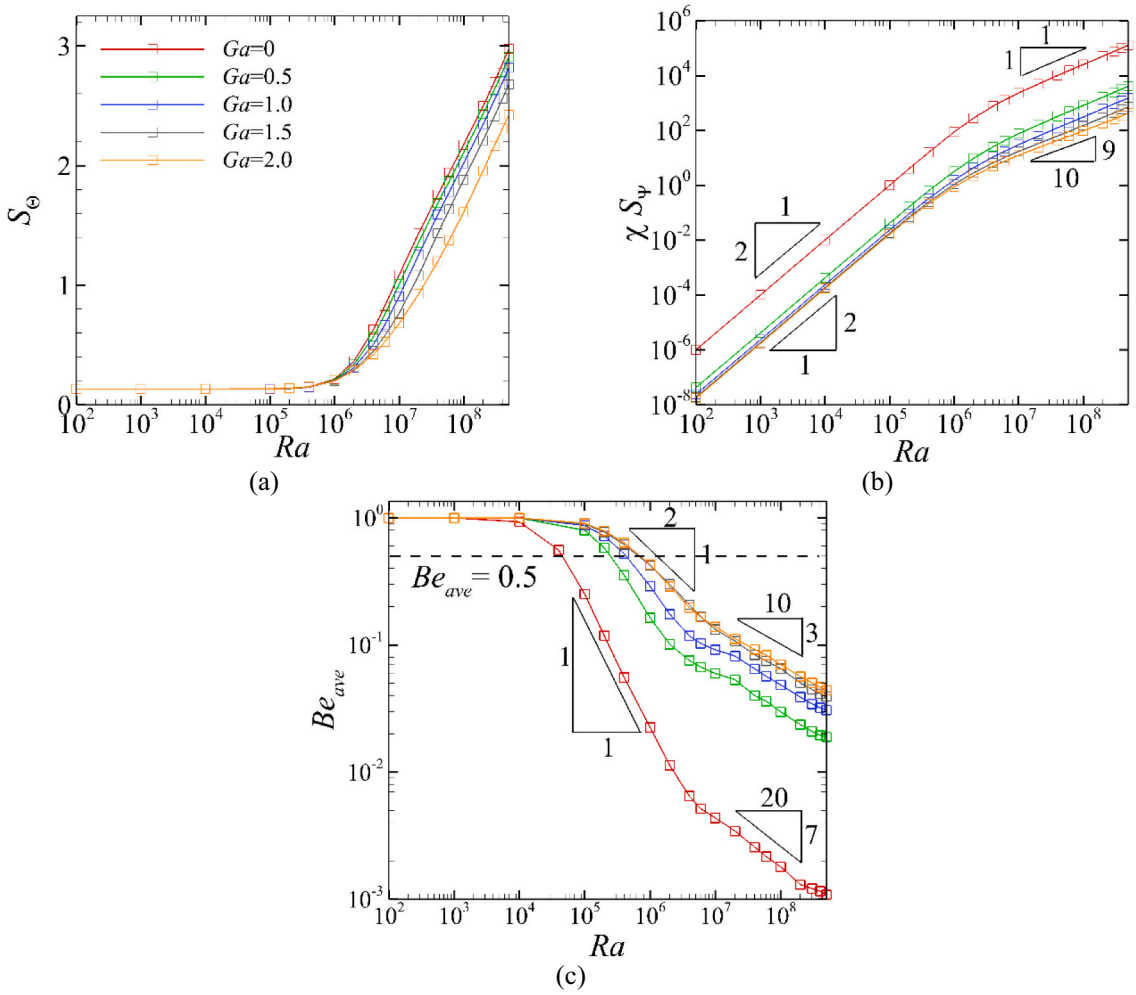

Fig. 2. Variation of different entropy related parameters against the Rayleigh number at different *Ga* including (a) Entropy generation due to heat transfer (b) Entropy generation due to fluid friction (c) Average Bejan number. Indicators of power-law exponent gradients are included for reference.

[3] (i.e. the reciprocal of the aforementioned $Ra^{-1/3}$ scaling) arising from the scenario whereby kinetic and thermal dissipation rates were both dominant within the interior rather than the boundary layer.

4.2. The effect of the Gay-Lussac parameter on the local irreversibilities and local Bejan number

To probe further, four Rayleigh numbers are selected and the rates of the local irreversibilities and the local Bejan number are scrutinized in detail at different *Ga* in the analysis to follow. These four Rayleigh numbers cover different regimes so that a Rayleigh number is selected from conduction dominated regime, one Rayleigh number is near $Be_{ave} = 0.5$ and two Rayleigh numbers are selected from the convection-dominated regime.

Fields of the local entropy generation due to fluid friction (S_ψ) are portrayed in Fig. 3. Results indicates that, in the conduction-dominated regime (Fig. 3a), S_ψ is small overall, with largest values being found adjacent to the top and bottom boundaries. A weaker zone extends centrally through the interior. This field is largely absent at right sidewall of the enclosure. In this regime, the apparent effect of *Ga* is to increase S_ψ over the cooling section. Fig. 3b represents S_ψ at $Ra = 6 \times 10^5$ (in the vicinity of $Be_{ave} = 0.5$ for most of *Ga* values except $Ga = 0$ in Fig. 2c) where the irreversibilities due to heat transfer and fluid friction are in balance. Here, while the patterns are similar S_ψ is three orders of magnitude larger than $Ra = 10^4$. In this regime, though its distribution is consistent, with the exception being slightly stronger values in the interior zone, increasing *Ga* draws larger S_ψ toward the cooling section with more strength meaning convection is becoming stronger at this region.

At the convection-dominated regime $Ra = 4 \times 10^7$ and 4×10^8 (Fig. 3c and d), S_ψ is two to three orders of magnitude larger than $Ra = 6 \times 10^5$. In this regime, convection effects S_ψ adopts a different distribution. It is relatively much stronger along the bottom boundary than the top likely due to the friction of the HC boundary layer adjacent to the bottom surface, and the interior zone has contracted and shifted downward and to the hot end of the enclosure. This reflects skewing of the overturning flow towards the lower-right of the enclosure [7] as the dark color shows stronger convection-dominated region. In other words, as the fluid moves relatively parallel to the bottom boundary, it receives stronger buoyancy forces by approaching to the bottom right corner as a linear temperature distribution is imposed along the bottom boundary. The location where the working fluid receives maximum energy coincidences with the region that it has to rotate due to geometry confinement. This generates large velocity gradients compared to other regions and consequently larger irreversibilities due to fluid friction.

Excitingly, significant *Ga*-dependence is reversed in the convection-dominated regime (Fig. 3a and b) compared to conduction-dominated regime (Fig. 3a and b). Strong entropy generation in the ascending plume adjacent to the right wall is seen at $Ga = 0$, though this becomes progressively weaker as *Ga* increases; being almost absent beyond $Ga \approx 1.5$. The strength of S_ψ in the interior zone also weakens as *Ga* is increased. These results suggest that centrifugal buoyancy effects are

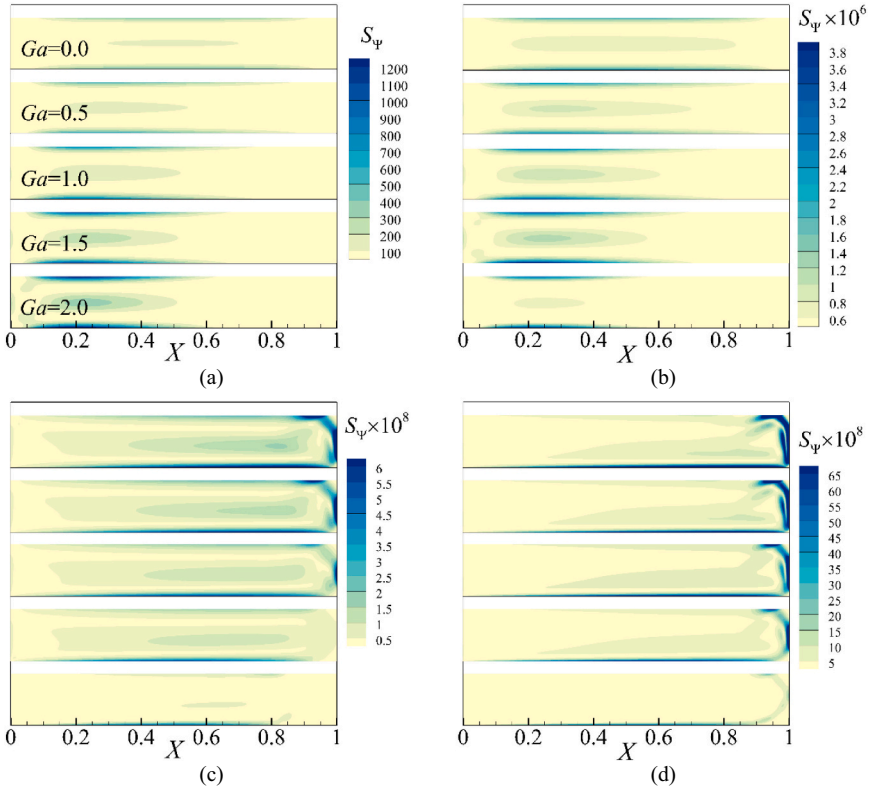

Fig. 3. Distribution of S_ψ over the physical domain with different Ga as stated at different Rayleigh numbers including (a) $Ra = 10^4$ (b) $Ra = 6 \times 10^5$ (c) $Ra = 4 \times 10^7$ and (d) $Ra = 4 \times 10^8$. Minimum and maximum of S_ψ are set equal in different frames of each figure.

weakening regions of most extreme vorticity in the flow, in turn weakening their contribution to S_ψ. Results at $Ra = 4 \times 10^8$ (Fig. 3d) further demonstrate the shift of S_ψ from the horizontal boundaries and interior to the plume region; here the low-Ga plume region dominates the distribution of S_ψ.

The influence of the end-wall plume region is further investigated by calculating the magnitude of the non-Boussinesq term, i.e. $|Ga\Theta((U \cdot \nabla)U)|$, over the physical domain in the convection-dominated regime at $Ra = 4 \times 10^7$ and 4×10^8 in Fig. 4. This term acts as a modifier through the advection part of momentum equation. As seen, stronger non-Boussinesq effects are visible across the plume region by increasing both Ga and Ra. The observed trend in the S_ψ irreversibilities at $Ra = 4 \times 10^7$ and 4×10^8 (Fig. 3c and d) by increasing Ga may be attributed to the presented non-Boussinesq effects in Fig. 4. For both cases, the non-Boussinesq effects are strongest at $Ga = 1$ and it progressively weakens by increasing Ga. Overlaid stream-lines of the $Ga\Theta((U \cdot \nabla)U)$ provide a topological perspective on the action of this term, which is apparently towards a focal point that migrates from near the upper right corner of the enclosure at $Ga = 0.5$ towards a more central position as Ga is increased; this correlates with the alleviation in S_ψ in the right side-wall plume as Ga is increased.

Local irreversibilities due to heat transfer (S_Θ) are portrayed in Fig. 5. Since three surfaces are thermally insulated, thermal conductive effects are important across the bottom boundary compared to the other boundaries. In the conduction-dominated regime (Fig. 5a), this effect is more tangible at the two bottom corners where the maximum

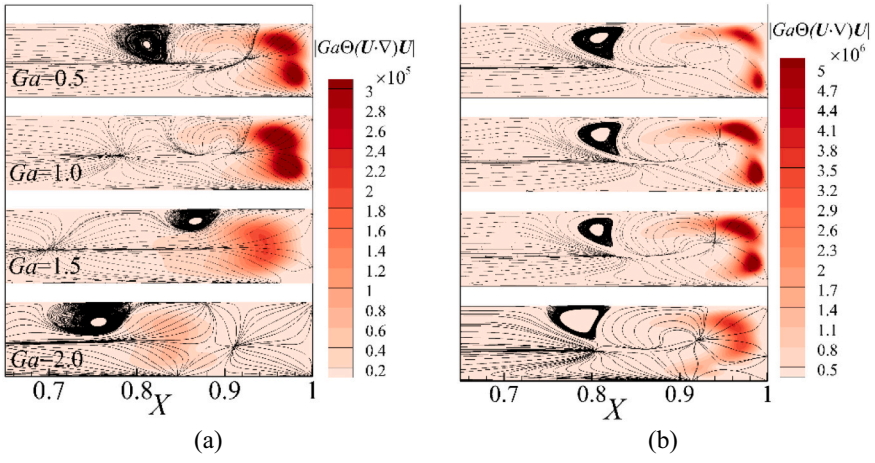

Fig. 4. Magnitude of the non-Boussinesq term ($|Ga\Theta((U \cdot \nabla)U)|$) over right-half of the physical domain at different Ga as stated in the convection-dominated regime (a) $Ra = 4 \times 10^7$ and (b) $Ra = 4 \times 10^8$.

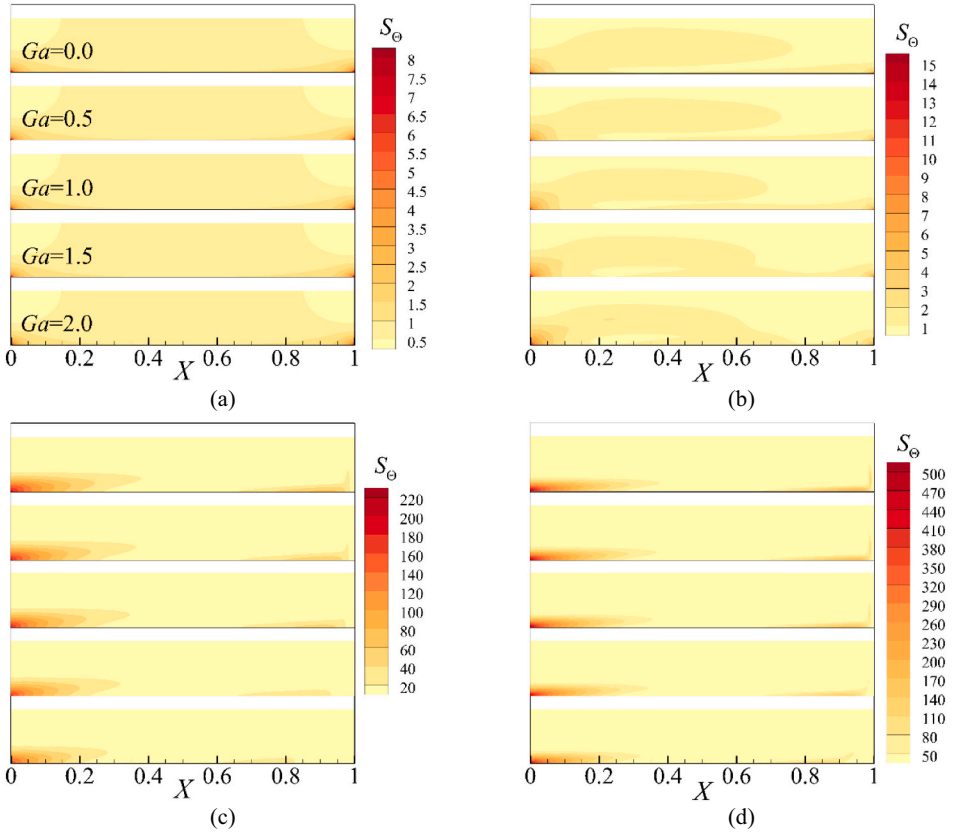

Fig. 5. Distribution of S_Θ over the physical domain with different Ga as stated at different Rayleigh numbers including (a) $Ra = 10^4$ (b) $Ra = 6 \times 10^5$ (c) $Ra = 4 \times 10^7$ and (d) $Ra = 4 \times 10^8$. Minimum and maximum of S_Θ are set equal in different frames of each figure.

temperature differences due to applied linear temperature distribution across the base. As can be seen, the Ga-dependence on the S_Θ distribution is visible in the conduction-dominated regime, and also at $Ra = 1.5 \times 10^5$ (Fig. 5b). By increasing the Rayleigh number (Fig. 5c and d), conduction effects become isolated to the cooling section of the boundary. This is consistent with Rayleigh—Bénard convection in which a cooling substrate located at the bottom side of the system de-energizes the fluid via conduction [35]. In the convection-dominated regime, this region extends further along the cooling section of the bottom boundary as thermal conduction is progressively superseded by convective heat transport at these higher Rayleigh number. A weak Ga-dependence can be seen in Fig. 5c and d, where the S_Θ strong zones shown by dark color, exhibit slightly different lengths as Ga is increased. In other words, different frames of Fig. 5c and d show negligible sensitivity to Ga alteration in this regime.

The local Bejan number distribution for different cases is presented in Fig. 6. As expected, in the conduction-dominated regime at $Ra = 10^4$ (Fig. 6a), computed Be_{loc} is almost uniformly distributed over the domain with a value close to unity, and variation in Ga has no effect. An interesting feature of the local Bejan number is noticed at $Ra = 6 \times 10^5$, where the average Bejan number is close to 0.5 for $Ga \gtrsim 0.5$ in Fig. 2c and the local Bejan number represents a general balance between S_ψ and S_Θ in Fig. 6b for mentioned values of Ga, with $Be_{loc} > 0.5$ indicating $S_\Theta > S_\psi$ and vice versa for $Be_{loc} < 0.5$. As mentioned before, S_Θ and S_ψ represent local irreversibilities due to heat conduction and viscous heat dissipation that correlates with velocity gradients. When the local Bejan number takes a value of 0.5, it means conduction and convection have the same power at that point. At this Rayleigh number the flow is convection-dominated at $Ga = 0$ but for $Ga \gtrsim 0.5$, conduction is dominant across the two bottom corners of the enclosure where the temperature difference is maximum and two parallel stretched cores close to the horizontal boundaries. As can be seen, the region under the influence of conduction expands over the heating section by increasing the Ga. On the other hand, the local Bejan number distribution shows a convection-dominated regime along the forcing boundary layer in the range of $0.15 \lesssim X \lesssim 0.65$ and a similar region along the top boundary that shrinks by increasing the Ga. These are the regions where the fluid is compelled to move due to buoyancy forces and to deflect vertically due to confining boundaries. A convection-dominated regime is also observed in the upper-half of the plume region at $Ga = 0.5$ that is annihilated by increasing Ga. A similar region exists at the top-left corner where the flow has to rotate, however part of the rotation is under the effect of cooling section that makes heat conduction as the dominant part of the heat transfer mechanism.

At $Ra = 4 \times 10^7$ and 4×10^8 (Fig. 6c and d), the whole flow is dominated by viscous entropy generation associated with convection except in the lower-left region where conductive cooling occurs. Comparing different frames of Fig. 6d indicates that by increasing Ga in the convection-dominated regime, the conduction effects become more important across the cooling section and stronger across the overturning plume region. The lowest local Bejan numbers are found adjacent to the right-hand side wall and along the top boundary. This reflects the fast convective flow upward in the buoyancy plume, which then progresses leftward along the top boundary; this is the return region of the overturning circulation. Ultimately, diffusive cooling at the left end takes over as described in [10].

5. Conclusion

An entropy generation analysis of horizontal convection under the centrifugal buoyancy approximation was conducted at unity Prandtl number for the first time to map different conduction and convection dominated regimes in terms of the irreversibilities due to heat transfer and fluid friction associated with the local and average Bejan number.

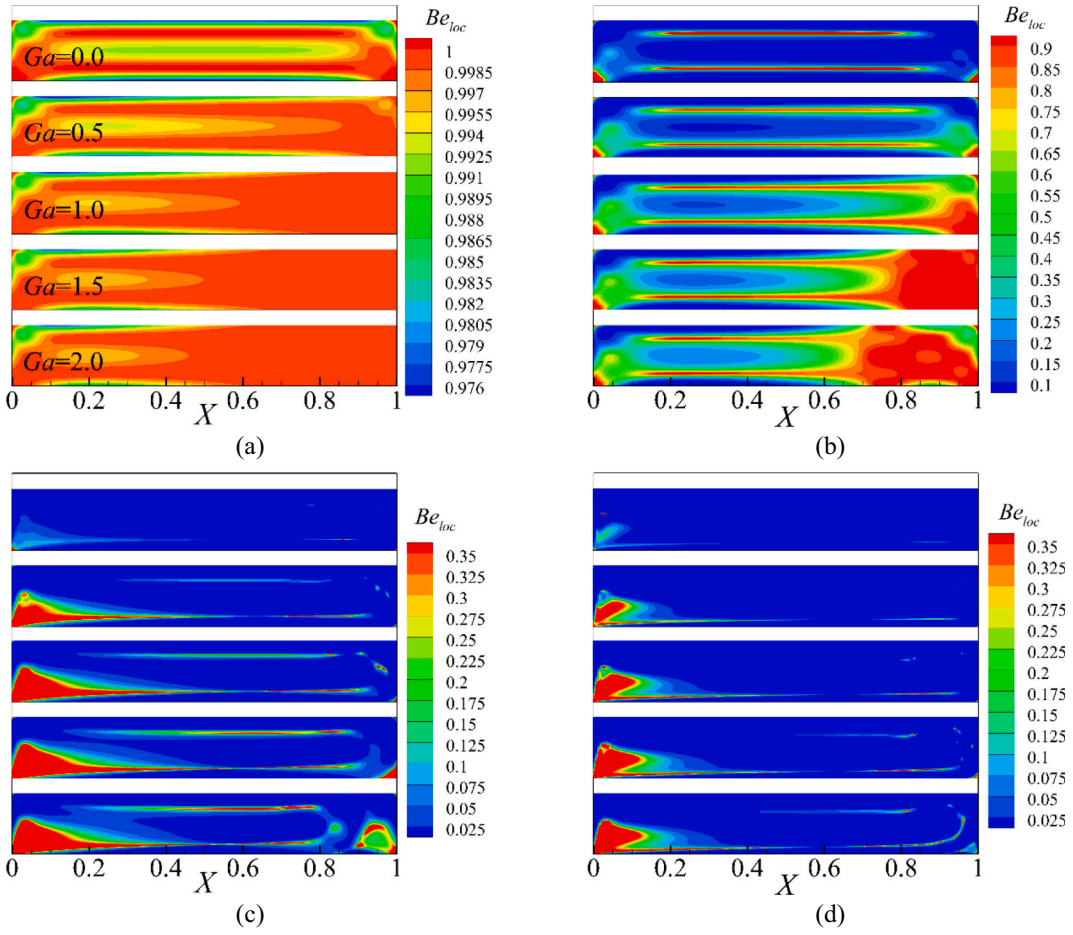

Fig. 6. Distribution of Be_{loc} over the physical domain with different Ga as stated at different Rayleigh numbers including (a) $Ra = 10^4$ (b) $Ra = 6 \times 10^5$ (c) $Ra = 4 \times 10^7$ and (d) $Ra = 4 \times 10^8$. Minimum and maximum of Be_{loc} are set equal in different frames of each figure.

The following items were the important findings/novelty of this study:

- The irreversibility distribution ratio is expressed using the Brinkman number and the Gay-Lussac parameter for the first time ($\chi = Br/Ga$).
- Entropy generation analysis was performed with a variable irreversibility distribution ratio at a fixed Brinkman number of $Br = 2 \times 10^{-5}$ and different Gay-Lussac parameters ranging $0 \leq Ga \leq 2$ up to $Ra = 5 \times 10^8$.
- At $Ra \approx 6 \times 10^5$ for $Ga \gtrsim 0.5$, the average Bejan number crosses with $Be_{ave} = 0.5$ where conduction and convection heat transfer mechanisms are in balance.
- The transition of the average Bejan number from conduction to convection-dominated regime follows closely to reciprocal ($Be_{ave} \sim Ra^{-1}$) for $Ga = 0$ but the same process occurs with $Be_{ave} \sim Ra^{-0.5}$ relation at $Ga = 2$.
- Ga has almost no role/effect on the buoyancy-driven flow field in the conduction-dominated regime ($Ra \lesssim 10^4$) but it expands regions under the influence of heat conduction in the convection-dominated regime.

Declaration of Competing Interest

No deceleration of interest.

Acknowledgements

This research was supported by the Australian Research Council through Discovery Project DP180102647. P. M. is supported by a Monash Graduate Scholarship and a Monash International Postgraduate Research Scholarship. The authors are also supported by time allocations on the National Computational Infrastructure (NCI) peak facility and the Pawsey Supercomputing Centre through NCMAS grants. NCI is supported by the Australian Government.

References

[1] T.K. Tsai, W.K. Hussam, M.P. King, G.J. Sheard, Transitions and scaling in horizontal convection driven by different temperature profiles, Int. J. Therm. Sci. 148 (2020), 106166.
[2] K. Brayn, M.D. Cox, A numerical investigation of the oceanic general circulation, Tellus 19 (1) (1967) 54–80.
[3] B.J. Foley, D. Bercovici, W. Landuyt, The conditions for plate tectonics on super-Earths: Inferences from convection models with damage, Earth Planet. Sci. Lett. 331-332 (2012) 281–290.
[4] H.J.J. Gramberg, P.D. Howell, J.R. Ockendon, Convection by a horizontal thermal gradient, J. Fluid Mech. 586 (2007) 41–57.
[5] H.T. Rossby, On thermal convection driven by non-uniform heating from below: an experimental study, Deep Sea Res. Oceanogr. Abstr. 12 (1965) 9–16.
[6] J.H. Siggers, R.R. Kerswell, N.J. Balmforth, Bounds on horizontal convection, J. Fluid Mech. 517 (2004) 55–70.
[7] G.J. Sheard, M.P. King, Horizontal convection: effect of aspect ratio on Rayleigh-number scaling and stability, Appl. Math. Model. 35 (4) (2011) 1647–1655.
[8] O. Shishkina, S. Grossmann, D. Lohse, Heat and momentum transport scalings in horizontal convection, Geophys. Res. Lett. 43 (2016) 1219–1225.
[9] S. Grossmann, D. Lohse, Scaling in thermal convection: a unifying theory, J. Fluid Mech. 407 (2000) 27–56.
[10] G.O. Hughes, R.W. Griffiths, Horizontal convection, Annu. Rev. Fluid Mech. 40 (2008) 185–208.
[11] J.M. Lopez, F. Marques, M. Avila, The Boussinesq approximation in rapidly rotating flows, J. Fluid Mech. 737 (2013) (2013) 56–77.
[12] T. Pesso, S. Piva, Laminar natural convection in a square cavity: low Prandtl numbers and large density differences, Int. J. Heat Mass Transf. 52 (3-4) (2009) 1036–1043.

[13] P. Mayeli, G. J. Sheard, An efficient and simplified Gay-Lussac approach in secondary variables form for the Non-Boussinesq simulation of free convection problems. Int. J. Numer. Methods Fluids 93 (11), 3264-3279.
[14] P. Mayeli, G. J. Sheard, A simplified and efficient Gay-Lussac approach for non-Boussinesq treatment of natural convection problems. Numer. Heat Transf. B 80 (5-6), 115-135.
[15] P. Mayeli, G.J. Sheard, A centrifugal buoyancy formulation for Boussinesq-type natural convection flows applied to the annulus cavity problem, Int. J. Numer. Methods Fluids 93 (3) (2021) 683–702.
[16] P. Mayeli, G.J. Sheard, Natural convection and entropy generation in square and skew cavities due to large temperature differences: a Gay-Lussac type vorticity stream-function approach, Int. J. Numer. Methods Fluids 93 (7) (2021) 2396–2420.
[17] P. Mayeli, G.J. Sheard, Buoyancy-driven flows beyond the Boussinesq approximation: a brief review, Int. Commun. Heat Mass Transf. 125 (2021), 105316.
[18] P. Mayeli, T.K. Tsai, G.J. Sheard, Linear stability analysis of horizontal convection under a Gay-Lussac type approximation, Int. J. Heat Mass Transf. 182 (2022), 121929.
[19] G. Huminic, A. Huminic, Entropy generation of nanofluid and hybrid nanofluid flow in thermal systems: a review, J. Mol. Liq. 302 (2020), 112533.
[20] T. Tayebi, A.J. Chamkha, Entropy generation analysis due to MHD natural convection flow in a cavity occupied with hybrid nanofluid and equipped with a conducting hollow cylinder, J. Therm. Anal. Calorim. 139 (2020) 2165–2179.
[21] T. Tayebi, A. Sattar Dogonchi, N. Karimi, H. Ge-JiLe, A.J. Chamkha, Y. Elmasry, Thermo-economic and entropy generation analyses of magnetic natural convective flow in a nanofluid-filled annular enclosure fitted with fins, Sustain. Energy Technol. Assess. 46 (2021), 101274.
[22] T. Tayebi, H.F. Öztop, Entropy production during natural convection of hybrid nanofluid in an annular passage between horizontal confocal elliptic cylinders, Int. J. Mech. Sci. 171 (2020) 105378.
[23] T. Tayebi, H.F. Öztop, A.J. Chamkha, Natural convection and entropy production in hybrid nanofluid filled-annular elliptical cavity with internal heat generation or absorption, Therm. Sci. Eng. Prog. 19 (2021), 100605.
[24] S. Dutta, N. Goswami, A.K. Biswas, S. Pati, Numerical investigation of magnetohydrodynamic natural convection heat transfer and entropy generation in a rhombic enclosure filled with Cu-water nanofluid, Int. J. Heat Mass Transf. 136 (2019) 777–798.
[25] A.I. Alsabery, T. Tayebi, R. Roslan, A.J. Chamkha, I. Hashim, Entropy generation and mixed convection flow inside a wavy-walled enclosure containing a rotating solid cylinder and a heat source, Entropy 22 (2020) 606.
[26] A.K. Hussein, Entropy generation due to the transient mixed convection in a three-dimensional right-angle triangular cavity, Int. J. Mech. Sci. 146-147 (2018) 141–151.
[27] A.A.A.A. Al-Rashed, K. Kalidasan, L. Kolsi, R. Velkennedy, A. Aydi, A.K. Hussein, E. H. Malekshah, Mixed convection and entropy generation in a nanofluid filled cubical open cavity with a central isothermal block, Int. J. Mech. Sci. 135 (2018) 362–375.
[28] K. Ghachem, L. Kolsi, C. Mâatki, A.K. Hussein, M.N. Borjini, Numerical simulation of three-dimensional double diffusive free convection flow and irreversibility studies in a solar distiller, Int. Commun. Heat Mass Transf. 39 (2012) 869–876.
[29] A.K. Hussein, K. Lioua, R. Chand, S. Sivasankaran, R. Nikbakhti, D. Li, B.M. Naceur, B.A. Habib, Three-dimensional unsteady natural convection and entropy generation in an inclined cubical trapezoidal cavity with an isothermal bottom wall, Alex. Eng. J. 55 (2016) 741–755.
[30] A. Al-Rashed, L. Kolsib, A.K. Hussein, W. Hassen, M. Aichouni, M.N. Borjini, Numerical study of three-dimensional natural convection and entropy generation in a cubical cavity with partially active vertical walls, Case Stud. Therm. Eng. 10 (2017) 100–110.
[31] S. Dutta, N. Goswami, A.K. Biswas, S. Pati, Natural convection heat transfer and entropy generation inside porous quadrantal enclosure with nonisothermal heating at the bottom wall, Numer. Heat Transf. A 73 (2018) 222–240.
[32] S. Dutta, N. Goswami, A.K. Biswas, S. Pati, Natural convection heat transfer and entropy generation in a porous rhombic enclosure: influence of non-uniform heating, J. Therm. Anal. Calorim. 144 (2021) 1493–1515.
[33] S. Bhardwaj, A. Dalal, S. Pati, Influence of wavy wall and non-uniform heating on natural convection heat transfer and entropy generation inside porous complex enclosure, Energy 79 (2015) 467–481.
[34] A. Bejan, A study of entropy generation in fundamental convective heat transfer, J. Heat Transf. 10 (1979) 718–725.
[35] P. Kaur, R. Ganesh, Negative entropy-production rate in Rayleigh-Bénard convection in two-dimensional yukawa liquids, Phys. Rev. 39 (2012) 869–876.

5.4 Linearised perturbation equations for the local stability analysis

This section deals with the local stability analysis. In this state, stability is sought over one-dimensional vertical base flow profiles that are extracted in one direction from a two-dimensional base flow. Local stability is evaluated against the small three-dimensional time-dependent perturbations by solving an eigenvalue problem. In this state, it is supposed that, the variation of the velocity is important just in one direction (in vertical direction here) so that the velocity variations may be ignored in the other directions i.e. $\partial/\partial X, \partial/\partial Z \ll \partial/\partial Y$. To derive the eigenvalue problem, a base flow containing perturbations is defined in a general form of

$$\phi = \phi_b(y) + \epsilon\tilde{\phi}(Y)e^{i(\alpha X+\beta Z-\omega t)}, \tag{5.8}$$

in which ϕ refers to any flow variables and ϵ is an infinitesimal perturbation and $\tilde{\phi}$ is a complex eigenfunction. The perturbation comprises traveling wave numbers α and β in X and Z directions, respectively, and also a frequency dictated by ω. For one-dimensional stability analysis, regions where the vertical velocities are below a tenth of the horizontal velocity are of interest. The same criteria is considered for the horizontal velocity gradients as an extra credit for a one-dimensional flow assumption.

The eigenvalue problem is derived by implementing perturbations into the governing equations. The system of equations are then linearised by the retaining terms of order $O(\epsilon)$ in the resultant equations. In brief, the boundary layer flow assumptions are used to simplify the linearsied Navier—Stokes equations, so that the $\tilde{U}$, $\tilde{W}$ and $\tilde{P}$ are removed from the final equation. The result is as follows

$$\begin{aligned} i\alpha[(1-Ga\bar{\Theta})\bar{U}'' - (1-Ga\bar{\Theta})\bar{U}'(D^2-k^2) + (1-Ga\bar{\Theta}')(\bar{U}' - \bar{U}D)]\tilde{V} \\ +Pr(D^2-k^2)^2\tilde{V} - k^2RaPr\tilde{\Theta} = -i\omega(D^2-k^2)\tilde{V}, \end{aligned} \tag{5.9}$$

$$\bar{\Theta}'\tilde{V} + [i\alpha\bar{U} - (D^2-k^2)]\tilde{\Theta} = i\omega\tilde{\Theta}. \tag{5.10}$$

The derivation procedure of the linearised perturbation equations has been provided in Appendix B. The eigenvalue problem is constructed from Eqs. 5.9 and 5.10 for $\tilde{V}$ and $\tilde{\Theta}$ in which, D and prime sign represent partial derivatives and differentiation with

respect to vertical direction, respectively. The wave number is expressed by $k^2 = \alpha^2 + \beta^2$. The eigenvalue problem is constructed in a general form of $\mathbf{AX}_k = \omega_k \mathbf{BX}_k$, where $\mathbf{A}$ and $\mathbf{B}$ represent $\tilde{V}$ and $\tilde{\Theta}$ coefficients from LHS and RHS of Eqs. 5.9 and 5.10, respectively. Regarding a complex eigenvalue problem i.e. $\omega = \omega_{Re} + i\sigma_{Im}$ and the corresponding spatio-temporal mode evolution through $\omega = e^{\sigma_{Im}}[cos(\omega_{Re}) + isin(\omega_{Re})]$, the imaginary part provides the growth rate of perturbations, with instability corresponding to $\sigma_{Im} > 0$, while the real part gives the angular frequency of any oscillatory component of the instability mode.

It should be noted that in buoyancy-driven flow, when instability has a thermal rather than hydrodynamic (shear) origin, shear selects the preferred stability mode [25]. Therefore, both longitudinal and transverse roll instabilities are considered in this study. Transverse roll instability is investigated by setting $\beta = 0$ and finding α corresponding to the maximum imaginary part of ω, and vice versa for the longitudinal roll instability.

The eigenvalue problem is solved using a pseudo-spectral method. Accurate performance of the solver was tested against the numerical result for plane Poiseuille flow [26], where it reproduced the exact critical Reynolds number $Re_{cr} = 5772.22$ and wavenumber $k_{cr} = 1.02056$. Also, a test against a thermal instability benchmark, Rayleigh-Bénard convection, delivered the expected critical Rayleigh number $Ra_{cr} = 1707.76$ and wavenumber $k_{cr} = 3.177$ [27].

5.5 Local stability analysis under the centrifugal buoyancy approximation

To initiate local stability analysis, regions where the one-dimensional flow assumption is valid are determined. The HC flow in this study is not strictly parallel, but it is approximately parallel except towards the upstream and downstream end-walls. The parallel flow assumption is verified by comparing the horizontal and vertical velocity components magnitude as well as the shear deformation of the horizontal velocity as shown in Figs. 5.3a and 5.3b at $Ra = 10^9$ at different GL parameters. Results indicate that in the convection-dominated regime, just in the region of $0.4 \lesssim X \lesssim 0.85$ both $\sum|U|/\sum|V|$ and $\sum|\partial U/\partial X|/\sum|\partial U/\partial Y|$ lie below 10%, so the one-dimensional stability analysis is restricted to this region. A mesh independency test is also performed for the stability analysis problem and it is found that Chebyshev polynomial basis function of order 30 is enough to keep the stability results independent of further resolution. The horizontal

velocity and temperature profiles at an arbitrary location from the considered range ($X = 0.8$ for example) are plotted in Figs. 5.3c and 5.3d. These profiles at different X-locations serve as the base flow data (shown with an over bar in Eqs. 5.9 and 5.10) to conduct the local stability analysis.

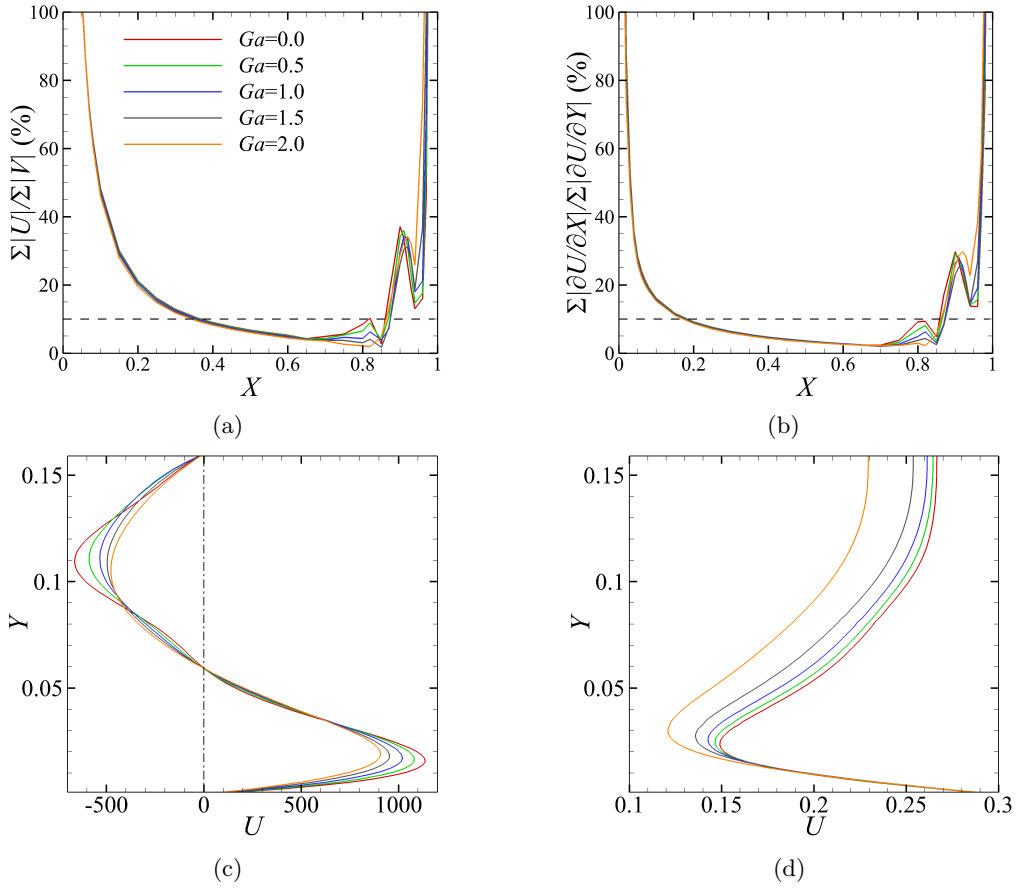

Figure 5.2: Verification of the parallel flow assumption at $Ra = 10^9$ with different GL parameters (a) A comparison of vertical and horizontal velocity magnitude summing over the depth of the enclosure, (b) Comparison of the horizontal velocity gradients in the X- and Y-direction summing over the depth of the enclosure, (c) horizontal velocity profile at $X = 0.8$ (d) temperature profile at $X = 0.8$. The horizontal dash-dotted lines in (a) and (b) represents the 10% level appropriate for 1D stability analysis.

The first part of the Orr–Sommerfeld type stability results are presented in Fig. 5.4, that are devoted to investigate when the buoyancy-driven flow becomes locally unstable over the considered region for the first time. In this figure, results corresponding to the transverse ($\beta = 0$) and longitudinal ($\alpha = 0$) roll instabilities are plotted by the solid and dashed lines, respectively, along the four vertical lines including $X = 0.70, 0.75, 80$ and 0.85 and three GL parameters including $Ga = 0, 1$ and 2. Stability results indicate that, the convectively unstable region grows from the hot end of the forcing boundary and it becomes progressively stable by approaching toward the cooling section. Up to

$Ra = 5 \times 10^6$ (Figs. 5.4a and 5.4b), the flow is locally stable to both transverse and longitudinal roll instabilities at $Ga = 0$ and 1 over the considered length but the growth rate of the perturbations at $Ga = 2$ and $X = 0.85$ crosses with $\sigma = 0$ at wavenumber $k = 19$ for the first time. Regarding the predicted critical Rayleigh number of $Ra = 4.23 \times 10^8$ at $Ga = 2$, presented data in Fig. 5.4c indicates that, the buoyancy-driven flow becomes locally unstable two order of magnitude lower than the computed critical Rayleigh number by the global linear stability analysis. At this Rayleigh number, there is no precedence between the transverse and longitudinal roll instabilities in crossing with $\sigma = 0$ but there is a clear difference between the two roll types at higher Rayleigh numbers.

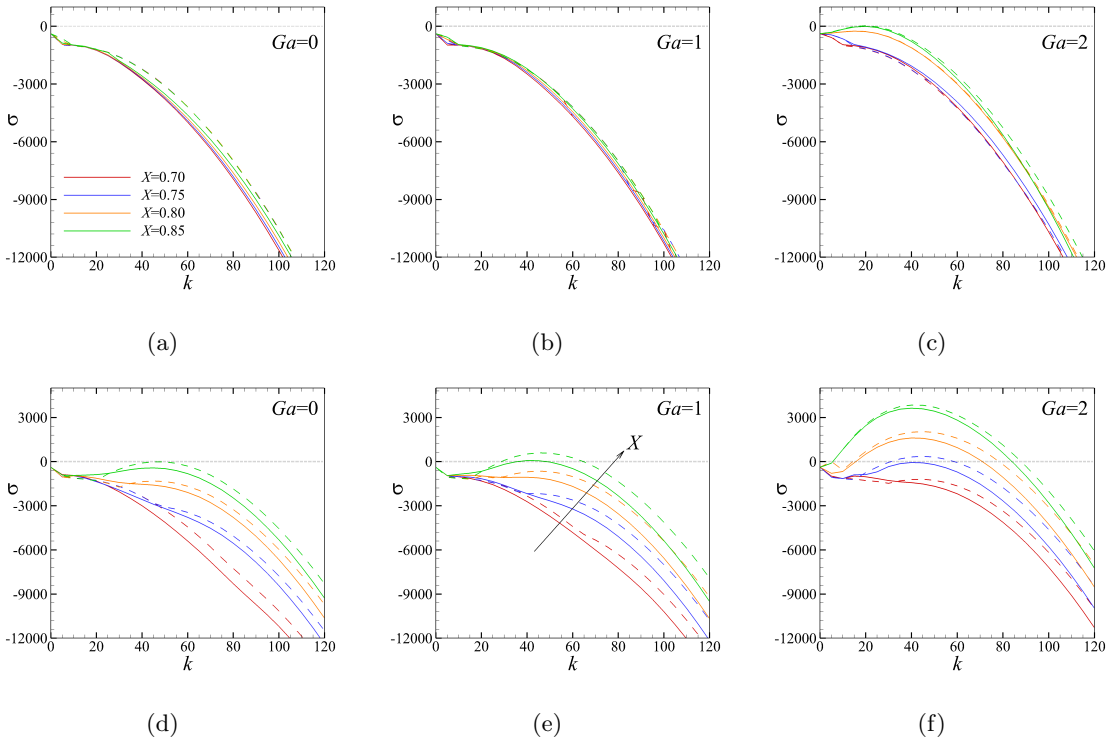

Figure 5.3: Orr-Sommerfeld stability analysis results at different X locations and GL parameters as stated at (a, b, c) $Ra = 5 \times 10^6$, (d, e, f)$Ra = 5 \times 10^7$. Solid lines represents transverse roll instability ($\beta = 0$) and the dashed line corresponds to longitudinal instability ($\alpha = 0$).

Figs. 5.4d to 5.4f present the local stability analysis results at one order of magnitude higher Rayleigh number i.e. $Ra = 5 \times 10^7$. At this (and higher) Rayleigh numbers, perturbations growth rates corresponding to the transverse rolls locate higher than longitudinal rolls in $\sigma - k$ space, which indicates the precedence of the transverse compared to the longitudinal rolls instabilities transitions to unstable region. Presented data in Fig. 5.4d also indicates that at $Ra = 5 \times 10^7$ and $Ga = 0$, transverse roll instabilities

becomes neutrally stable at $X = 0.85$, while the predicted critical Rayleigh number at $Ga = 0$ from the linear stability analysis was found equal to $Ra_{cr} = 6.46 \times 10^8$, which is one order of magnitude higher than the predicted value by the local stability analysis. Presented local stability results at the same Rayleigh number at $Ga = 1$ (Fig. 5.4e) shows crossing of the maximum longitudinal roll instability over the considered wavenumbers with $\sigma = 0$ while the maximum growth rate of the perturbations corresponding to the transverse roll instability has already passed this region. Similar to $Ga = 0$, this shows one order of magnitude lower value for the critical Rayleigh number at $Ga = 1$ compared to predicted critical Rayleigh number via linear stability analysis.

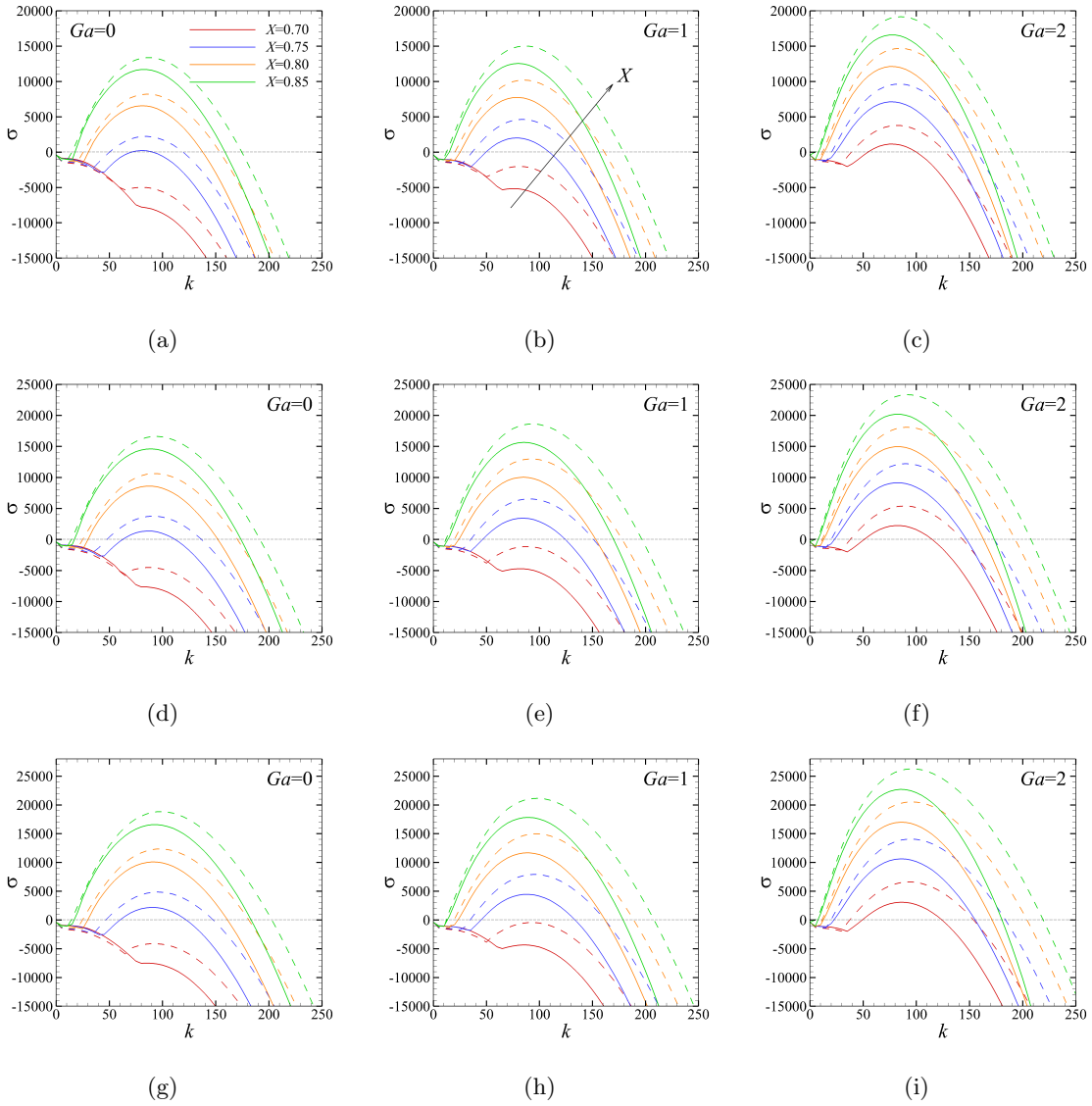

Figure 5.4: Orr-Sommerfeld stability analysis results at different X locations and GL parameters as stated at (a, b, c) $Ra = 5 \times 10^6$, (d, e, f)$Ra = 5 \times 10^7$. Solid lines represents transverse roll instability ($\beta = 0$) and the dashed line corresponds to longitudinal instability ($\alpha = 0$).

Fig. 5.5 shows local stability analysis of HC that are conducted at the critical Rayleigh number corresponding to $Ga = 0, 1$ and 2 predicted by the linear stability analysis. Figs. 5.5a to 5.5c show the local stability analysis results at $Ra = 4.23 \times 10^8$, Figs. 5.5d to 5.5f show the local stability analysis results at $Ra = 5.50 \times 10^8$ and Figs. 5.5g to 5.5i show the local stability analysis results at $Ra = 6.46 \times 10^8$ corresponding to critical Rayleigh number at $Ga = 2$. As seen, the maximum of the perturbations growth rates for all considered X-locations are above $\sigma = 0$ at $Ga = 2$ in Figs. 5.5c, 5.5f and 5.5i, but the optimum of the perturbations growth rate at $X = 0.7$ remains in the stable region ($\sigma \leq 0$) for $Ga = 0$ and 1. This reflects the non-Boussinesq effects of GL parameter to push the buoyancy-driven flow toward the local instability by increasing Ga. A feature of the presented data in Fig. 5.5 is alteration the dominant wavenumber of the transverse and longitudinal rolls. One-dimensional stability results indicate that, by increasing Ga in the convection-dominated regime, transverse roll are preceded to unstable region and the location of the optimum growth rate occurs at a higher wavenumber compared to the longitudinal roll. This feature is consistent with the observed decrease in distance between the transverse roll structures by increasing the Rayleigh number in simulations reported by Gayen et al. [28].

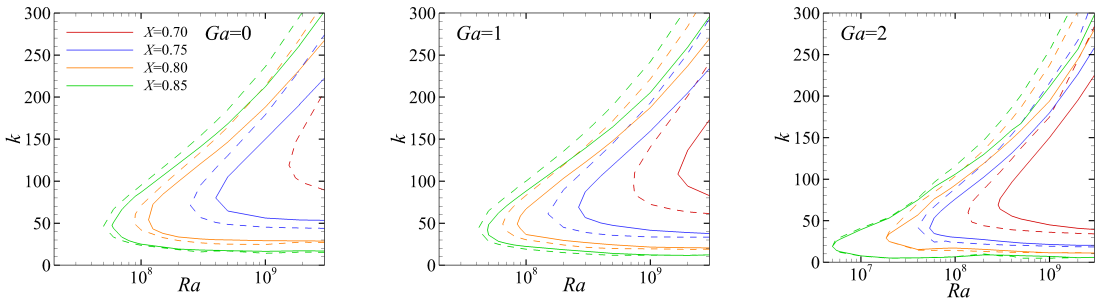

Figure 5.5: Marginal stability charts at different X locations and GL parameters including (a) $Ga = 0$ (b) $Ga = 1$ (c) $Ga = 2$. Solid lines represents transverse roll instability ($\beta = 0$) and the dashed line corresponds to longitudinal instability ($\alpha = 0$).

The marginal stability charts are mapped in Fig. 5.6 for different X-locations and three GL parameters including $Ga = 0, 1$ and 2. Similar to Figs. 5.4 and 5.5, solid lines represents transverse rolls instability and the dashed line corresponds to longitudinal instability rolls. Results demonstrate that the transverse rolls to be slightly more unstable than longitudinal rolls (having a slightly lower dominant Rayleigh number for each X). At $Ga = 0$ and 1, precedence of the transverse rolls is clear against the longitudinal

ones at $X = 0.85$ and lower X-locations but at $Ga = 2$, transition of the transverse and longitudinal instability rolls to unstable region occurs almost concurrently and remains unaltered up to $Ra \leq 9 \times 10^7$. It is also found that for $Ra \geq 10^9$ (especially for $Ga = 1$ and 2), the marginal stability lines of the transverse rolls from a relatively more stable region farther the hot end-wall exceed from the longitudinal instability rolls from a location closer to the right side wall which is in agreement with the observed replacement of transverse-roll structures by longitudinal-roll structures within the horizontal convection boundary layer in the three-dimensional simulations by Gayen et al. [28].

5.6 Summary of the chapter

In this chapter, the average Nusselt number was scaled against the Rayleigh number at different GL parameters concluding that, a higher Ga leads to a lower Nu_{avg} in the convection-dominated regime. An entropy generation analysis is conducted to map heat transfer evolution from conduction to convection using a variable irreversibility distribution ratio in terms of the Brinkman number and GL parameter. It is found that at $Ra \approx 6 \times 10^5$ for $Ga \gtrsim 0.5$, the average Bejan number crosses with $Be_{avg} = 0.5$ where conduction and convection heat transfer mechanisms are in balance. The transition of the average Bejan number from conduction to convection-dominated regime follows closely to reciprocal ($Be_{avg} \sim Ra^{-1}$) for $Ga = 0$ but the same process occurs with $Be_{avg} \sim Ra^{-0.5}$ relation at $Ga = 2$. A local Orr–Sommerfeld type stability analysis is also conducted for a limited range of the enclosure in which buoyancy-driven flow is strictly parallel to the horizontal boundary to check the transverse and longitudinal roll instabilities. Local stability analysis results demonstrate that, HC becomes locally unstable two orders of magnitude lower than the critical Rayleigh number predicted by the linear stability analysis at $Ga = 2$. This difference becomes smaller to one order of magnitude at $Ga = 0$ and 1. Local stability analysis results predict a higher wavenumber for the dominant eigenmode by increasing the Rayleigh number with precedence of transverse rolls against the longitudinal ones to unstable region.

Chapter 6

6 Conclusions and directions for future research

In this thesis, horizontal convection has been studied under the centrifugal buoyancy approximation as a subclass of Gay-Lussac approximation. The thesis achievements are outlined in the following. Thereafter, two ideas are proposed to study HC regarding the non-Boussinesq theme of the thesis as directions for future studies.

Chapter 1 was dedicated to define/categorise different possible scenarios for numerical simulation of natural convection problems. A general structure overarching two major classes of compressible and incompressible approaches was constructed to show the location of the selected strategy among others in the incompressible category.

Chapter 2 dealt with the introduction of the Gay-Lussac approach and how it distinguishes against the Boussinesq approximation. It is shown that how extending the density variations beyond only the gravity term via a linear density state equations leads to emergence of the Gay-Lussac parameter as a product of the volumetric thermal expansion coefficient and reference temperature difference. It is also shown that how appearance of the Gay-Lussac parameter appears in the linear density state equation, restricts the minimum and maximum values that this parameter may take. In the next step, a simplified version of the Gay-Lussac approach was presented in which, the density variations were removed from the continuity equation. It was shown that the simplified approach gives identical results with the original one with a lower computational cost and no difference in the convergence rate.

In chapter 3, the centrifugal buoyancy approximation was introduced as a Gay-Lussac type approach. The philosophy behind extension of density variations to the advection term as well as the gravity term was discussed and it shown that the centrifugal buoyancy approximation works slightly better than the Boussinesq approximation in comparison with a robust method such as the weakly compressible approach.

In chapter 4, horizontal convection studied in a rather shallow enclosure with an aspect ration of height to length 0.16 at a fixed unity Prandtl number under the centrifugal buoyancy approximation. Different temperature fields and flow patterns (in the context of vorticity fields) were scrutinised over the physical range of the Gay-Lussac parameter. To conduct the linear stability analysis, a new form of the linearised momentum equation incorporating the Gay-Lussac parameter was derived. It was found that in the

range of $Ra \geq 4.23 \times 10^8$, the buoyancy-driven flow is likely to be unstable beyond a specified Ga value. Linear stability analysis results predict that all three-dimensional transitions are via an oscillatory instability mode of the steady flow and the spanwise wavelength of the perturbations increases by increasing the Rayleigh number. Linear stability analysis results were verified against the 3D-DNS simulations with a maximum discrepancy of 4% in growth rate of the perturbations. A Stuart–Landau stability analysis was also performed to ascertain the non-linear nature of transition to an unstable state concluding that the three-dimensional flow transition consistently occurs through a supercritical bifurcation.

In chapter 5, Nusselt number scaled against the Rayleigh number at different Gay-Lussac parameters indicating that, in the convection-dominated regime, a higher Gay-Lussac parameter is associated with a lower average Nusselt number. Heat transfer mechanism evolution from conduction to convection were analysed using entropy generation analysis. It is shown that the irreversibility distribution ratio may be expressed in terms of the Brinkman number and Gay-Lussac parameter. Entropy generation analysis indicates that Ga has no effect in the conduction-dominated regime while it expands regions under the influence of conduction in the convection-dominated regime. A local stability analysis capturing transverse and longitudinal rolls is also conducted on extracted velocity profiles from a limited range of the physical domain in which the one dimensional flow assumption was found valid. The local stability analysis demonstrates the buoyancy-driven flow becomes locally unstable two order of magnitude lower at $Ga = 2$ and one order of magnitude lower at $Ga = 0$ and 1 compared to global stability analysis predicted by the linear stability analysis with precedence of the transverse rolls instability compared to longitudinal ones in transition to unstable region.

6.1 Directions for future research

Based on the two main aspects of this thesis, i.e. non-Boussinesq approximations for buoyancy and their application to benchmark problems and horizontal convection, two ideas are proposed as directions for future research.

Regarding the presented structure in the first section and different possible scenarios for numerical simulation of natural convection problems and application of the horizontal convection in oceanic flow patterns, it is suggested to replicate the current research with consideration of the inversion parameter. The inversion parameter is a dimensionless

temperature that appears in the momentum equation when the working fluid is close to the temperature of its maximum density. There are many sea levels with a temperature around 4 ^{o}C close to the water's temperature of maximum density. Hence, the linear state relation between density and temperature is in fact quiet inaccurate.

Another suggestion to extend this work is to consider salinity effects when horizontal convection is simulated to stand for oceanic flow patterns. In this state, the density variations are not approximated just by temperature variations but both temperature and salinity differences are taken into account. Considering salinity effects requires solving concentration equation accompanied by other governing equations. Extension of the density variations to the advection term of the conecntration equation leads to emerging a new dimensionless parameter as a product of concentration expansion coefficient and concentration difference.

Finally, further stability analysis is possible through foundation of the adjoint linearised equations, facilitating exploration of the contribution of non-Boussinesq approximation effects towards the linearised transient growth in these systems, adapting the method developed by [29–31].

The following references are pertinent to citations in the body of the thesis, and excludes references in each of the included published works.

References

1. Bergman, T. L., Lavine, A. S., Incropera, F. P. & DeWitt, D. P. *Introduction to heat transfer* (John Wiley & Sons, 2011).

2. Kuehn, T. & Goldstein, R. An experimental and theoretical study of natural convection in the annulus between horizontal concentric cylinders. *Journal of Fluid mechanics* **74,** 695–719 (1976).

3. Mayeli, P. & Sheard, G. J. Buoyancy-driven flows beyond the Boussinesq approximation: A brief review. *International Communications in Heat and Mass Transfer* **125,** 105316 (2021).

4. Pesso, T. & Piva, S. Laminar natural convection in a square cavity: low Prandtl numbers and large density differences. *International Journal of Heat and Mass Transfer* **52,** 1036–1043 (2009).

5. Mayeli, P. & Sheard, G. J. Natural convection and entropy generation in square and skew cavities due to large temperature differences: A Gay–Lussac-type vorticity stream-function approach. *International Journal for Numerical Methods in Fluids* (2021).

6. Mayeli, P. & Sheard, G. J. A centrifugal buoyancy formulation for Boussinesq-type natural convection flows applied to the annulus cavity problem. *International Journal for Numerical Methods in Fluids* **93,** 683–702 (2021).

7. Lopez, J. M., Marques, F. & Avila, M. The Boussinesq approximation in rapidly rotating flows. *Journal of fluid mechanics* **737,** 56–77 (2013).

8. Bryan, K. & Cox, M. D. A numerical investigation of the oceanic general circulation. *Tellus* **19,** 54–80 (1967).

9. King, S. D. & Anderson, D. L. Edge-driven convection. *Earth and Planetary Science Letters* **160,** 289–296 (1998).

10. Chiu-Webster, S., Hinch, E. & Lister, J. Very viscous horizontal convection. *Journal of Fluid Mechanics* **611,** 395–426 (2008).

11. Leigh, M. A., Tsai, T. & Sheard, G. J. Probing horizontal convection instability via perturbation of the forcing boundary layer using a synthetic jet. *International Journal of Thermal Sciences* **110,** 251–260 (2016).

12. Sheard, G. J. & King, M. P. Horizontal convection: effect of aspect ratio on Rayleigh number scaling and stability. *Applied Mathematical Modelling* **35,** 1647–1655 (2011).

13. Karniadakis, G. E., Israeli, M. & Orszag, S. A. High-order splitting methods for the incompressible Navier-Stokes equations. *Journal of computational physics* **97,** 414–443 (1991).

14. Drazin, P. G. & Reid, W. H. *Hydrodynamic stability* (Cambridge university press, 2004).

15. Sheard, G. J., Thompson, M. C. & Hourigan, K. Asymmetric structure and non-linear transition behaviour of the wakes of toroidal bodies. *European Journal of Mechanics-B/Fluids* **23,** 167–179 (2004).

16. Sheard, G. J., Fitzgerald, M. J. & Ryan, K. Cylinders with square cross-section: wake instabilities with incidence angle variation. *Journal of Fluid Mechanics* **630,** 43–69 (2009).

17. Sapardi, A. M., Hussam, W. K., Pothérat, A. & Sheard, G. J. Linear stability of confined flow around a 180-degree sharp bend. *Journal of Fluid Mechanics* **822,** 813–847 (2017).

18. Vo, T., Montabone, L., Read, P. L. & Sheard, G. J. Non-axisymmetric flows in a differential-disk rotating system. *Journal of Fluid Mechanics* **775,** 349–386 (2015).

19. Rossby, H. *On thermal convection driven by non-uniform heating from below: an experimental study* in *Deep Sea Research and Oceanographic Abstracts* **12** (1965), 9–16.

20. Bejan, A. A study of entropy generation in fundamental convective heat transfer (1979).

21. Basak, T., Kaluri, R. S. & Balakrishnan, A. Effects of thermal boundary conditions on entropy generation during natural convection. *Numerical Heat Transfer, Part A: Applications* **59,** 372–402 (2011).

22. Ilis, G. G., Mobedi, M. & Sunden, B. Effect of aspect ratio on entropy generation in a rectangular cavity with differentially heated vertical walls. *International Communications in Heat and Mass Transfer* **35,** 696–703 (2008).

23. Siggers, J., Kerswell, R. & Balmforth, N. Bounds on horizontal convection. *Journal of Fluid Mechanics* **517,** 55–70 (2004).

24. Shishkina, O., Grossmann, S. & Lohse, D. Heat and momentum transport scalings in horizontal convection. *Geophysical research letters* **43,** 1219–1225 (2016).

25. Tsai, T., Hussam, W. K., Fouras, A. & Sheard, G. J. The origin of instability in enclosed horizontally driven convection. *International Journal of Heat and Mass Transfer* **94,** 509–515 (2016).

26. Orszag, S. A. Accurate solution of the Orr–Sommerfeld stability equation. *Journal of Fluid Mechanics* **50,** 689–703 (1971).

27. Reid, W. & Harris, D. Some further results on the Bénard problem. *The Physics of fluids* **1,** 102–110 (1958).

28. Gayen, B., Griffiths, R. W. & Hughes, G. O. Stability transitions and turbulence in horizontal convection. *Journal of Fluid Mechanics* **751,** 698–724 (2014).

29. Giannetti, F. & Luchini, P. Structural sensitivity of the first instability of the cylinder wake. *Journal of Fluid Mechanics* **581,** 167–197 (2007).

30. Marquet, O., Sipp, D. & Jacquin, L. Sensitivity analysis and passive control of cylinder flow. *Journal of Fluid Mechanics* **615,** 221–252 (2008).

31. Marquet, O. & Lesshafft, L. Identifying the active flow regions that drive linear and nonlinear instabilities. *arXiv preprint arXiv:1508.07620* (2015).

Appendix

Linearised perturbation equations incorporating the GL parameter for the linear stability analysis and Orr–Sommerfeld type analysis are derived here.

A Derivation of the linearised perturbation equations under the centrifugal buoyancy approximation

For the linear stability analysis under the centrifugal buoyancy approximation, continuity and energy equations are not modified from their traditional form, thus here, only the linearised momentum equation is derived. Derivation starts with inserting an infinitesimal three-dimensional perturbation $\epsilon \boldsymbol{U}'(X,Y,Z)$ and $\epsilon\Theta'(X,Y,Z)$ to the dimensionless form of the governing equation under the Boussinesq approximation as follows:

$$\begin{aligned}\frac{\partial(\boldsymbol{U}+\epsilon\boldsymbol{U}')}{\partial t} = -[1-Ga(\Theta+\epsilon\Theta')]((\boldsymbol{U}+\epsilon\boldsymbol{U}')\cdot\nabla)(\boldsymbol{U}+\epsilon\boldsymbol{U}') \\ -\nabla(P+P') + Pr\nabla^2(\boldsymbol{U}+\epsilon\boldsymbol{U}') - RaPr(\Theta+\epsilon\Theta')\mathbf{e}_g.\end{aligned} \tag{A.1}$$

Using the gradient rule of $\nabla(\boldsymbol{f}+\boldsymbol{g}) = \nabla\boldsymbol{f}+\nabla\boldsymbol{g}$ where $\boldsymbol{f}$ and $\boldsymbol{g}$ are two vectors, the LHS and the second to fourth terms of the RHS can be split to the following parts:

$$\begin{aligned}\frac{\partial\boldsymbol{U}}{\partial t} + \frac{\partial\epsilon\boldsymbol{U}'}{\partial t} = -[1-Ga(\Theta+\epsilon\Theta')]((\boldsymbol{U}+\epsilon\boldsymbol{U}')\cdot\nabla)(\boldsymbol{U}+\epsilon\boldsymbol{U}') \\ -\nabla P - \nabla P' + Pr\nabla^2\boldsymbol{U} + Pr\nabla^2\epsilon\boldsymbol{U}' - RaPr\Theta\mathbf{e}_g - RaPr\epsilon\Theta'\mathbf{e}_g.\end{aligned} \tag{A.2}$$

Expanding the advection term using the $\boldsymbol{f}\cdot\boldsymbol{g} = \boldsymbol{f}^T\boldsymbol{g}$ rule yields,

$$\begin{aligned}[1-Ga(\Theta+\epsilon\Theta')]((\boldsymbol{U}+\epsilon\boldsymbol{U}')\cdot\nabla)(\boldsymbol{U}+\epsilon\boldsymbol{U}') = \\ [1-Ga(\Theta+\epsilon\Theta')](\boldsymbol{U}+\epsilon\boldsymbol{U}')^T\nabla((\boldsymbol{U}+\epsilon\boldsymbol{U}')),\end{aligned} \tag{A.3}$$

which can be further expanded to

$$\begin{aligned}[1-Ga(\Theta+\epsilon\Theta')](\boldsymbol{U}+\epsilon\boldsymbol{U}')^T\nabla((\boldsymbol{U}+\epsilon\boldsymbol{U}')) = \\ [1-Ga(\Theta+\epsilon\Theta')]\,\boldsymbol{U}^T\nabla((\boldsymbol{U}+\epsilon\boldsymbol{U}')) \\ +[1-Ga(\Theta+\epsilon\Theta')]\epsilon\boldsymbol{U}'^T\nabla((\boldsymbol{U}+\epsilon\boldsymbol{U}')),\end{aligned} \tag{A.4}$$

and then further to

$$\begin{aligned}[1-Ga(\Theta+\epsilon\Theta')][\boldsymbol{U}^T\nabla\boldsymbol{U}+\boldsymbol{U}^T\nabla\epsilon\boldsymbol{U}'+\epsilon\boldsymbol{U}'^T\nabla\boldsymbol{U}+\epsilon\boldsymbol{U}'^T\nabla\epsilon\boldsymbol{U}'] = \\ \boldsymbol{U}^T\nabla\boldsymbol{U}+\boldsymbol{U}^T\nabla\epsilon\boldsymbol{U}'+\epsilon\boldsymbol{U}'^T\nabla\boldsymbol{U}+\epsilon\boldsymbol{U}'^T\nabla\epsilon\boldsymbol{U}' \\ -Ga\Theta[\boldsymbol{U}^T\nabla\boldsymbol{U}+\boldsymbol{U}^T\nabla\epsilon\boldsymbol{U}'+\epsilon\boldsymbol{U}'^T\nabla\boldsymbol{U}+\epsilon\boldsymbol{U}'^T\nabla\epsilon\boldsymbol{U}'] \\ -Ga\epsilon\Theta'[\boldsymbol{U}^T\nabla\boldsymbol{U}+\boldsymbol{U}^T\nabla\epsilon\boldsymbol{U}'+\epsilon\boldsymbol{U}'^T\nabla\boldsymbol{U}+\epsilon\boldsymbol{U}'^T\nabla\epsilon\boldsymbol{U}'].\end{aligned} \tag{A.5}$$

Ignoring terms of order $O(\epsilon^2)$ and $O(\epsilon^3)$, as these are negligible for small ϵ, and using the $\boldsymbol{f}\cdot\boldsymbol{g}=\boldsymbol{f}^T\boldsymbol{g}$ rule in reverse, yields the following expression for the advection term

$$\begin{aligned}[1-Ga(\Theta+\epsilon\Theta')](((\boldsymbol{U}+\epsilon\boldsymbol{U}')\cdot\nabla)(\boldsymbol{U}+\epsilon\boldsymbol{U}') = (\boldsymbol{U}\cdot\nabla)\boldsymbol{U}+(\boldsymbol{U}\cdot\nabla)\epsilon\boldsymbol{U}'+ \\ (\epsilon\boldsymbol{U}'\cdot\nabla)\boldsymbol{U}-Ga\Theta[\boldsymbol{U}^T\nabla\boldsymbol{U}+\boldsymbol{U}^T\nabla\epsilon\boldsymbol{U}'+\epsilon\boldsymbol{U}'^T\nabla\boldsymbol{U}]-Ga\epsilon\Theta'[\boldsymbol{U}^T\nabla\boldsymbol{U}]+O(\epsilon^2) \\ =[1-Ga\Theta](((\boldsymbol{U}\cdot\nabla)\boldsymbol{U}+(\boldsymbol{U}\cdot\nabla)\epsilon\boldsymbol{U}'+(\epsilon\boldsymbol{U}'\cdot\nabla)\boldsymbol{U})-Ga\epsilon\Theta'[(\boldsymbol{U}\cdot\nabla)\boldsymbol{U}]+O(\epsilon^2).\end{aligned} \tag{A.6}$$

In the next step, the linearised advection term is implemented into Eq. A.2 as follows:

$$\begin{aligned}\frac{\partial\boldsymbol{U}}{\partial t}+\frac{\partial\epsilon\boldsymbol{U}'}{\partial t} = -[1-Ga\Theta](((\boldsymbol{U}\cdot\nabla)\boldsymbol{U}+(\boldsymbol{U}\cdot\nabla)\epsilon\boldsymbol{U}'+(\epsilon\boldsymbol{U}'\cdot\nabla)\boldsymbol{U}) \\ +Ga\epsilon\Theta'[(\boldsymbol{U}\cdot\nabla)\boldsymbol{U}]-\nabla P-\nabla P'+Pr\nabla^2\boldsymbol{U}+Pr\nabla^2\epsilon\boldsymbol{U}'-RaPr\Theta\mathbf{e}_g \\ -RaPr\epsilon\Theta'\mathbf{e}_g.\end{aligned} \tag{A.7}$$

Subtraction of Eq. A.7 from the dimensionless form of the momentum equation containing just the base flow and dropping ϵ coefficients yields

$$\begin{aligned}\frac{\partial\boldsymbol{U}'}{\partial t} = -[1-Ga\Theta](((\boldsymbol{U}\cdot\nabla)\boldsymbol{U}'+(\boldsymbol{U}'\cdot\nabla)\boldsymbol{U})+Ga\Theta'[(\boldsymbol{U}\cdot\nabla)\boldsymbol{U}] \\ -\nabla P'+Pr\nabla^2\boldsymbol{U}'-RaPr\Theta'\mathbf{e}_g.\end{aligned} \tag{A.8}$$

Replacing the GL parameter with the Rayleigh, Prandtl and Froude number, Eq. A.8 may be also expressed as

$$\begin{aligned}\frac{\partial\boldsymbol{U}'}{\partial t} = -[1-Ga\Theta](((\boldsymbol{U}\cdot\nabla)\boldsymbol{U}'+(\boldsymbol{U}'\cdot\nabla)\boldsymbol{U})-\nabla P'+Pr\nabla^2\boldsymbol{U}' \\ -RaPr\Theta'(\mathbf{e}_g-Fr(\boldsymbol{U}\cdot\nabla)\boldsymbol{U}).\end{aligned} \tag{A.9}$$

B Derivation of the linearised perturbation equations under the centrifugal buoyancy approximation for the local stability analysis

The derivation procedure of the governing equations starts by assuming that perturbations adopt a general form of $\tilde{\phi}(y)e^{i(\alpha x+\beta z-\omega t)}$. Substitution of this into the linearised Navier—Stokes equations under the centrifugal buoyancy approximation yields

$$\nabla \cdot \tilde{U}(y)e^{i(\alpha x+\beta z-\omega t)} = 0, \tag{B.1}$$

$$\begin{aligned}\frac{\partial \tilde{U}(y)e^{i(\alpha x+\beta z-\omega t)}}{\partial t} = &-[1-Ga\Theta]((U\cdot\nabla)\tilde{U}(y)e^{i(\alpha x+\beta z-\omega t)} + (\tilde{U}(y)e^{i(\alpha x+\beta z-\omega t)}\cdot\nabla)\, U) \\ &+Ga\tilde{\Theta}(y)e^{i(\alpha x+\beta z-\omega t)}[(U\cdot\nabla)\, U] - \nabla\tilde{P}e^{i(\alpha x+\beta z-\omega t)} \\ &+Pr\nabla^2\tilde{U}(y)e^{i(\alpha x+\beta z-\omega t)} - RaPr\tilde{\Theta}(y)e^{i(\alpha x+\beta z-\omega t)}e_g.\end{aligned} \tag{B.2}$$

$$\begin{aligned}\frac{\partial \tilde{\Theta}(y)e^{i(\alpha x+\beta z-\omega t)}}{\partial t} = &-((U\cdot\nabla)\tilde{\Theta}(y)e^{i(\alpha x+\beta z-\omega t)} + (\tilde{\Theta}(y)e^{i(\alpha x+\beta z-\omega t)}\cdot\nabla)\, U) \\ &+\nabla^2\tilde{\Theta}(y)e^{i(\alpha x+\beta z-\omega t)}.\end{aligned} \tag{B.3}$$

The advection tnesor part of the momentum equations simplifies to

$$\begin{aligned}(U\cdot\nabla)\tilde{U}e^{i(\alpha x+\beta z-\omega t)} = e^{i(\alpha x+\beta z-\omega t)}&\begin{bmatrix} i\alpha U\tilde{U} & VD\tilde{U} & i\beta W\tilde{U} \\ i\alpha U\tilde{V} & VD\tilde{V} & i\beta W\tilde{V} \\ i\alpha U\tilde{W} & VD\tilde{W} & i\beta W\tilde{W}\end{bmatrix} = \\ e^{i(\alpha x+\beta z-\omega t)}&\begin{bmatrix} i\alpha U\tilde{U} & VD\tilde{U} & 0 \\ i\alpha U\tilde{V} & VD\tilde{V} & 0 \\ i\alpha U\tilde{W} & VD\tilde{W} & 0\end{bmatrix},\end{aligned} \tag{B.4}$$

$$\begin{aligned}(\tilde{U}e^{i(\alpha x+\beta z-\omega t)}\cdot\nabla)\, U = e^{i(\alpha x+\beta z-\omega t)}&\begin{bmatrix} \tilde{U}\frac{\partial U}{\partial X} & \tilde{V}\frac{\partial U}{\partial Y} & \tilde{W}\frac{\partial U}{\partial Z} \\ \tilde{U}\frac{\partial V}{\partial X} & \tilde{V}\frac{\partial V}{\partial Y} & \tilde{W}\frac{\partial V}{\partial Z} \\ \tilde{U}\frac{\partial W}{\partial X} & \tilde{V}\frac{\partial W}{\partial Y} & \tilde{W}\frac{\partial W}{\partial Z}\end{bmatrix} = \\ e^{i(\alpha x+\beta z-\omega t)}&\begin{bmatrix} 0 & \tilde{V}\frac{\partial U}{\partial Y} & 0 \\ 0 & \tilde{V}\frac{\partial V}{\partial Y} & 0 \\ 0 & 0 & 0\end{bmatrix},\end{aligned} \tag{B.5}$$

$$(U\cdot\nabla)U = \begin{bmatrix} U\frac{\partial U}{\partial X} & V\frac{\partial U}{\partial Y} & W\frac{\partial U}{\partial Z} \\ U\frac{\partial V}{\partial X} & V\frac{\partial V}{\partial Y} & W\frac{\partial V}{\partial Z} \\ U\frac{\partial W}{\partial X} & V\frac{\partial W}{\partial Y} & W\frac{\partial W}{\partial Z} \end{bmatrix} = \begin{bmatrix} 0 & V\frac{\partial U}{\partial Y} & 0 \\ 0 & V\frac{\partial V}{\partial Y} & 0 \\ 0 & 0 & 0 \end{bmatrix}, \tag{B.6}$$

where D represents the partial derivatives with respect to Y. Zero terms include terms involving W (the base flow is 2D, i.e.$W = 0$) and invariant in time and the X and Z directions i.e. $\partial/\partial X = \partial/\partial Z = 0$. Applying these assumptions in the continuity equation requires V to be zero,

$$\partial U/\partial X + \partial V/\partial Y + \partial W/\partial Z = 0 \rightarrow \partial V/\partial Y = 0 \rightarrow V = 0. \tag{B.7}$$

Thus, the advection tensor becomes more simplified as follows,

$$(U\cdot\nabla)\tilde{U}e^{i(\alpha x+\beta z-\omega t)} = e^{i(\alpha x+\beta z-\omega t)} \begin{bmatrix} i\alpha U\tilde{U} & 0 & 0 \\ i\alpha U\tilde{V} & 0 & 0 \\ i\alpha U\tilde{W} & 0 & 0 \end{bmatrix}, \tag{B.8}$$

$$(\tilde{U}e^{i(\alpha x+\beta z-\omega t)}\cdot\nabla)U = e^{i(\alpha x+\beta z-\omega t)} \begin{bmatrix} 0 & \tilde{V}\frac{\partial U}{\partial Y} & 0 \\ 0 & 0 & 0 \\ 0 & 0 & 0 \end{bmatrix}, \tag{B.9}$$

$$(U\cdot\nabla)U = \begin{bmatrix} U\frac{\partial U}{\partial X} & V\frac{\partial U}{\partial Y} & W\frac{\partial U}{\partial Z} \\ U\frac{\partial V}{\partial X} & V\frac{\partial V}{\partial Y} & W\frac{\partial V}{\partial Z} \\ U\frac{\partial W}{\partial X} & V\frac{\partial W}{\partial Y} & W\frac{\partial W}{\partial Z} \end{bmatrix} = \begin{bmatrix} 0 & 0 & 0 \\ 0 & 0 & 0 \\ 0 & 0 & 0 \end{bmatrix}, \tag{B.10}$$

The X and Z-momentum perturbation equations after being divided by $e^{i(\alpha X+\beta Z-\omega t)}$ may be expressed as

$$-i\omega\tilde{U} = -(1-Ga\Theta)[i\alpha U\tilde{U} + \tilde{V}U'] - i\alpha\tilde{P} + Pr(D^2-k^2)\tilde{U}, \tag{B.11}$$

$$-i\omega\tilde{W} = -(1-Ga\Theta)[i\alpha U\tilde{W}] - i\beta\tilde{P} + Pr(D^2-k^2)\tilde{W}, \tag{B.12}$$

where $k^2 = \alpha^2 + \beta^2$. Now, multiplying the X-momentum perturbation equation by $i\alpha$ and the

Z-momentum perturbation equation by $i\beta$ and summing the two equations yields

$$\begin{aligned} i\omega D\tilde{V} = i\alpha(1-Ga\Theta)UD\tilde{V} - i\alpha(1-Ga\Theta)\tilde{V}U' + k^2\tilde{P} \\ -Pr(D^2-k^2)(D\tilde{V}). \end{aligned} \tag{B.13}$$

In Eq. B.13, continuity is incorporated in the following form,

$$i(\alpha\tilde{U}+\beta\tilde{W}) + D\tilde{V} = 0 \rightarrow -i(\alpha\tilde{U}+\beta\tilde{W}) = D\tilde{V}. \tag{B.14}$$

Applying the D operator on the both sides of Eq. B.13 gives

$$\begin{aligned} k^2 D\tilde{P} = i(\omega - \alpha(1-Ga\Theta)U)D^2\tilde{V} + i\alpha(1-Ga\Theta)\tilde{V}U'' \\ +i\alpha(1-Ga\Theta')(VU' - UD\tilde{V}) + Pr(D^2-k^2)(D^2\tilde{V}). \end{aligned} \tag{B.15}$$

On the other hand, Y-momentum perturbation equation after being divided by an $e^{i(\alpha X+\beta Z-\omega t)}$ and multiplied by k^2 gives,

$$\begin{aligned} -i\omega k^2\tilde{V} = i\alpha(1-Ga\Theta)Uk^2\tilde{V} - k^2 D\tilde{P} + Pr(D^2-k^2)k^2\tilde{V} \\ -k^2 RaPr\tilde{\Theta}e_g. \end{aligned} \tag{B.16}$$

Finally, replacing the $k^2 D\tilde{P}$ term derived from Eq. B.15 in Eq. B.16 after some algebraic rearrangement yields

$$\begin{aligned} i\alpha[(1-Ga\bar{\Theta})\bar{U}'' - (1-Ga\bar{\Theta})\bar{U}'(D^2-k^2) + (1-Ga\bar{\Theta}')(\bar{U}' - \bar{U}D)]\tilde{V} \\ +Pr(D^2-k^2)^2\tilde{V} + k^2 RaPr\tilde{\Theta}e_g = -i\omega(D^2-k^2)\tilde{V}. \end{aligned} \tag{B.17}$$

A similar derivation procedure is used for the perturbation energy equation. After substitution of the perturbation and applying introduced assumptions for the convection part,

$$(U\cdot\nabla)\tilde{\Theta}(y)e^{i(\alpha x+\beta z-\omega t)} \rightarrow i\alpha U\tilde{\Theta} + VD\tilde{\Theta} + i\beta W\tilde{\Theta} = i\alpha U\tilde{\Theta}, \tag{B.18}$$

$$\begin{aligned} (\tilde{\Theta}(y)e^{i(\alpha x+\beta z-\omega t)}\cdot\nabla)U \rightarrow \tilde{U}\partial\Theta/\partial X + \tilde{V}\partial\Theta/\partial Y + \tilde{W}\partial\Theta/\partial Z = \\ \tilde{V}\partial\Theta/\partial Y. \end{aligned} \tag{B.19}$$

Thus the perturbation energy equation may be expressed as

$$-i\omega\tilde{\Theta} = -[i\alpha U\tilde{\Theta} + \tilde{V}\Theta'] + (D^2-k^2)\tilde{\Theta}, \tag{B.20}$$

that can be arranged as

$$\Theta'\tilde{V} + [i\alpha U + (D^2 - k^2)]\tilde{\Theta} = i\omega\tilde{\Theta}. \tag{B.21}$$

Finally an eigenvalue problem is constructed using Eqs. B.17 and B.21 as $\mathbf{A}\mathbf{X}_k = \omega_k \mathbf{B}\mathbf{X}_k$, as stated in chapter 5, section 5.1. The matrices are constructed as follows,

$$\mathbf{A} = \begin{bmatrix} a & -k^2 RaPr \\ \Theta' & i\alpha U - (D^2 - k^2) \end{bmatrix}, \tag{B.22}$$

$$\mathbf{B} = \begin{bmatrix} -i(D^2 - k^2) & 0 \\ 0 & i \end{bmatrix}, \tag{B.23}$$

where in Eq. B.22, $a = i\alpha[(1 - Ga\bar{\Theta})\bar{U}'' - (1 - Ga\bar{\Theta})\bar{U}'(D^2 - k^2) + (1 - Ga\bar{\Theta}')(\bar{U}' - \bar{U}D) + Pr(D^2 - k^2)^2]$.